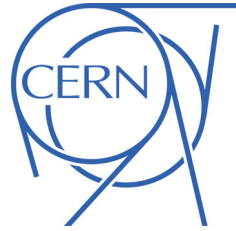




ATLAS NOTE

April 26, 2012



Search for the Standard Model Higgs boson in the decay channel

$H \rightarrow ZZ^{(*)} \rightarrow 4\ell$ with 4.8 fb^{-1} of pp collisions at $\sqrt{s} = 7 \text{ TeV}$

T. Alexopoulos⁵, C. Anastopoulos², B. Acharya³¹, G. Artoni¹, K. Assamagan³, M. Aurousseau⁴, K. Bachas², E. Benhar Noccioli²¹, T. Bernasconi²¹, N. Benekos²³, C. Bini¹, A. Calandri¹, M. Casolino²⁵, F. Cerutti³³, F. Conventi²⁶, S. Connell⁴, G. Carrillo Montoya⁶, L. Chevalier¹², T. Cuhadar Donszelmann⁸, A. Denton-Farnworth⁸, C. Di Donato²⁵, A. Di Simone⁹, C. Dionisi¹, R. Donnarumma¹, D. Fassouliotis¹⁰, O. Fedin²², L. R. Flores Castillo⁶, S. Giagu¹, M. Giunta²⁰, M. Goblirsch¹¹, S. Hassani¹², J. Hoffman¹³, M. Hoffmann³², L. Iconomidou-Fayard¹⁴, K. Iordanidou^{10,3}, V. Ippolito¹, X. Ju⁶, T. Koffas¹⁵, O. Kortner¹¹, C. Kourkoumelis¹⁰, T. Lagouri¹⁶, C. Lee^{4,30}, F. Lo Sterzo¹, C. Luci¹, C. Maiani¹, B. Mansoulie¹², J. Meyer²⁴, N. Morange¹², E. Monnier¹⁷, A. Morley², E. Mountricha^{5,12}, L. Nisati²⁷, R. Nicolaïdou¹², K. Nikolopoulos³, P. Ntsoeile⁴, J. Odier¹⁷, L. Pontecorvo²⁷, E. Paganis⁸, G. Pásztor²¹, A. Sanchez Pineda²⁵, S. Raddum²⁹, R. Rios¹³, A. Read²⁹, M. Rescigno²⁷, S. Rosati²⁷, E. Rossi¹, A. Schaffer¹⁴, O. Simard¹², R. Stroynowski¹³, F. Tarrade¹⁵, M. Teinturier¹⁴, E. Tiouchichine¹⁷, M. Vincter¹⁵, K. Whalen¹⁵, S. L. Wu⁶, H. Yang⁶

¹Sapienza Università di Roma and INFN Sezione di Roma, Roma

²CERN, Geneva

³Brookhaven National Laboratory, Upton

⁴University of Johannesburg, Johannesburg

⁵National Technical University Athens, Athens

⁶University of Wisconsin, Madison

⁸University of Sheffield, Sheffield

⁹Università degli Studi di Roma Tor Vergata, Roma

¹⁰University of Athens, Athens

¹¹MPG, Munich

¹²CEA Saclay (Commissariat à l'Energie Atomique), Gif-sur-Yvette

¹³Southern Methodist University, Dallas

¹⁴Laboratoire de l'accélérateur linéaire, Orsay

¹⁵Carleton University, Ottawa

¹⁶Universidad Autónoma de Madrid, Madrid

¹⁷Centre de Physique des Particules de Marseille, Marseille

²⁰Université de Montréal, Montréal

²¹Université de Genève, Geneva

²²Petersburg NPI, Gatchina

²³University of Illinois, Urbana IL

²⁴Julius-Maximilians-Universitat,Wurzburg

²⁵Università di Napoli Federico II and INFN Sezione di Napoli, Napoli

²⁶Università di Napoli Parthenope and INFN sezione di Napoli, Napoli

²⁷INFN Sezione di Roma, Roma

²⁸University of Copenhagen, Copenhagen

²⁹University of Oslo, Oslo

³⁰Academia Sinica, Taiwan

³¹Universita degli Studi di Udine, Udine

³²Niels Bohr Institute, Copenhagen

³³INFN,Laboratori Nazionali di Frascati, Roma

Abstract

This Note presents a search for the Standard Model Higgs boson in the decay channel $H \rightarrow ZZ^{(*)} \rightarrow \ell^+\ell^-\ell^+\ell^-$, where $\ell, \ell' = e$ or μ , using proton-proton collisions at $\sqrt{s} = 7$ TeV recorded with the ATLAS detector and corresponding to an integrated luminosity of 4.8 fb^{-1} . The four-lepton invariant mass distribution is compared with Standard Model background expectations to derive upper limits on the cross section of a Standard Model Higgs boson with a mass between 110 GeV and 600 GeV. The mass ranges 134 – 156 GeV, 182 – 233 GeV, 256 – 265 GeV and 268 – 415 GeV are excluded at the 95% confidence level. The largest upward deviations from the background-only hypothesis are observed for Higgs boson masses of 125 GeV, 244 GeV and 500 GeV with local significances of 2.1, 2.2 and 2.1 standard deviations, respectively. Once the look-elsewhere effect is considered, none of these excesses are significant.

Contents

1	Introduction	4
2	Data and Monte Carlo samples	5
2.1	Data samples	5
2.2	Signal Monte Carlo samples and cross-sections	5
2.3	Background Monte Carlo samples and cross-sections	5
2.4	Pile-up reweighting of Monte Carlo samples	7
3	Lepton reconstruction and identification	9
3.1	Electrons: energy scale, resolution and efficiency corrections	9
3.1.1	Comments on MC11 vs MC10	9
3.2	Muons: momentum scale, resolution and efficiency corrections	9
3.3	Electron charge misidentification	10
4	Electron reconstruction using the Gaussian-sum Filter	12
4.1	Performance of egammaBremRec	12
4.1.1	Monte Carlo Results	12
4.1.2	Data-Monte Carlo comparisons	12
	Selection of electrons from heavy flavor decays for data-MC comparisons	15
	$Z + b$ selection.	15
	$t\bar{t}$ selection.	15
5	Event selection	17
6	Data based study of the lepton selection criteria	21
6.1	Efficiency of additional lepton selection criteria	21
6.2	Selection efficiency for the Higgs signal	21
7	Background estimation methods	25
7.1	Data driven cross checks of the QCD background contribution	25
7.2	Data driven cross-checks of the $t\bar{t}$ background contribution	26
7.3	Estimation of the $Z+XX$ background	26
7.3.1	Data driven cross checks of the $Z(QQ \rightarrow \mu\mu)$ background	27
	$Z(QQ \rightarrow \mu^+\mu^-)$ normalization:	27
	$P(\pi/K \rightarrow \mu)$ contamination :	28
	Estimation of the $Z + (QQ \rightarrow \mu^+\mu^-)$ normalization:	28
	Efficiency of additional selection criteria for $Z + \mu$ events	29
7.3.2	$Z+XX$ ($X \rightarrow e$) background	29
	$Z+XX$ ($X \rightarrow e$) normalization	29
	$Z+jj$ and $Z+j\gamma$ relative normalization and rejection	32
	$Z+XX$ expectation in the signal region:	33
7.3.3	Data Monte Carlo comparison in control regions	35
7.4	$Z+XX$ Mass Shape	39
8	Higgs mass resolution	40
9	Results of event selection	47

10 Systematic uncertainties	55
11 Exclusion limits on $H \rightarrow ZZ^{(*)} \rightarrow 4\ell$	60
12 Summary	69
Appendices	74
A List of MC samples	74
A.1 Signal Samples	74
A.2 Background Samples	74
A.3 Background Samples cross-sections	75
B Data quality requirements	75
C Changes in the Muon stream due to the optimal GSF version for electrons	77
D $Z \rightarrow \ell\ell$ rate in different data-taking periods	78
E Observation of $Z + J/\psi$ production and effect in the analysis	78
F Mass resolution of the signal	79
G Shape of the $ZZ^{(*)}$ background	84
H Additional selection on electrons (efficiency determination with tag-and-probe)	88
Data samples	88
Electron selection	88
Tag-and-probe method	88
Electron isolation efficiencies	89
Conclusion	91
I Additional selection on muons (efficiency determination with tag and probe)	93
I.1 Combined or segment-tagged muons	93
J Trigger	102
K List of candidates	104
L Event displays of a few candidates	110
L.1 Low mass	110
L.2 Intermediate mass	111
L.3 High mass	112
M MC truth efficiencies as a function of number of primary vertices	113
N Maximum likelihood fits of background only and signal+background models	114
N.1 Constraining the ZZ production only from the data	116
N.2 Profiling nuisance parameters for expected p0	117
O CaloMuons	118

P SAMuons	121
Q Additional plots for the Z plus heavy quark and Z plus light jets backgrounds	123
R Signal selection optimization studies	124
R.1 Angular analysis	135
R.1.1 Montecarlo samples	135
R.1.2 Decay angles	135
R.1.3 Production angles	137

1 Introduction

The search for the Standard Model (SM) Higgs boson [1, 2, 3] is one of the most important aspects of the CERN Large Hadron Collider (LHC) physics programme. Direct searches performed at the CERN Large Electron-Positron Collider (LEP) excluded at 95% confidence level (CL) the production of a SM Higgs boson with mass, m_H , less than 114.4 GeV [4]. The searches at the Fermilab Tevatron $p\bar{p}$ collider have excluded at 95% CL the region $156 < m_H < 177$ GeV [5]. At the LHC, results from data collected in 2010 extended the search in the region $200 < m_H < 600$ GeV by excluding a Higgs boson with cross section larger than 5–20 times the SM prediction [6, 7]. In ATLAS these results were extended further using the first $1.04 - 2.28 \text{ fb}^{-1}$ of data recorded in 2011 [8, 9, 10, 11, 12, 13]. In particular, the $H \rightarrow WW^{(*)} \rightarrow \ell^+\nu\ell^-\bar{\nu}$ search [13] excluded at 95% CL the region $145 < m_H < 206$ GeV.

The search for the SM Higgs boson through the decay $H \rightarrow ZZ^{(*)} \rightarrow \ell^+\ell^-\ell^+\ell^-$, where $\ell, \ell' = e$ or μ , provides good sensitivity over a wide mass range. Previous results from ATLAS in this channel [9] excluded three mass regions between 191 GeV and 224 GeV at 95% CL with a 2.1 fb^{-1} data sample. This Letter presents an update of this search in the mass range from 110 GeV to 600 GeV, superseding Ref. [9]. Three distinct final states, $\mu^+\mu^-\mu^+\mu^-$ (4μ), $e^+e^-\mu^+\mu^-$ ($2e2\mu$), and $e^+e^-e^+e^-$ ($4e$), are selected. The largest background to this search comes from continuum $(Z^{(*)}/\gamma^*)(Z^{(*)}/\gamma^*)$ production, referred to as $ZZ^{(*)}$ hereafter. For $m_H < 180$ GeV, there are also important background contributions from $Z + \text{jets}$ and $t\bar{t}$ production, where the additional charged lepton candidates arise either from decays of hadrons with b - or c -quark content or from misidentification of jets.

The $\sqrt{s} = 7$ TeV $p\bar{p}$ collision data were recorded during 2011 with the ATLAS detector at the LHC and correspond to an integrated luminosity of 4.8 fb^{-1} [14, 15]. This analysis is using more than twice the integrated luminosity of Ref. [9], including the data therein. The electron identification efficiency has been improved; furthermore the electron tracks have been refitted using a Gaussian-sum filter [16], which corrects for energy losses due to bremsstrahlung. The analysis also benefits from recent significant improvements in the alignment of the inner detector and the muon spectrometer.

2 Data and Monte Carlo samples

2.1 Data samples

The data used in this analysis were recorded with the ATLAS detector during the 2011 LHC run. The data are subject to a number of quality requirements ensuring that all essential elements of the ATLAS detector are working as expected. A summary of the data quality criteria applied in this analysis is presented in the appendix B. The integrated luminosities are 4.8 fb^{-1} , 4.8 fb^{-1} and 4.9 fb^{-1} corresponding to data analysed for the 4μ , $2e2\mu$ and $4e$ final states respectively. In Table 1 the detailed breakdown of the integrated luminosity per period is given.

Table 1: Integrated Luminosity for Data 2011 (in pb^{-1}), using GoodRunLists version DetStatus-v36-pro10_CoolRunQuery-00-04-08

Period Channel	B	D	E	F	G	H	I	J	K	L	M	All
4μ	11.7	166.8	48.7	142.6	537.5	259.5	386.2	226.5	600.1	1401.9	1025.6	4807
$2e2\mu$	11.7	166.7	48.8	142.6	537.5	259.5	386.2	226.5	600.1	1401.9	1025.6	4807
$4e$	14.6	167.6	48.8	142.6	539.7	262.2	393.8	228.0	610.0	1457.8	1046.8	4910

2.2 Signal Monte Carlo samples and cross-sections

The $H \rightarrow ZZ^{(*)} \rightarrow 4\ell$ signal is modelled in the range 110 to 600 GeV using the POWHEG Monte Carlo (MC) event generator [17, 18], which calculates separately the gluon and vector-boson fusion production mechanisms of the Higgs boson with matrix elements up to next-to-leading order (NLO). POWHEG is interfaced to PYTHIA [19] for showering and hadronization, which in turn is interfaced to PHOTOS [20] for QED radiative corrections in the final-state and to TAUOLA [21] for the simulation of τ decays.

The cross sections for Higgs boson production, the corresponding branching fractions, as well as their uncertainties, are compiled in Ref. [22]. They correspond to next-to-next-to-leading order (NNLO) in QCD for the gluon fusion [23, 24, 25, 26, 27, 28] and vector boson fusion [29]. In addition, QCD soft-gluon resummations up to next-to-next-to-leading log (NNLL) are available for the gluon fusion process [30], while the NLO electroweak (EW) corrections are applied to both the gluon fusion [31, 32] and vector boson fusion [33, 34]. The Higgs boson decay branching ratio to the four-lepton final state is predicted by PROPHECY4F [35, 36], including the complete NLO QCD+EW corrections with all interference and leading two-loop heavy Higgs boson corrections to the four-fermion width.

The cross-section times the branching ratio values used in the following are listed in the second column of Table 2 and have been obtained as $\sigma(\text{ggF} + \text{VBF}) \times \text{BR}(H \rightarrow 4\ell)$, $\ell = e, \mu$ from Ref. [22].

From studies performed for EPS-2011 the signal efficiency between POWHEG and PYTHIA generators was found to be in agreement within a few % for both gluon and vector-boson fusion production mechanisms. An additional 2% uncertainty is added to the signal selection efficiency due to the modelling of the signal kinematics. This is evaluated by comparing signal samples generated with PYTHIA and the default POWHEG samples. We now use HqT2.0 that gives similar value.

2.3 Background Monte Carlo samples and cross-sections

The irreducible $ZZ^{(*)} \rightarrow 4\ell$ background is generated using PYTHIA, while the x-section is normalized to the NLO calculation using MCFM. PYTHIA implements the $q\bar{q}$ initial state and takes into account the $Z - \gamma$ interference. The inclusive total cross section and the shape of the $m_{ZZ^{(*)}}$ spectrum is calculated

Table 2: Higgs boson production cross-sections for both gluon and vector-boson fusion processes in pp collisions at $\sqrt{s} = 7$ TeV. The cross-sections include the branching ratio of $H \rightarrow 4\ell$, $\ell = e, \mu$.

m_H (GeV)	$\sigma \cdot \text{BR}(H \rightarrow 4\ell)$ (fb)	m_H (GeV)	$\sigma \cdot \text{BR}(H \rightarrow 4\ell)$ (fb)	m_H (GeV)	$\sigma \cdot \text{BR}(H \rightarrow 4\ell)$ (fb)
120	1.37	220	6.16	420	2.24
130	2.87	240	5.35	440	1.89
140	4.23	260	4.68	460	1.59
150	4.38	280	4.16	480	1.33
160	1.90	300	3.75	500	1.11
165	0.93	320	3.49	520	0.94
170	0.92	340	3.40	540	0.79
180	2.04	360	3.42	560	0.66
190	6.22	380	3.08	580	0.56
200	6.77	400	2.66	600	0.47

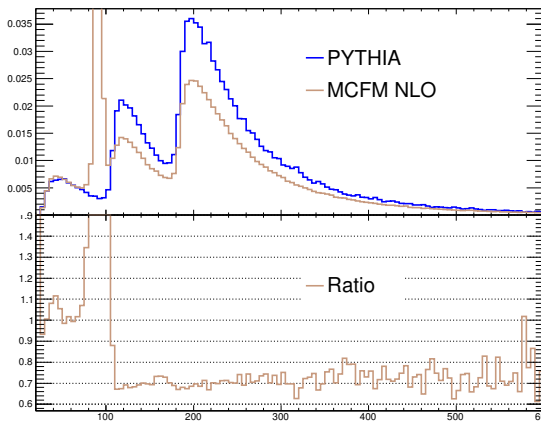


Figure 1: ZZ shape comparison between Pythia and MCFM for $m_Z > 12$ GeV. The K-factor is equal to 2.1. The $d(K - \text{Factor})/dm$ is 2.1 times the ratio presented in the plot, and is estimated using MCFMv6.1 and the MSTW2008 PDF set.

using MCFM [37, 38] (see Figure 1 for the shape comparison). MCFM v6.1 computes the cross section at LO and NLO for the process $q\bar{q} \rightarrow ZZ$ including ZZ , $Z\gamma^*$ and their interference, for the double resonant (or t-channel) and single resonant (or s-channel) diagrams, and for the process $gg \rightarrow ZZ$ including both quark-antiquark annihilation at QCD NLO and gluon fusion.

The inclusive Z boson and $Zb\bar{b}$ production is modelled using ALPGEN [39], while for the $t\bar{t}$ production MC@NLO [40, 41, 42] is employed. Both ALPGEN and MC@NLO generators are interfaced to HERWIG [43] for parton shower and hadronisation and JIMMY [44] for simulation of the underlying event. For the inclusive Z boson production PYTHIA is also used. For the inclusive Z boson and $Zb\bar{b}$ processes overlaps between the two samples are removed. Namely, $b\bar{b}$ pairs with separation $\Delta R = \sqrt{\Delta\phi^2 + \Delta\eta^2} \geq 0.4$ between the jets are taken from the matrix-element calculation, while for $\Delta R < 0.4$ the parton-shower jets are used. PYTHIA is also used as a cross-check of the ALPGEN results. The total inclusive cross section for Z boson production is normalized to the QCD NNLO prediction by FEWZ [45, 46], while $Zb\bar{b}$ is normalized to the MCFM prediction [37, 38]. Finally, the $t\bar{t}$ background is normalized to the approximate NNLO cross section calculated using HATHOR [47].

The simulated samples considered in this analysis are summarised in Table 3, along with their cross-sections, estimated as discussed above. The generated events are used as input to a full simulation of the ATLAS detector [48] using GEANT4 [49].

Table 3: Monte Carlo programs used for modelling signal and background processes and their corresponding cross-sections.

Process	Generator	$\sigma \times \text{BR}$
$gg, qq \rightarrow H$	POWHEG	See Table 2
$Z/\gamma^* \rightarrow \ell\ell$	ALPGEN, PYTHIA	
$m_{\ell\ell} > 60 \text{ GeV}$		0.989 nb [45, 50]
$Z/\gamma^* b\bar{b} \rightarrow \ell\ell b\bar{b}$	ALPGEN	
$m_{\ell\ell} > 30 \text{ GeV}$		12.4 pb
$qq, gg \rightarrow ZZ$	MCFM	
$m_Z > 12 \text{ GeV}$		14.4 pb[37, 38]
$t\bar{t}$	MC@NLO	164.6 pb [47]

2.4 Pile-up reweighting of Monte Carlo samples

During the 2011 LHC running the machine parameters evolved over time resulting in variations of the number of interactions occurring per bunch crossing and in the distance between consecutive bunches. Figures 2(a) and 2(b) shows the luminosity recorded versus the average number of interactions per bunch crossing per group of period and for each individual period. A reweighting procedure depending on the average number of interactions per bunch crossing is applied to the Monte-Carlo data and Figure 5(b) shows the average number of interactions per bunch crossing for the different periods of the Monte Carlo that simulates the data period. Figures 3(a), 3(b), 4(a) and 4(b) show that the Monte Carlo correctly reproduces the different data periods.

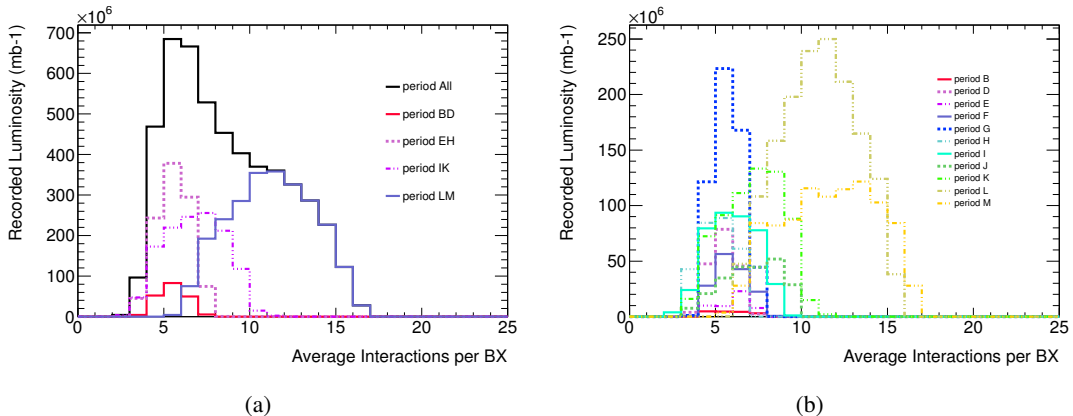


Figure 2: (a) Integrated luminosity for period B-D, E-H, I-K and L-M versus average number of interactions per bunch crossing. (b) Integrated luminosity per data period B to M versus average number of interactions per bunch crossing.

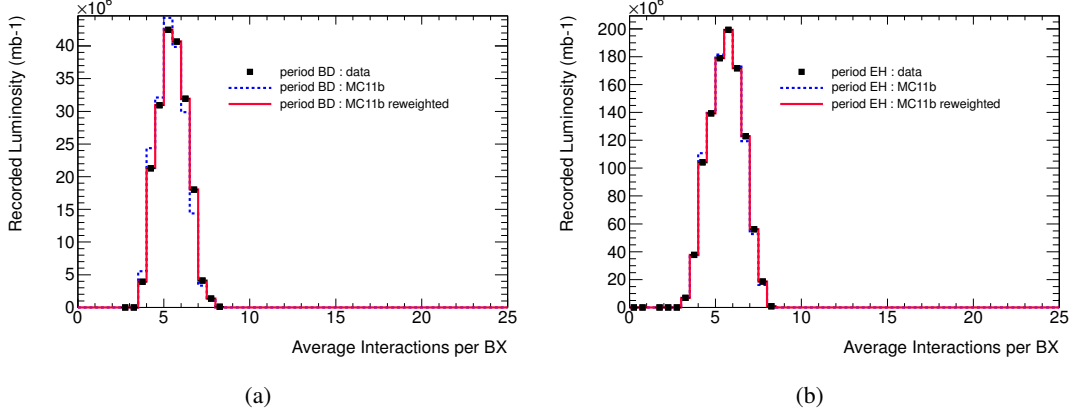


Figure 3: (a) Distribution of the average number of interactions per bunch crossing for data of MC11b prime after the pile up reweighting and data for period B-D. (a) Distribution of the average number of interactions per bunch crossing for data of MC11b prime after the pile up reweighting and data for period E-H.

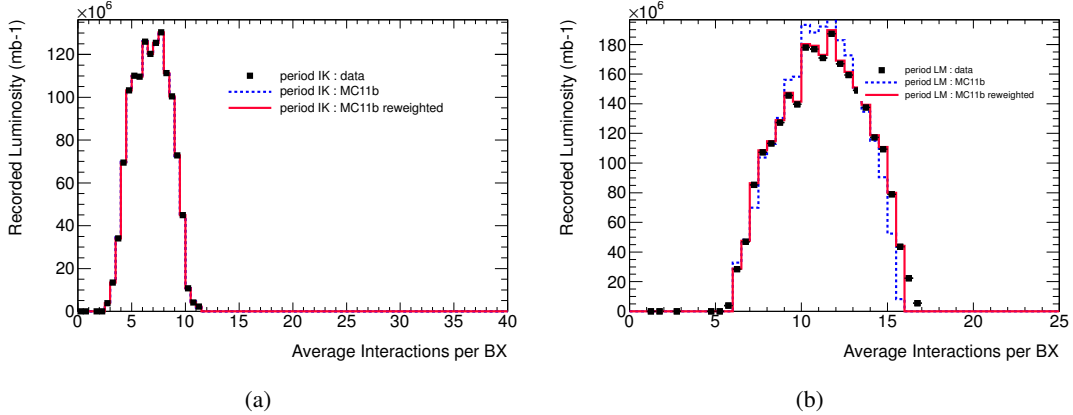


Figure 4: (a) Distribution of the average number of interactions per bunch crossing for data of MC11b prime after the pile up reweighting and data for period I-K. (b) Distribution of the average number of interactions per bunch crossing for data of MC11b prime after the pile up reweighting and data for period L-M.

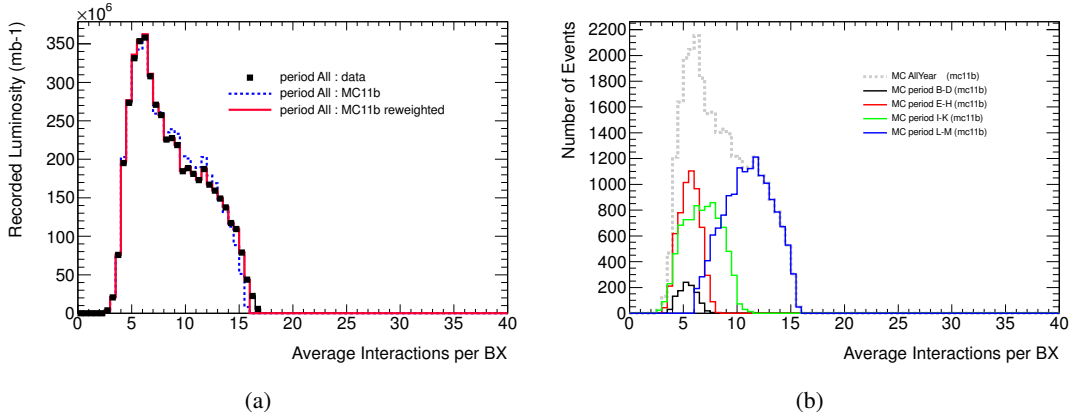


Figure 5: (a) Distribution of the average number of interactions per bunch crossing for data of MC11b prime after the pile up reweighting and data for period B-M. (b) Distribution of the average number of interactions per bunch crossing for MC11b and for period B-D, period E-H, period I-K and period L-M.

3 Lepton reconstruction and identification

Lepton identification and reconstruction is of particular importance for the $H \rightarrow 4\ell$ channel. In this section, the algorithms are briefly described and the baseline electron/muon selection for the analysis is defined. In addition, the scale factors used to correct for Data/MC differences are explained.

Electron candidates consist of electromagnetic clusters to which inner detector tracks are matched in a window between the cluster position and the extrapolated track. The baseline electron identification in ATLAS relies on cuts using variables that provide good separation between isolated electrons and jets [51]. These variables include calorimeter, tracker and combined calorimeter/tracker information. Cuts on those variables can be applied independently and the following three reference selections have been defined with increasing background rejection power: *loose++*, *medium++* and *tight++*. Shower shape variables of the first and second calorimeter layer, hadronic leakage variables, track quality and the $\Delta\eta$ between the extrapolated track and the cluster are used in the *loose++* selection. The *medium++* requires one b-layer hit (if the module is not dead) and adds extra selections on the impact parameter of the matched track and on the TRT high threshold hits ratio. The *tight++* selection adds requirements on E/p , on the $\Delta\phi$ between the extrapolated track and the cluster, and on the number of TRT hits and also checks for overlaps with reconstructed photon conversions.

Muons are identified by reconstruction of tracks in the muon spectrometer alone (“stand-alone”), by the fitted combination of inner detector and muon spectrometer tracks (“combined”) or by matching an inner detector track of sufficient momentum with a reconstructed track segment of the muon spectrometer (“segment-tagged”) [52, 53, 54].

Throughout this paper, the *loose++* electron and combined or segment-tagged muon selection are used if not explicitly stated otherwise.

3.1 Electrons: energy scale, resolution and efficiency corrections

Various corrections are provided by the EGamma group and summarized in the following twiki pages.

- Energy scale corrections and resolution smearing functions are applied and the correction procedure is described in the following twiki:
[https://twiki.cern.ch/twiki/bin/view/AtlasProtected/
EnergyScaleResolutionRecommendations](https://twiki.cern.ch/twiki/bin/view/AtlasProtected/EnergyScaleResolutionRecommendations)

3.1.1 Comments on MC11 vs MC10

It has to be noted that the MC11 describes the electron shower shapes observed in the data better than MC10. As a consequence :

- The scale factors are generally closer to unity.
- The raw efficiency (before application of scale factors) of the MC11 is 1-2 % per electron worse than MC10. This number depends on E_t , η , and pile-up conditions.

Furthermore, a slight decrease of the track quality cuts efficiency (< 1% per electron) is observed in MC11. It should be also noted that the E_{ratio} cut is not applied for $E_T < 10$ GeV at the *loose++* selection, resulting in a bit worse rejection than the *medium* selection used in the past.

3.2 Muons: momentum scale, resolution and efficiency corrections

- Scale factors provided by the muon combined performance (MCP) group are applied on Monte Carlo data to reproduce the efficiency measurements on data using Z and J/psi to muon events. They represent the ratio of the Data to Monte Carlo reconstruction/identification efficiency. The correction

procedure is described in the following twiki page:

<https://twiki.cern.ch/twiki/bin/view/AtlasProtected/MCPAnalysisGuidelinesRel17MC11a>

- Muon momentum scale corrections provided by the MCP group are applied to the data. These scales are extracted from the fitted Z mass distribution by comparing it to the fitted mass from Monte-Carlo. Details are given in:
<https://twiki.cern.ch/twiki/bin/view/AtlasProtected/MCPAnalysisGuidelinesRel17MC11a>
- Smearing functions provided by MCP are applied to the Monte Carlo E_T to reproduce the data momentum resolution. Details are given in:
<https://twiki.cern.ch/twiki/bin/view/AtlasProtected/MCPAnalysisGuidelinesRel17MC11a>

3.3 Electron charge misidentification

In Figure 6, the charge misidentification rate is studied using MC as a function of p_T for five η bins. The p_T - η bins have been populated using Higgs samples with $m_H = 120 - 145$ GeV and ALPGEN $Z \rightarrow ee$ samples. The true electron charge is found using the MC truth classifier. The reconstructed electrons are required to satisfy the *loose ++* identification criteria.

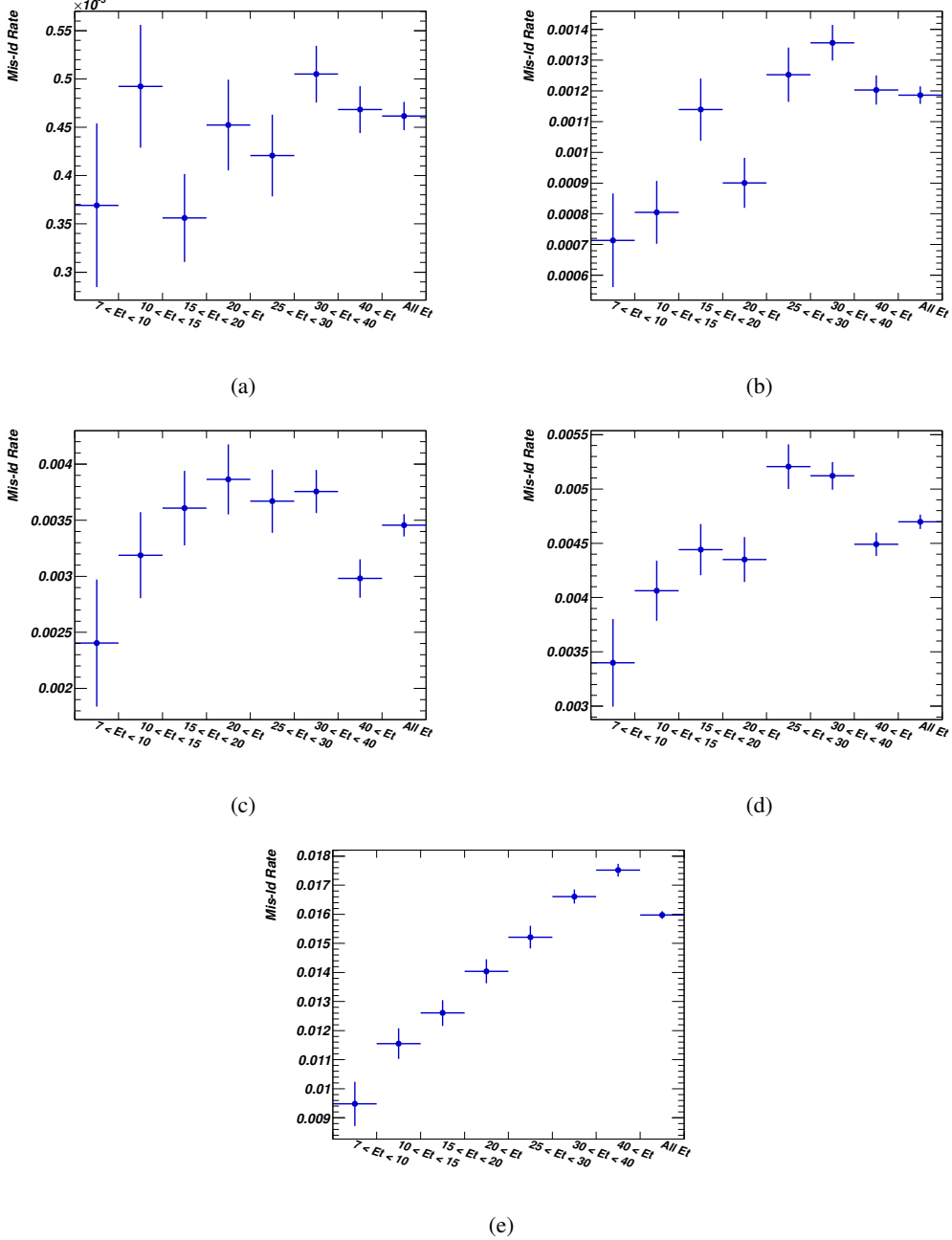


Figure 6: In (a)-(e) the electron charge misidentification is presented as a function of p_T for different η bins (0-0.8, 0.8-1.37, 1.37-1.52, 1.52-2, 2-2.47).

4 Electron reconstruction using the Gaussian-sum Filter

Electrons in ATLAS lose on average between 20 and 50 % of their energy (depending on $|\eta|$) by the time they have left the SCT [55]. The bremsstrahlung emission introduces, in general, non-Gaussian contributions to the event-by-event fluctuations of the calorimetry and tracking measurements. By fitting electron tracks in such a way as to allow for proper modeling of the energy loss due to bremsstrahlung, it is possible to improve the reconstructed track parameters.

In this work the Gaussian-sum filter (GSF) was used in order to account for energy losses due to bremsstrahlung. GSF is a non-linear generalization of the Kalman filter, which takes into account non-Gaussian noise by modeling it as a weighted sum of Gaussian components and therefore acts as weighted sum of Kalman filters operating in parallel [16]. By allowing for changes in the curvature of the track, the bremsstrahlung recovery algorithms follow the track better and correctly associate more of the hits. In this analysis, a dedicated algorithm was used in order to re-process the electrons (egammaBremRec) starting from the information available in the AOD. The egammaBremRec Algorithm works as follow:

- All tracks associated to existing electrons are fitted using GSF.
- The algorithm loops over the electron and photon clusters trying to match them with the “GSF” tracks.
- Given a successful match the “standard” chain of e/gamma Tools is executed for the “GSF Electrons”

4.1 Performance of egammaBremRec

In this section the performance of the new algorithm is evaluated by comparing results produced by the “standard” e/gamma and the egammaBremRec using Monte Carlo. Furthermore, the agreement between data and Monte Carlo is assessed for the electron variables of interest for the $H \rightarrow 4\ell$ analysis.

4.1.1 Monte Carlo Results

In this section the egammaBremRec algorithm is compared to the “standard” reconstruction using Monte Carlo Z \rightarrow ee inclusive samples. A slight increase of the tracking/track-matching efficiency is expected, especially after the application of track quality cuts (at least seven silicon and one pixel hits), this is shown in figures 7(a) and 8(a). In 9(a) the impact parameter significance (d_0/σ_{d_0}) for the egammaBremRec and the standard electron reconstruction are compared. As expected, including bremsstrahlung effects in the track fit results in a narrower distribution. The effect of the GSF fit can be better understood by looking at the response and resolution of the impact parameter significance as a function of $|\eta|$, shown in figures 10(a) and 10(b). The usage of GSF alleviates the dependence of this variable on the material traversed by the electron. The situation is similar for the q/p as can be seen in figures 9(b), 11(a) and 11(b). In general the GSF performs as expected, improving the estimation of the track parameters.

4.1.2 Data-Monte Carlo comparisons

The Monte Carlo description of the impact parameter significance (d_0/σ_{d_0}) is tested using a control region enriched with heavy mesons. The results are shown in figures 12(a) and 12(b) for both the standard and the egammabremRec algorithms respectively.

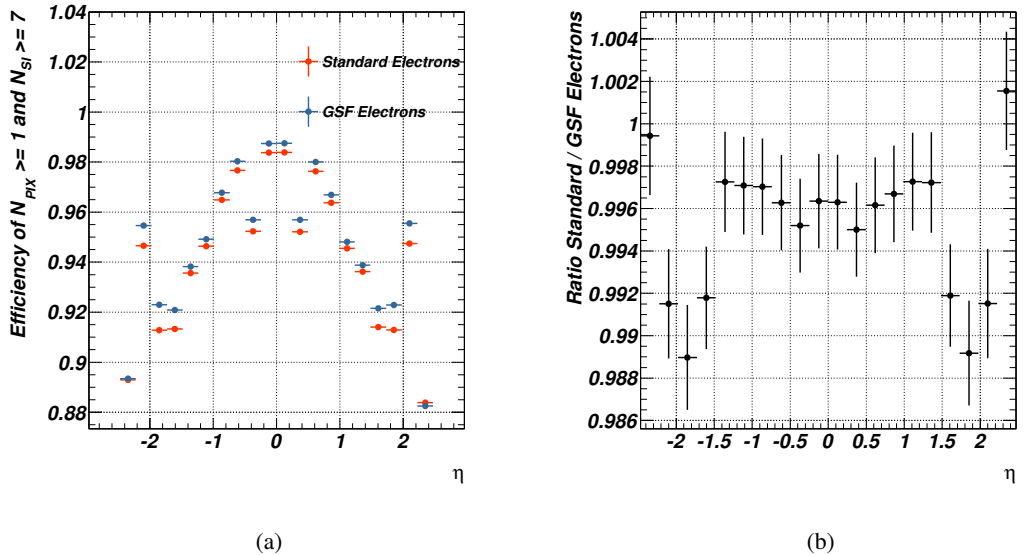


Figure 7: (a) Efficiency of egammaBremRec (blue) and standard electrons (red) as a function of $|\eta|$. (b) Ratio of the two efficiencies as a function of $|\eta|$.

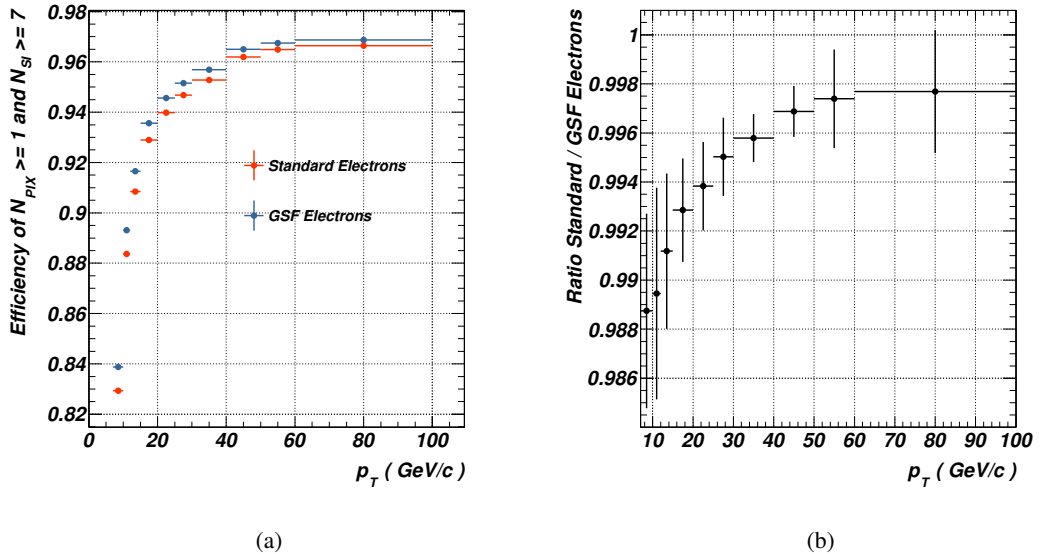


Figure 8: (a) Efficiency of egammaBremRec (blue) and standard electrons (red) as a function of $|p_t|$. (b) Ratio of the two efficiencies as a function of p_t .

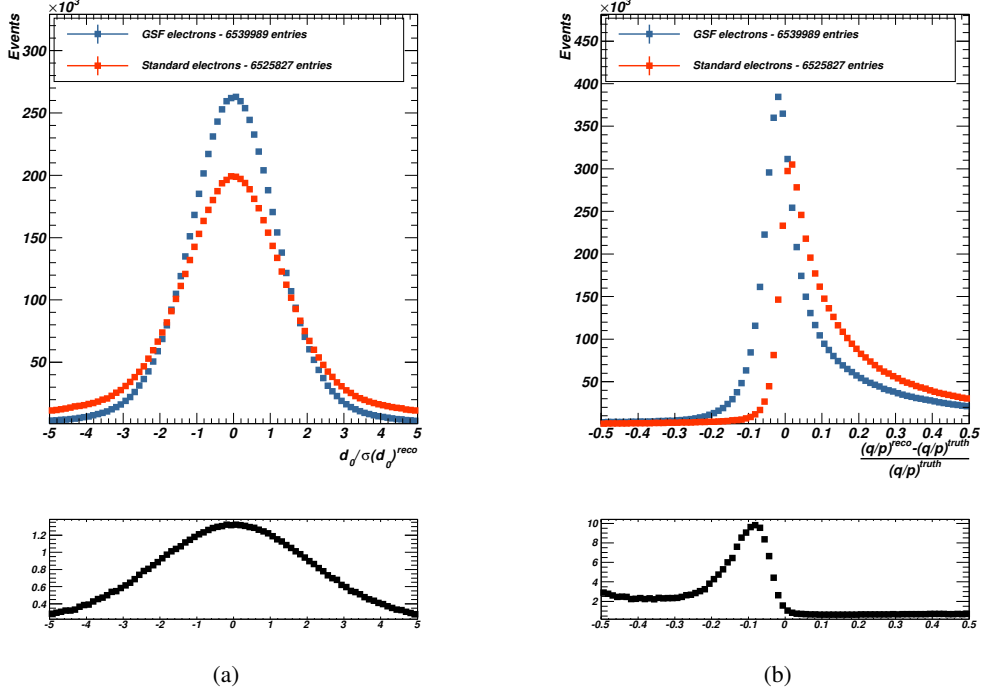


Figure 9: (a) Impact parameter significance (d_0/σ_{d_0}) for egammaBremRec (blue) and standard electrons (red). (b) q/p for egammaBremRec (blue) and standard electrons (red).

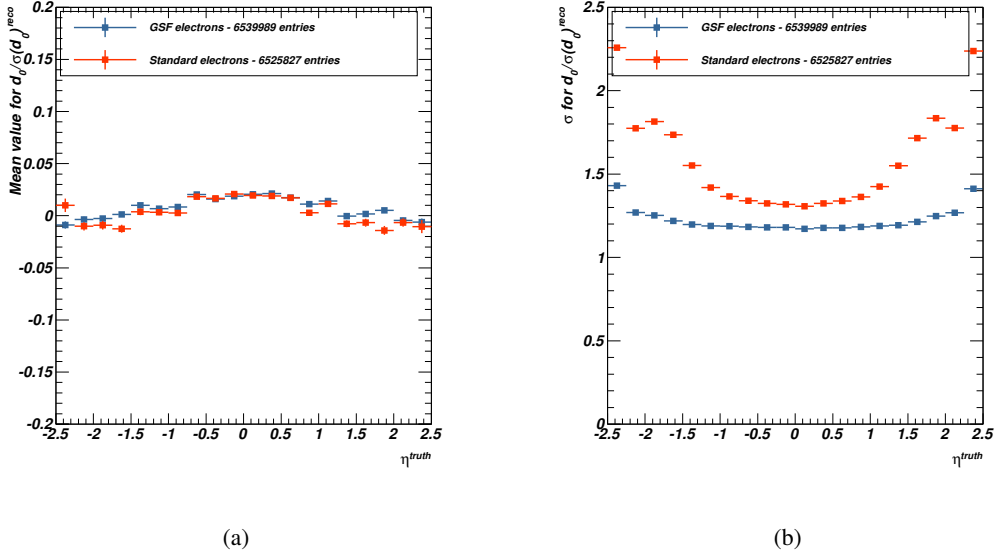


Figure 10: (a) Response of impact parameter significance (d_0/σ_{d_0}) as a function of $|\eta|$ for egammaBremRec (blue) and standard electrons (red). (b) Resolution of impact parameter significance (d_0/σ_{d_0}) as a function of $|\eta|$ for egammaBremRec (blue) and standard electrons (red).

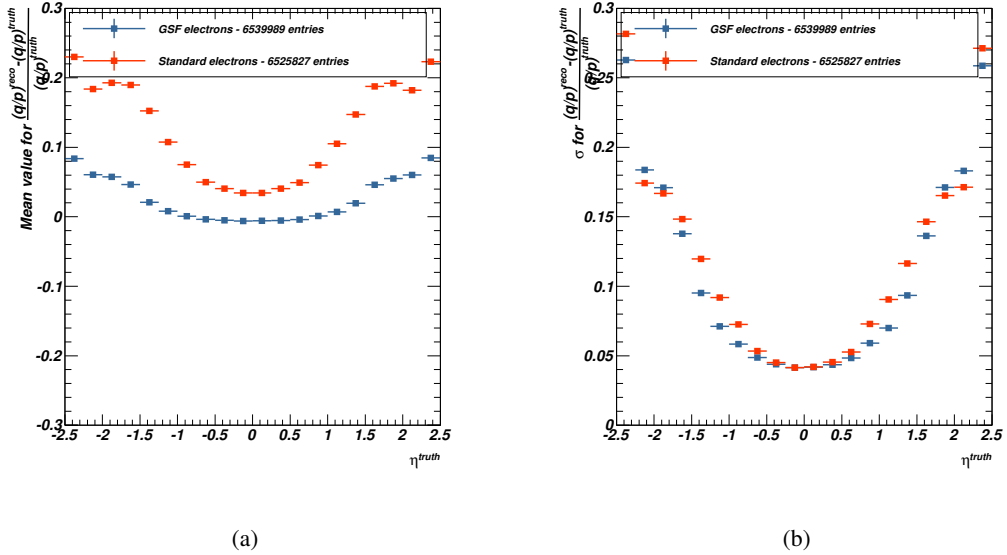


Figure 11: (a) Response of q/p as a function of $|\eta|$ for egammaBremRec (blue) and standard electrons (red). (b) Resolution of q/p as a function of $|\eta|$ for egammaBremRec (blue) and standard electrons (red).

Selection of electrons from heavy flavor decays for data-MC comparisons Electrons from heavy flavor decays are looked for in $t\bar{t}$ (dilepton channel) and $Z + b$ events, in order to study topologies close to that of the backgrounds to the $H \rightarrow 4\ell$ search. After a $t\bar{t}$ or $Z + b$ selection, additional electrons are kept and studied when they are matched to b -tagged jets. The study is based on data taken between periods D to K, which amount to a luminosity of 2.04fb^{-1} after applying the SM $W/Z+\text{jets}$ good runs list (equivalent to top GRL). As b -tagging calibration is unavailable for Athena release 17 at present, the study is done using the release 16.

Both $t\bar{t}$ and $Z + b$ selections begin by requiring that a primary vertex with at least three tracks is reconstructed, and that the liquid argon calorimeter is exempt from problems. Then high p_T leptons are selected. Electrons from the standard e-gamma container are selected in $|\eta| < 2.47$, with $p_T > 20\text{ GeV}$ ($Z + b$) or $p_T > 25\text{ GeV}$ ($t\bar{t}$). They must not fall into problematic regions of the calorimeter (*OQMaps*). They are required to be of medium ($Z + b$) or tight ($t\bar{t}$) quality. Electrons for the $t\bar{t}$ selection need also be isolated (calorimetric isolation of 3.5 GeV). Combined or tagged Staco muons are considered within $|\eta| < 2.5$, with a p_T cut at 20 GeV . They must fulfill the recommended silicon hits and TRT requirements, and have a d_0 of less than $0.5mm$ wrt the primary vertex. $t\bar{t}$ selection requires them to be isolated (both track and calorimetric isolation $< 4\text{ GeV}$). Jets reconstructed by an AntiKt algorithm with a parameter of 0.4 are selected when $|\eta| < 2.5$ and $p_T > 20\text{ GeV}$.

The selections then go as follows:

$Z + b$ selection. A pair of same flavor opposite sign leptons must have an invariant mass in $m_Z \pm 15\text{ GeV}$. Jets estimated to originate from background (*bad* jets) and jets close to the leading leptons ($\Delta R < 0.3$) are discarded.

$t\bar{t}$ selection. A pair of opposite sign leptons with $m_{\ell\ell} > 15\text{ GeV}$ is selected. If the leptons are of same flavor, a Z mass veto of $\pm 15\text{ GeV}$ is applied. In order not to bias the E_T^{miss} calculation, events with jets coming from backgrounds or jets falling in the LAr hole are discarded. The event must have at least two jets with $p_T > 25\text{ GeV}$ well separated ($\Delta R > 0.3$) from the leading leptons. In the ee and $\mu\mu$ channels, a E_T^{miss} cut at 40 GeV is applied, while a H_T cut at 140 GeV is applied in the $e\mu$ channel.

At least one of the leading leptons is required to pass the lowest unprescaled trigger: for the electrons, 20 GeV medium up to period J and in the later periods 22 GeV medium; for the muons, 18 GeV up to period I and in the later periods 18 GeV medium. The remaining jets in the selected events are subjected to a high efficiency (70%) b -tagging algorithm (JetFitterCombNN) [1]. The electrons finally selected are GSF or standard ones, with $p_T > 7$ GeV and $|\eta| < 2.47$, away from the problematic regions of the calorimeter, and within $\Delta R = 0.5$ of the b -tagged jets. According to the Monte Carlo, the purity for the selected electrons to originate from heavy flavor decays is 56% if a *loose ++* quality is required, and 84% for *medium ++* electrons. The main contamination comes from light hadrons. The Monte Carlos are corrected for various detector effects, using scale factors: lepton identification efficiencies, leptons energy scales, trigger efficiencies, and b -tagging efficiency.

It should be noticed that an overall excess of data over MC is observed in both $t\bar{t}$ and $Z + b$ selections. The origin of this discrepancy is not yet understood. However, this difference is already present when looking at tagged jets, before the selection of additional electrons, and seems to be an overall scale factor: all the shapes of the studied distributions are correctly described by the MC within the statistical error bars, and only the normalizations are off.

Distributions related to impact parameter and track-calor matching have been studied. Everywhere, the data-MC agreement is as good for brem-refitted electrons as for standard ones. No showstopper for the use of brem-refitted electrons has been found.

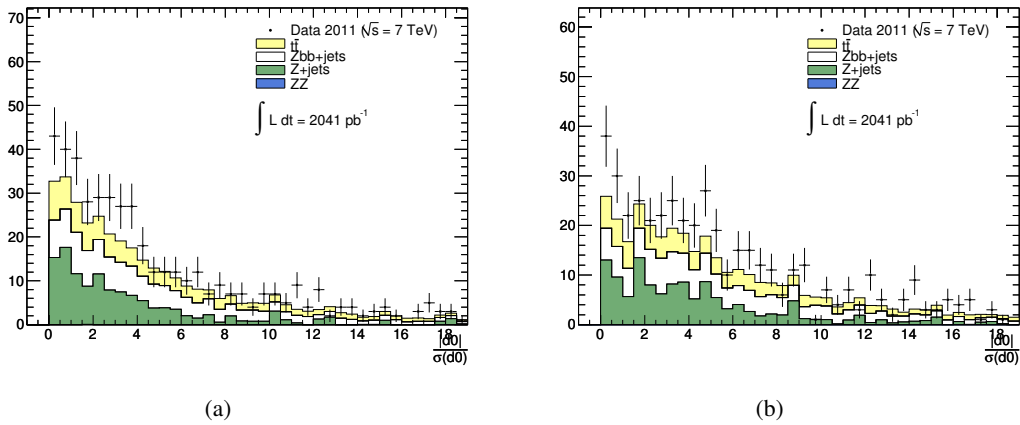


Figure 12: (a) Comparison of d_0/σ_{d_0} between data and Monte Carlo for egammaBremRec algorithm. (b) Comparison of d_0/σ_{d_0} between data and Monte Carlo for the standard algorithm.

5 Event selection

Events are selected using single/double lepton(s) high p_T triggers. The list of triggers used is provided in Table 4 for Monte Carlo and in Table 5 for data. The efficiency of these triggers on signal events, with respect to the offline selection, is close to 100%. Collision candidates are selected by requiring a primary vertex with at least three tracks¹. In the following, *loose* ++ electrons and combined or segment-tagged muons are used.

Table 4: Triggers used in the Monte Carlo.

MC	to match unprescaled trigger during data taking
4μ	EF_mu18_MG, EF_mu18_MG_medium OR EF_2mu10_loose
$4e$	EF_e20_medium, EF_e22_medium, EF_e22_medium1 OR EF_2e12_medium, EF_2e12T_medium
$2e2\mu$	4μ OR $4e$

Table 5: Triggers used in the Data. In each data taking period, the OR of single- and di-lepton triggers is used to select each signature.

Single-lepton triggers				
Period	B-I	J	K	L-M
4μ	EF_mu18_MG	EF_mu18_MG_medium	EF_mu18_MG_medium	EF_mu18_MG_medium
$4e$	EF_e20_medium	EF_e20_medium	EF_e22_medium	EF_e22vh_medium1
$2e2\mu$			4μ OR $4e$	

Di-lepton triggers				
Period	B-I	J	K	L-M
4μ	EF_2mu10_loose	EF_2mu10_loose	EF_2mu10_loose	EF_2mu10_loose
$4e$	EF_2e12_medium	EF_2e12_medium	EF_2e12T_medium	EF_2e12Tvh_medium
$2e2\mu$			4μ OR $4e$	

¹It is noted that during vertex finding/reconstruction the beam spot constraint is applied

Not reviewed, for internal circulation only

Trigger:	w/ m_H	w/o 4μ	Eff. (%)	w/ $2e2\mu$	w/o $2e2\mu$	Eff. (%)	w/ $4e$	w/o $4e$	Eff. (%)
ggF									
110	260	275	94.545	306	313	97.764	92	92	100
115	631	654	96.483	775	790	98.101	237	238	99.58
120	951	975	97.538	1268	1286	98.6	427	429	99.534
125	1283	1307	98.164	1685	1718	98.079	612	613	99.837
130	1597	1623	98.398	2037	2063	98.74	712	715	99.58
135	1760	1786	98.544	2426	2449	99.061	829	830	99.88
140	1892	1922	98.439	2711	2731	99.268	1045	1047	99.809
145	2084	2103	99.097	2912	2931	99.352	1158	1161	99.742
150	2280	2301	99.087	3121	3134	99.585	1237	1239	99.839
180	3203	3235	99.011	4896	4904	99.837	2010	2015	99.752
200	3363	3383	99.409	5400	5410	99.815	2155	2159	99.815
260	3251	3272	99.358	5614	5626	99.787	2317	2321	99.828
360	3567	3589	99.387	5863	5878	99.745	2613	2613	100
460	3537	3553	99.55	6389	6396	99.891	2783	2786	99.892
600	3522	3548	99.267	6560	6577	99.742	3088	3095	99.774
Trigger:	w/ m_H	w/o 4μ	Eff. (%)	w/ $2e2\mu$	w/o $2e2\mu$	Eff. (%)	w/ $4e$	w/o $4e$	Eff. (%)
VBF									
110	181	185	97.838	223	227	98.238	67	68	98.529
115	400	411	97.324	511	522	97.893	152	152	100
120	654	682	95.894	952	964	98.755	315	315	100
125	872	887	98.309	1135	1150	98.696	408	408	100
130	940	952	98.739	1377	1387	99.279	513	514	99.805
135	1121	1134	98.854	1583	1601	98.876	638	641	99.532
140	1217	1234	98.622	1757	1763	99.66	659	660	99.848
145	1320	1340	98.507	1888	1899	99.421	776	776	100
150	1469	1490	98.591	2009	2017	99.603	800	801	99.875
180	1901	1912	99.425	3133	3144	99.65	1346	1346	100
200	2083	2097	99.332	3441	3452	99.681	1367	1368	99.927
260	2066	2079	99.375	3494	3499	99.857	1458	1462	99.726
360	2078	2089	99.473	3571	3584	99.637	1568	1571	99.809
460	2039	2044	99.755	3620	3624	99.89	1643	1647	99.757
600	1990	1997	99.649	3622	3629	99.807	1664	1664	100

Trigger:	w/ m_H	w/o 4μ	Eff.	w/ $2e2\mu$	w/o $2e2\mu$	Eff.	w/ $4e$	w/o $4e$	Eff.
	(%)	(%)	(%)	(%)	(%)	(%)			
WH									
110	148	149	99.329	187	190	98.421	65	65	100
115	317	325	97.538	395	399	98.997	121	122	99.18
120	431	441	97.732	575	582	98.797	210	210	100
125	571	578	98.789	766	773	99.094	278	278	100
130	645	655	98.473	961	967	99.38	343	343	100
135	714	724	98.619	984	990	99.394	415	415	100
140	782	790	98.987	1072	1076	99.628	404	405	99.753
145	824	834	98.801	1159	1163	99.656	490	490	100
150	935	947	98.733	1269	1276	99.451	538	538	100
180	1231	1238	99.435	1972	1974	99.899	791	792	99.874
200	1257	1268	99.132	2151	2153	99.907	863	864	99.884
260	1371	1380	99.348	2361	2369	99.662	953	955	99.791
Trigger:	w/ m_H	w/o 4μ	Eff.	w/ $2e2\mu$	w/o $2e2\mu$	Eff.	w/ $4e$	w/o $4e$	Eff.
	(%)	(%)	(%)	(%)	(%)	(%)			
ZH									
110	244	246	99.187	350	358	97.765	125	126	99.206
115	403	415	97.108	457	461	99.132	193	193	100
120	528	534	98.876	707	719	98.331	258	259	99.614
125	672	677	99.261	896	904	99.115	313	313	100
130	763	775	98.452	1014	1021	99.314	402	403	99.752
135	816	828	98.551	1104	1114	99.102	450	451	99.778
140	837	843	99.288	1205	1212	99.422	476	476	100
145	939	945	99.365	1383	1390	99.496	498	498	100
150	990	997	99.298	1413	1415	99.859	595	596	99.832
180	1400	1413	99.08	2048	2052	99.805	971	971	100
200	1494	1506	99.203	2318	2322	99.828	1007	1009	99.802
260	1511	1519	99.473	2602	2609	99.732	1128	1130	99.823

The event selection criteria, consisting of kinematic selection, isolation criteria and impact parameter significance, are presented in Table 6. The candidate quadruplet is formed by selecting two opposite sign, same flavour di-lepton pairs in an event. Muons are required to have $p_T > 7 \text{ GeV}$ and $|\eta| < 2.7^2$, where η denotes the pseudorapidity, while electrons are required to have $E_T > 7 \text{ GeV}$ and $|\eta| < 2.47$. The four leptons of the quadruplets are required to be well separated, $\Delta R = \sqrt{\Delta\eta^2 + \Delta\phi^2} > 0.10$. The di-lepton pair with a mass m_{12} of the quadruplet closest to the nominal Z boson mass is called the leading di-lepton pair, while the second di-lepton pair of the quadruplet with a mass m_{34} is the sub-leading one. For each event there is a mass window requirement applied to the invariant mass of each of the two di-lepton pairs. The cut values are chosen event-by-event using the reconstructed four-lepton invariant mass. This results in a unique mass spectrum for each background regardless of the hypothetised Higgs mass. m_{12} is required to be within 15 GeV of the nominal Z mass. m_{34} is required to exceed a threshold, $m_{\text{threshold}}$, which varies as a function of the four-lepton invariant mass, $m_{4\ell}$, and it should always be below 115 GeV. A set of threshold cut values is shown in Table 7, where the actual cut value used is obtained by linear interpolation between these mass points.

The normalised track isolation discriminant is defined as the sum of the transverse momenta of tracks, Σp_T , inside a cone of $\Delta R < 0.20$ around the lepton, divided by the lepton p_T . Summed tracks are of good

²Following the MCP recommendation, the η requirement has been removed completely for combined and segment-tagged muons. The acceptance is limited by the acceptance of the muon spectrometer and the inner detector.

quality and pass a minimum p_T cut (at least four silicon hits and $p_T > 1$ GeV). Each lepton is required to have a normalised track isolation smaller than 0.15. The normalized calorimetric isolation discriminant is defined as the sum of the calorimeter cells, ΣE_T , inside an isolation cone of 0.20 around the lepton, divided by the lepton E_T . In case of electromagnetic showers, the corresponding cells are excluded from the sum. Each lepton is required to have a normalised calorimetric isolation less than 0.30. The impact parameter significance, d_0/σ_{d0} , is required to be lower than 3.5 for muons and 6 for electrons. The electron impact parameter is affected by Bremsstrahlung and is thus broader. The performance of the isolation and impact parameter criteria has been studied using $Z \rightarrow \ell\ell$ and $b, c \rightarrow \mu$ events and the efficiency of the criteria in the Monte Carlo was found to be in close agreement with that observed in the data.

The final discrimination variable is the mass of the lepton quadruplet. Further details on the applied event selection can be found in Ref. [56].

Table 6: Summary of the event selection requirements. The two lepton pairs are denoted as m_{12} and m_{34} . The threshold values for m_{34} are defined through linear interpolation of the values in Table 7.

Event Preselection	
Electrons: loose++ quality GSF electrons with $E_T > 7$ GeV and $ \eta < 2.47$	
Muons: Combined or segment-tagged muons with $p_T > 7$ GeV and $ \eta < 2.7$	
Event Selection	
Kinematic Selection	Require at least one quadruplet of leptons consisting of two pairs of same flavour opposite charge leptons fulfilling the following requirements. At least two leptons in the quadruplet with $p_T > 20$ GeV. Leading di-lepton pair mass requirement $ m_{12} - m_Z < 15$ GeV Sub-leading di-lepton pair mass requirement $m_{threshold} < m_{34} < 115$ GeV $\Delta R(\ell, \ell') > 0.10$ for all leptons in the quadruplet.
Isolation	Lepton track isolation ($\Delta R = 0.20$): $\Sigma p_T/p_T < 0.15$ Lepton calorimeter isolation ($\Delta R = 0.20$): $\Sigma E_T/E_T < 0.30$
Impact Parameter Significance	Apply impact parameter significance cut to the 2 less energetic leptons of the quadruplet. For electrons : $d_0/\sigma_{d0} < 6$ For muons : $d_0/\sigma_{d0} < 3.5$ For $m_{4\ell} > 190$ GeV no requirement applied

Table 7: Summary of thresholds applied to m_{34} for reference values of $m_{4\ell}$. For other $m_{4\ell}$ values, the selection requirement is obtained via linear interpolation.

$m_{4\ell}$ (GeV)	≤ 120	130	140	150	160	165	180	190	≥ 200
threshold (GeV)	15	20	25	30	30	35	40	50	60

6 Data based study of the lepton selection criteria

In this section the efficiency measurements for the additional lepton selection criteria are described. These criteria include calorimeter and tracking isolation as well as impact parameter significance. For the signal the efficiency is evaluated on Z decay events. For the background comprising leptons from heavy quark decays, the efficiency is evaluated on heavy flavour dijet events.

6.1 Efficiency of additional lepton selection criteria

The efficiency of the isolation and impact parameter criteria is estimated from data using a sample of lepton pairs originating from Z decays, similarly to the tag and probe method. These leptons are expected to be isolated and originating from the primary vertex. One lepton, used as a tag, fulfills all the Z selection criteria (including isolation). A second, opposite sign, same flavour lepton is used as probe. For the probe lepton the additional selection criteria are applied individually (or simultaneously) and the surviving number of candidates is estimated with a fit on the dilepton invariant mass. A convolution of a Breit-Wigner with a Crystal-Ball function is used for the signal and an exponential one is used for the background in the electron case while fitting with templates is used in the muon case. The ratios between data and MC efficiencies obtained in this way are shown in Fig. 13.

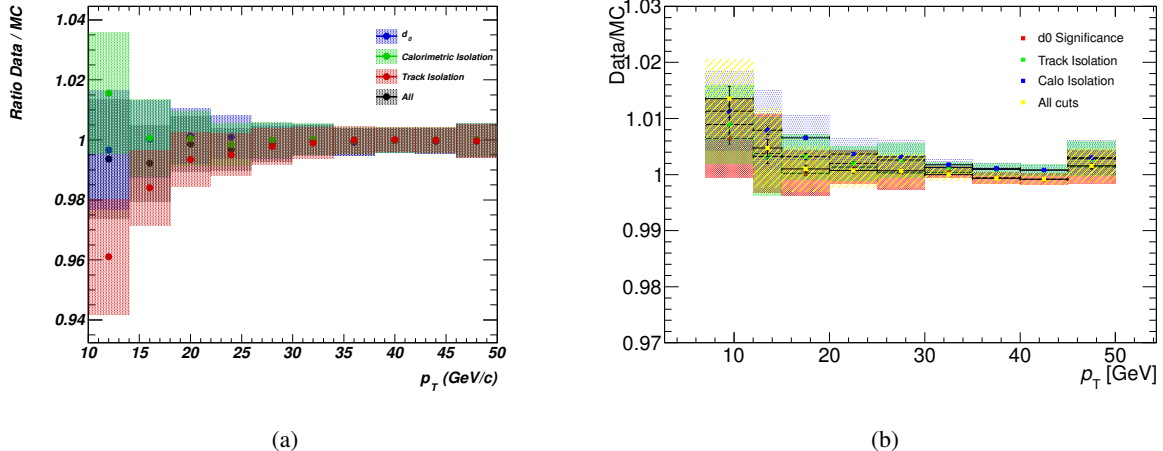


Figure 13: The ratio between data and MC for the efficiency of the additional selection criteria on electrons (a) and muons (b) as a function of p_T (4.48 fb^{-1}).

Scale factors (shown in Fig. 13) are applied to the MC to correct for the observed data/MC difference. The overall efficiencies in data and MC, as well as their ratios, are summarized in Table 8. The errors on the ratios quoted in Table 8 and shown in Fig. 13 are due to systematic effects stemming from the fit procedure on the data samples. Details of these studies can be found in Appendices H and I.

6.2 Selection efficiency for the Higgs signal

Applying the previously described selection criteria to generated samples of Higgs decays to ZZ^* at different masses one evaluates the global analysis efficiency to reconstruct the final state. Table 9 gives acceptance values for selected Higgs masses for the three final states, i.e $4\mu, 2e2\mu$ and $4e$.

Selection variable	Efficiency in Data	Efficiency in MC	Ratio
Electrons			
$d_0/\sigma_{d0} < 6.0$	99.4	99.5	0.999 ± 0.002
Norm. Calo. isolation < 0.3	99.7	99.7	0.999 ± 0.002
Norm. Track isolation < 0.15	99.4	99.5	0.998 ± 0.002
All cuts	98.6	98.8	0.997 ± 0.002
Muons			
$d_0/\sigma_{d0} < 3.5$	99.4	99.3	1.001 ± 0.002
Norm. Calo. isolation < 0.3	100.0	99.7	1.004 ± 0.003
Norm. Track isolation < 0.15	99.7	99.4	1.003 ± 0.002
All cuts	99.1	98.8	1.003 ± 0.002

Table 8: Efficiency in data, MC Z events and their ratio using the additional lepton selection requirements imposed in the analysis.

Analysis efficiency in %			
Higgs mass	4μ	$2e2\mu$	$4e$
110	10.5	6.12	3.55
115	23.4	14.7	8.68
120	32.2	21.5	14.8
125	39.5	25.9	18.5
130	44.5	29.9	21.4
135	47.4	33.1	23
140	49	35.3	27.9
145	52.4	36.4	28.7
150	54	39.3	30
180	70.2	54.1	44.5
200	71.8	58	47.4
260	69.7	59.1	49.7
360	70	61	52.8
460	69.5	63.2	56
600	68.9	64.1	59.8

Table 9: Efficiency of reconstructing the Higgs signal after the selection criteria described above. The MC is weighted to match the pileup conditions measured in data. The truth events were required to pass the following criteria: final state electron and muon $p_T > 5.5$ GeV, $|\eta| < 2.7$, and $m_Z, m_{Z^*} > 12$ GeV in the event.

Higgs mass	Analysis efficiency in %		
	4μ	$2e2\mu$	$4e$
110	4.38	2.55	1.89
115	10.6	6.56	4.8
120	16.2	10.7	8.46
125	22	14.5	11.5
130	26.9	17.7	13.8
135	30.4	21	15.7
140	33.4	23.4	19.6
145	36.3	25.1	20.5
150	38.8	27.7	21.7
180	55.7	42.6	35.1
200	57.7	46.5	37.9
260	57.1	48.6	41.1
360	60.1	51.8	45
460	61.1	55.4	48.6
600	61.2	57	53.1

Table 10: Efficiency of reconstructing the Higgs signal after the selection criteria described above. The MC is weighted to match the pileup conditions measured in data. There are no cuts imposed on the final state truth electron or muon p_T and η or event m_{Z/Z^*} .

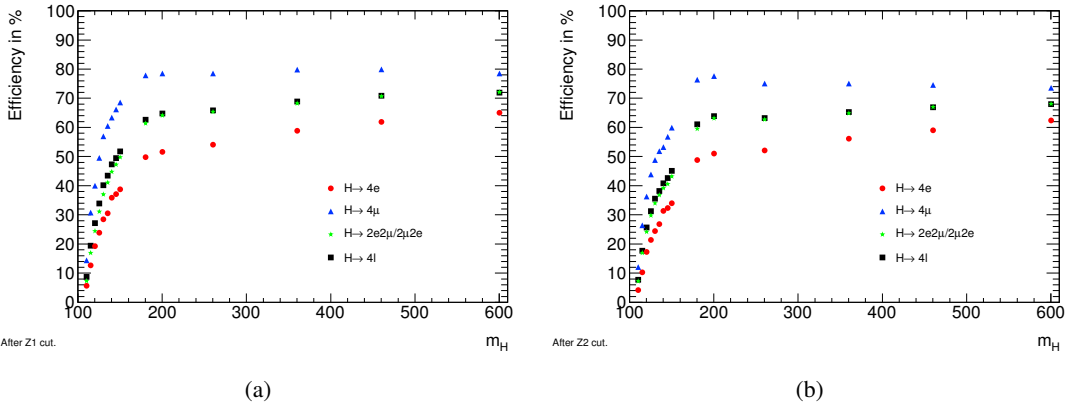


Figure 14: The efficiencies in each plot correspond to ggF+VBF+WH+ZH (when WH and ZH is applicable) and they are normalized to the truth cuts mention in Table 9. Figure (a) is after Z1 cut and Figure (b) after Z2 cut .

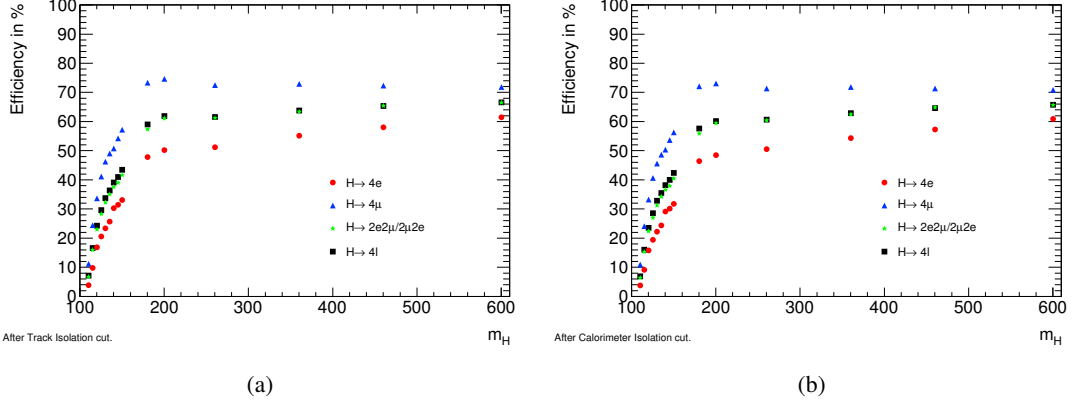


Figure 15: The efficiencies in each plot correspond to ggF+VBF+WH+ZH (when WH and ZH is applicable) and they are normalized to the truth cuts mention in Table 9. Figure (a) is after track isolation and Figure (b) after calorimeter isolation.

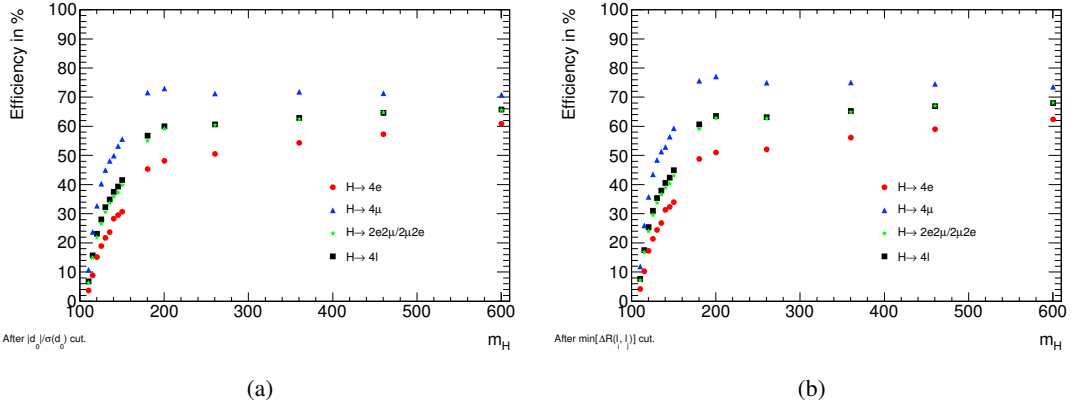


Figure 16: The efficiencies in each plot correspond to ggF+VBF+WH+ZH (when WH and ZH is applicable) and they are normalized to the truth cuts mention in Table 9. Figure (a) is after impact parameters significance and Figure (b) . is after Δ_R

7 Background estimation methods

This section describes the data-driven background estimation techniques and checks performed in different control-regions in the data.

The first control region aims at constraining a possible residual contribution from QCD multi-jet production. Then a $t\bar{t}$ control region is constructed using $e^\pm\mu^\mp$ pairs consistent with the Z mass and requiring the presence of an additional pair of leptons in the event. The observed events are then compared to the $t\bar{t}$ expectation from Monte-Carlo. Finally, the estimation of the most important reducible background $Z+XX$, where X denotes one additional lepton, is discussed in section 7.3.

7.1 Data driven cross checks of the QCD background contribution

In this analysis, where the presence of four isolated leptons with low impact parameter significance is required in the final state, the possible contributions from QCD multi-jet production is expected to be minimal.

However, since the production cross-sections of these processes are several orders of magnitude higher than the signal and other major backgrounds considered in this analysis, it is useful to study this background using the data.

The control region is constructed by selecting events where the primary di-lepton is formed by same sign leptons and that fulfil all the other criteria of the analysis. One should also take into account the expected number of events from other processes like ZZ , $Z+jets$ and $t\bar{t}$, especially for the electrons where the charge mis-identification rate is non-negligible,. From MC, the ratio of same-sign to opposite-sign QCD events is expected to be $O(50\%)$.

The event yields in the QCD control region are summarized in Table 11 where the MC includes only ZZ , $Z+jets$ and $t\bar{t}$. Applying the track isolation to the leptons, rejects all QCD events in the leading di-lepton mass window. For example in the $4e$ final state we are left with one surviving event in the data which is compatible with the expectation from ZZ , $Z+jets$ and $t\bar{t}$ alone (1.39). Thus, no QCD events are expected after the application of the full analysis selection.

In Figure 17 (a) the four-lepton invariant mass for the measured and expected events in the QCD control region after applying the selection in the first row of the previous tables is presented. In Figure 17 (b) and (c) the corresponding plots for the leading and subleading dilepton invariant mass are shown.

Figure 17: The four-lepton invariant mass (a), leading dilepton invariant mass (b) and subleading dilepton invariant mass (c) for the measured and expected events in the QCD control region after applying the analysis cuts without isolation and impact parameter cuts.

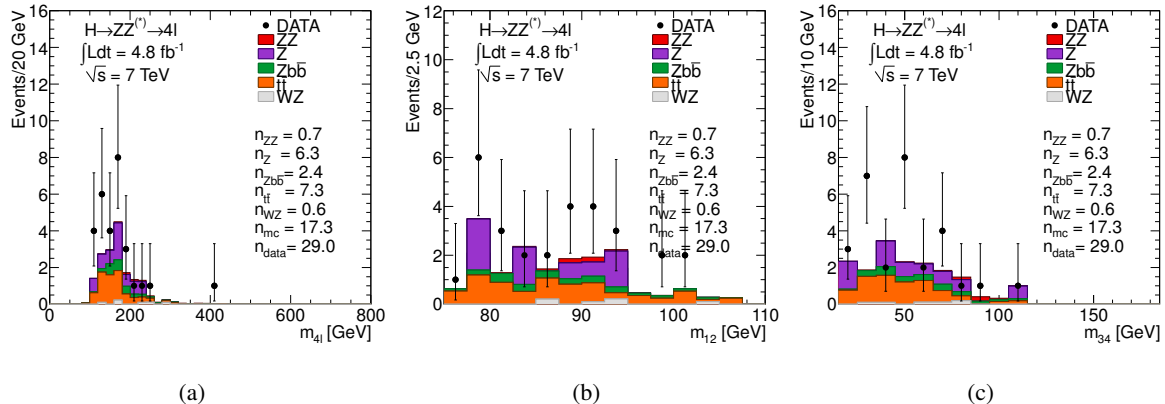


Table 11: Number of QCD events in the control region for data and Monte Carlo after applying the kinematic selection of the 4ℓ analysis. All the events in this table fulfill the data quality and trigger requirements. Note that the integrated luminosities of the 4μ , $4e$ and $2e2\mu$ channel are 4.81 fb^{-1} , 4.81 fb^{-1} and 4.92 fb^{-1} respectively.

Selection	4μ		$2e2\mu$		$4e$	
	Data	MC	Data	MC	Data	MC
Lepton quadruplet, both di-leptons $m_{2\ell} > 15\text{ GeV}$, ≥ 2 leptons with $p_T > 20\text{ GeV}$ and charge requirement, leading di-lepton mass, sub-leading di-lepton mass, $\Delta R(\ell, \ell') > 0.10$						
	13	5.53	6	4.24	10	7.68
Application of additional cuts independently						
Track isolation on leading dilepton	1	0.43	1	1.43	5	3.76
Track and calorimeter isolation on leading dilepton	1	0.36	1	1.33	4	3.37
Track isolation on all leptons	0	0.04	1	0.48	1	2.66
Track and calorimeter isolation on all leptons	0	0.04	1	0.39	1	1.47
Isolation on all leptons and d0 significance	0	0.02	0	0.38	1	1.39

7.2 Data driven cross-checks of the $t\bar{t}$ background contribution

A control region for $t\bar{t}$ is constructed by selecting events with an $e\mu$ opposite-sign di-lepton pair with a mass within 15 GeV of the Z boson mass and two additional opposite-sign same-flavour leptons. The leptons satisfy the identification criteria mentioned in the previous sections, while the p_T requirement is 20 GeV for the leptons of the $e\mu$ pair and 7 GeV for the additional leptons. Finally, track isolation requirements are applied to the leptons of the $e\mu$ pair. The contribution of other electroweak processes is negligible. Possible contributions from QCD events are estimated using a control region constructed with the same selection as above but same-sign $e\mu$ di-leptons. The ratio of same and opposite sign QCD $e\mu$ di-leptons events is taken from MC. In Table 12 the expected and observed yields are summarized for an integrated luminosity of 4.8 fb^{-1} . In Table 13 the effect of the additional analysis cuts on the selected events is presented. Out of the events passing the $e^\pm\mu^\mp + \mu\mu$ and $e^\pm\mu^\mp + ee$, the number of them passing isolation and impact parameter criteria is presented.

7.3 Estimation of the $Z+XX$ background

The most important reducible background for a low mass Higgs signal (below 180 GeV) with a sub-leading muon pair is the four-lepton final state of the ZQQ production process (where Q denotes heavy flavour jets originating from b and c quarks). Furthermore, in the case of electrons the most significant contributions arise from jets faking an electrons and photon conversions.

The estimation of the dominant reducible backgrounds can be extracted in a data-driven way by selecting appropriate control regions where no signal is expected and extrapolating the background contributions to the signal region using the cross-checked MC simulation. This idea is followed in this section for the estimation of the Z plus heavy quark and Z plus light jets backgrounds.

Since the contaminating sources for electrons and muons in the mentioned control regions are of different nature, two separate control samples are defined for the $Z(QQ \rightarrow \mu^+\mu^-)$ and the $Z(XX \rightarrow e^+e^-)$ processes. The various control samples and resulting background estimations will be discussed in the following sections.

Table 12: Observed and expected $e\mu$ events with two additional same-flavour leptons for an integrated luminosity of 4.8 fb^{-1} . Events after $M_{34} > 15 \text{ GeV}$ cut are also presented. Statistical and systematic uncertainties are included in the errors. For the $e^\pm\mu^\mp + ee$ the estimation is based on the standard electron algorithm.

	$e^\pm\mu^\mp + \mu\mu$	$e^\pm\mu^\mp + ee$
$t\bar{t}$	16.5 ± 1.9	1.9 ± 0.4
QCD	2.00 ± 0.5	1.4 ± 0.4
Total Expectations	18.5 ± 2.0	3.3 ± 0.6
Data	18 ± 4	2.0 ± 1.4
<hr/>		
$M_{34} > 15 \text{ GeV}$		
	$e^\pm\mu^\mp + \mu\mu$	$e^\pm\mu^\mp + ee$
$t\bar{t}$	12.4 ± 1.4	0.9 ± 0.3
QCD	0.9 ± 0.3	0.9 ± 0.4
Total Expectation	13.3 ± 1.4	1.8 ± 0.5
Data	12 ± 3	0 ± 1

Table 13: Observed and expected $e^\pm\mu^\mp + \mu\mu$ and $e^\pm\mu^\mp + ee$ events, where both the additional leptons passing isolation and impact parameter criteria.

	Data	MC	ttbar	QCD
<hr/> $e^\pm\mu^\mp + \mu\mu$ <hr/>				
Norm. Track isolation < 0.15	1 ± 1	1.17 ± 0.23	0.19 ± 0.09	0.98 ± 0.21
Norm. Calo. isolation < 0.3	5.0 ± 2.2	4.3 ± 0.5	3.1 ± 0.3	1.2 ± 0.4
$d_0/\sigma_{d0} < 3.5$	6 ± 2.4	6.7 ± 0.6	5.5 ± 0.4	1.2 ± 0.4
All Cuts	0 ± 1	0.04 ± 0.25	0.01 ± 0.20	0.03 ± 0.15
<hr/> $e^\pm\mu^\mp + ee$ <hr/>				
Norm. Track isolation < 0.15	1	1.5 ± 0.3	0.31 ± 0.11	1.2 ± 0.3
Norm. Calo. isolation < 0.3	1	0.5 ± 0.3	0.31 ± 0.11	0.16 ± 0.25
$d_0/\sigma_{d0} < 6$	2	1.3 ± 0.3	0.60 ± 0.15	0.7 ± 0.3
All Cuts	0	0.9 ± 1.0	0.3 ± 0.9	0.6 ± 0.5

7.3.1 Data driven cross checks of the $Z(QQ \rightarrow \mu\mu)$ background

In the following, “ $Q \rightarrow \mu$ ” will indicate reconstructed lepton candidates originating from heavy flavour. The MC prediction of the $Z(QQ \rightarrow \mu^+\mu^-)$ background contribution is affected by the theoretical uncertainty on the ZQQ production cross section and by uncertainties related to lepton reconstruction within b -jets. The estimation of this background contribution can be done via control samples in which the $ZQQ \rightarrow 4\ell$ fraction is measured. The extrapolation to the signal region is then performed using $ZQQ \rightarrow 4\ell$ Monte Carlo samples. The control samples are a compromise between high $ZQQ \rightarrow 4\ell$ purity and reasonable statistics.

$Z(QQ \rightarrow \mu^+\mu^-)$ normalization: The control sample for the estimation of the $Z(QQ \rightarrow \mu^+\mu^-)$ contribution is defined as follows. Events with at least four leptons in the final state are selected using the preselection criteria described in Section 5. The two leptons (electrons or muons) that constitute a Z candidate are required to follow the selection of the leading di-lepton pair of the analysis. A second pair

of muons is searched with $m_{34} > 15 \text{ GeV}$, without requiring isolation or impact parameter criteria. For all additional muons a threshold of $p_T > 7 \text{ GeV}$ is required. A cut $m_{34} < 72 \text{ GeV}$ is applied to reduce the ZZ contribution. Both the second di-muon mass, m_{34} , and charge can be used to control $Z(QQ \rightarrow \mu^+ \mu^-)$. The main contributions in this final state are muons from heavy quark decays ($Q \rightarrow \mu$) produced in association with a Z boson, muons from ZZ , WZ and $t\bar{t}$ decays and muons from in-flight pion and kaon decays and punch-through hadrons ($q \rightarrow \mu$) in events with a Z candidate.

$P(\pi/K \rightarrow \mu)$ contamination : The contamination due to pion and kaon decays can be estimated and subtracted by a track weighting procedure in event with a Z boson and at least one additional muon. Each charged track satisfying the analysis selection requirements, is assigned a p_T - and η -dependent probability $P(\pi/K \rightarrow \mu)$ to be reconstructed as a muon. These rates have been obtained from Monte Carlo and were compared to the data using $K_S^0 \rightarrow \pi^+ \pi^-$ decays [57]. The systematic uncertainty assigned to this rates is 20%. This method has been tested on the simulated $Z \rightarrow \ell\ell$ sample. The estimated rates of muons from heavy flavor decays are shown in Table 14, for both $Z \rightarrow \mu\mu$ and $Z \rightarrow ee$, along with the rates for true muons from heavy flavor decays.

Figure 18: The distribution of the multiplicity of additional muons with $p_T > 7 \text{ GeV}$ in $Z \rightarrow \ell\ell$ events.

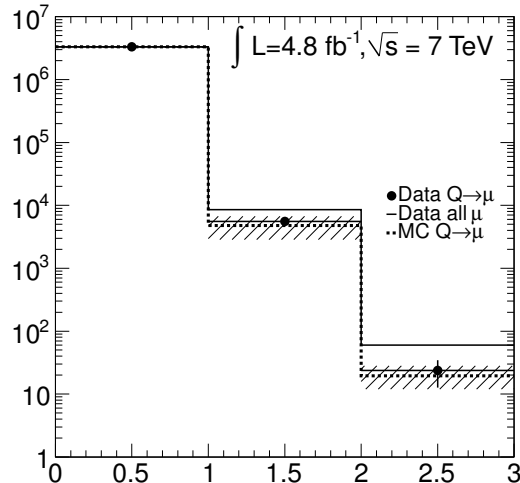


Table 14: Estimated and true events of $Z(QQ \rightarrow \mu\mu)$ and $Z(QQ \rightarrow \mu^+ \mu^-)$ in simulated events for the additional muons for an integrated luminosity of 4.5 fb^{-1} for both the muon stream and the egamma stream.

	$Z + \mu\mu$ from QQ	$Z + \mu^+ \mu^-$ from QQ
Estimated	20.9 ± 2.1	12.8 ± 1.7
True	20.8 ± 2.5	13.3 ± 1.8

Estimation of the $Z + (QQ \rightarrow \mu^+ \mu^-)$ normalization : The final estimate for the $Z + (QQ \rightarrow \mu^+ \mu^-)$ is presented in Table 15. Studies by the MCP group indicate that the total fake rate is in ruther

good agreement with the MC. Thus the systematic uncertainty of 20% is rather conservative.

Table 15: Total number of observed $Z + \mu^+ \mu^-$ events with $m_{34} < 72$ GeV and number of such events originating from ZZ , WZ $t\bar{t}$ decays (using MC) and $P(\pi/K \rightarrow \mu)$ in light jets (data-driven). The estimation of the $Z(QQ \rightarrow \mu^+ \mu^-)$ is also derived.

	$Z + \mu^+ \mu^-$
Observed	34
$ZZ(\text{MC})$	8.2 ± 0.2
$WZ(\text{MC})$	0.2 ± 0.1
$t\bar{t}(\text{MC})$	6.4 ± 0.4
$Z + \text{ light jets (DATA)}$	7 ± 2
Total without $Z(QQ \rightarrow \mu^+ \mu^-)$	22 ± 2
Estimated $Z(QQ \rightarrow \mu^+ \mu^-)$	12 ± 7
True $Z(QQ \rightarrow \mu^+ \mu^-)$	13.3 ± 1.8

Efficiency of additional selection criteria for $Z + \mu$ events The efficiency of the isolation and impact parameter cuts for $Z + \mu$ is presented in table 16 for both data and MC. The invariant mass spectra of the non-leading dilepton and the quadruplet of the events with 4ℓ are presented in Figure 19.

Table 16: Efficiency of isolation and impact parameter criteria when applied to the additional muon of $Z + \mu$ cases.

	Data (%)	MC (%)
Norm. Track isolation < 0.15	31.9 ± 0.9	32.6 ± 0.24
Norm. Calo. isolation < 0.3	43.0 ± 0.8	44.01 ± 0.23
All isolation cuts	25.0 ± 1.0	25.3 ± 0.25
$d_0/\sigma_{d0} < 3.5$	82.6 ± 0.5	81.8 ± 0.13
All cuts	20 ± 1	20.3 ± 0.4

7.3.2 $Z+XX (X \rightarrow e)$ background

In this section the estimation of the $Z+XX$ background, where X denotes a possible additional electron, is described. The additional electrons can originate from hadrons in jets faking an electron (denoted by j), photons e.g. from π^0 decays (denoted by γ), or heavy quark mesons decaying semi-leptonically (denoted as Q). To estimate the $Z+XX$ background in the Higgs signal region, the MC prediction is normalized in a control region, and then using the relative composition and the efficiency for each component, predicted by the MC, an extrapolation to the $H \rightarrow 4\ell$ signal region is performed. In this section the normalization factor is derived and several cross-checks are made in order to check the MC description of the efficiencies and the composition.

In Table 17 the relative fractions of events with one or more additional electrons, produced in association with a Z boson, is shown.

$Z+XX (X \rightarrow e)$ normalization In the case of a subleading electron pair, the main contribution is expected from $Z+jX$ events. Moreover, the $Z+b$ cross-section was measured [?] and was found to be in

Figure 19: (a) Non-leading opposite sign dilepton invariant mass spectrum and (b) the corresponding quadruplet mass of opposite dimuon pairs for an integrated luminosity of 4.5 fb^{-1} . The $m_{34} < 72 \text{ GeV}$ cut was not applied.

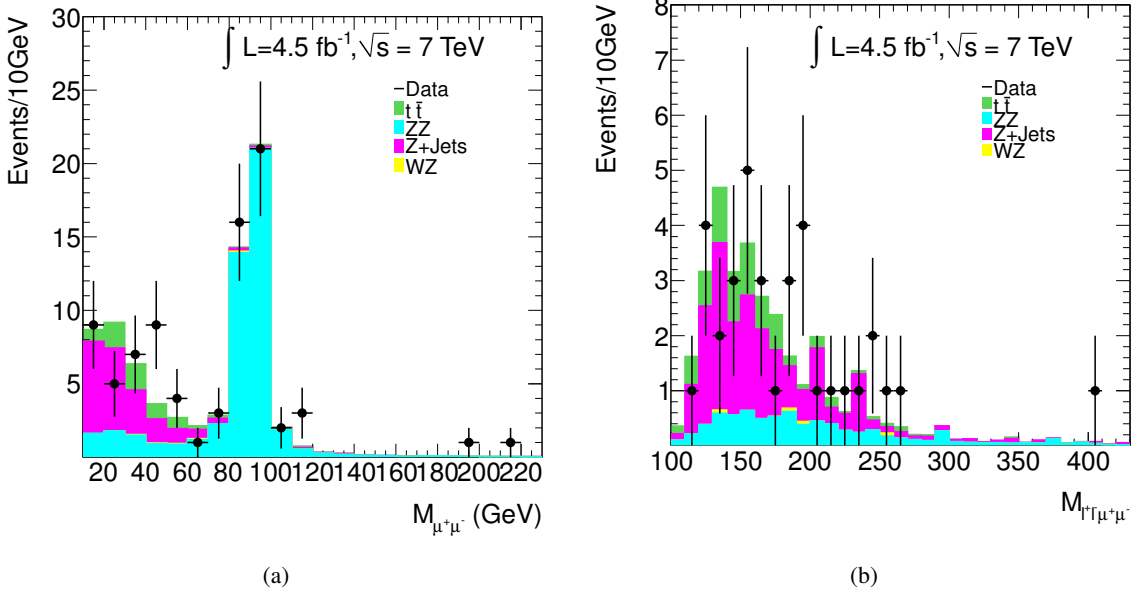


Table 17: Predicted and measured fractions of Z decays accompanied by zero, one and two additional electron candidates.

Fractions	Predicted (%)	Measured (%)
Z+0	99.40	99.39
Z+one additional electron	0.59	0.60
Z+two additional electrons	0.006	0.007

agreement within the systematic errors between data and MC. Studies of ZQQ events presented in this note with a subleading muon pair also show a good modelling of such events by the MC simulation. As previous studies of the electron performance, in particular the identification efficiencies for $Q \rightarrow e$ in the inclusive electron cross-section analysis [58] and in $J/\psi \rightarrow ee$ decays [59] demonstrated an adequate modelling by the MC simulation, as well, the emphasis is placed here on the normalization of the Z+jX component.

The method employed [60] to estimate the Z+jX component (denoted as $N_{ZjX} = N_{Zjj} + N_{Zj\gamma} + N_{ZjQ}$), uses events with a Z boson selected as in the present analysis – and two extra electrons passing the *loose ++* selection criteria. After *loose ++*, the background is still dominated by the jet component (ZjX).

The ZjX contribution can be estimated, from Monte Carlo, using a jets-dominated control region. As shown in Figure 20, R_η offers a good separation between hadrons and heavy quark contributions: for $R_\eta < 0.7$ the distribution is fully dominated by jets. One can thus normalize a Z inclusive MC sample to the data in the region $R_\eta < 0.7$ and then use the scaled MC to predict the Zjx yields after *loose ++* selection. The predicted ZjX yields are given by the following formula:

$$N_{jX}(\text{loose}++) = N_{ZjX}^{CR} \times \frac{N_{R_\eta < 0.7}^{\text{Data}}}{N_{R_\eta < 0.7}^{\text{MC}}} \times \varepsilon_{\text{MC}}(\text{loose}++), \quad (1)$$

where N_{ZjX}^{CR} is the number of ZjX events in the control region (Z plus two additional reconstructed electrons) in MC and ε_{MC} is the efficiency for ZjX events to pass *loose*++. The ratio $\frac{N_{R_\eta < 0.7}^{\text{Data}}}{N_{R_\eta < 0.7}^{\text{MC}}}$ is calculated with a statistical uncertainty of 1.5%. To ensure $\varepsilon_{\text{MC}}(\text{loose}++)$ probably describes the efficiency in data one has to correct for possible shifts in the shower shapes. As an example the shift in R_η is shown in figure 21.

Figure 20: R_η shower shape distributions for electron candidates (track-EM cluster matches) in Z+X MC events. These candidates are not associated with the Z-boson. The contributions of photons, jets and heavy quarks are shown.

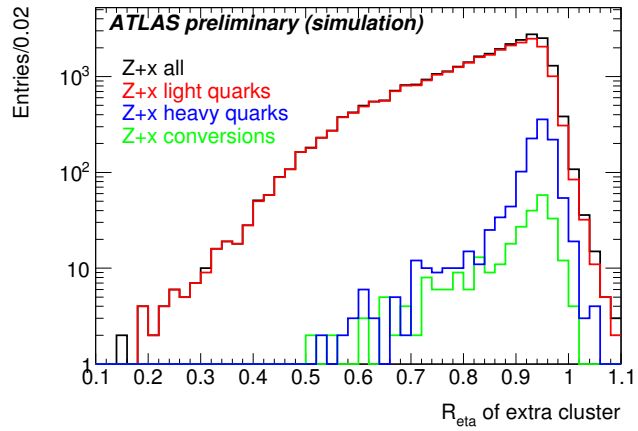
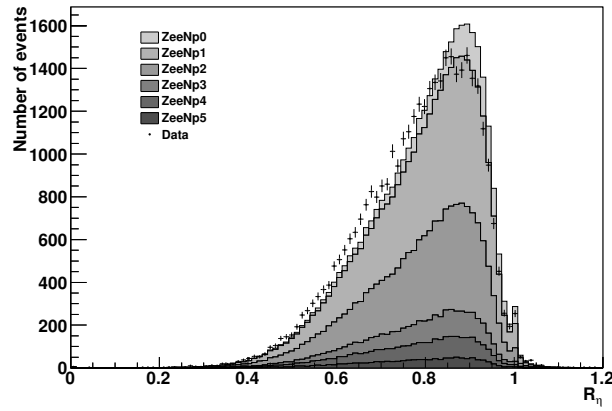
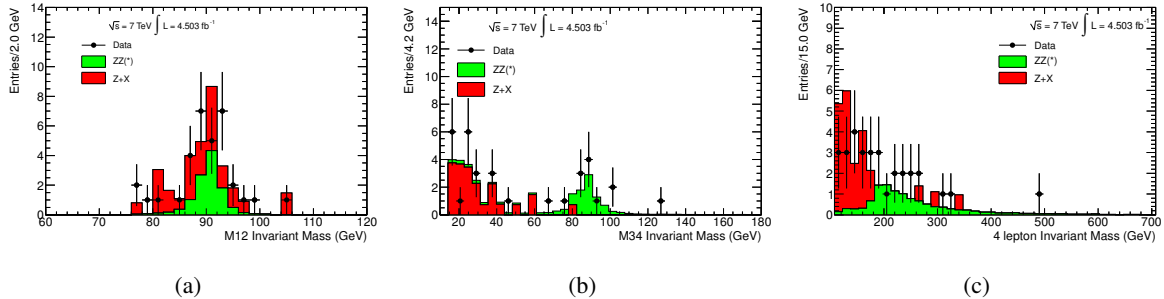


Figure 21: R_η of additional electrons after identification of a Z candidate, $p_T > 7\text{GeV}$, and $|\eta| < 2.47$ in data and Alpgen Z \rightarrow ee with Np=0-5 additional partons. Z candidate selection is as for H \rightarrow 4l. The combined MC is normalised to the number of entries in data. Data correspond to periods B-M.



The performance of the method was tested using Z+X MC events (closure test). Table 18 shows the predicted ZjX yields after application of Eq.1, for both MC and data. The total systematic uncertainty of these expectations is of order 20%, arising mainly from the variation of the shower-shapes ($\simeq 15\%$),

Figure 22: Prediction of $Z+X \rightarrow 4e$ background (red) after *loose ++* plus $m_{34} > 15\text{GeV}$ selection and comparison with data. The ZZ expectation is shown in green.



the available statistics in the normalization region ($\simeq 1.5\%$) and the intrinsic accuracy of the normalization method ($< 3\%$ from the closure test). Note that because the ZjX control region normalization is performed on single electrons, although the $Q \rightarrow e$ has a large R_η , jQ pairs present in the data also contribute. This means that the extrapolation predicts the $N_{ZjX} = N_{Zjj} + N_{Zj\gamma} + N_{ZjQ}$. For example after the application of the *loose ++* selection and the final m_{34} cuts the Monte Carlo predicts 19 ZjX events ($Z \rightarrow ee + XX=8\pm 2$, $Z \rightarrow \mu\mu + XX=11\pm 3$). Comparing these numbers a scale factor of $1.2 \pm 0.2\%$ is derived and used in order to normalize the MC prediction in the control region (23 events as given in Table 18).

The remaining ZQQ component can be extracted by subtracting the dominant ZjX component for

Table 18: Predicted ZqX yields, $N_{ZjX} = N_{Zjj}N_{Zj\gamma} + N_{ZqQ}$ after *loose ++* electron selection for the additional electrons in reconstructed $Z \rightarrow \ell\ell$ events, using extrapolation from a high statistics control data region, (see Eq. (1)). The extrapolation is first done at the point after *loose ++* and $m_{34} > 15\text{GeV}$, then to the point after the final m_{34} cuts, and finally to the signal region. The level of agreement between data and MC is presented in Figs.22,23,24. The ZQQ expectation is also shown. The quoted uncertainties are statistical. The systematic uncertainties of these predictions are of order 20% (see text).

Electron Quality	Predicted $ZjX \rightarrow 4e$	Predicted $ZjX \rightarrow 2\mu 2e$	Predicted ZQQ
<i>loose ++</i> $m_{34} > 15\text{GeV}$	20 ± 4	32 ± 6	< 7
<i>loose ++</i> final m_{34} cuts	11 ± 3	12 ± 3	-
<i>loose ++</i> Final Selection	3 ± 2	1.7 ± 0.7	-

masses below 80GeV, albeit with a large combined statistical and systematic uncertainty. Here we only report an upper bound. All predictions are reported in Table 18. In Figures 22, 23, and 24 the data/MC comparison is presented for the leading Z , the subleading Z and the 4-lepton invariant mass. The ZjX prediction is shown in red demonstrating a reasonable agreement with data.

Z+jj and Z+j γ relative normalization and rejection The relative normalization between $Z+jj$, $Z+j\gamma$ and $Z+\gamma\gamma$ and the corresponding rejections are studied in both data and MC. A control region can be built for jets and photons based on pixel and silicon hits requirements. Jets are expected to have B-Layer hits or, in cases where the b-layer module is dead, at least an extra pixel hit (loose++ requires already 1 pixel and 7 total silicon hits). In this sub-section jets include all non-photon contribution. Otherwise, the electron candidate is considered to be a photon. The purity, estimated using Z inclusive MC, is 92.3% for the jet category and 90.7% for the photon category. Table 19 presents the events with two

Figure 23: Prediction of $Z+X \rightarrow 2\mu 2e$ background (red) after *loose ++* plus $m_{34} > 15\text{GeV}$ selection and comparison with data. The ZZ expectation is shown in green.

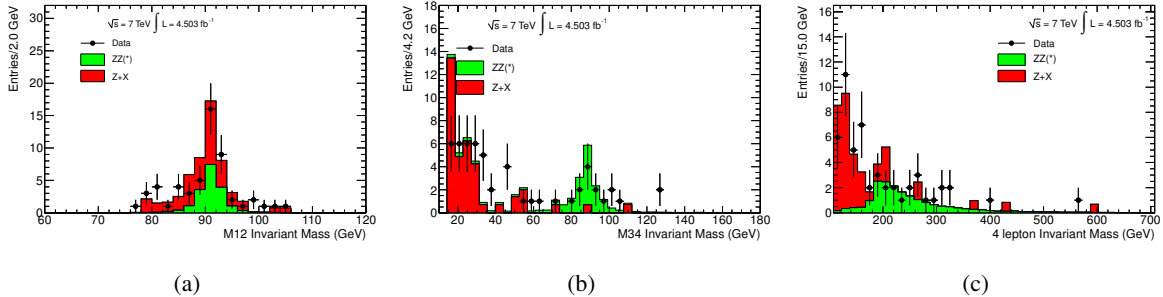
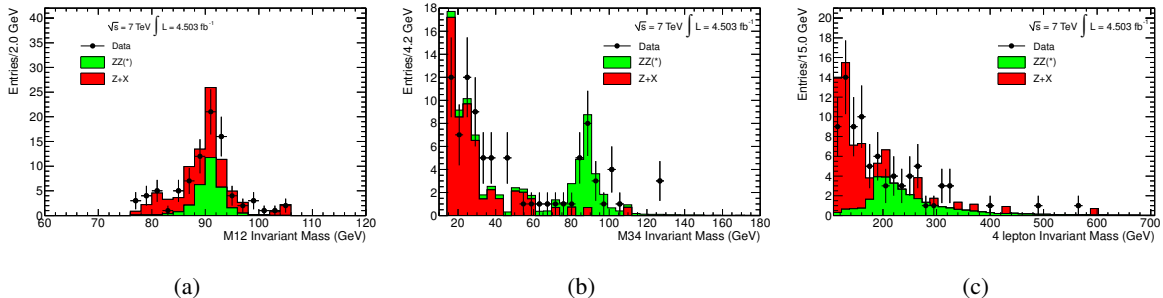


Figure 24: Prediction of $Z+X \rightarrow 4e + 2\mu 2e$ background (red) after *loose ++* plus $m_{34} > 15\text{GeV}$ selection and comparison with data. The ZZ expectation is shown in green.



additional electrons classified both as jets, as photons or as one jet and one photons using the above definition. A comparison between data and Monte Carlo is made before and after the application of impact parameter significance and isolation cuts, as well as before and after a $m_{34} < 72\text{ GeV}$ (in order to suppress potential contributions from ZZ). The efficiencies of the track and calorimetric isolation and of the impact parameter significance, for each of the jet and photon control regions (as defined previously) were also studied. In Table 20, 21 and 22 the efficiencies for these selection criteria for the electron accompanying the Z candidate are presented.

Z+XX expectation in the signal region: In this section the final estimation of the Z+XX background is presented. The expected Z+XX after the *loose ++* and final m_{34} criteria in the Monte Carlo is:

- $Z \rightarrow ee + XX = 8 \pm 2$
- $Z \rightarrow \mu\mu + XX = 11 \pm 3$

The above numbers are scaled by $20 \pm 20\%$ to take into account their relative difference with 19 events expected in the pure MC and 23 after rescaling. The estimated (from MC) relative Z+jX background composition is:

- $Z \rightarrow ee + XX:$
 - $Z \rightarrow ee + jj \simeq 25\%,$
 - $Z \rightarrow ee + j\gamma \simeq 25\%,$

Table 19: Percentage of jets and conversions categories (based on pixel and B-Layer requirement hits see text) in Z+ee events. Results are provided before and after the application of impact parameter significance and isolation cuts. A cut $m_{34} < 72$ GeV has been applied. This plot demonstrates a reasonable agreement between data and MC.

Both Jets		
	Before Cuts(%)	After Cuts (%)
Data	65±9	73±25
Z+jets MC	57±6	58±13
Both Conversions		
	Before Cuts(%)	After Cuts (%)
Data	1.0±1.0	0.0±7
Z+jets MC	0.8±0.2	0.0±7
Jet - Conversion		
	Before Cuts(%)	After Cuts (%)
Data	34±8	27±15
Z+jets MC	42±6	42±20

Table 20: Efficiency of isolation and impact parameter criteria when applied to the additional electron of Z + e cases classified as jets (see text).

	Data (%)	Monte Carlo (%)	Truth light Hadrons (%)
Norm. Track isolation < 0.15	48.3 ± 0.6	48.57 ± 0.23	
Norm. Calo. isolation < 0.3	47.4 ± 0.6	46.91 ± 0.22	
All isolation cuts	32.4 ± 0.7	31.80 ± 0.26	
$d_0/\sigma_{d0} < 6$	91.4 ± 0.3	92.92 ± 0.10	
All cuts	28.7 ± 0.7	28.5 ± 0.3	26 ± 2

Table 21: Efficiency of isolation and impact parameter criteria when applied to the additional electron of Z + e cases classified as photons (see text).

	Data (%)	Monte Carlo (%)	Truth Photons (%)
Norm. Track isolation < 0.15	71.6 ± 0.7	68.2 ± 0.4	
Norm. Calo. isolation < 0.3	59.4 ± 0.9	59.88 ± 0.5	
All isolation cuts	50.4 ± 1.0	48.98 ± 0.6	
$d_0/\sigma_{d0} < 6$	67.7 ± 0.8	62.12 ± 0.4	
All cuts	34.1 ± 1.1	33.9 ± 0.3	34.5 ± 1.3

- $Z \rightarrow ee + ej \simeq 21\%$,
 - $Z \rightarrow ee + \gamma\gamma \simeq 7\%$,
 - $Z \rightarrow ee + jQ \simeq 7\%$,
 - $Z \rightarrow ee + \gamma Q \simeq 7\%$,
 - $Z \rightarrow ee + \gamma e \simeq 7\%$.
- $Z \rightarrow \mu\mu + XX$:

Table 22: Efficiency of isolation and impact parameter criteria when applied to the additional electron (see text).

	Data (%)	Monte Carlo (%)
Norm. Track isolation < 0.15	54.6 ± 0.5	54.3 ± 0.3
Norm. Calo. isolation < 0.3	50.6 ± 0.5	50.0 ± 0.3
All isolation cuts	37.3 ± 0.6	36.5 ± 0.3
$d_0/\sigma_{d0} < 6$	84.5 ± 0.3	85.6 ± 0.2
All cuts	29.9 ± 0.6	30.4 ± 0.4

- $Z \rightarrow \mu\mu + jj \simeq 35\%$,
- $Z \rightarrow \mu\mu + j\gamma \simeq 57\%$,
- $Z \rightarrow \mu\mu + \gamma\gamma \simeq 8\%$,

where a $Z \rightarrow \ell\ell$ is first selected (using the analysis criteria) and then truth matching is applied to the extra leptons. Thus, there is a non-zero probability of selecting a wrong electron for the leading pair (e.g due to charge misidentification), which can lead to cases such as $Z \rightarrow ee + ej$. The corresponding efficiencies for $j \rightarrow e$ ($\simeq 28\%$), $\gamma \rightarrow e$ ($\simeq 35\%$), calculated using Table 20, 21 and the corresponding purities, and for $Q \rightarrow e$ and isolated electrons calculated in the previous and next sections are used in order to extrapolate to the $H \rightarrow 4l$ signal region. Toy pseudo-experiments are thrown using all the above inputs. For each experiment the individual background components are generated independently using Poisson statistics, while a Gaussian uncertainty of 20 % is taken into account for the normalization. The final estimates for $4.5 ifb$ are:

- $Z \rightarrow ee + XX = 1.5 \pm 0.7$ events
- $Z \rightarrow \mu\mu + XX = 1.2 \pm 0.5$ events

The above numbers are compatible with the ones presented in Table 18, taking into account the errors. It should be noted that although the control regions used in this analysis indicate that the Monte Carlo describes the relative composition rather well, the amount of available statistics after the *loose ++* selection is extremely limited, constituting the main limiting factor in this study.

7.3.3 Data Monte Carlo comparison in control regions

For this study, a four-lepton final state is selected as in the standard analysis, but the flavor, charge and invariant mass requirements applied on the subleading dilepton are relaxed. For all the plots in this section the ZjX contribution in the Monte Carlo is scaled by 1.2 (see previous section).

The invariant mass distributions for data and the relevant Monte Carlo samples are shown in Figure 25 for the three final states ($Z+\mu\mu$, $Z+ee$ and $Z+e\mu$) after applying the kinematic and invariant mass requirements of the standard analysis as well as tracking and calorimetric isolation for the leading dilepton pair. In this step, the irreducible contribution from the ZZ background is visible for the first two final states as well as the main contributions, arising from $Zb\bar{b}$ for the $Z+\mu\mu$ and $Z+jets$ for the $Z+ee$ final state. In the above cases, the data are described by the MC, while for the $Z+e\mu$ state a disagreement is observed, due to other background contributions such as $Zb\bar{j}$.

In Figure 26, in addition to what has been explained before, inverted selection criteria for the impact parameter significance of the subleading dilepton are applied in order to form a $Zb\bar{b}$ control region. No

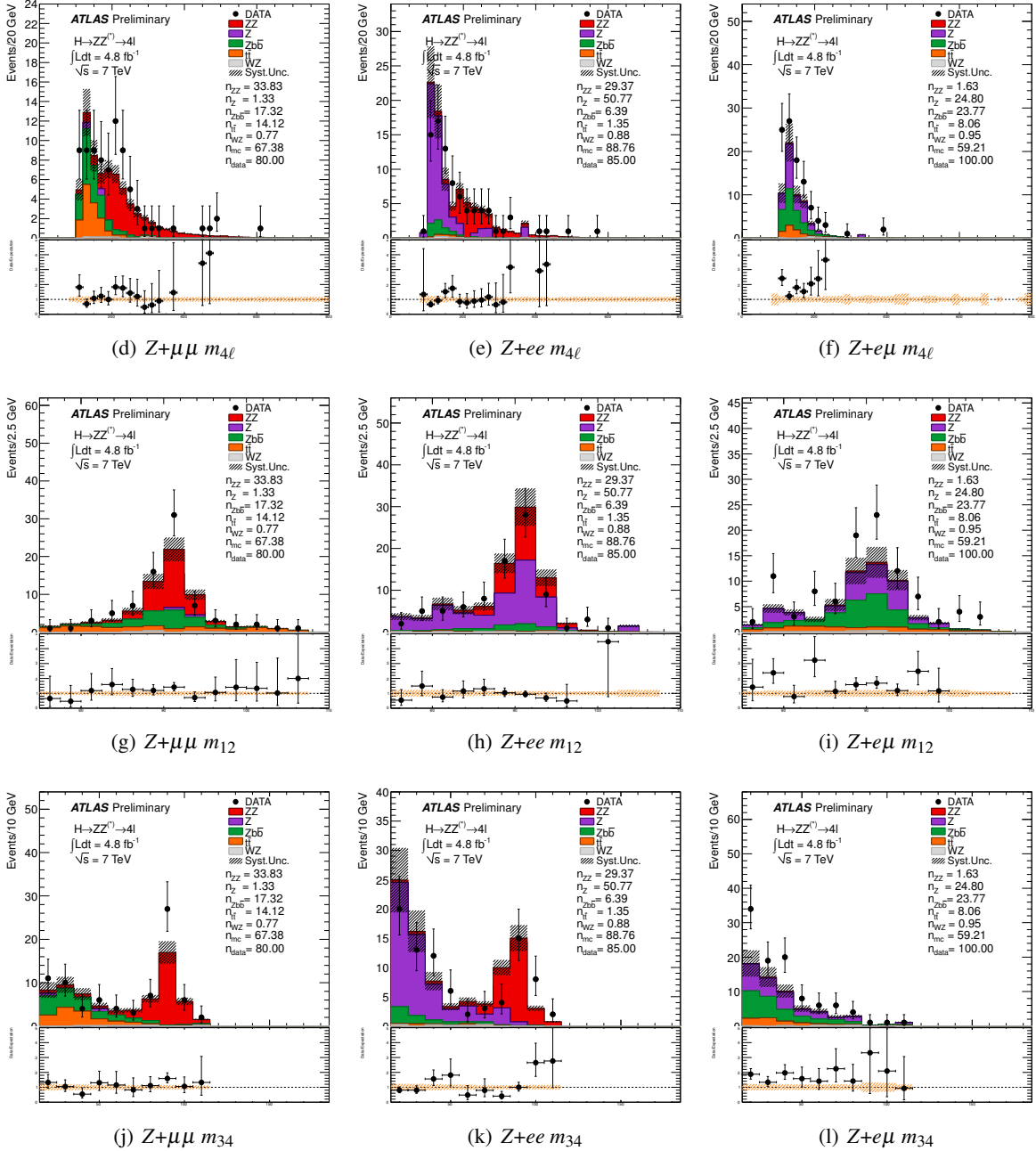


Figure 25: The invariant mass distributions for the three final states after the kinematic, invariant mass requirements and track and calorimetric isolation of the leading dilepton pair.

significant contribution is shown to this control region by the $Z+ee$ case. The number of events in the data and the expected ones for the various backgrounds are quoted on the plots.

In Figure 27, apart from the selection in Figure 25, the standard selection criteria for the impact parameter significance of the subleading dilepton have been applied, while inverted track isolation criteria for subleading dilepton have been applied in order to form a $Z+jets$ control region. This is the dominant background for the $Z+ee$ and the $Z+e\mu$ final states. An agreement is observed between data and Monte Carlo. The number of events in the data for this control region and the expected ones for the various backgrounds are quoted on the plots. Additional plots can be found in section Q of the appendix.

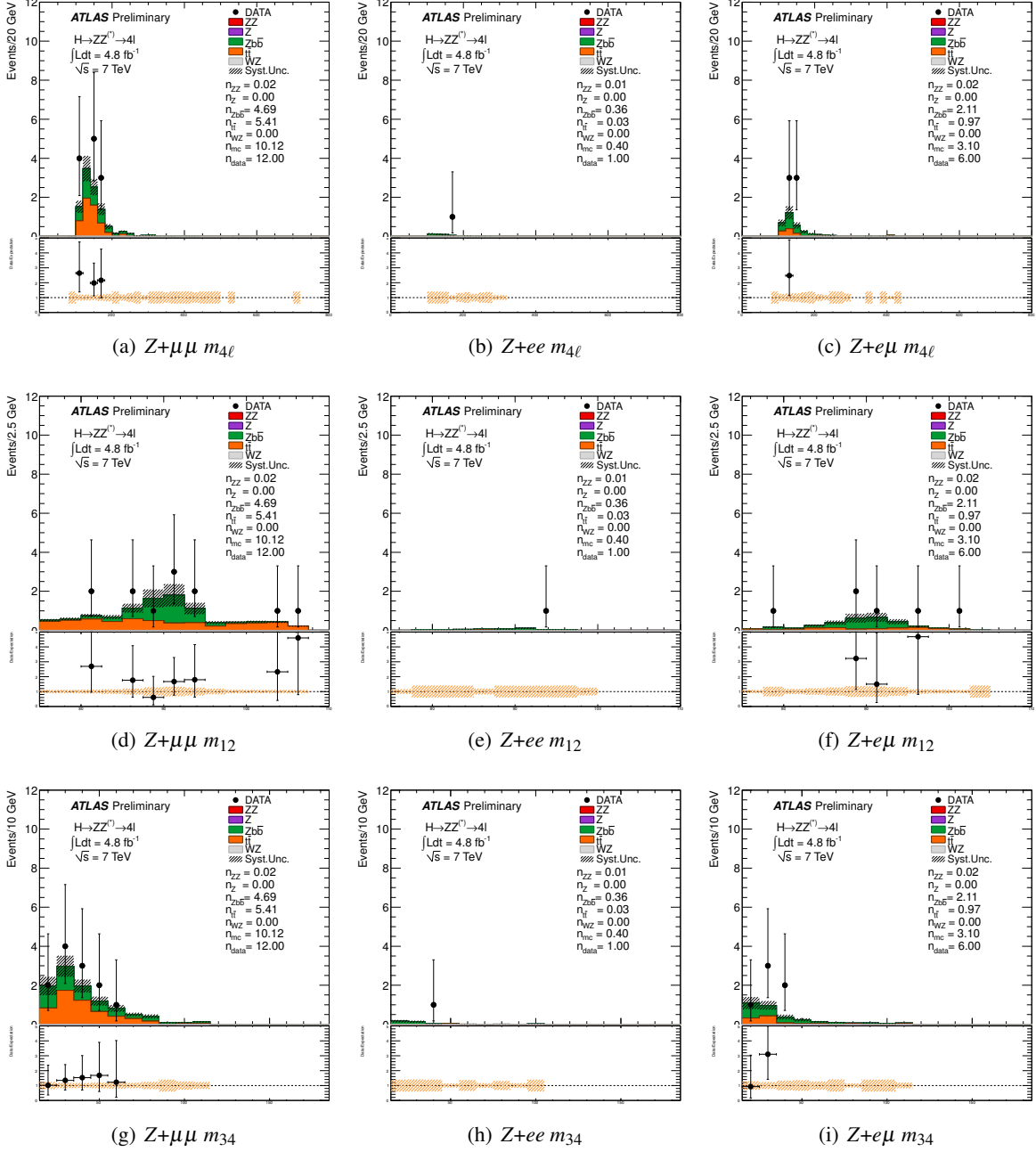


Figure 26: The invariant mass distributions for the three final states after the kinematic cuts, invariant mass requirements, track and calorimetric isolation of the leading dilepton pair and inverted impact parameter significance cuts for the subleading dilepton so that the $Zb\bar{b}$ control region is formed.

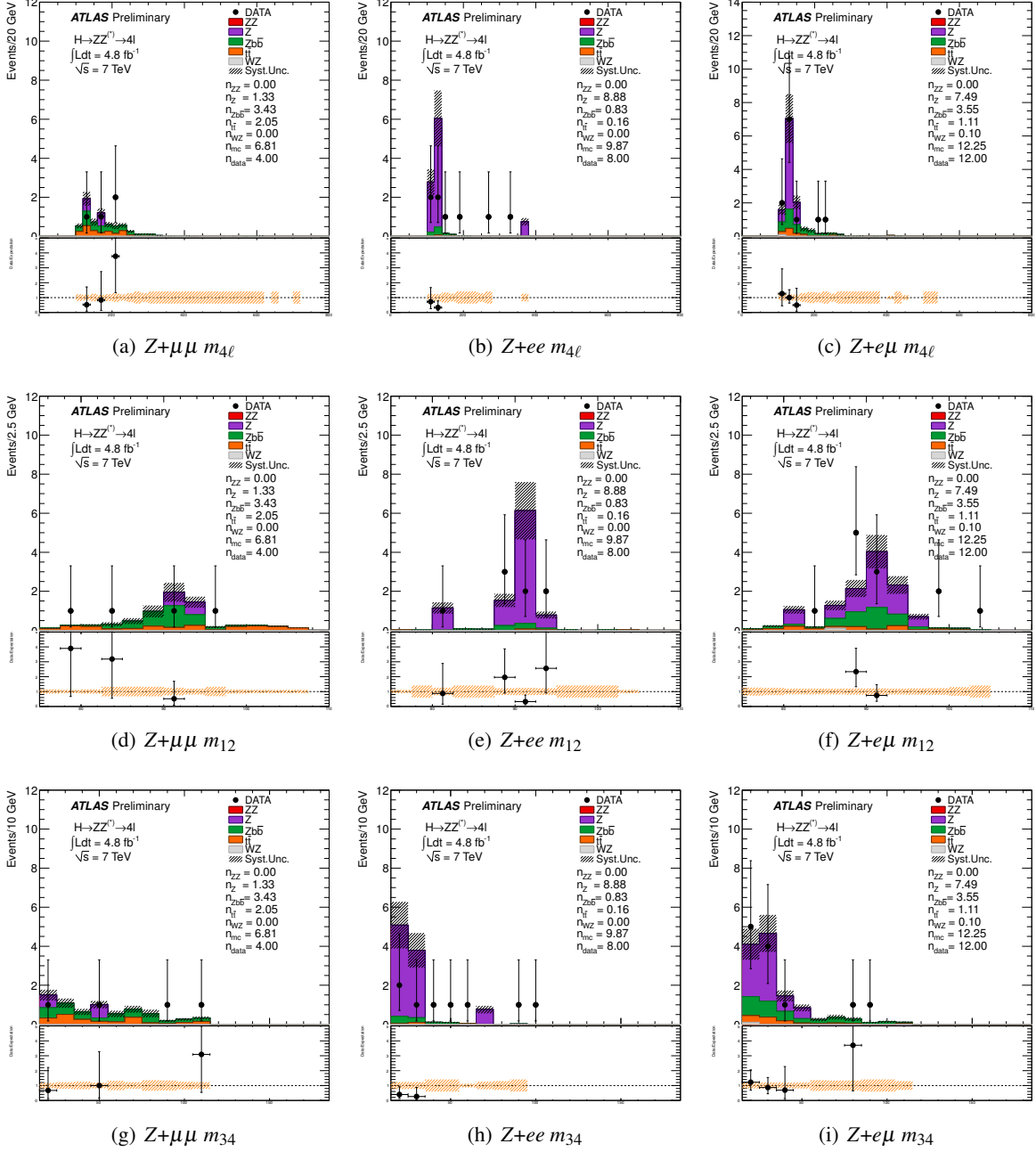
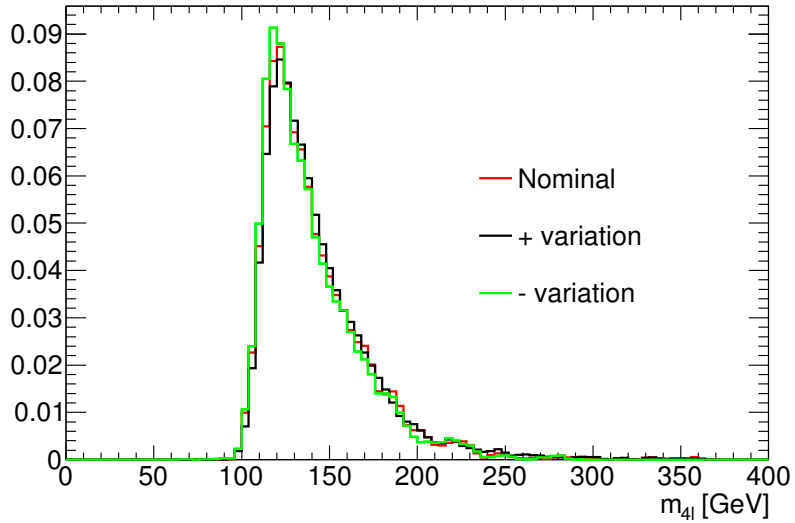


Figure 27: The invariant mass distributions for the three final states after the kinematic cuts, invariant mass requirements, track and calorimetric isolation of the leading dilepton pair, impact parameter significance cuts and inverted track isolation for the subleading dilepton for the $Z+jets$ control region.

Figure 28: The shape of the $Z+XX$ background used in this analysis.



7.4 $Z+XX$ Mass Shape

The M_{4l} shape for the $Z+XX$ background, after the application of all analysis selection criteria, is estimated using a $Zb\bar{b}$ MC sample considering all the final states together and is shown in Figure 28. Unfortunately, the remaining ZjX statistics in the MC, after the full analysis selection, do not allow for its inclusion. The uncertainty in the M_{4l} shape is estimated by relaxing/tightening the isolation selection criteria.

8 Higgs mass resolution

Higgs mass resolution is obtained from an unbinned maximum likelihood fit of a gaussian model to the four lepton invariant mass distribution, in the $\mu\mu\mu\mu$, $eeee$, $\mu\mu ee$ and $ee\mu\mu$ channels. Figure 29 shows the invariant mass resolution for a simulated MC sample with $m_H = 130$ GeV, while figure 30 shows the same distributions before applying lepton energy/momentum smearing.

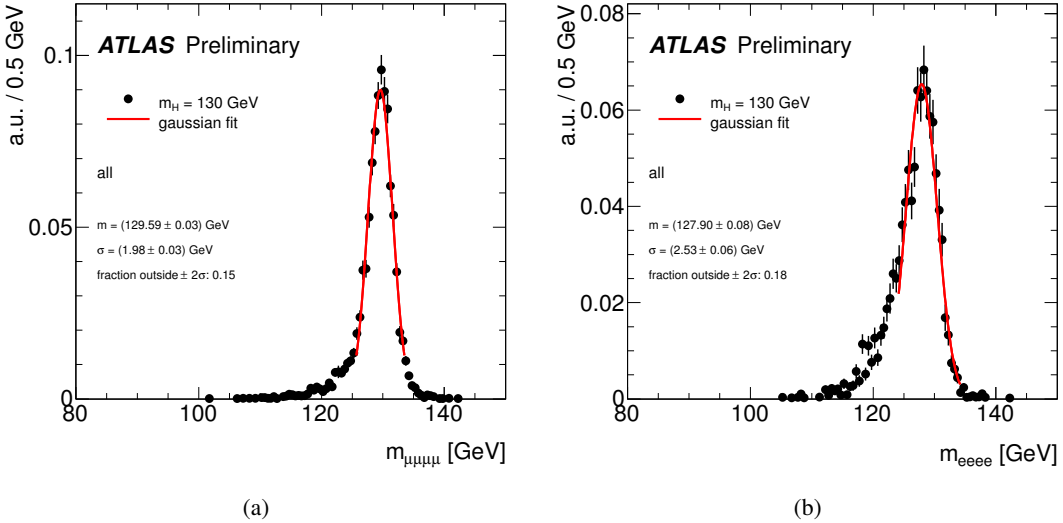


Figure 29: Invariant mass distribution for a simulated MC sample with $m_H = 130$ GeV, in the $\mu\mu\mu\mu$ and $eeee$ channels (black points); superimposed is the gaussian fit to the $m_{4\ell}$ peak (red line).

The dependence of resolution on the detector region where leptons are reconstructed has also been investigated. Table 23 reports the results of the resolution studies for different event categories; fit results are shown in figures 31–34.

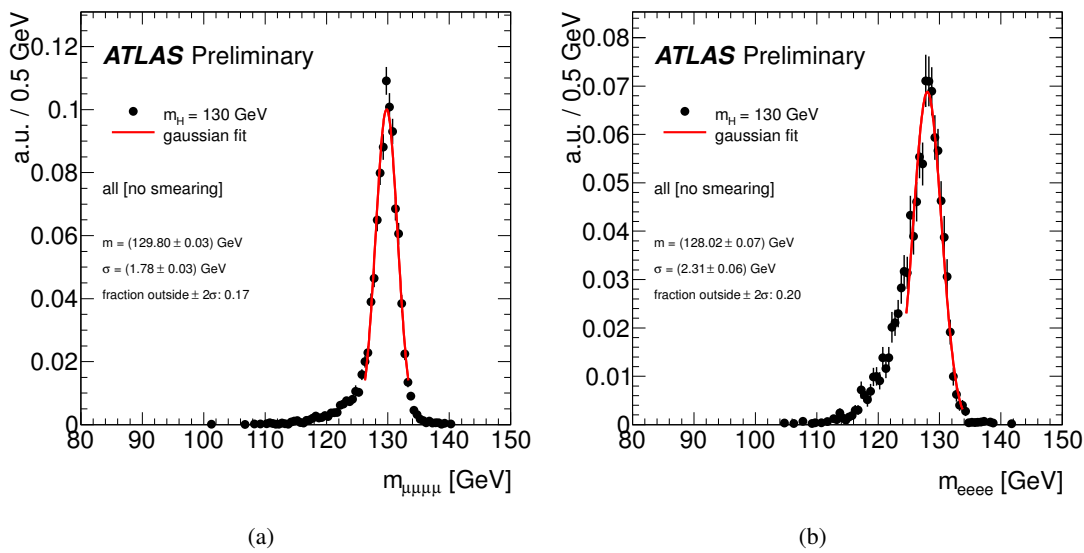


Figure 30: Invariant mass distribution for a simulated MC sample with $m_H = 130 \text{ GeV}$, in the $\mu\mu\mu\mu$ and $eeee$ channels, without the application of momentum/energy smearing (black points); superimposed is the gaussian fit to the $m_{4\ell}$ peak (red line).

channel	name	description	frequency	m [GeV]	σ [GeV]	events outside $\pm 2\sigma$
$\mu\mu\mu\mu$	all	all events	1.00	129.59 ± 0.03	1.98 ± 0.03	0.15
$\mu\mu\mu\mu$	bbbb	all muons in the barrel	0.21	129.61 ± 0.06	1.58 ± 0.06	0.16
$\mu\mu\mu\mu$	bbb	three muons in the barrel	0.28	129.55 ± 0.06	1.79 ± 0.06	0.14
$\mu\mu\mu\mu$	bb	two muons in the barrel	0.26	129.54 ± 0.07	2.16 ± 0.06	0.14
$\mu\mu\mu\mu$	other	any other event	0.25	129.72 ± 0.08	2.36 ± 0.08	0.17
$\mu\mu ee$	all	all events	1.00	128.70 ± 0.05	2.51 ± 0.06	0.14
$\mu\mu ee$	any-onecrk	at least one electron in the crack region	0.09	127.29 ± 0.27	3.56 ± 0.26	0.11
$\mu\mu ee$	bb_bb	all leptons in the barrel	0.32	128.99 ± 0.08	2.13 ± 0.08	0.15
$\mu\mu ee$	other_bb	muons in the endcaps, electrons in the barrel	0.33	128.99 ± 0.09	2.41 ± 0.09	0.15
$\mu\mu ee$	other_other	any other event	0.26	128.20 ± 0.12	2.75 ± 0.12	0.13
$e\bar{e}\mu\mu$	all	all events	1.00	128.58 ± 0.05	2.31 ± 0.05	0.15
$e\bar{e}\mu\mu$	onecrk_any	at least one electron in the crack	0.09	126.50 ± 0.28	4.11 ± 0.29	0.07
$e\bar{e}\mu\mu$	bb_bb	all leptons in the barrel	0.33	128.93 ± 0.06	1.87 ± 0.06	0.17
$e\bar{e}\mu\mu$	bb_other	electrons in the barrel, muons in the endcaps	0.28	128.76 ± 0.08	2.12 ± 0.08	0.16
$e\bar{e}\mu\mu$	other_other	any other event	0.31	128.08 ± 0.10	2.78 ± 0.09	0.14
$eee\bar{e}$	all	all events	1.00	127.90 ± 0.08	2.53 ± 0.06	0.18
$eee\bar{e}$	bbbb	all electrons in the barrel	0.47	128.62 ± 0.08	1.93 ± 0.07	0.21
$eee\bar{e}$	onecrk	at least one electron in the crack region	0.18	126.00 ± 0.24	3.62 ± 0.20	0.13
$eee\bar{e}$	bbb	three electrons in the barrel (none in the crack)	0.20	127.21 ± 0.18	3.03 ± 0.16	0.12
$eee\bar{e}$	other	any other event	0.14	127.29 ± 0.22	2.73 ± 0.19	0.15

Table 23: Resolution on the four lepton invariant mass, estimated from a signal MC sample ($m_H = 130$ GeV), in different detector reconstruction regions. Barrel for muons is defined as $|\eta| < 1.05$; for electrons, barrel is defined as $|\eta| < 1.37$, crack region as $1.37 < |\eta| < 1.52$.

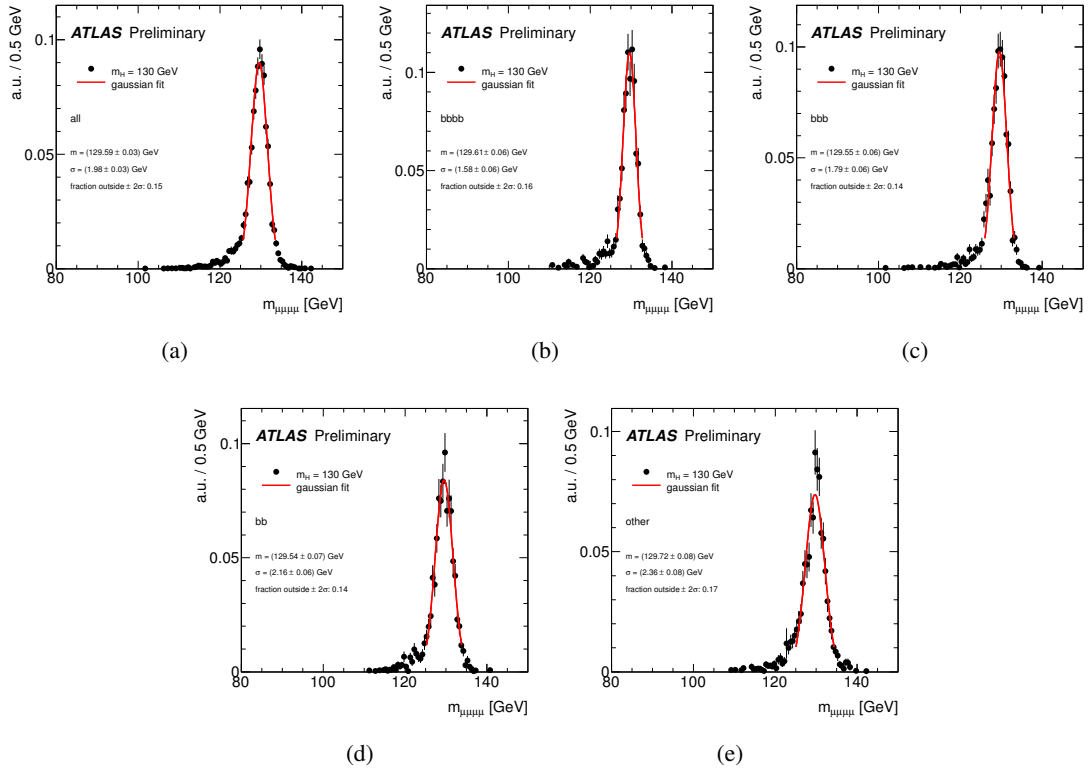


Figure 31: Invariant mass distribution for a simulated MC sample with $m_H = 130$ GeV, in the $\mu\mu\mu\mu$ channel (black points); superimposed is the gaussian fit to the $m_{4\ell}$ peak (red line).

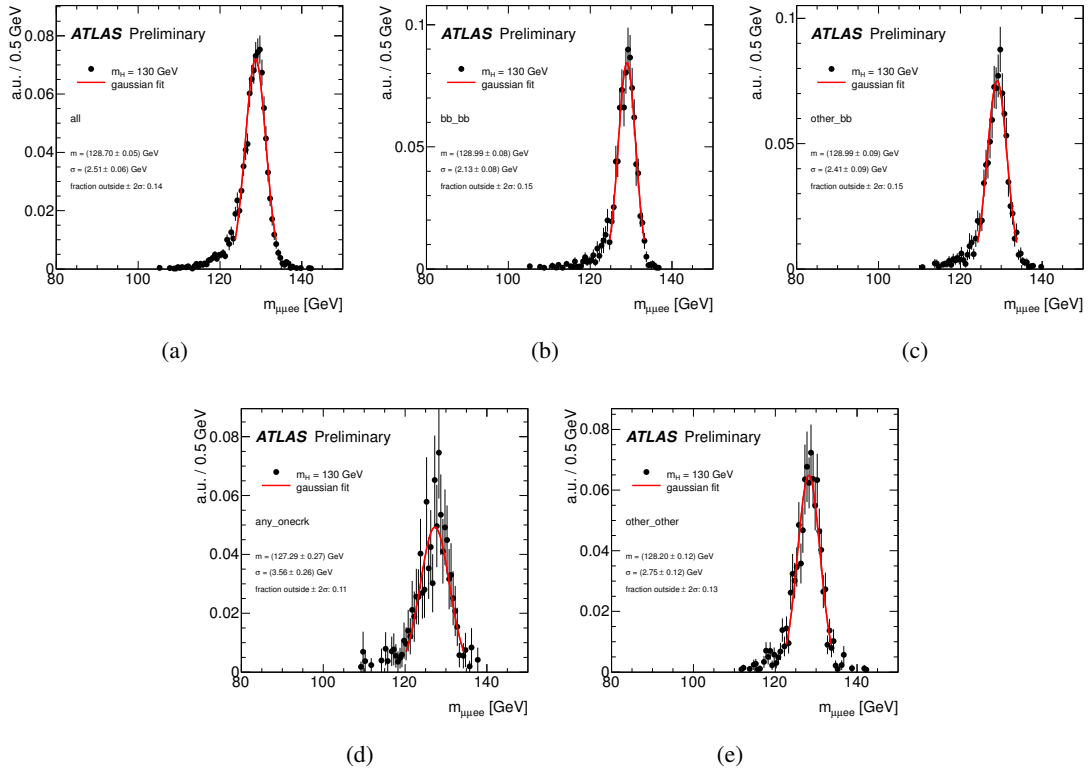


Figure 32: Invariant mass distribution for a simulated MC sample with $m_H = 130$ GeV, in the $\mu\mu ee$ channel (black points); superimposed is the gaussian fit to the $m_{4\ell}$ peak (red line).

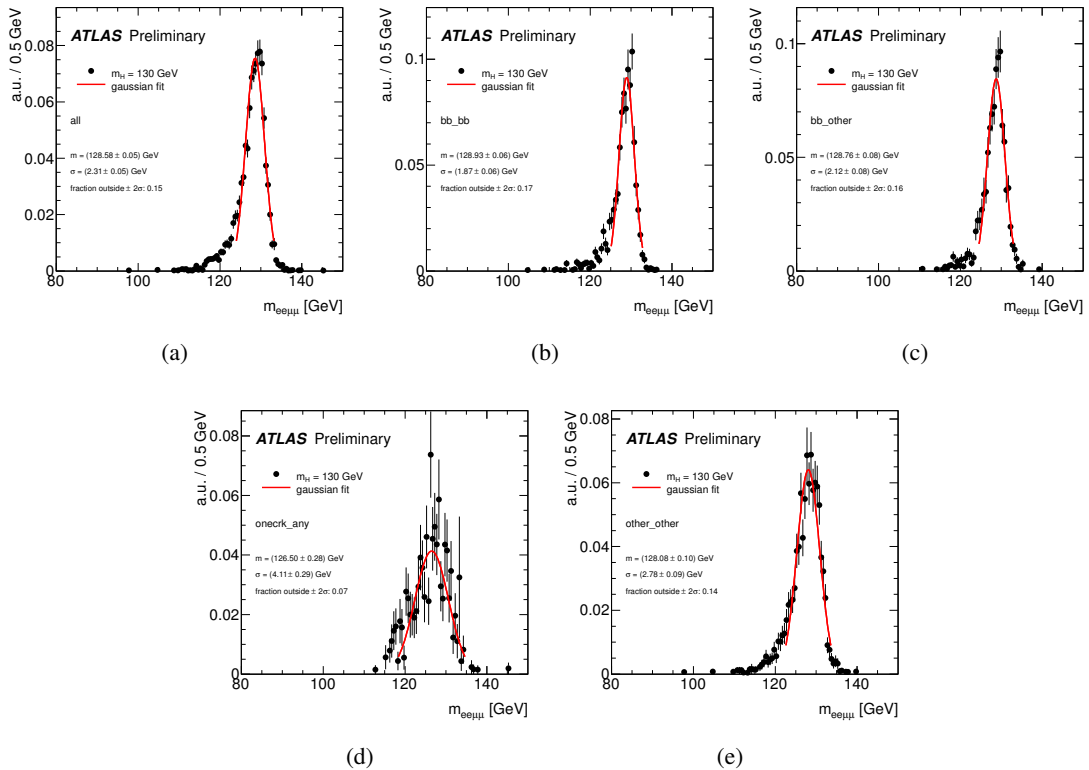


Figure 33: Invariant mass distribution for a simulated MC sample with $m_H = 130 \text{ GeV}$, in the $ee\mu\mu$ channel (black points); superimposed is the gaussian fit to the $m_{4\ell}$ peak (red line).

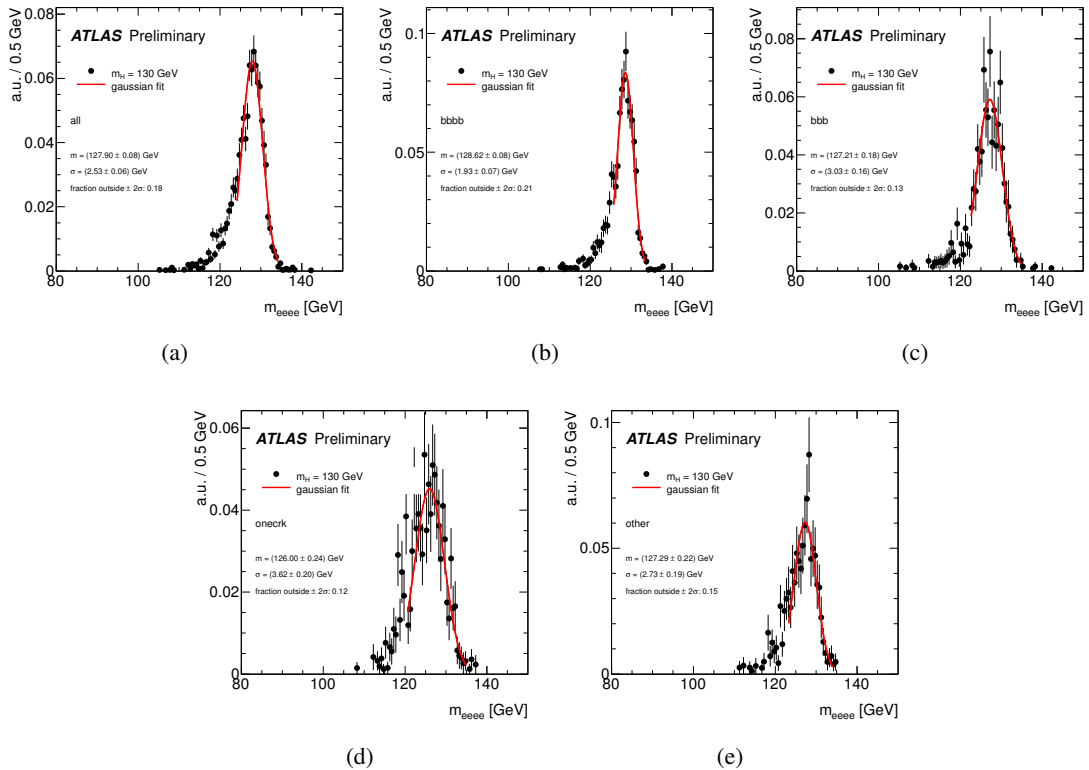


Figure 34: Invariant mass distribution for a simulated MC sample with $m_H = 130 \text{ GeV}$, in the $eeee$ channel (black points); superimposed is the gaussian fit to the $m_{4\ell}$ peak (red line).

9 Results of event selection

The criteria described in Section 5 are applied to the 2011 data corresponding to a average luminosity of 4.8 fb^{-1} . In total 71 candidate events are selected by the analysis: 24 4μ , 30 $2e2\mu$, and 17 $4e$ events. In the same mass range 62 ± 9 events are expected from the background processes. The number of events observed in each final state, separately for $m_{4\ell} < 180 \text{ GeV}$ and $m_{4\ell} \geq 180 \text{ GeV}$, compared with the expectations for background are shown in Table 24. The expected signal yields for various m_H values are also presented. The mass spectra for m_{12} , m_{34} , and $m_{4\ell}$ are shown in Figure 39. Figure 35 shows the $m_{4\ell}$ spectrum with superimposed the total expected background and the Higgs signal expected from three mass hypotheses, while in Figure 36 the different sub-channels of the analysis are presented seperately. In Table 25 the evolution of observed candidates during the 2011 data taking is presented, while in Figure 38 the rate of candidate appearance is given as a function of the data-taking period.

Figure 40 shows the η and E_T or p_T distributions of the leptons in the selected candidates. In Figure 41(a)-(c) the p_T distributions of the leptons ordered in decreasing p_T are presented. In Figure 42, the distribution of m_{12} versus m_{34} for the selected candidates, together with the background expectation, is shown. Details on the selected candidates are provided in Section K - Table 41, Table 42 and Table 43.

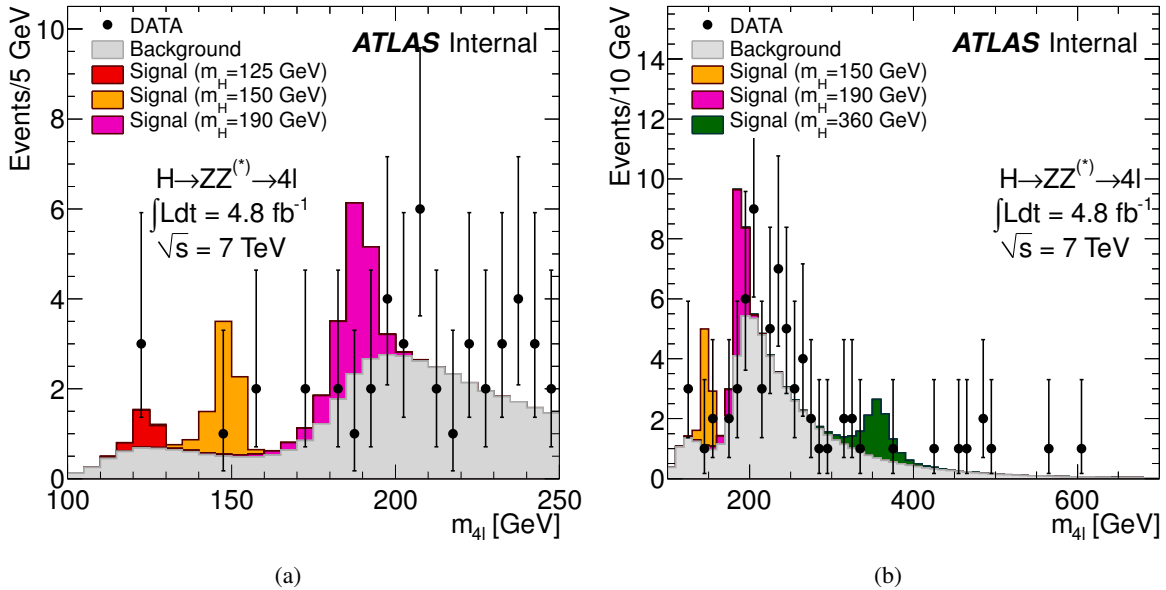


Figure 35: $m_{4\ell}$ distribution of the selected candidates, compared to the background expectation (a) in the low mass region and (b) in the whole mass spectrum of the analysis. Error bars represent 68.3% central confidence intervals. The signal expectation for several m_H hypotheses is also shown. The resolution of the reconstructed Higgs mass is dominated by experimental performances at low m_H values and by the natural Higgs boson width at high m_H .

Table 24: The expected number of signal and background events, with their systematic uncertainty, separated into “Low mass” ($m_{4\ell} < 180$ GeV) and “High mass” ($m_{4\ell} \geq 180$ GeV) regions. The observed numbers of events are also presented.

Int. Luminosity	$\mu\mu\mu\mu$		$ee\mu\mu$		$eeee$	
	Low mass	High mass	Low mass	High mass	Low mass	High mass
	4.8 fb $^{-1}$		4.8 fb $^{-1}$		4.9 fb $^{-1}$	
$ZZ^{(*)}$	2.1±0.3	16.3±2.4	2.8±0.6	25.2±3.8	1.2±0.3	10.4±1.5
Z	0±0.	0±0.	1.16±0.5	0.13±0.08	1.4±0.6	0.16±0.09
Zbb	0.16±0.06	0.02±0.01	0.26±0.08	0.03±0.01	0.20±0.07	0.02±0.01
tt	0.005±0.01	0.003±0.01	0.03±0.01	0.02±0.01	0.01±0.01	0.01±0.01
Z, Zbb , and $t\bar{t}$	0.16±0.06	0.02±0.01	1.4±0.5	0.17±0.08	1.6±0.7	0.18±0.08
Total Background	2.2±0.3	16.3±2.4	4.3±0.8	25.4±3.8	2.8±0.8	10.6±1.5
Data	3	21	3	27	2	15
$m_H = 130$ GeV	1.00 ± 0.17		1.22 ± 0.21		0.43 ± 0.08	
$m_H = 150$ GeV	2.1 ± 0.4		2.9 ± 0.4		1.12 ± 0.18	
$m_H = 200$ GeV	4.9 ± 0.7		7.7 ± 1.0		3.1 ± 0.4	
$m_H = 400$ GeV	2.0 ± 0.3		3.3 ± 0.5		1.49 ± 0.21	
$m_H = 600$ GeV	0.34 ± 0.04		0.62 ± 0.10		0.30 ± 0.06	

Table 25: The observed numbers of events separated into “Low mass” ($m_{4\ell} < 180$ GeV) and “High mass” ($m_{4\ell} \geq 180$ GeV) regions (LP: Lepton-Photon). It is noted that the disappearance of a 4μ candidate between Release16 and Release17 is due to the change of GRL for the 4μ channel and the re-evaluation of the LuminosityBlocks affected by NoiseBurts in the LAr during the reprocessing (event 101085723 in run 183081 and lumiblock 537).

	$\mu\mu\mu\mu$		$ee\mu\mu$		$eeee$	
	Low mass	High mass	Low mass	High mass	Low mass	High mass
LP Rel16	1	11	1	8	1	5
LP Rel17	0	11	2	11	1	7
2011 Rel17	3	21	3	27	2	15

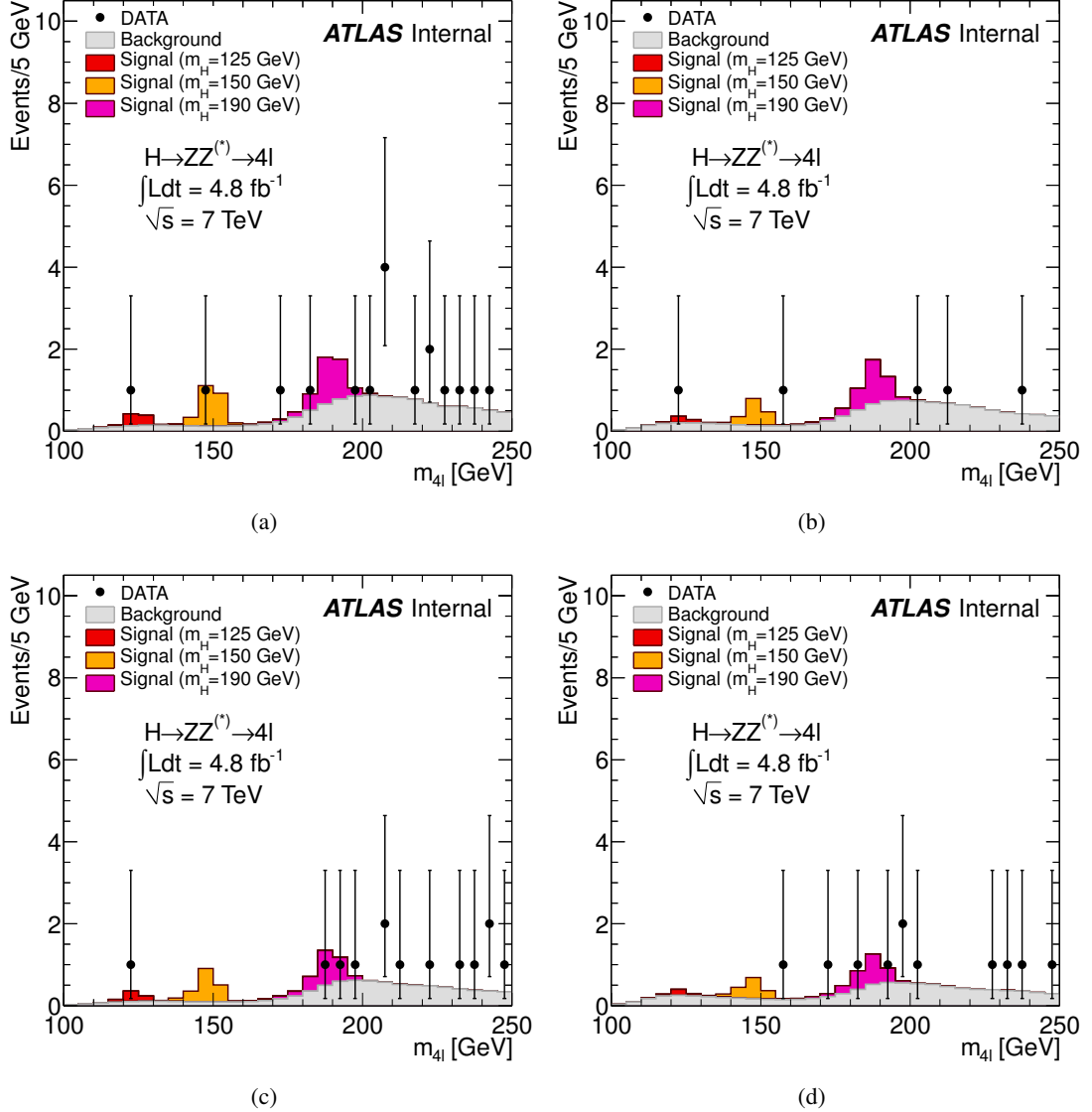


Figure 36: m_{4l} distribution of the selected candidates for the different sub-channels of the analysis, compared to the background expectation: (a) 4μ , (b) $2\mu 2e$, (c) $2e 2\mu$, (d) $4e$. Error bars represent 68.3% central confidence intervals. The signal expectation for several m_H hypotheses is also shown.

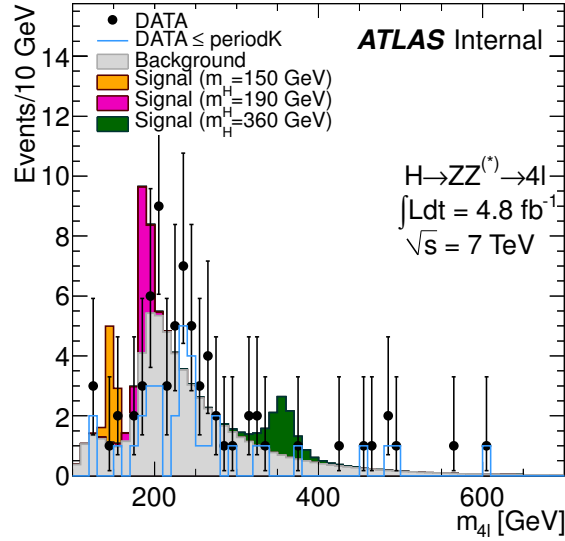


Figure 37: Break-down of event yields in the two data-taking periods.

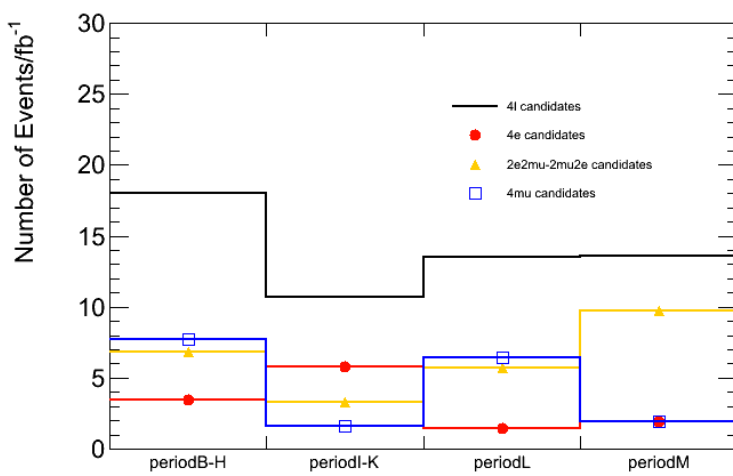


Figure 38: Rate of observation of four lepton candidates in the different data-taking periods.

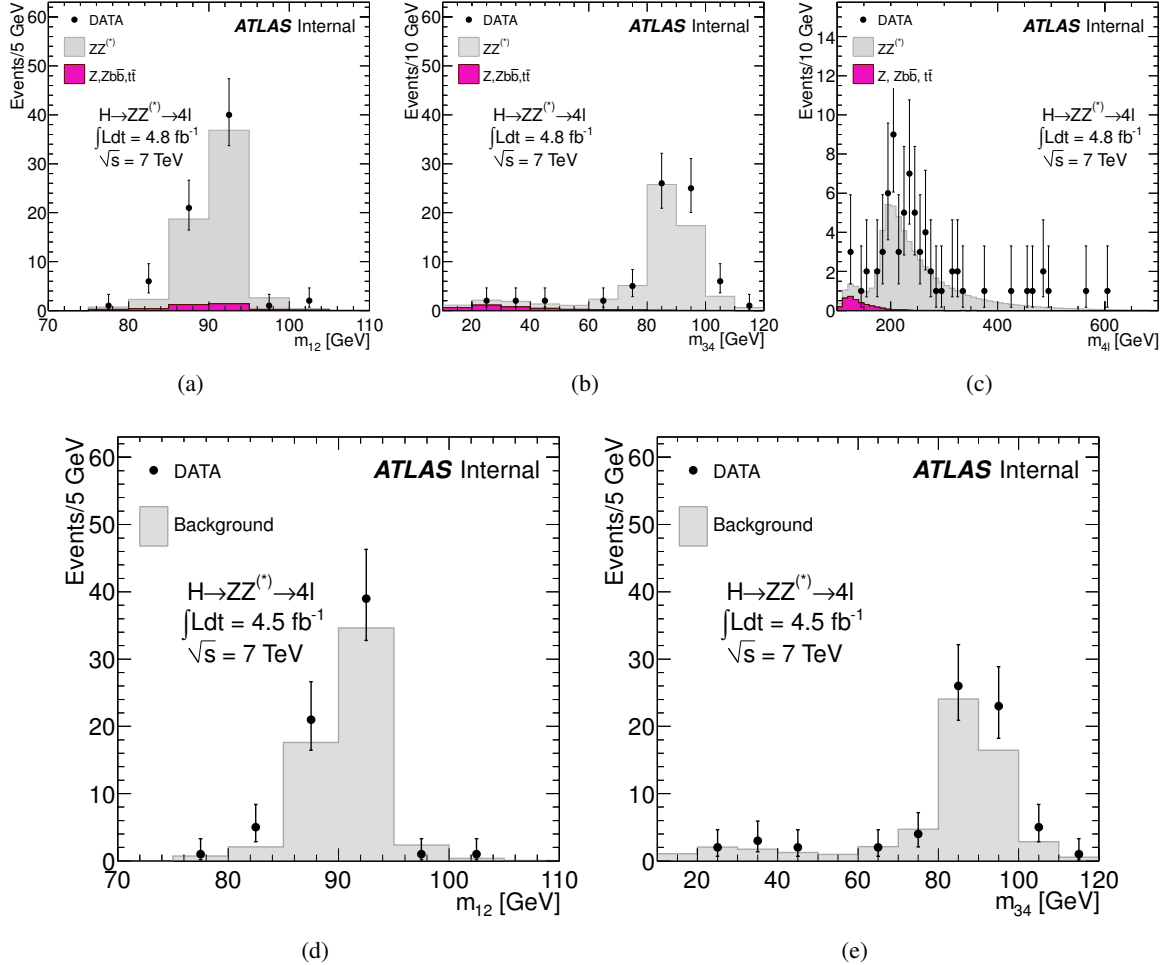


Figure 39: Invariant mass distributions (a) m_{12} , (b) m_{34} , and (c) m_{4l} for the selected candidates. All plots show comparisons with background expectation from the dominant ZZ^* and the sum of $t\bar{t}$, $Zb\bar{b}$ and $Z+jets$ processes. In (d) and (e) the m_{12} and m_{34} are shown respectively, with the backgrounds summed. Error bars respect 68.3% central confidence intervals.

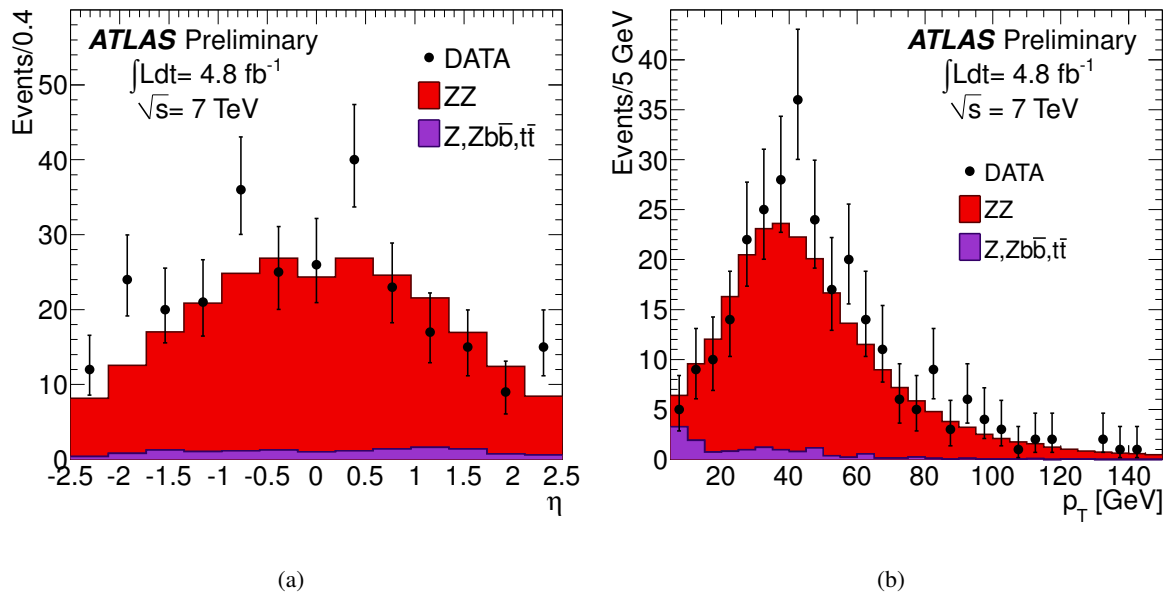


Figure 40: (b) η and (a) p_T distribution for the leptons of the 68 candidates surviving the selection criteria. The expected background distributions are also shown. Error bars represent 68.3% central confidence intervals.

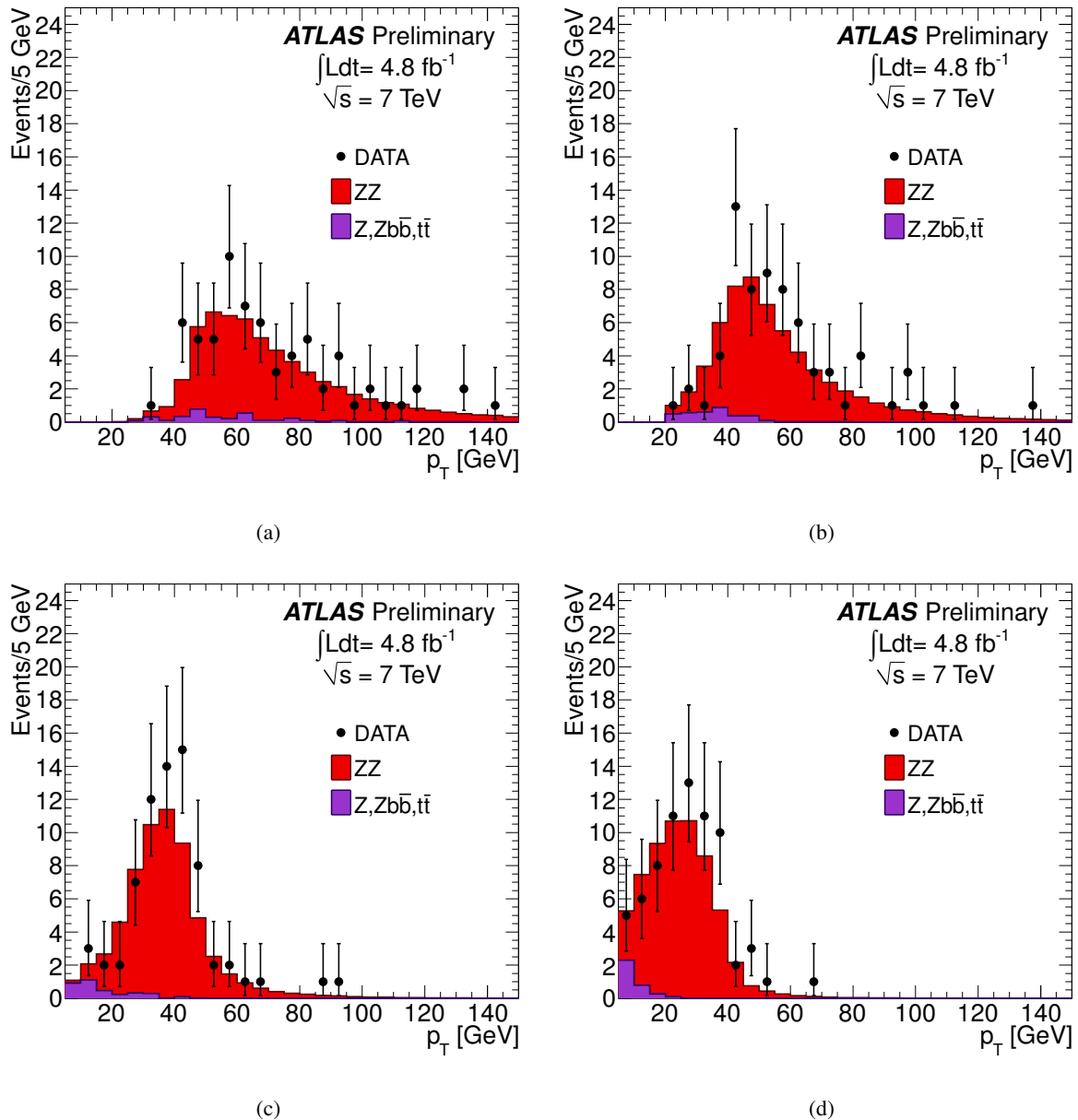


Figure 41: p_T distribution for the (a) highest- p_T , (b) second highest- p_T , (c) third highest- p_T and (c) lowest- p_T leptons of the 68 candidates surviving the selection criteria. The expected background distributions are also shown. Error bars represent 68.3% central confidence intervals.

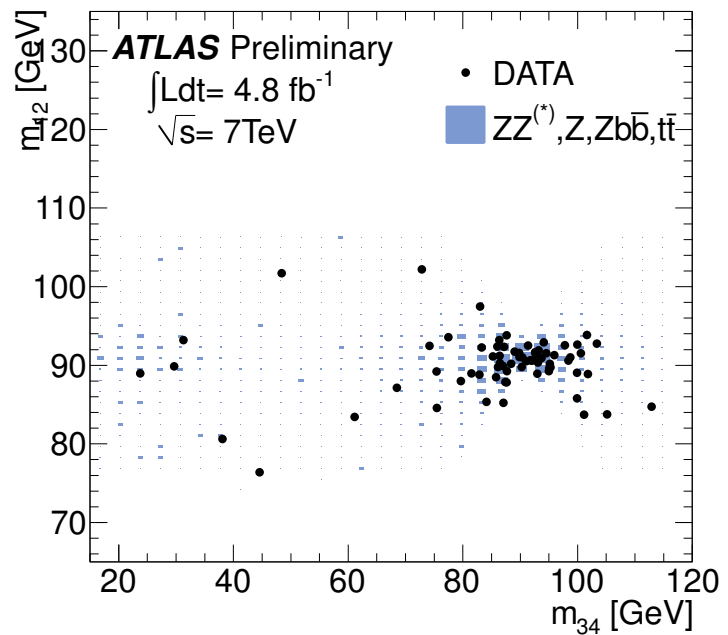


Figure 42: The invariant mass distribution m_{12} with respect to m_{34} for the selected candidates. Comparison with background expectation is shown for the sum of the dominant ZZ^* , the $t\bar{t}$, the $Zb\bar{b}$ and the $Z+jets$ processes.

10 Systematic uncertainties

The sources of systematic uncertainty considered in this search and their magnitudes are discussed.

Luminosity: An overall normalisation uncertainty of 3.9 % is assumed for the luminosity. This uncertainty is only applied to MC samples for which the normalisation is not obtained from the data. When it is applied, this systematic is assumed to be correlated across samples.

Cross-sections of the Higgs boson production: The Higgs boson production cross-sections have been studied extensively by the LHC Higgs cross-section working group and the results are compiled in Ref. [22]. The theoretical uncertainties on the cross-sections have been estimated to be between 15 – 20% for $gg \rightarrow H$, 5% for $qq \rightarrow qqH$, 3.5% for $qq \rightarrow W/ZH$. We use all process for Higgs production: $gg \rightarrow H$, $qq \rightarrow H$ and $qq \rightarrow WZH$ and their uncertainty that are applied to the signal samples for all mass points. We are following the LHC Higgs combination recommendation and split the uncertainty in PDF+ α_s and QCD scale as shown in Table 26. Recent studies [22, 61] have indicated that effects related to off-shell Higgs boson production and interference with other SM processes may become sizeable at the highest masses ($m_H > 400$ GeV) considered in this search. In the absence of a full calculation, a conservative estimate of the possible size of such effects was included as a signal normalization systematic uncertainty following a parameterization as a function of m_H : $150\% \times (m_H[\text{TeV}])^3$, for $m_H \geq 300$ GeV.

Table 26: Higgs mass dependent PDF and scale uncertainties are available at
<https://twiki.cern.ch/twiki/bin/view/LHCPhysics/CERNYellowReportPageAt7TeV>

group	nuisance	comments	typical uncertainty
PDFs+ α_s (cross sections)	gg $qq\bar{q}$	$gg \rightarrow H, t\bar{t}H, gg \rightarrow VV$ $VBF H, VH, VV@NLO$	8 % 4 %
Higher-order uncertainties on cross sections	ggH qqH VH VV $ggVV$ $t\bar{t}$	total inclusive $gg \rightarrow H$ $VBF H$ associate VH $VW, VZ,$ and ZZ up to NLO $gg \rightarrow WW$ and $gg \rightarrow ZZ$ $t\bar{t}$	$+12\%$ -7% 1 % 1 % 5 % 30 % $+3\%$ -6%

Cross-sections of background processes: A normalisation error of 15% is assigned to the ZZ contribution, which accounts for the theoretical uncertainties in the cross-section calculation and the uncertainty due to the use of the $gg \rightarrow ZZ$ correction. An uncertainty of 45% and 40% is assigned on the normalization of the $Z+$ light-flavour-jets and $Zb\bar{b}$ samples, respectively, to account for the uncertainty on their data-driven estimation (statistical uncertainty in the control sample and the MC-based extrapolation to the signal region). The theoretical uncertainties on the $t\bar{t}$ cross-section, approximately 10%, are included with the PDFs correlated. The additional uncertainty in the $t\bar{t}$ selection efficiency, estimated to be 10%, is negligible in comparison with the errors on the larger backgrounds.

Electron Reconstruction and Identification: The electron energy scale uncertainty is found to be less than 1% in most of the η region of interest, while the energy resolution uncertainty is estimated to vary between 0.1% and 0.4%. The effect of the energy resolution in the final state is on average a few per mil, c.f. Figure 44, 45 and 46. The reconstruction and identification efficiency uncertainty (summarized in Table 27) is 2.5% in the E_T region relevant for electrons from $Z \rightarrow ee$ decays. Systematic uncertainties in all final states are given in Table 28 for the signal, and in Table 30 and Figure 43 for the $ZZ \rightarrow 4\ell$ background.

Muon Reconstruction and Identification: The muon momentum scale uncertainty is generally found to be less than 1% c.f. Table 29, while the uncertainty in the momentum resolution is negligible

and less than 1%. The effect of momentum resolution uncertainty for the Muon Spectrometer (MS) and Inner Detector (ID) is of the order of a few per mil, c.f. Figure 44 and 45. Finally, the uncertainty on the identification efficiency of muons (summarized in Table 27) is estimated to be between 0.5% and 1% for the phase space of interest. The muon final state systematic uncertainties are given in Table 28 for the signal and Table 30 and Figure 43 for the $ZZ \rightarrow 4\ell$ background.

Trigger: Owing to the high lepton trigger efficiency and the presence of multiple high p_T leptons in the final state, a trigger efficiency very close to 100% is achieved, while the corresponding uncertainties are found to be negligible.

Table 27: Systematic uncertainty on the signal yield owing to the electron and muon reconstruction efficiency, energy scale and resolution uncertainty; in % for $m_H = 110$ GeV .

Channel	4μ	$2e2\mu$	$2\mu2e$	$4e$
Luminosity	± 3.9	± 3.9	± 3.9	± 3.9
e/ γ efficiency	-	± 1.6	± 8.0	± 8.2
e/ γ energy scale	-	-	-	-
e/ γ resolution	-	-	-	-
μ efficiency	± 0.22	± 0.16	± 0.16	-
μ energy scale	-	-	-	-
μ resolution	-	-	-	-

Table 28: Systematic uncertainty on the signal yield owing to the electron and muon reconstruction efficiency uncertainty; in %.

m_H	Electron Uncertainties				Muon Uncertainties			
	$H \rightarrow 4\mu$	$H \rightarrow 2e2\mu$	$H \rightarrow 2\mu2e$	$H \rightarrow 4e$	$H \rightarrow 4\mu$	$H \rightarrow 2e2\mu$	$H \rightarrow 2\mu2e$	$H \rightarrow 4e$
110	-	1.673	13.618	13.254	0.223	0.157	0.157	-
115	-	1.769	13.254	13.625	0.224	0.160	0.157	-
120	-	1.810	12.237	12.682	0.224	0.158	0.158	-
125	-	1.791	11.296	11.781	0.225	0.158	0.158	-
130	-	1.891	9.777	10.641	0.224	0.159	0.157	-
135	-	1.943	8.401	9.542	0.224	0.158	0.157	-
140	-	2.012	7.564	8.206	0.225	0.157	0.159	-
145	-	2.067	6.493	7.418	0.225	0.157	0.156	-
150	-	2.034	5.789	6.541	0.224	0.157	0.156	-
180	-	2.017	2.833	3.888	0.224	0.158	0.157	-
200	-	1.996	2.683	3.635	0.224	0.157	0.157	-
260	-	1.953	2.440	3.507	0.225	0.157	0.157	-
360	-	1.774	2.123	2.957	0.224	0.158	0.157	-
460	-	1.695	1.953	2.767	0.225	0.158	0.158	-
600	-	1.554	1.893	2.475	0.226	0.158	0.158	-

Table 29: Effect of using fixed and non-fixed energy scales for muons when smearing the p_T measured in the MS for several gluon-gluon fusion samples.

m_H	Number of Events	Number of Events	Difference
	Fixed Energy Scale	Non-Fixed Energy Scale	
110	269	264	-1.86
130	1543	1535	-0.52
200	3276	3274	-0.06
360	2769	2757	-0.43

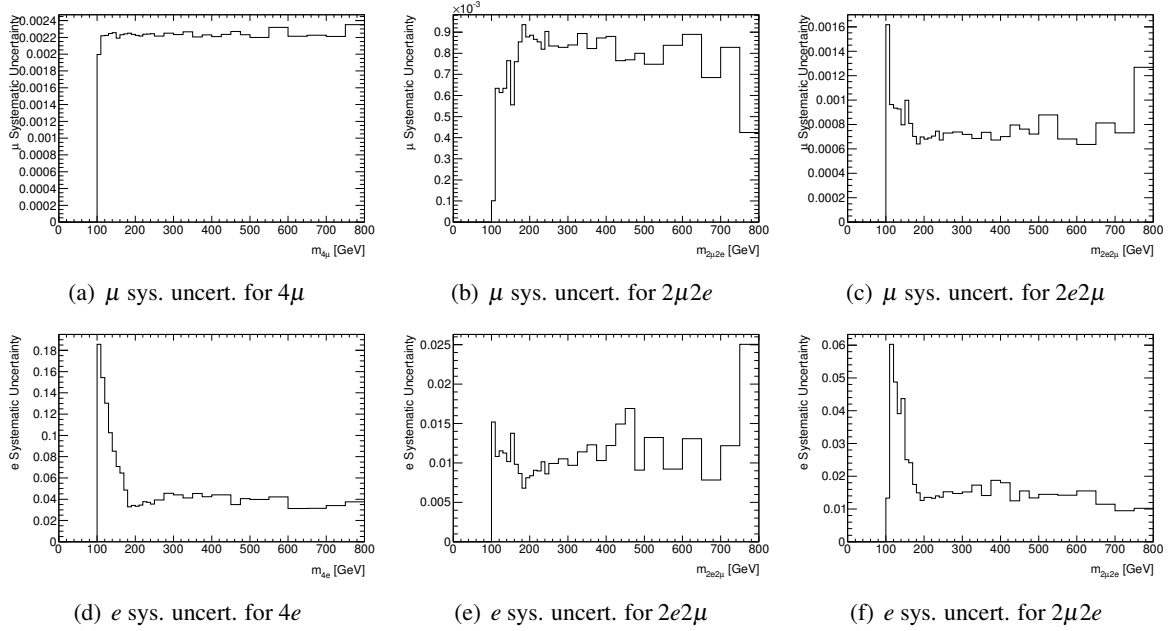


Figure 43: Systematic uncertainties for the $ZZ \rightarrow 4\ell$ background per 10 GeV for masses 100 - 250 GeV, per 25 GeV for masses 250 - 500 GeV and per 50 GeV for masses higher than 500 GeV.

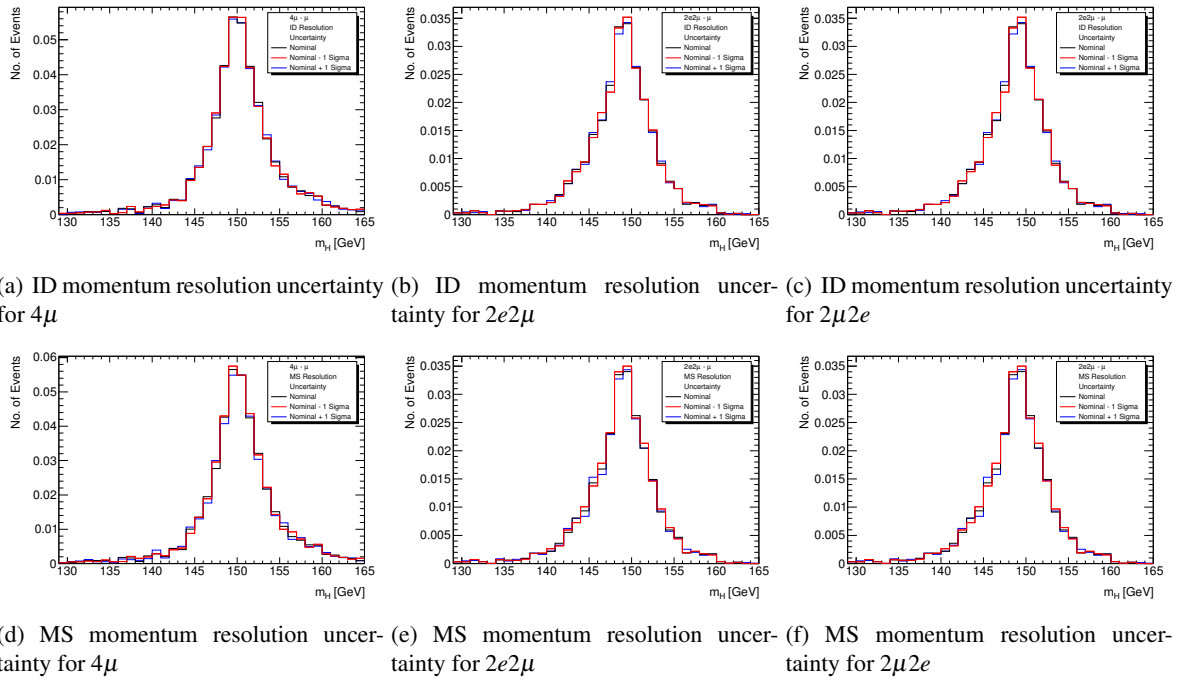


Figure 44: m_{4l} obtained varying the resolution by 1σ in the case of $m_H = 150$ GeV.

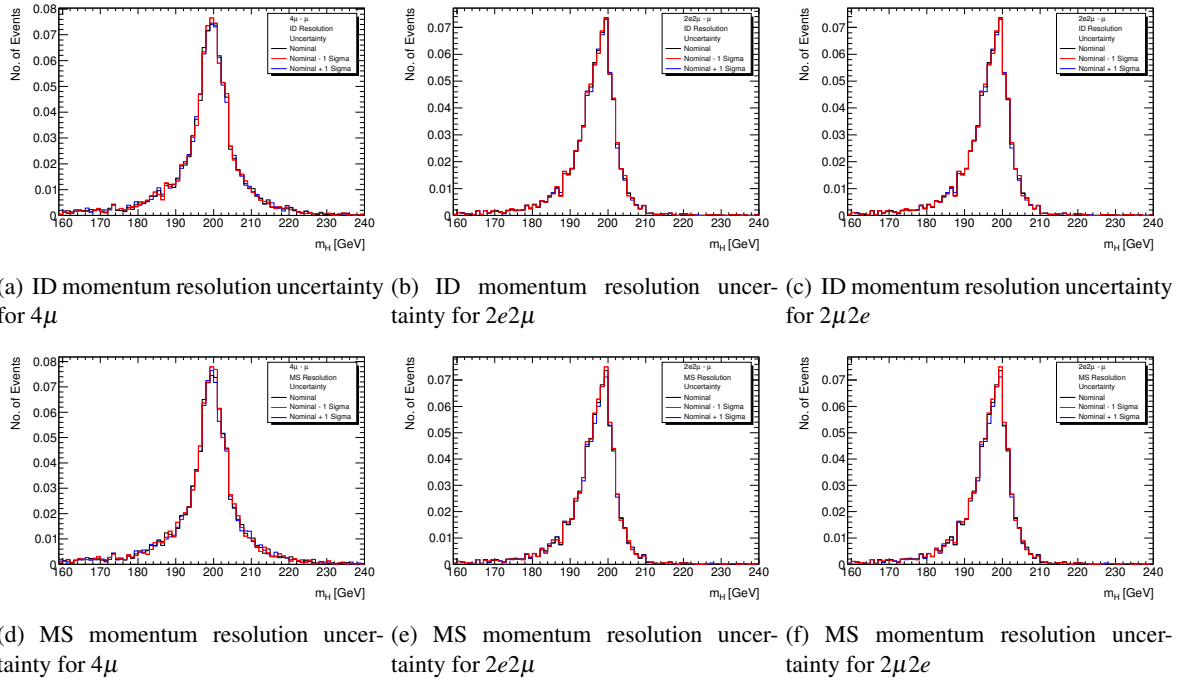


Figure 45: m_{4l} obtained varying the resolution by 1σ in the case of $m_H = 200$ GeV.

Not reviewed, for internal circulation only

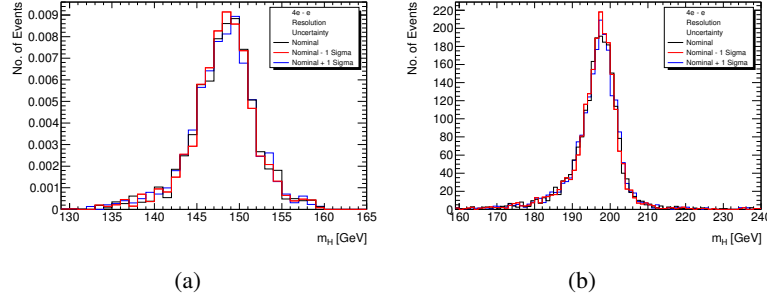


Figure 46: m_{4l} obtained varying the resolution by 1σ for the electrons in the case of (a) $m_H = 150$ GeV and (b) $m_H = 200$ GeV.

Table 30: Systematic uncertainty yield on the $ZZ \rightarrow 4\ell$ background owing to the electron and muon reconstruction efficiency uncertainty; in %.

m_H	Electron Uncertainties				Muon Uncertainties			
	$H \rightarrow 4\mu$	$H \rightarrow 2e2\mu$	$H \rightarrow 2\mu 2e$	$H \rightarrow 4e$	$H \rightarrow 4\mu$	$H \rightarrow 2e2\mu$	$H \rightarrow 2\mu 2e$	$H \rightarrow 4e$
100.00 - 110.00	-	1.52	1.33	18.57	0.20	0.16	0.01	-
110.00 - 120.00	-	1.08	6.03	15.43	0.22	0.10	0.06	-
120.00 - 130.00	-	1.15	4.88	13.02	0.22	0.09	0.06	-
130.00 - 140.00	-	1.13	3.91	10.25	0.22	0.09	0.06	-
140.00 - 150.00	-	1.02	4.37	8.52	0.23	0.08	0.08	-
150.00 - 160.00	-	1.38	2.50	7.07	0.22	0.10	0.06	-
160.00 - 170.00	-	0.98	2.41	6.47	0.22	0.08	0.08	-
170.00 - 180.00	-	0.87	1.75	4.85	0.22	0.07	0.09	-
180.00 - 190.00	-	0.68	1.49	3.29	0.22	0.06	0.09	-
190.00 - 200.00	-	0.81	1.26	3.42	0.22	0.07	0.09	-
200.00 - 210.00	-	0.84	1.36	3.34	0.22	0.07	0.09	-
210.00 - 220.00	-	0.91	1.35	3.45	0.22	0.07	0.09	-
220.00 - 230.00	-	0.90	1.33	3.77	0.22	0.07	0.09	-
230.00 - 240.00	-	1.02	1.40	3.71	0.22	0.07	0.08	-
240.00 - 250.00	-	0.86	1.36	3.54	0.22	0.07	0.09	-
250.00 - 275.00	-	0.99	1.53	3.93	0.22	0.07	0.08	-
275.00 - 300.00	-	1.05	1.47	4.56	0.22	0.07	0.08	-
300.00 - 325.00	-	0.97	1.52	4.41	0.22	0.07	0.08	-
325.00 - 350.00	-	1.14	1.73	4.13	0.23	0.07	0.09	-
350.00 - 375.00	-	1.23	1.41	4.54	0.22	0.07	0.08	-
375.00 - 400.00	-	1.03	1.87	4.24	0.22	0.07	0.09	-
400.00 - 425.00	-	1.22	1.80	4.41	0.22	0.07	0.09	-
425.00 - 450.00	-	1.49	1.25	4.42	0.22	0.08	0.08	-
450.00 - 475.00	-	1.69	1.55	3.50	0.23	0.08	0.08	-
475.00 - 500.00	-	0.91	1.34	4.06	0.22	0.07	0.08	-
500.00 - 550.00	-	1.32	1.45	3.99	0.22	0.09	0.07	-
550.00 - 600.00	-	0.92	1.42	4.22	0.23	0.07	0.08	-
600.00 - 650.00	-	1.31	1.55	3.13	0.22	0.06	0.09	-
650.00 - 700.00	-	0.78	1.15	3.15	0.22	0.08	0.07	-
700.00 - 750.00	-	1.22	0.95	3.40	0.22	0.07	0.08	-
750.00 - 800.00	-	2.50	1.02	3.75	0.24	0.13	0.04	-

11 Exclusion limits on $H \rightarrow ZZ^{(*)} \rightarrow 4\ell$

The number of events observed in each final state, separately for $m_{4\ell} < 180$ GeV and $m_{4\ell} \geq 180$ GeV, compared with the expectations for background and signal for various m_H hypotheses are shown in Table 24. In total 71 candidate events are selected by the analysis: 24 4μ , 30 $2e2\mu$, and 17 $4e$ events, while in the same mass range 62 ± 9 events are expected from the background processes. The mass spectra for m_{12} , m_{34} , and $m_{4\ell}$ are shown in Fig. 39, while in Fig. 35 $m_{4\ell}$ for the total background and several signal hypotheses are compared to the observed data.

Upper limits are derived for the Higgs boson production cross section at 95% CL, using the CL_s modified frequentist formalism [62] with the profile likelihood test statistic [63] and using RooStats [64]. The test statistic is evaluated with a maximum likelihood fit of signal and background models to data. Figures 47 and 48 show the expected and observed exclusions as a function of m_H and Table 31 and Table 32 summarize the numerical values for selected m_H points. The SM Higgs boson is excluded at 95% CL in the mass ranges 134 – 156 GeV, 182 – 233 GeV, 256 – 265 GeV and 268 – 415 GeV. The expected exclusion ranges are 136 – 157 GeV and 184 – 400 GeV.

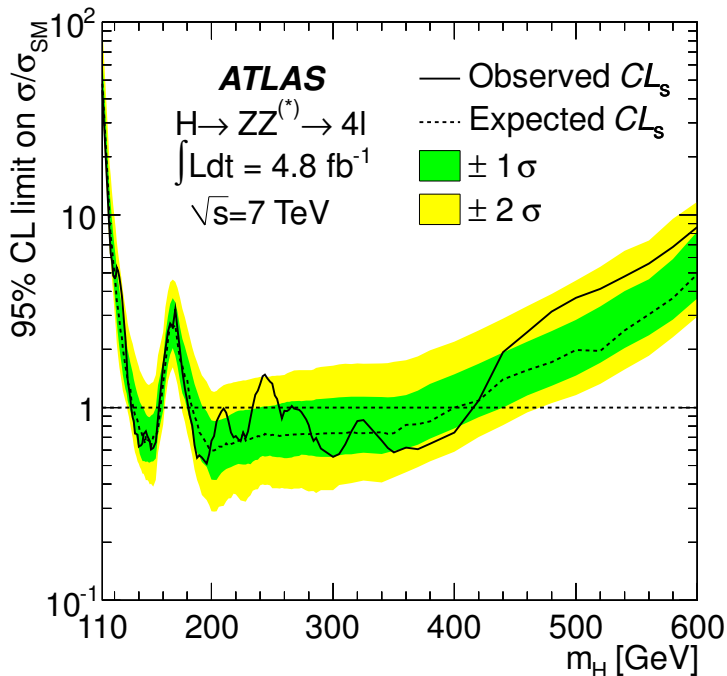


Figure 47: Expected (dashed) and observed (full line) 95% CL upper limit on the SM Higgs boson production cross section as a function of the Higgs boson mass, expressed in multiples of the SM rate.

Fig. 49 shows, for a luminosity of 4.5 fb^{-1} the exclusion limits obtained using toy Monte-Carlo pseudoexperiments (top plots) with those obtained using the asymptotic approximation [63]. In Fig. 50 the expected exclusion limits are provided for the sub-channels of this analysis using the same approximation. Fig. 51 presents the effect of the systematic uncertainties on the limit results.

The p -value is the probability of upward fluctuations in the background as high as or higher than the excesses observed in data. The consistency of the observed results with the background-only hypothesis expressed as p -values is shown in Fig. 52; Fig 53 compares the results obtained using toy Monte Carlo (labeled as 'ensemble') with those from the asymptotic approximation [63].

The significance of an excess is given by the probability, p_0 , that a background-only experiment is more signal-like than that observed. In Fig. 52 the p_0 -values, calculated using an ensemble of simulated

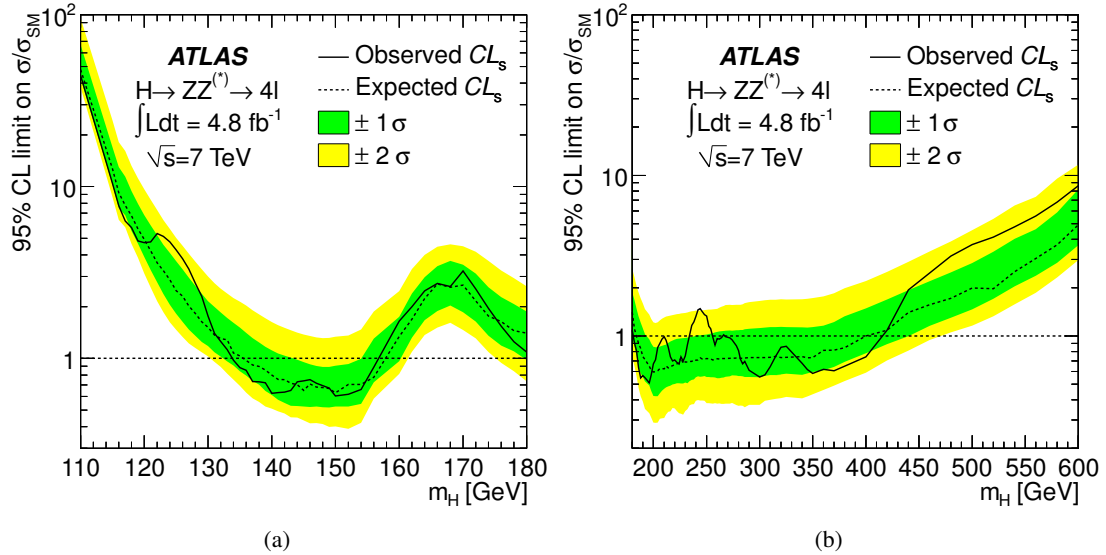


Figure 48: As figure 47, for low (a) and high (b) Higgs boson mass.

Table 31: Median expected and observed 95% CL upper limits using asymptotics on the Higgs boson production cross section for several Higgs boson masses, divided by the expected SM Higgs boson cross section.

Mass (GeV)	Expected	Observed
120	5.05	4.71
130	1.56	1.73
150	0.68	0.83
200	0.59	0.67
300	0.79	0.52
400	1.02	0.72
600	5.07	8.44

Table 32: Median expected and observed 95% CL upper limit using toys on the SM Higgs boson production cross section, in multiples of the SM rate, as a function of the Higgs boson mass in GeV, obtained with CL_s .

Mass (GeV)	Expected	Observed
120	5.32	5.40
130	1.66	1.89
150	0.72	0.85
200	0.59	0.68
300	0.85	0.55
400	1.00	0.77
600	5.29	8.55

pseudo-experiments, are given as a function of m_H for the full mass range of the analysis. The most significant upward deviations from the background-only hypothesis are observed for $m_H = 125$ GeV

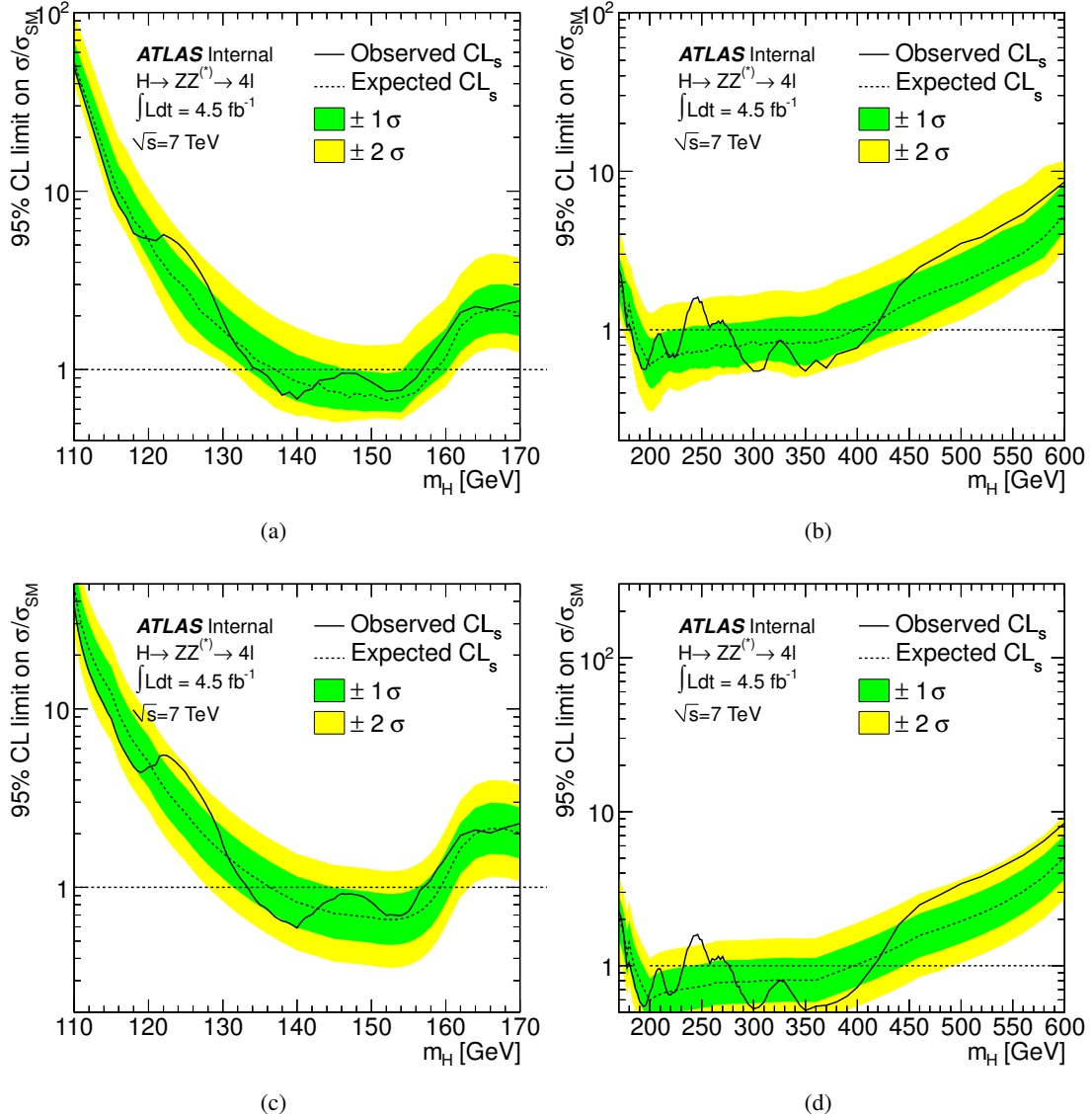


Figure 49: Expected (dashed) and observed (full line) 95% CL upper limit on the SM Higgs boson production cross section as a function of the Higgs boson mass, expressed in multiples of the SM rate. Top plots: using toy Monte Carlo; bottom plots: with the asymptotic approximation.

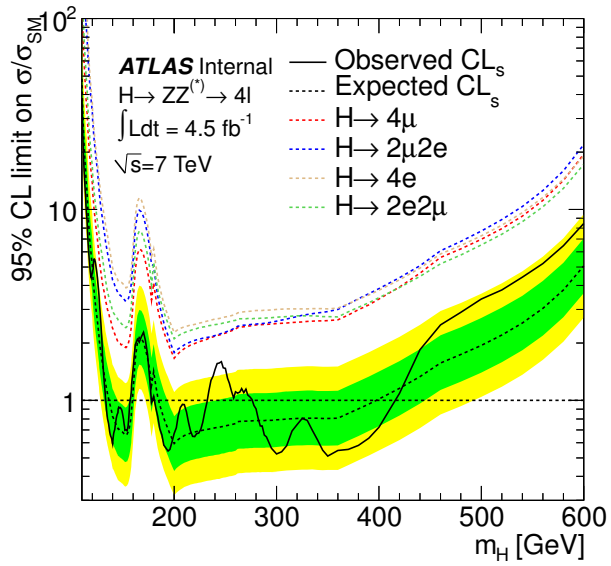


Figure 50: Expected (dashed) and observed (full line) 95% CL upper limit on the SM Higgs boson production cross section calculated with the asymptotic approximation as a function of the Higgs boson mass, expressed in multiples of the SM rate with 4.5 fb^{-1} for the different sub-channels of the analysis.

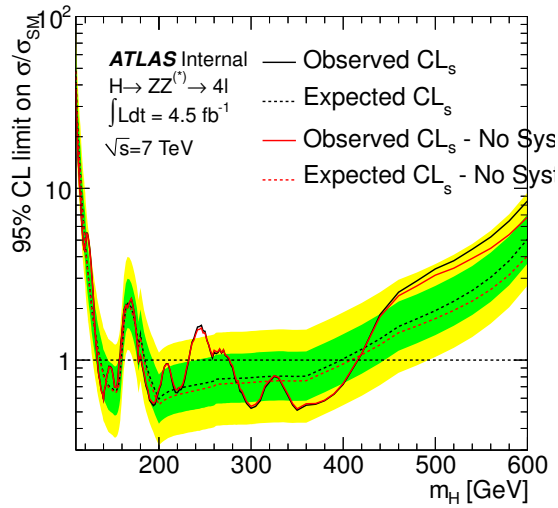


Figure 51: Comparison of the observed limit when systematic uncertainties are neglected. This calculation is performed using the asymptotic approximation.

with a local p_0 of 1.6% (2.1 standard deviations), $m_H = 244 \text{ GeV}$ with a local p_0 of 1.3% (2.2 standard deviations) and $m_H = 500 \text{ GeV}$ with a local p_0 of 1.8% (2.1 standard deviations). The median expected local p_0 in the presence of a SM Higgs boson are 10.6% (1.3 standard deviations), 0.14% (3.0 standard deviations) and 7.1% (1.5 standard deviations) for $m_H = 125 \text{ GeV}$, 244 GeV and 500 GeV , respectively. An alternative calculation, using the asymptotic approximation of Ref. [63], yielded compatible results — within 0.2 standard deviations — in the entire mass range.

The quoted values do not account for the so-called look-elsewhere effect, which takes into account that such an excess (or a larger one) can appear anywhere in the search range as a result of an upward fluctuation of the background. When considering the complete mass range of this search, using the method of Ref. [65], the global p_0 -value for each of the three excesses becomes of $O(50\%)$. Thus, once the look-elsewhere effect is considered, none of the observed local excesses are significant.

For an estimate of the LEE the method of Ref. [65] can be used. In the region for $m_H < 146$ GeV, i.e. the low-mass region not excluded at 99% by the HCP combination, 2 up-crossings are observed and 8 in the whole mass range. Adding 1 for possible signal bias (conservative) the global p -values increase to 40% (considering only the low-mass range) and more than 50% (considering the whole mass range). These high p -values correspond to 0.24σ and 0σ . With such low significances, and ambiguity about which mass range in which to count crossings, the accuracy of the look-elsewhere correction is not high, but the indication is clear: these excesses are not significant on their own.

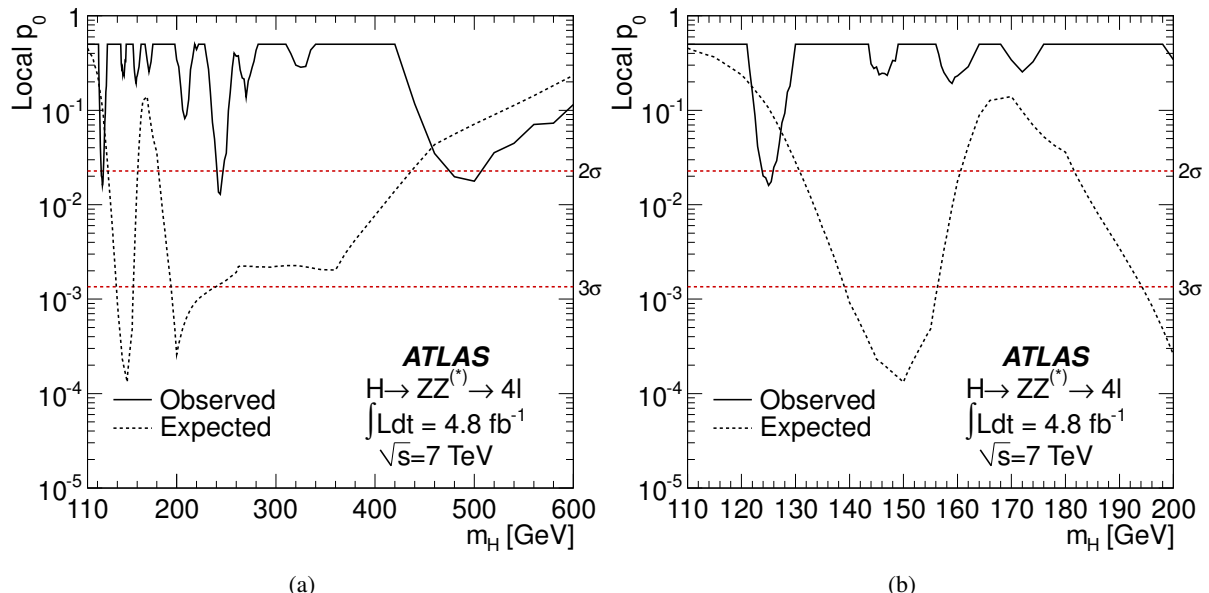


Figure 52: The consistency of the observed results with the background-only hypothesis expressed as p -values is shown in the full mass range of the analysis. The dashed line shows the median expected significance in the hypothesis of a Standard Model Higgs boson production. The two horizontal dashed lines indicate the p -values corresponding to local significances of 2σ and 3σ (a) for the full mass range under consideration and (b) for low Higgs boson mass hypotheses.

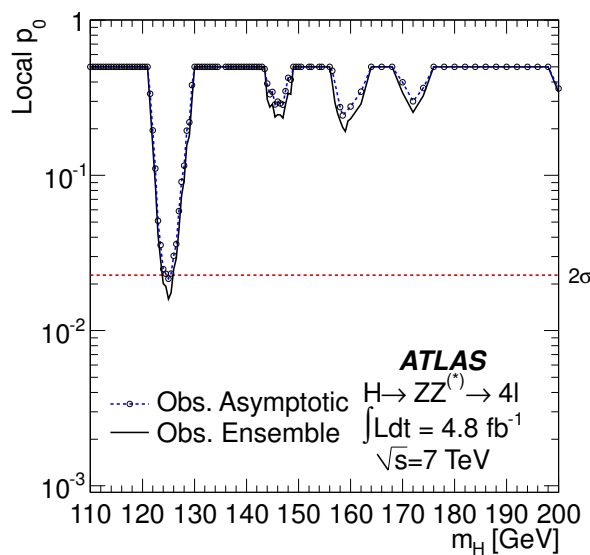


Figure 53: Comparison of the p -values obtained using toy Monte-Carlo pseudoexperiments (ensemble) and using the asymptotic approximation.

Table 33: Expected signal and background events for 4.8fb^{-1} in a window containing 90% and 95% of the expected signal. the observed events in the window are also provided.

Mass (GeV)	Window					Window					
	Low	High	signal	bkg	observed	Low	High	signal	bkg	obs	
	window with 90% of the exp. signal						window with 95% of exp. signal				
110	104.5	114.0	0.06	0.62	0	103.1	118.9	0.06	1.23	0	
115	108.3	118.2	0.26	0.98	0	106.4	119.1	0.27	1.20	0	
120	112.6	123.1	0.70	1.33	0	110.4	124.2	0.73	1.66	2	
125	117.1	127.9	1.41	1.47	3	114.5	128.8	1.49	1.93	3	
130	120.9	133.0	2.43	1.74	3	118.4	134.1	2.54	2.19	3	
135	125.4	138.2	3.51	1.74	0	122.9	139.2	3.67	2.20	3	
140	129.9	143.4	4.58	1.68	0	127.3	144.5	4.83	2.17	0	
145	133.9	148.4	5.30	1.68	1	131.1	149.5	5.58	2.14	1	
150	139.0	153.4	5.55	1.54	1	135.5	154.6	5.86	2.11	1	
155	143.2	158.5	5.04	1.57	3	139.4	159.6	5.28	2.11	3	
160	147.5	163.5	2.93	1.67	2	143.6	164.7	3.05	2.14	3	
170	155.8	174.2	1.57	2.34	4	150.4	175.6	1.64	3.17	4	
180	162.3	184.7	4.0	4.8	4	153.0	186.4	4.2	6.5	6	
190	168.8	195.5	9.2	9.6	7	157.2	197.7	9.6	11.9	10	
200	175.4	206.5	14.3	14.5	12	161.2	209.1	15.1	18.0	20	
210	183.8	217.6	13.6	17.8	20	168.8	221.3	14.3	22.9	25	
220	192.3	228.8	12.8	18.2	22	177.2	233.5	13.5	26.0	27	
230	200.7	239.9	12.1	17.8	24	185.1	245.6	12.8	27.4	35	
240	209.2	251.0	11.5	16.5	26	192.8	257.7	12.0	27.3	37	
244	212.5	255.5	11.1	16.0	22	196.1	262.6	11.7	26.3	36	
250	217.6	262.2	10.7	15.3	20	201.0	269.8	11.3	25.6	36	
260	226.1	273.3	10.0	13.7	21	208.9	281.9	10.5	23.6	35	
270	232.7	285.5	9.6	13.6	21	213.4	295.6	10.1	23.2	30	
280	239.3	297.9	9.4	13.0	17	217.7	309.6	9.9	23.2	28	
290	245.9	310.3	9.2	12.7	13	221.8	323.5	9.7	22.9	30	
300	252.6	322.7	9.0	12.1	11	225.9	337.5	9.5	22.5	30	
310	259.3	335.1	8.8	11.5	13	230.2	351.5	9.2	21.7	28	
320	265.9	347.4	8.5	11.1	11	234.5	365.6	9.0	21.1	27	
330	272.6	359.9	8.3	10.4	8	239.0	379.7	8.8	20.5	25	
340	279.2	372.2	8.1	9.9	8	243.4	393.8	8.5	19.6	20	
350	285.9	384.7	7.9	9.5	7	247.6	408.0	8.3	19.0	18	
360	293.0	397.2	7.7	9.0	6	252.0	422.3	8.1	18.3	15	
370	295.4	411.9	7.3	9.1	6	253.3	439.7	7.7	18.3	15	
380	297.7	426.9	6.9	9.3	7	254.0	458.1	7.3	18.8	16	
390	300.2	441.9	6.5	9.3	7	254.4	475.9	6.8	18.9	17	
400	302.6	457.1	6.1	9.5	8	254.8	494.7	6.4	19.2	20	
420	307.7	487.0	5.3	9.4	11	255.6	531.0	5.6	19.4	20	
440	312.6	516.9	4.5	9.2	12	256.0	567.5	4.8	19.5	20	
460	317.3	546.8	3.7	9.0	10	256.6	604.3	3.9	19.7	22	
480	315.7	572.5	3.4	9.4	12	253.2	630.0	3.5	20.6	22	
500	312.4	598.4	3.0	9.9	13	249.2	656.9	3.2	21.8	25	
520	308.9	624.2	2.6	10.5	14	244.3	683.0	2.8	23.4	28	
540	305.4	650.0	2.3	11.0	14	239.6	709.4	2.4	25.1	31	
560	301.2	675.5	1.9	11.6	14	233.2	735.1	2.0	27.2	36	
580	296.7	700.9	1.5	12.4	66	227.3	760.6	1.6	29.5	37	
600	288.6	726.3	1.1	13.6	15	220.2	786.7	1.2	32.5	42	

Not reviewed, for internal circulation only

Table 34: Expected signal and background events for 4.8fb^{-1} in a window containing 90% and 95% of the expected signal. the observed events in the window are also provided. for $m_H = 125\text{GeV}, 244\text{GeV}$ and 480GeV and the four channels individually. here also the mass ranges for 90% and 95% signal efficiency are estimated separately for each channel.

Mass (GeV)	Window					Window				
	signal		bkg	observed	Low	signal		bkg	obs	High
	Low	High			Low	High				
window with 90% of the exp. signal										
4μ										
125	117.1	127.9	0.53	0.28	1	114.5	128.8	0.55	0.36	1
244	212.5	255.5	3.28	5.16	8	196.1	262.6	3.48	8.40	14
480	315.7	572.5	0.92	2.94	3	253.2	630.0	0.97	6.43	6
$2\mu 2e$										
125	117.1	127.9	0.42	0.22	1	114.5	128.8	0.44	0.28	1
244	212.5	255.5	2.55	3.56	6	196.1	262.6	2.68	5.82	10
480	315.7	572.5	0.91	2.25	3	253.2	630.0	0.96	4.83	6
$4e$										
125	117.1	127.9	0.25	0.44	1	114.5	128.8	0.26	0.58	1
244	212.5	255.5	3.02	4.19	4	196.1	262.6	3.15	6.92	5
480	315.7	572.5	0.78	2.37	2	253.2	630.0	0.82	5.21	4
$2e 2\mu$										
125	117.1	127.9	0.22	0.53	0	114.5	128.8	0.24	0.70	0
244	212.5	255.5	2.30	3.12	4	196.1	262.6	2.41	5.15	7
480	315.7	572.5	0.76	1.83	4	253.2	630.0	0.79	4.17	6

Table 35: Expected signal and background events for 4.8fb^{-1} in a window containing 90% and 95% of the expected signal. the observed events in the window are also provided. for $m_H = 125\text{GeV}, 244\text{GeV}$ and 480GeV and the four channels individually. here also the mass ranges for 90% and 95% signal efficiency are estimated separately for each channel.

Mass (GeV)	Window					Window				
	signal		bkg	observed		signal		bkg	obs	
	Low	High				Low	High			
window with 90% of the exp. signal										
4μ										
125	118.8	128.3	0.53	0.26	1	116.3	129.5	0.55	0.34	1
244	212.4	257.0	3.31	5.2	8	195.4	263.7	3.5	8.6	14
480	297.7	575.3	0.93	3.7	3	235.4	637.1	0.98	8.2	9
$2\mu 2e$										
125	116.8	127.8	0.25	0.46	1	114.5	128.5	0.26	0.55	1
244	215.6	254.5	3.0	3.7	3	202.1	263.1	3.1	6.1	4
480	319.9	569.5	0.77	2.3	2	264.3	618.4	0.8	4.5	4
$4e$										
125	114.8	127.6	0.23	0.64	0	113.2	128.4	0.24	0.72	0
244	209.4	253.3	2.3	3.3	4	189.5	259.7	2.4	5.8	8
480	310.1	566.3	0.75	1.9	4	244.9	621.5	0.79	4.7	7
$2e 2\mu$										
125	117.0	127.5	0.41	0.20	1	114.5	128.2	0.43	0.26	1
244	212.4	256.0	2.5	3.6	6	196.3	263.8	2.7	5.9	10
480	330.8	576.6	0.91	1.9	2	273.0	637.1	0.96	3.8	5

12 Summary

A search for the SM Higgs boson in the decay channel $H \rightarrow ZZ^{(*)} \rightarrow 4\ell$ based on 4.8 fb^{-1} of data recorded by the ATLAS detector at $\sqrt{s} = 7 \text{ TeV}$ during the 2011 run has been presented. The SM Higgs boson is excluded at 95% CL in the mass ranges $134 - 156 \text{ GeV}$, $182 - 233 \text{ GeV}$, $256 - 265 \text{ GeV}$ and $268 - 415 \text{ GeV}$. The largest upward deviations from the background-only hypothesis are observed for $m_H = 125 \text{ GeV}$, 244 GeV and 500 GeV with local significances of 2.1, 2.2 and 2.1 standard deviations, respectively. Once the look-elsewhere effect is considered, none of these excesses are significant.

References

- [1] F. Englert and R. Brout, *Broken Symmetry and the Mass of Gauge Vector Mesons*, Phys. Rev. Lett. **13** (1964) 321–323.
- [2] P. W. Higgs, *Broken Symmetries and the Masses of Gauge Bosons*, Phys. Rev. Lett. **13** (1964) 508–509.
- [3] G. S. Guralnik, C. R. Hagen, and T. W. B. Kibble, *Global Conservation Laws and Massless Particles*, Phys. Rev. Lett. **13** (1964) 585–587.
- [4] LEP Working Group for Higgs boson searches, ALEPH, DELPHI, L3 and OPAL Collaborations, *Search for the standard model Higgs boson at LEP*, Phys. Lett. **B 565** (2003) 61–75, [arXiv:hep-ex/0306033](https://arxiv.org/abs/hep-ex/0306033).
- [5] The Tevatron New Physics and Higgs Working Group, *Combined CDF and D0 Upper Limits on Standard Model Higgs Boson Production with up to 8.6 fb^{-1} of Data*, 2011. [arXiv:1107.5518 \[hep-ex\]](https://arxiv.org/abs/1107.5518).
- [6] ATLAS Collaboration, *Limits on the production of the Standard Model Higgs Boson in pp collisions at $\sqrt{s} = 7 \text{ TeV}$ with the ATLAS detector*, Eur. Phys. J. **C 71** (2011) 1728, [arXiv:1106.2748 \[hep-ex\]](https://arxiv.org/abs/1106.2748).
- [7] CMS Collaboration, *Measurement of W^+W^- Production and Search for the Higgs Boson in pp Collisions at $\sqrt{s} = 7 \text{ TeV}$* , Phys. Lett. **B 699** (2011) 25–47, [arXiv:1102.5429 \[hep-ex\]](https://arxiv.org/abs/1102.5429).
- [8] ATLAS Collaboration, *Search for the Standard Model Higgs boson in the two photon decay channel with the ATLAS detector at the LHC*, Phys. Lett. **B 705** (2011) 452–470, [arXiv:1108.5895 \[hep-ex\]](https://arxiv.org/abs/1108.5895).
- [9] ATLAS Collaboration, *Search for the Standard Model Higgs boson in the decay channel $H \rightarrow ZZ^{(*)} \rightarrow 4\ell$ with the ATLAS detector*, Phys. Lett. **B 705** (2011) 435–451, [arXiv:1109.5945 \[hep-ex\]](https://arxiv.org/abs/1109.5945).
- [10] ATLAS Collaboration, *Search for a Standard Model Higgs boson in the $H \rightarrow ZZ \rightarrow \ell^+\ell^- v\bar{v}$ decay channel with the ATLAS detector*, Phys. Rev. Lett. **107** (2011) 221802, [arXiv:1109.3357 \[hep-ex\]](https://arxiv.org/abs/1109.3357).
- [11] ATLAS Collaboration, *Search for a heavy Standard Model Higgs boson in the channel $H \rightarrow ZZ \rightarrow \ell^+\ell^- q\bar{q}$ using the ATLAS detector*, Phys. Lett. **B 707** (2012) 27–45, [arXiv:1108.5064 \[hep-ex\]](https://arxiv.org/abs/1108.5064).

- [12] ATLAS Collaboration, *Search for the Higgs boson in the $H \rightarrow WW \rightarrow \ell\nu jj$ decay channel in pp collisions at $\sqrt{s} = 7$ TeV with the ATLAS detector*, Phys. Rev. Lett. **107** (2011) 231801, arXiv:1109.3615 [hep-ex].
- [13] ATLAS Collaboration, *Search for the Higgs boson in the $H \rightarrow WW^{(*)} \rightarrow \ell\nu\ell\nu$ decay channel in pp collisions at $\sqrt{s} = 7$ TeV with the ATLAS detector*, 2011. arXiv:1112.2577 [hep-ex]. submitted to Phys. Rev. Lett.
- [14] ATLAS Collaboration, *Luminosity Determination in pp Collisions at $\sqrt{s} = 7$ TeV Using the ATLAS Detector at the LHC*, Eur. Phys. J. **C 71** (2011) 1630, arXiv:1101.2185 [hep-ex].
- [15] ATLAS Collaboration, *Luminosity Determination in pp Collisions at $\sqrt{s} = 7$ TeV using the ATLAS Detector in 2011*, .
- [16] R. Fröhlich, *Track fitting with non-Gaussian noise*, Comput. Phys. Commun. **100** (1997) no. 1-2, 1 – 16.
- [17] S. Alioli, P. Nason, C. Oleari, and E. Re, *NLO Higgs boson production via gluon fusion matched with shower in POWHEG*, JHEP **04** (2009) 002, arXiv:0812.0578 [hep-ph].
- [18] P. Nason and C. Oleari, *NLO Higgs boson production via vector-boson fusion matched with shower in POWHEG*, JHEP **02** (2010) 037, arXiv:0911.5299 [hep-ph].
- [19] T. Sjostrand, S. Mrenna, and P. Z. Skands, *PYTHIA 6.4 Physics and Manual*, JHEP **05** (2006) 026, arXiv:hep-ph/0603175.
- [20] P. Golonka and Z. Was, *PHOTOS Monte Carlo: A Precision tool for QED corrections in Z and W decays*, Eur. Phys. J. **C 45** (2006) 97–107, arXiv:hep-ph/0506026.
- [21] Z. Was, *TAUOLA the library for tau lepton decay, and KKMC/KORALB/KORALZ/... status report*, Nucl. Phys. Proc. Suppl. **98** (2001) 96–102, arXiv:hep-ph/0011305.
- [22] LHC Higgs Cross Section Working Group, S. Dittmaier, C. Mariotti, G. Passarino, and R. Tanaka (Eds.), *Handbook of LHC Higgs cross sections: 1. Inclusive observables*, 2011. arXiv:1101.0593 [hep-ph]. CERN-2011-002.
- [23] R. V. Harlander and W. B. Kilgore, *Next-to-next-to-leading order Higgs production at hadron colliders*, Phys. Rev. Lett. **88** (2002) 201801, arXiv:hep-ph/0201206.
- [24] C. Anastasiou and K. Melnikov, *Higgs boson production at hadron colliders in NNLO QCD*, Nucl. Phys. **B 646** (2002) 220–256, arXiv:hep-ph/0207004.
- [25] V. Ravindran, J. Smith, and W. L. van Neerven, *NNLO corrections to the total cross section for Higgs boson production in hadron hadron collisions*, Nucl. Phys. **B 665** (2003) 325–366, arXiv:hep-ph/0302135.
- [26] C. Anastasiou, R. Boughezal, and F. Petriello, *Mixed QCD-electroweak corrections to Higgs boson production in gluon fusion*, JHEP **04** (2009) 003, arXiv:0811.3458 [hep-ph].
- [27] D. de Florian and M. Grazzini, *Higgs production through gluon fusion: updated cross sections at the Tevatron and the LHC*, Phys. Lett. **B 674** (2009) 291–294, arXiv:0901.2427 [hep-ph].
- [28] J. Baglio and A. Djouadi, *Higgs production at the LHC*, JHEP **03** (2011) 055.

- [29] P. Bolzoni, F. Maltoni, S.-O. Moch, and M. Zaro, *Higgs production via vector-boson fusion at NNLO in QCD*, Phys. Rev. Lett. **105** (2010) 011801, arXiv:1003.4451 [hep-ph].
- [30] S. Catani, D. de Florian, M. Grazzini, and P. Nason, *Soft-gluon resummation for Higgs boson production at hadron colliders*, JHEP **07** (2003) 028, arXiv:hep-ph/0306211.
- [31] U. Aglietti, R. Bonciani, G. Degrassi, and A. Vicini, *Two-loop light fermion contribution to Higgs production and decays*, Phys. Lett. **B 595** (2004) 432–441, arXiv:hep-ph/0404071.
- [32] S. Actis, G. Passarino, C. Sturm, and S. Uccirati, *NLO Electroweak Corrections to Higgs Boson Production at Hadron Colliders*, Phys. Lett. **B 670** (2008) 12–17, arXiv:0809.1301 [hep-ph].
- [33] M. Ciccolini, A. Denner, and S. Dittmaier, *Strong and electroweak corrections to the production of Higgs+2jets via weak interactions at the LHC*, Phys. Rev. Lett. **99** (2007) 161803, arXiv:0707.0381 [hep-ph].
- [34] M. Ciccolini, A. Denner, and S. Dittmaier, *Electroweak and QCD corrections to Higgs production via vector-boson fusion at the LHC*, Phys. Rev. **D 77** (2008) 013002, arXiv:0710.4749 [hep-ph].
- [35] A. Bredenstein, A. Denner, S. Dittmaier, and M. M. Weber, *Precise predictions for the Higgs-boson decay $H \rightarrow WW/ZZ \rightarrow 4\text{leptons}$* , Phys. Rev. **D 74** (2006) 013004, arXiv:hep-ph/0604011.
- [36] A. Bredenstein, A. Denner, S. Dittmaier, and M. M. Weber, *Radiative corrections to the semileptonic and hadronic Higgs-boson decays $H \rightarrow WW/ZZ \rightarrow 4\text{fermions}$* , JHEP **02** (2007) 080, arXiv:hep-ph/0611234.
- [37] J. M. Campbell and R. K. Ellis, *An update on vector boson pair production at hadron colliders*, Phys. Rev. **D 60** (1999) 113006, arXiv:hep-ph/9905386.
- [38] J. M. Campbell, R. K. Ellis, and C. Williams, *Vector boson pair production at the LHC*, JHEP **07** (2011) 018, arXiv:1105.0020 [hep-ph].
- [39] M. L. Mangano et al., *ALPGEN, a generator for hard multiparton processes in hadronic collisions*, JHEP **07** (2003) 001, arXiv:hep-ph/0206293.
- [40] S. Frixione and B. R. Webber, *The MC@NLO event generator*, arXiv:hep-ph/0207182.
- [41] S. Frixione and B. R. Webber, *Matching NLO QCD computations and parton shower simulations*, JHEP **06** (2002) 029, arXiv:hep-ph/0204244.
- [42] S. Frixione, P. Nason, and B. R. Webber, *Matching NLO QCD and parton showers in heavy flavour production*, JHEP **08** (2003) 007, arXiv:hep-ph/0305252.
- [43] G. Corcella et al., *HERWIG 6.5 release note*, arXiv:hep-ph/0210213.
- [44] J. M. Butterworth, J. R. Forshaw, and M. H. Seymour, *Multiparton interactions in photoproduction at HERA*, Z. Phys. **C72** (1996) 637–646, arXiv:hep-ph/9601371.
- [45] K. Melnikov and F. Petriello, *Electroweak gauge boson production at hadron colliders through $O(\alpha_s^2)$* , Phys. Rev. **D 74** (2006) 114017, arXiv:hep-ph/0609070.

- [46] C. Anastasiou, L. J. Dixon, K. Melnikov, and F. Petriello, *High precision QCD at hadron colliders: Electroweak gauge boson rapidity distributions at NNLO*, Phys. Rev. **D 69** (2004) 094008, arXiv:hep-ph/0312266.
- [47] M. Aliev et al., *HATHOR: HAdronic Top and Heavy quarks crOss section calculatoR*, Comput. Phys. Commun. **182** (2011) 1034, arXiv:1007.1327 [hep-ph].
- [48] ATLAS Collaboration, *The ATLAS Simulation Infrastructure*, Eur. Phys. J. **C70** (2010) 823–874, arXiv:1005.4568 [physics.ins-det].
- [49] S. Agostinelli et al., *GEANT4: A simulation toolkit*, Nucl. Instrum. Meth. **A 506** (2003) 250–303.
- [50] S. Catani, L. Cieri, G. Ferrera, D. de Florian, and M. Grazzini, *Vector boson production at hadron colliders: a fully exclusive QCD calculation at NNLO*, Phys. Rev. Lett. **103** (2009) 082001, arXiv:0903.2120 [hep-ph].
- [51] ATLAS Collaboration, *Electron performance measurements with the ATLAS detector using the 2010 LHC proton-proton collision data*, 2011. ATLAS-COM-PHYS-2011-546.
- [52] ATLAS Collaboration, *A measurement of the ATLAS muon reconstruction and trigger efficiency using J/ψ decays*, 2011. ATLAS-CONF-2011-021.
- [53] ATLAS Collaboration, *ATLAS Muon Momentum Resolution in the First Pass Reconstruction of the 2010 $p\text{-}p$ Collision Data at $\sqrt{s}=7$ TeV*, 2011. ATLAS-CONF-2011-046.
- [54] ATLAS Collaboration, *Muon reconstruction efficiency in reprocessed 2010 LHC $p\text{-}p$ collision data recorded with the ATLAS detector*, 2011. ATLAS-CONF-2011-063.
- [55] The ATLAS Collaboration Collaboration, ATLAS Collaboration, *Expected Performance of the ATLAS Experiment — Detector, Trigger and Physics*, 2009. arXiv:0901.0512 [hep-ex].
- [56] C. Anastopoulos et al, *ATLAS sensitivity prospects for the Standard Model Higgs boson in the decay channel $H \rightarrow ZZ^{(*)} \rightarrow 4\ell$ at $\sqrt{s} = 10$ TeV and 7 TeV*, ATL-PHYS-INT-2010-062 (2010).
- [57] ATLAS Collaboration, *Muon Reconstruction Performance*, ATLAS-CONF-2010-064 (2010).
- [58] ATLAS Collaboration Collaboration, G. Aad et al., *Measurements of the electron and muon inclusive cross-sections in proton-proton collisions at $\sqrt{s} = 7$ TeV with the ATLAS detector*, arXiv:1109.0525 [hep-ex].
- [59] ATLAS Collaboration, *Electron performance measurements with the ATLAS detector using the 2010 LHC proton-proton collision data*, arXiv:1110.3174 [hep-ex]. submitted to Eur. Phys. J. C.
- [60] ATLAS Collaboration, *A technique for measuring the pp to Z+X background to the H to $4l$ channel for the discovery of the Higgs Boson at the LHC*, 2009. ATL-COM-PHYS-2009-400.
- [61] C. Anastasiou, S. Buehler, F. Herzog, and A. Lazopoulos, *Total cross-section for Higgs boson hadroproduction with anomalous Standard Model interactions*, JHEP **12** (2011) 058, arXiv:1107.0683 [hep-ph].
- [62] A. L. Read, *Presentation of search results: The $CL(s)$ technique*, J. Phys. G **28** (2002) 2693–2704.
- [63] G. Cowan, K. Cranmer, E. Gross, and O. Vitells, *Asymptotic formulae for likelihood-based tests of new physics*, Eur. Phys. J. **C 71** (2011) 1554, arXiv:1007.1727 [physics.data-an].

- [64] L. Moneta et al., *The RooStats Project*, PoS **ACAT2010** (2010) 057, arXiv:1009.1003 [physics.data-an].
- [65] E. Gross and O. Vitells, *Trial factors for the look elsewhere effect in high energy physics*, Eur. Phys. J. **C 70** (2010) 525–530, arXiv:1005.1891 [physics.data-an].
- [66] Y. e. a. Gao, *Spin determination of single-produced resonances at hadron colliders*, Phys. Rev. **D 81** (2010) , arXiv:1001.3396v2 [hep-ph].
- [67] J. e. a. Gainer, *Improving the sensitivity of Higgs boson searches in the golden channel*, arXiv:1108.2274v2 [hep-ph].

Appendices

A List of MC samples

We use D3PD produce centrally by the Higgs group. D3PD contents are mainly based on SMWZD3PD, since they are amongst the most widely used samples in ATLAS. However, in an attempt to avoid (or at least reduce) the need of producing slimmed D4PDs, some information not relevant to HSG2 analyses has been removed ab origine. Some small bits (like the Heavy Flavour overlap flag for MC) have been ported from the top-D3PD. For the data the D3PD tag to use is “p762” while for MC the tag is “p768”.

A.1 Signal Samples

```
mc11_7TeV.116XXX.PowHegPythia_ggHXXX_ZZ4lep.merge.NTUP_HSG2.e873_s1310_s1300_r2820_r2872_p768/
mc11_7TeV.125XXX.PowHegPythia_VBFHXXX_ZZ4lep.merge.NTUP_HSG2.e920_s1310_s1300_r2820_r2872_p768/
mc11_7TeV.125XXX.PythiaWHXXX_ZZ4lep.merge.NTUP_HSG2.e825_s1310_s1300_r2820_r2872_p768/
mc11_7TeV.125XXX.PythiaZHXXX_ZZ4lep.merge.NTUP_HSG2.e825_s1310_s1300_r2820_r2872_p768/
```

A.2 Background Samples

```
mc11_7TeV.105200.T1_McAtNlo_Jimmy.merge.NTUP_HSG2.e835_s1272_s1274_r2820_r2872_p768/
mc11_7TeV.109345.T1_McAtNlo_Jimmy_2LeptonsM1160GeV.merge.NTUP_HSG2.e961_s1310_s1300_r2820_r2872_p768/
mc11_7TeV.109346.T1_McAtNlo_Jimmy_4LepMass_M1160GeV12GeV.merge.NTUP_HSG2.e961_s1310_s1300_r2820_r2872_p768/
mc11_7TeV.109292.Pythiazz4l_3MultiLeptonFilterElecMu.merge.NTUP_HSG2.e825_s1310_s1300_r2820_r2872_p768/
mc11_7TeV.105987.WZ_Herwig.merge.NTUP_HSG2.e825_s1310_s1300_r2820_r2872_p768/
mc11_7TeV.107650.AlpgenJimmyZeeNp0_pt20.merge.NTUP_HSG2.e835_s1299_s1300_r2820_r2872_p768/
mc11_7TeV.107651.AlpgenJimmyZeeNp1_pt20.merge.NTUP_HSG2.e835_s1299_s1300_r2820_r2872_p768/
mc11_7TeV.107652.AlpgenJimmyZeeNp2_pt20.merge.NTUP_HSG2.e835_s1299_s1300_r2820_r2872_p768/
mc11_7TeV.107653.AlpgenJimmyZeeNp3_pt20.merge.NTUP_HSG2.e835_s1299_s1300_r2820_r2872_p768/
mc11_7TeV.107654.AlpgenJimmyZeeNp4_pt20.merge.NTUP_HSG2.e835_s1299_s1300_r2820_r2872_p768/
mc11_7TeV.107655.AlpgenJimmyZeeNp5_pt20.merge.NTUP_HSG2.e835_s1299_s1300_r2820_r2872_p768/
mc11_7TeV.107660.AlpgenJimmyZmumuNp0_pt20.merge.NTUP_HSG2.e835_s1299_s1300_r2820_r2872_p768/
mc11_7TeV.107661.AlpgenJimmyZmumuNp1_pt20.merge.NTUP_HSG2.e835_s1299_s1300_r2820_r2872_p768/
mc11_7TeV.107662.AlpgenJimmyZmumuNp2_pt20.merge.NTUP_HSG2.e835_s1299_s1300_r2820_r2872_p768/
mc11_7TeV.107663.AlpgenJimmyZmumuNp3_pt20.merge.NTUP_HSG2.e835_s1299_s1300_r2820_r2872_p768/
mc11_7TeV.107664.AlpgenJimmyZmumuNp4_pt20.merge.NTUP_HSG2.e835_s1299_s1300_r2820_r2872_p768/
mc11_7TeV.107665.AlpgenJimmyZmumuNp5_pt20.merge.NTUP_HSG2.e835_s1299_s1300_r2820_r2872_p768/
mc11_7TeV.107670.AlpgenJimmyZtautauNp0_pt20.merge.NTUP_HSG2.e835_s1299_s1300_r2820_r2872_p768/
mc11_7TeV.107671.AlpgenJimmyZtautauNp1_pt20.merge.NTUP_HSG2.e835_s1299_s1300_r2820_r2872_p768/
mc11_7TeV.107672.AlpgenJimmyZtautauNp2_pt20.merge.NTUP_HSG2.e835_s1299_s1300_r2820_r2872_p768/
mc11_7TeV.107673.AlpgenJimmyZtautauNp3_pt20.merge.NTUP_HSG2.e835_s1299_s1300_r2820_r2872_p768/
mc11_7TeV.107674.AlpgenJimmyZtautauNp4_pt20.merge.NTUP_HSG2.e835_s1299_s1300_r2820_r2872_p768/
mc11_7TeV.107675.AlpgenJimmyZtautauNp5_pt20.merge.NTUP_HSG2.e835_s1299_s1300_r2820_r2872_p768/
mc11_7TeV.116950.AlpgenHwfZeebbNp0_Veto4LepM_Pass3Lep.merge.NTUP_HSG2.e835_s1310_s1300_r2820_r2872_p768/
mc11_7TeV.116951.AlpgenHwfZeebbNp1_Veto4LepM_Pass3Lep.merge.NTUP_HSG2.e835_s1310_s1300_r2820_r2872_p768/
mc11_7TeV.116952.AlpgenHwfZeebbNp2_Veto4LepM_Pass3Lep.merge.NTUP_HSG2.e835_s1310_s1300_r2820_r2872_p768/
mc11_7TeV.116953.AlpgenHwfZeebbNp3_Veto4LepM_Pass3Lep.merge.NTUP_HSG2.e835_s1310_s1300_r2820_r2872_p768/
mc11_7TeV.116955.AlpgenHwfZmumubbNp0_Veto4LepM_Pass3Lep.merge.NTUP_HSG2.e835_s1310_s1300_r2820_r2872_p768/
mc11_7TeV.116956.AlpgenHwfZmumubbNp1_Veto4LepM_Pass3Lep.merge.NTUP_HSG2.e835_s1310_s1300_r2820_r2872_p768/
mc11_7TeV.116957.AlpgenHwfZmumubbNp2_Veto4LepM_Pass3Lep.merge.NTUP_HSG2.e835_s1310_s1300_r2820_r2872_p768/
mc11_7TeV.116958.AlpgenHwfZmumubbNp3_Veto4LepM_Pass3Lep.merge.NTUP_HSG2.e835_s1310_s1300_r2820_r2872_p768/
mc11_7TeV.116960.AlpgenHwfZeebbNp0_4LepM.merge.NTUP_HSG2.e835_s1310_s1300_r2820_r2872_p768/
mc11_7TeV.116961.AlpgenHwfZeebbNp1_4LepM.merge.NTUP_HSG2.e835_s1310_s1300_r2820_r2872_p768/
mc11_7TeV.116962.AlpgenHwfZeebbNp2_4LepM.merge.NTUP_HSG2.e835_s1310_s1300_r2820_r2872_p768/
mc11_7TeV.116963.AlpgenHwfZeebbNp3_4LepM.merge.NTUP_HSG2.e835_s1310_s1300_r2820_r2872_p768/
mc11_7TeV.116965.AlpgenHwfZmumubbNp0_4LepM.merge.NTUP_HSG2.e835_s1310_s1300_r2820_r2872_p768/
mc11_7TeV.116966.AlpgenHwfZmumubbNp1_4LepM.merge.NTUP_HSG2.e835_s1310_s1300_r2820_r2872_p768/
```

mc11_7TeV.116967.AlpgenHWfZmumubbNp2_4LepM.merge.NTUP_HSG2.e835_s1310_s1300_r2820_r2872_p768/
mc11_7TeV.116968.AlpgenHWfZmumubbNp3_4LepM.merge.NTUP_HSG2.e835_s1310_s1300_r2820_r2872_p768/
mc11_7TeV.116600.gg2ZZ_JIMMY_ZZ4lep.merge.NTUP_HSG2.e922_s1310_s1300_r2820_r2872_p768/

A.3 Background Samples cross-sections

In Table 36 the cross sections of the most used background samples are presented.

B Data quality requirements

The data are required to satisfy a number of conditions ensuring that all essential elements of the ATLAS detector – detectors, magnets, trigger, etc. – were performing as expected while the data were collected during LHC collisions and this is summarized in Table 37. The Good Run Lists (GRLs) are centrally produced by the Data Quality and Data Preparation groups.

The Good Run Lists (GRLs) are produced centrally and can be found here :

<http://atlasdqm.web.cern.ch/atlasdqm/grlgen/>

The following GRLs are used for the analysis and with the following tag "*data11_7TeV.periodAllYear_DetStatus-v35-pro09-03_CoolRunQuery-00-04-08-* .xml*" :

1. For the $H \rightarrow ZZ \rightarrow \mu\mu\mu\mu$ channel (**.Higgs_4l4mu.xml*) :

http://atlasdqm.web.cern.ch/atlasdqm/grlgen/Higgs/Higgs_4l_4mu_v1/

2. For the $H \rightarrow ZZ \rightarrow ee\mu\mu$ channel (**.Higgs_4l2e2mu.xml*) :

http://atlasdqm.web.cern.ch/atlasdqm/grlgen/Higgs/Higgs_4l_2e2mu_v3/

3. For the $H \rightarrow ZZ \rightarrow eeee$ channel (**.Eg_standard.xml*) :

http://atlasdqm.web.cern.ch/atlasdqm/grlgen/CombinedPerf/Egamma/Eg_standard_v5/

This twiki page contains a lot of information about the Good Run Lists :

<https://twiki.cern.ch/twiki/bin/view/AtlasProtected/GoodRunListsForAnalysis>

The five main sources of data loss for physics in 2011 are only coming from LAr calorimeters issues that represent a loss of 6.20% of the data and are summarized in Table 38.

Some of these problems are now treated in a different way to minimize the losses (time window of few seconds around the noise burst/data corruption event instead of the 1 minute lumiblock) and the following percentage of data was recovered :

1. Noise burst: <5%
2. Noisy channel : 2 %
3. Data corruption: 2%
4. HV ramping-up: < 2%

This was a big success with the reprocessing campaign of the 2011 data thanks to the LAr, Data Preparation and Data Quality group.

107650	Alpgen+Jimmy Zee + 0 partons	827375
107651	Alpgen+Jimmy Zee + 1 partons	166625
107652	Alpgen+Jimmy Zee + 2 partons	50375
107653	Alpgen+Jimmy Zee + 3 partons	14000
107654	Alpgen+Jimmy Zee + 4 partons	3375
107655	Alpgen+Jimmy Zee + 5 partons	1000
107660	Alpgen+Jimmy Zmumu + 0 partons	822125
107661	Alpgen+Jimmy Zmumu + 1 partons	166000
107662	Alpgen+Jimmy Zmumu + 2 partons	49500
107663	Alpgen+Jimmy Zmumu + 3 partons	13875
107664	Alpgen+Jimmy Zmumu + 4 partons	3500
107665	Alpgen+Jimmy Zmumu + 5 partons	1000
107670	Alpgen+Jimmy Ztautau + 0 partons	828125
107671	Alpgen+Jimmy Ztautau + 1 partons	167375
107672	Alpgen+Jimmy Ztautau + 2 partons	50375
107673	Alpgen+Jimmy Ztautau + 3 partons	13750
107674	Alpgen+Jimmy Ztautau + 4 partons	3500
107675	Alpgen+Jimmy Ztautau + 5 partons	1000
116960	Zbb, Z \rightarrow ee ($ l >30$ GeV) + 0 parton [m_{4l} 60/12 GeV]	20.701
116961	Zbb, Z \rightarrow ee ($ l >30$ GeV) + 1 parton [m_{4l} 60/12 GeV]	18.8029
116962	Zbb, Z \rightarrow ee ($ l >30$ GeV) + 2 parton [m_{4l} 60/12 GeV]	10.505
116963	Zbb, Z \rightarrow ee ($ l >30$ GeV) + 3 parton [m_{4l} 60/12 GeV]	7.30463
116965	Zbb, Z \rightarrow mumu ($ l >30$ GeV) + 0 parton [m_{4l} 60/12 GeV]	21.516
116966	Zbb, Z \rightarrow mumu ($ l >30$ GeV) + 1 parton [m_{4l} 60/12 GeV]	19.6674
116967	Zbb, Z \rightarrow mumu ($ l >30$ GeV) + 2 parton [m_{4l} 60/12 GeV]	10.516
116968	Zbb, Z \rightarrow mumu ($ l >30$ GeV) + 3 parton [m_{4l} 60/12 GeV]	7.93834
116950	Zbb, Z \rightarrow ee ($ l >30$ GeV) + 0 parton 3l filter, veto on m_{4l} 60/12 GeV	756.32x1.4
116951	Zbb, Z \rightarrow ee ($ l >30$ GeV) + 1 parton 3l filter, veto on m_{4l} 60/12 GeV	432.25x1.4
116952	Zbb, Z \rightarrow ee ($ l >30$ GeV) + 2 parton 3l filter, veto on m_{4l} 60/12 GeV	176x1.4
116953	Zbb, Z \rightarrow ee ($ l >30$ GeV) + 3 parton 3l filter, veto on m_{4l} 60/12 GeV	96.75x1.4
116955	Zbb, Z \rightarrow mumu ($ l >30$ GeV) + 0 parton 3l filter, veto on m_{4l} 60/12 GeV	730.24x1.4
116956	Zbb, Z \rightarrow mumu ($ l >30$ GeV) + 1 parton 3l filter, veto on m_{4l} 60/12 GeV	432.25x1.4
116957	Zbb, Z \rightarrow mumu ($ l >30$ GeV) + 2 parton 3l filter, veto on m_{4l} 60/12 GeV	179.3x1.4
116958	Zbb, Z \rightarrow mumu ($ l >30$ GeV) + 3 parton 3l filter, veto on m_{4l} 60/12 GeV	92.3962x1.4
105200	ttbar (at least 1lepton filter)	91550.6
109345	ttbar (with Mll>60 GeV filter)	12707.2
109346	ttbar (with Mll>60 GeV filter and Mll>12 GeV)	515.2
109292	ZZ \rightarrow 4l 3LepFilter	91.54

Table 36: Background Samples and their cross-sections.

Channel	Description	Data quality flags requirement
common	center-of-mass energy	data11_7TeV
	global status	global_status g
	detector running	partition atlas
	database	db data
	magnet (solenoid)	dq atlsol g
	beam spot	dq idbs g
	vertex	dq idvx g
	luminosity	dq lumi g
4e	L1 and HLT trigger	dq trig_ele g and dq trig_gam g
	electron object	cp eg_electron_barrel g and cp eg_electron_crack g and cp eg_electron_endcap g
	photon object	cp eg_photon_barrel g and cp eg_photon_crack g and cp eg_photon_endcap g
4μ	magnet (toroid)	dq atltau g
	L1 and HLT trigger	dq trig_muo g
	muon object	cp mu_mstaco g and cp mu_mmuidcb g
	calorimetry object	cp global_all_calo_cg_no_fcal g
$2e2\mu$	magnet (toroid)	dq atltau g
	L1 and HLT trigger	dq trig_ele g and dq trig_muo g
	electron object	cp eg_electron_barrel g and cp eg_electron_crack g and cp eg_electron_endcap g
	muon object	cp mu_mstacog and cp mu_mmuidcb g

Table 37: Data quality flags required to produce the Good Run List (GRL) for the analysis.

Period	LAr defects name	loss (pb^{-1})	loss (%)
B-M	“HVRAMPUP”	0.00	0.00
B-M	“NOISEBURTS”	52.18	1.10
B-M	“DATACORRUPTION”	1.87	0.04
B-M	“HVTRIP”	45.46	0.96
B-M	“SEVNOISYCHANNEL”	184.69	3.79
B-M	“RECOCORRUPT”	14.86	0.32
B-M	All	299.06	6.20

Table 38: Main sources of data loss for physics in 2011 coming from LAr calorimeters issues (defects).

C Changes in the Muon stream due to the optimal GSF version for electrons

One difference with respect to the previous draft (D3PD tag p695) is that the 2e2mu event at 147.5 is not selected by our analysis anymore (D3PD tag p768). when the initial draft was released, a small fraction of the muon stream was processed with Rel 17.0.3.2.1(D3PD tag p695) instead for Rel 17.0.4.1.1 (D3PD tag p768) which is the final processing we used for our analysis. In both cases GSF refits were ran on the electron candidates, and this lead to the change of the best matching track to the e/gamma cluster. However in Rel 17.0.3.2.1(D3PD tag p695) the trackIsolation was not re-calculated as is the case for 17.0.4.1.1(D3PD tag p768).

D $Z \rightarrow \ell\ell$ rate in different data-taking periods

The rate of $Z \rightarrow \ell\ell$ events can be used to diagnose potential issues with our data quality or event selection efficiency. In Figure 54 the rate of observed $Z \rightarrow ee$ and $Z \rightarrow \mu\mu$ events is given separately for the different data taking periods. In Figure 54(a), $Z \rightarrow ee$ candidates are reconstructed using opposite sign electron pairs fulfilling the analysis selection criteria. Both leptons were required to have $p_T > 20\text{ GeV}$ and with a combined mass in a window of 15 GeV around the nominal Z mass (red histograms) and also with the track isolation applied (blue histograms); full lines are for data and dashed lines are for Monte Carlo. In Figure 54(b) the quality selection of the muons is identical to that of the analysis and the kinematic cuts are the same as the electron channel and track-based isolation is applied.

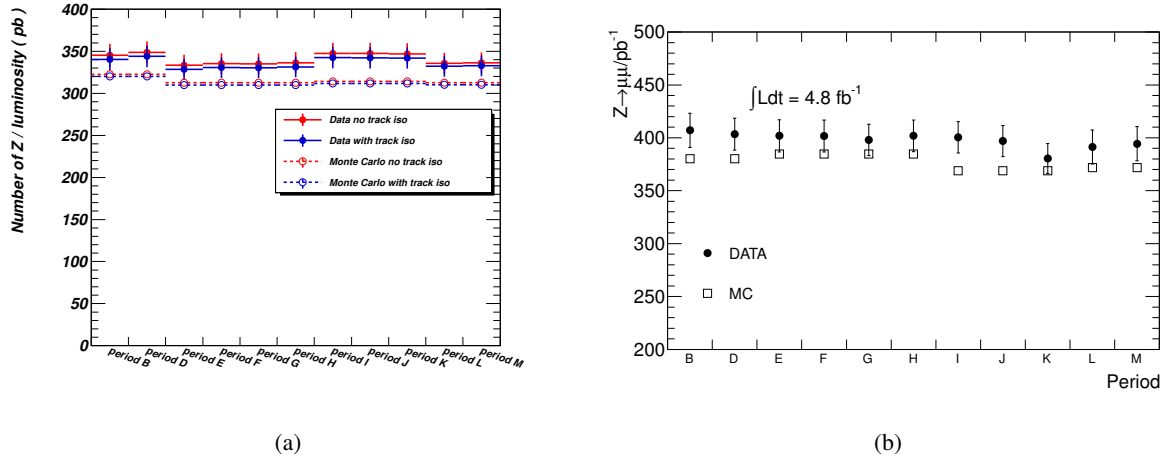


Figure 54: Number of reconstructed $Z \rightarrow \ell\ell$ events as a function of the data taking period normalized to the luminosity of each period, both for electrons and muons.

E Observation of $Z + J/\psi$ production and effect in the analysis

In this section, the possibility of muons coming from J/ψ decays and contributing to $H \rightarrow 4\ell$ analysis is studied. The method is based on $Z + \mu^+ \mu^-$ selection, where the Z boson is decaying either to electrons or muons and the dimuon pair has $M_{34} < 15\text{GeV}$. Leptons coming from the Z decay are required to be isolated, have $p_T > 20\text{GeV}$, in order to minimize the QCD contribution, and passing the impacting parameter cuts, whereas the muons accompanying the Z are not required to be isolated and pass the impact parameter significance cuts. The non - leading dimuon mass distribution and the quadraplet mass are presented in Figure 55 for both data and MC. The comparison between data and MC, also presented in Table 39, does not show agreement as expected due to the MC fragmentation. Although, after imposing the additional selection, isolation and impact parameter criteria, discrepancies are not expected since the MC describes the heavy flavor. Table 39 also provides the events surviving each of the additional cuts and the entire selection. The number of events after the impact parameter cut shows discrepancy, but the events after isolation cuts are in agreement. None event survive all the additional selection in data.

Since in the $H \rightarrow ZZ^{(*)} \rightarrow 4\ell$ analysis, the p_T threshold of 20GeV is applied not necessarily on the leading dilepton, the possibility of mispairing events is investigated, only when the mispairing leads to a dilepton invariant mass within a wide Z mass range, [60, 105]. The study is performed on MC and the ℓ_3, ℓ_4 are not required to pass the additional selection. 0.11 events pass the selection and gives a dilepton mass near the nominal Z mass. Taking into account that mispairing between electrons and muons is

Figure 55: (a) Non-leading opposite sign dilepton invariant mass spectrum and (b) the corresponding quadruplet mass of opposite dimuon pairs for an integrated luminosity of 4.8 fb^{-1} . The M_{34} is required to be less than 15 GeV in order to study the $Z + J/\psi$ production.

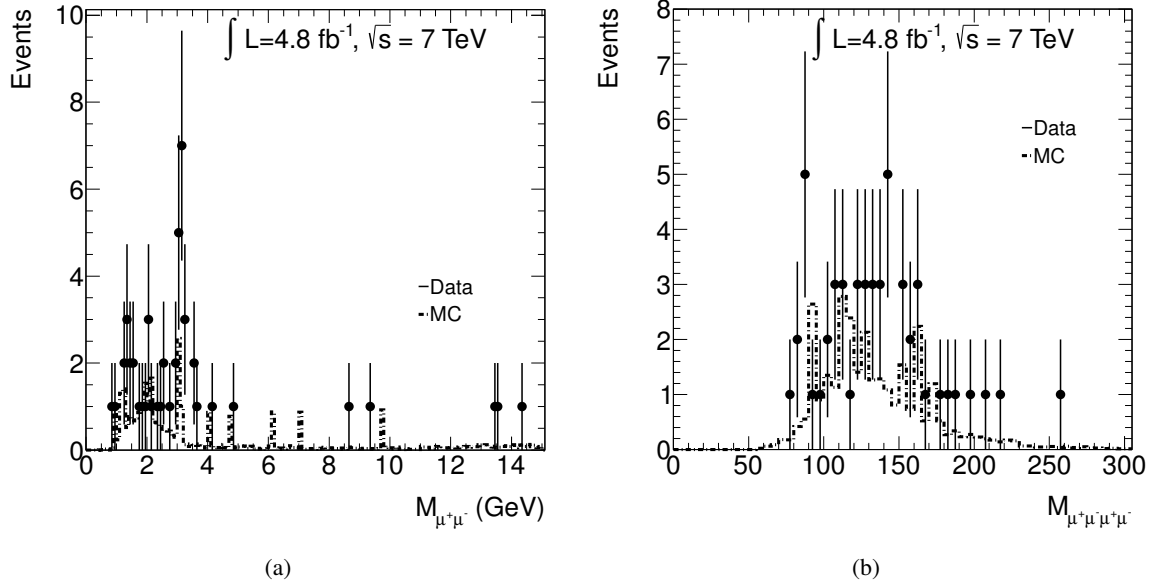


Table 39: Events surviving isolation and impact parameter criteria, when these are applied to the muons accompanying the Z . The number before the application of the cuts shows discrepancies between data and MC due to MC fragmentation. The events after isolation and all cuts are in agreement. The errors are statistical only.

	Data	MC
Before Cuts	50 ± 7	31.01 ± 0.15
Norm. Track isolation < 0.15	2.0 ± 1.4	1.78 ± 0.03
Norm. Calo. isolation < 0.3	3.0 ± 1.7	4.95 ± 0.03
$d_0/\sigma_{d0} < 3.5$	27 ± 5	12.03 ± 0.06
All cuts	0 ± 1	1.37 ± 0.04

impossible the number of these events is about half, 0.055, considering that when $M_{4\ell}$ and non-leading mispaired dilepton mass cuts applied the number will further suppressed.

For the 4.8 fb^{-1} of data none event with muon pair from J/ψ decay fulfilled the selection. The MC predicts less than 0.055 events.

F Mass resolution of the signal

The 4-lepton invariant mass resolution has been studied, in the four channels, as a function of simulated Higgs mass, combining POWHEG gluon fusion and vector boson fusion samples.

Resolution has been extracted from the reconstructed Higgs candidate invariant mass, performing a binned maximum likelihood fit of a probability density function which is the convolution of a physical

Not reviewed, for internal circulation only

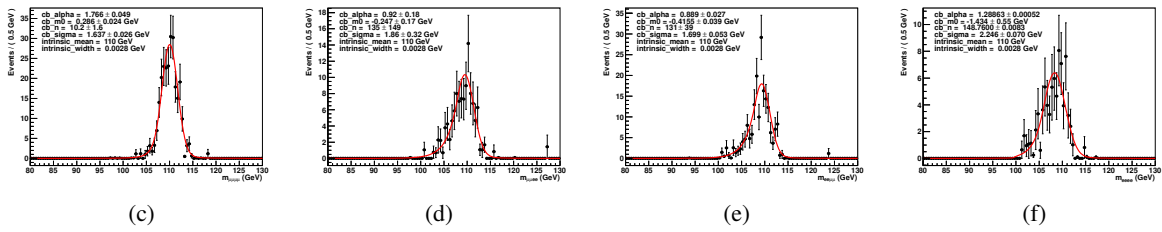


Figure 56: Invariant mass distribution for $m_H = 110$ GeV (black histogram); the invariant mass fit of the distribution is shown in the red line (2).

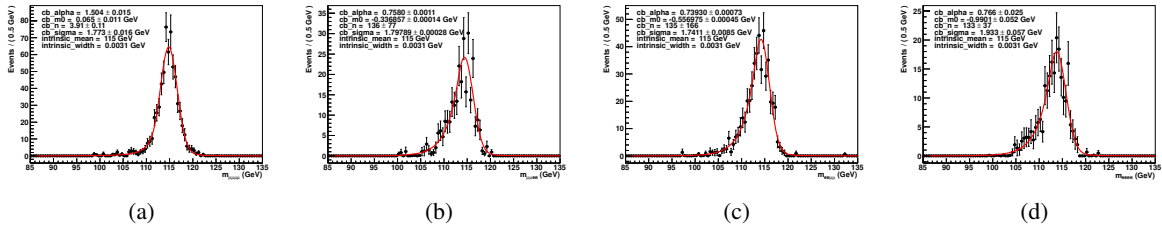


Figure 57: Invariant mass distribution for $m_H = 115$ GeV (black histogram); the invariant mass fit of the distribution is shown in the red line (2).

Breit–Wigner and a resolution Crystal Ball distribution,

$$f(m_{4l}|m_0, \sigma, \alpha, n) = \text{BW}(m_{4l}; m_H, \Gamma_H) \otimes \text{CrystalBall}(m_{4l}|m_0, \sigma, \alpha, n), \quad (2)$$

where m_{4l} is the reconstructed Higgs invariant mass, m_H and Γ_H are the Higgs true mass and intrinsic width (fixed to the theoretical value), m_0 accounts for biases in Higgs mass reconstruction and σ, α and n are the parameters of the Crystall Ball.

Figures 56–70 show the fit of this model to reconstructed invariant mass distributions, for various masses. Only the Crystal Ball parameters are let to vary during the fitting procedure; mass resolution is then extracted as the FWHM of the Crystall Ball probability density function, separately for each channel ($\mu\mu\mu\mu, \mu\mu ee, ee\mu\mu, eeee$), for each value of m_H .

The difference between the reconstructed and simulated Higgs mass, $m_{4l} - \tilde{m}_H$, has also been used for extracting the invariant mass resolution, defined as the FWHM of a Crystal Ball p.d.f. fitted to the distribution. Figures 56–70 show the result of these fits.

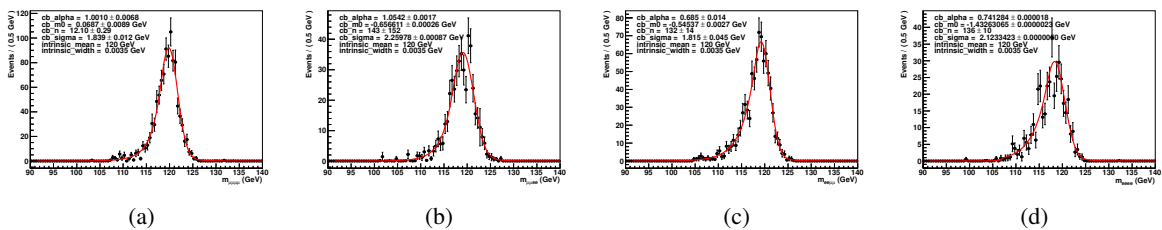


Figure 58: Invariant mass distribution for $m_H = 120$ GeV (black histogram); the invariant mass fit of the distribution is shown in the red line (2).

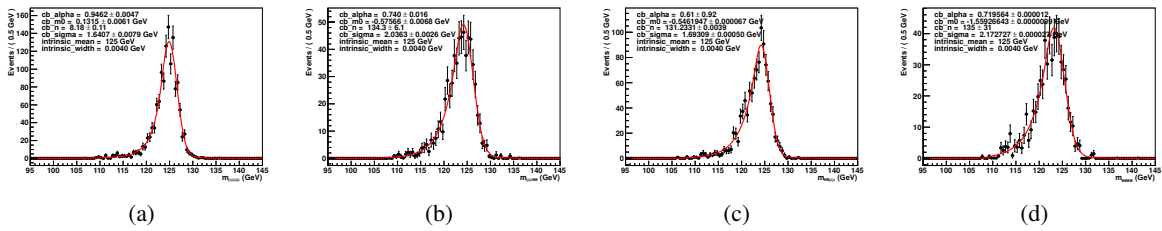


Figure 59: Invariant mass distribution for $m_H = 125$ GeV (black histogram); the invariant mass fit of the distribution is shown in the red line (2).

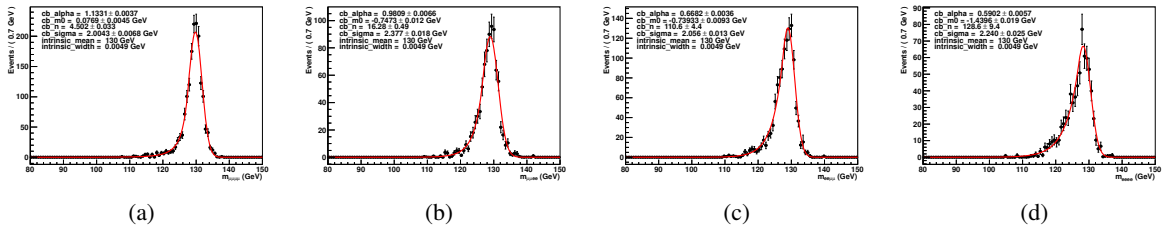


Figure 60: Invariant mass distribution for $m_H = 130$ GeV (black histogram); the invariant mass fit of the distribution is shown in the red line (2).

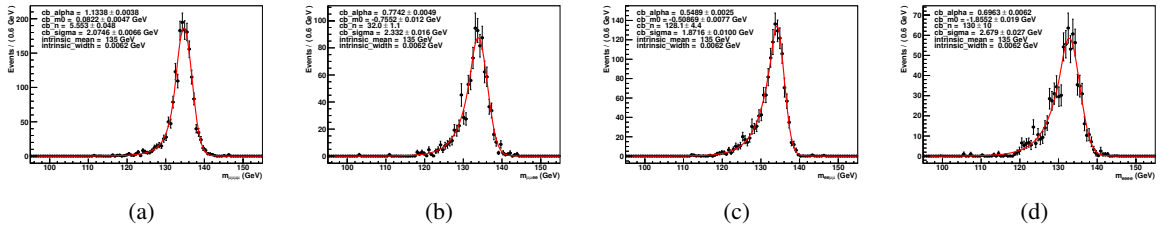


Figure 61: Invariant mass distribution for $m_H = 135$ GeV (black histogram); the invariant mass fit of the distribution is shown in the red line (2).

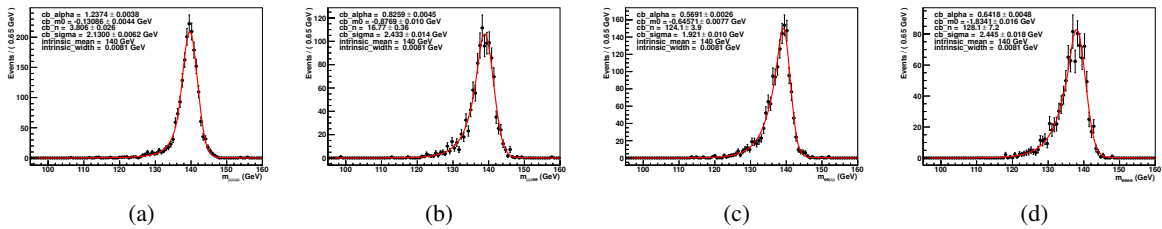


Figure 62: Invariant mass distribution for $m_H = 140$ GeV (black histogram); the invariant mass fit of the distribution is shown in the red line (2).

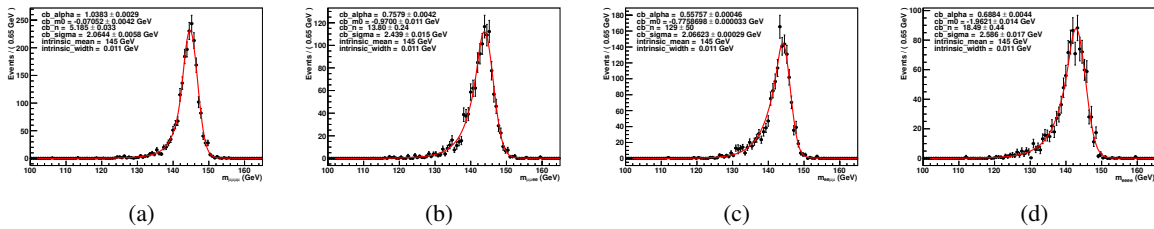


Figure 63: Invariant mass distribution for $m_H = 145$ GeV (black histogram); the invariant mass fit of the distribution is shown in the red line (2).

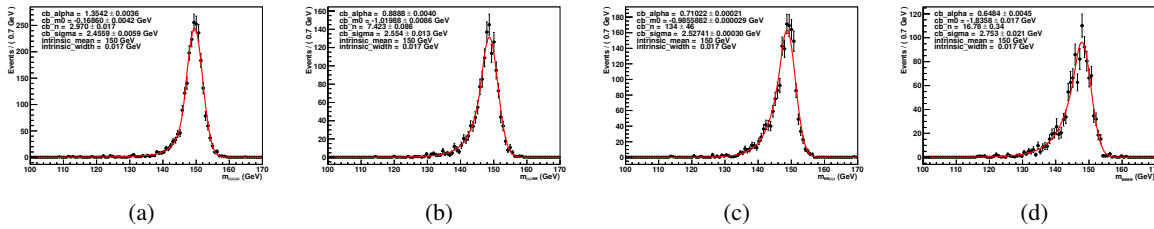


Figure 64: Invariant mass distribution for $m_H = 150$ GeV (black histogram); the invariant mass fit of the distribution is shown in the red line (2).

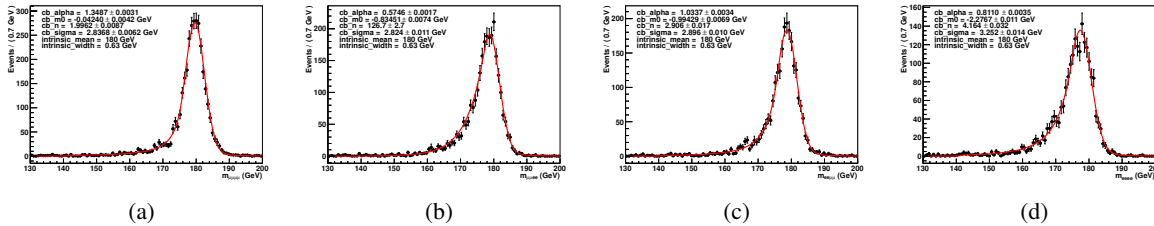


Figure 65: Invariant mass distribution for $m_H = 180$ GeV (black histogram); the invariant mass fit of the distribution is shown in the red line (2).

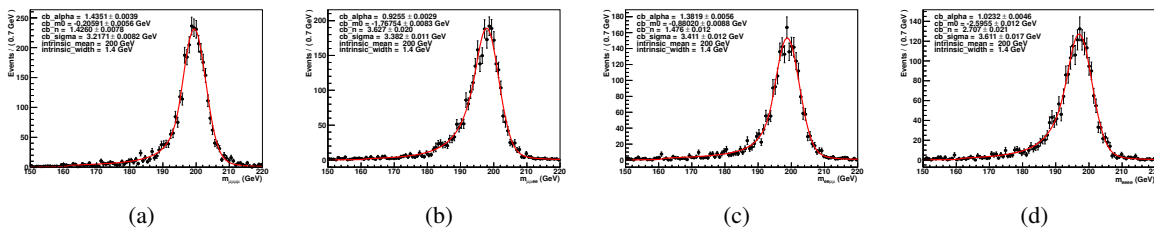


Figure 66: Invariant mass distribution for $m_H = 200$ GeV (black histogram); the invariant mass fit of the distribution is shown in the red line (2).

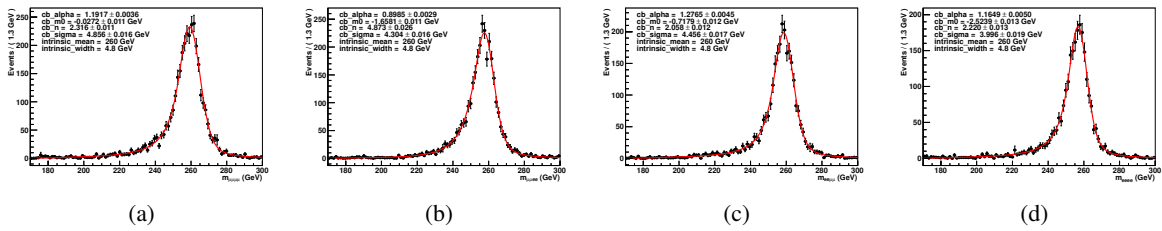


Figure 67: Invariant mass distribution for $m_H = 260$ GeV (black histogram); the invariant mass fit of the distribution is shown in the red line (2).

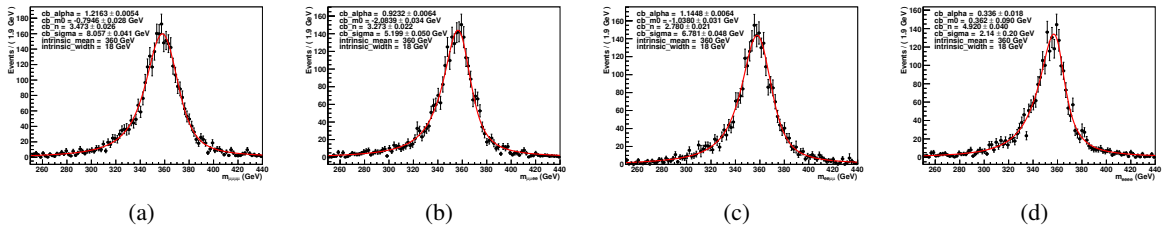


Figure 68: Invariant mass distribution for $m_H = 360$ GeV (black histogram); the invariant mass fit of the distribution is shown in the red line (2).

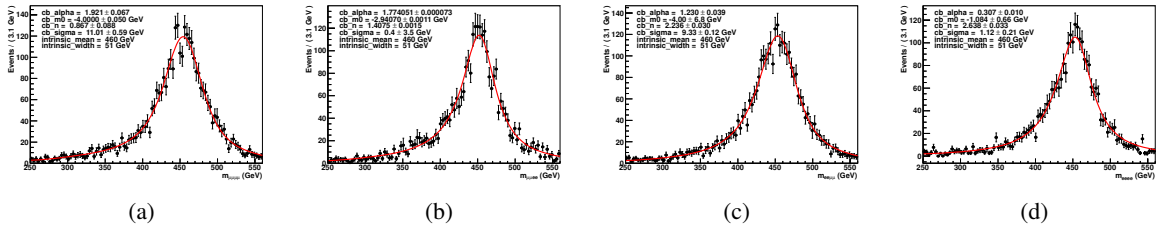


Figure 69: Invariant mass distribution for $m_H = 460$ GeV (black histogram); the invariant mass fit of the distribution is shown in the red line (2).

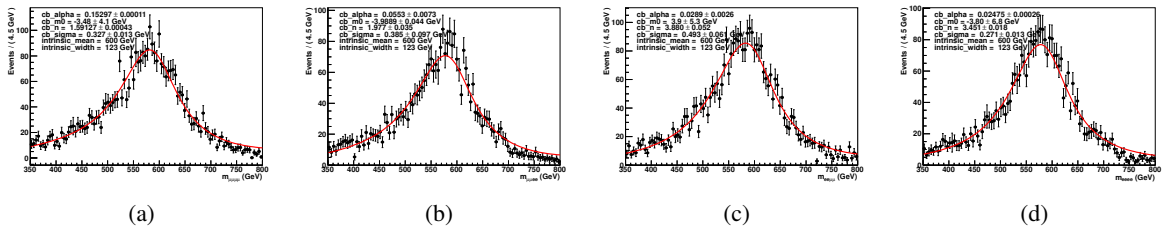


Figure 70: Invariant mass distribution for $m_H = 600$ GeV (black histogram); the invariant mass fit of the distribution is shown in the red line (2).

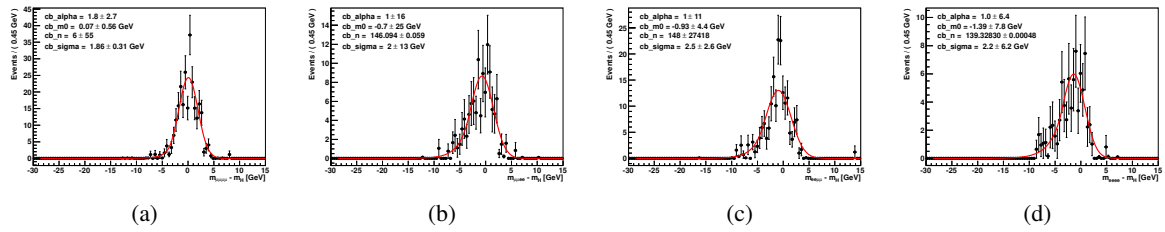


Figure 71: Difference between reconstructed and simulated Higgs masses for $m_H = 110$ GeV (black histogram); the fit to a Crystal Ball distribution is shown in red line.

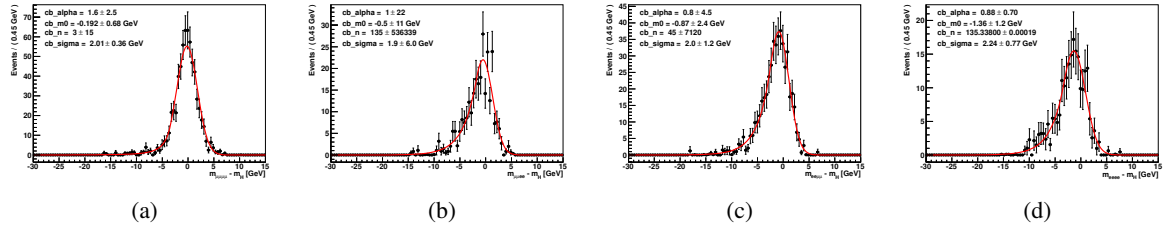


Figure 72: Difference between reconstructed and simulated Higgs masses for $m_H = 115$ GeV (black histogram); the fit to a Crystal Ball distribution is shown in red line.

G Shape of the $ZZ^{(*)}$ background

The effect of the m_{34} threshold to the $ZZ \rightarrow 4\ell$ mass spectrum is presented in Figure 86. To obtain a smooth $ZZ^{(*)}$ mass spectrum shape, a kernel density estimation was used. The initial and smooth histograms are presented in Figure 87 for the different sub-channels of the analysis.

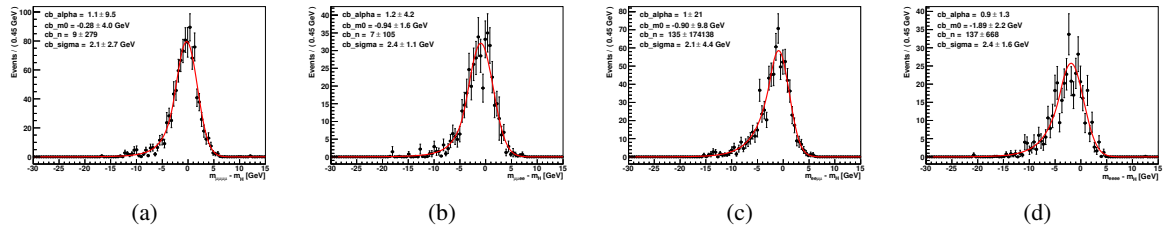


Figure 73: Difference between reconstructed and simulated Higgs masses for $m_H = 120$ GeV (black histogram); the fit to a Crystal Ball distribution is shown in red line.

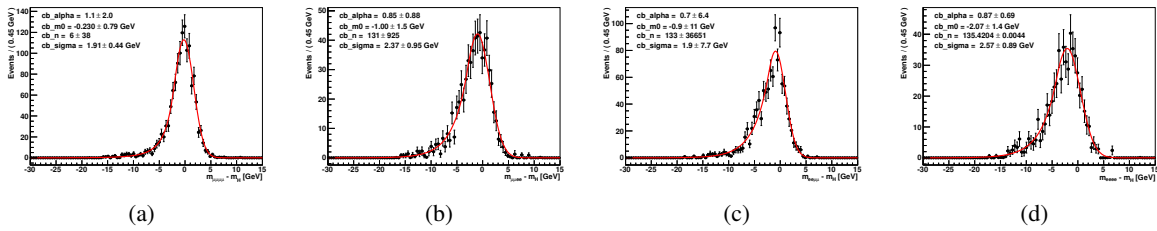


Figure 74: Difference between reconstructed and simulated Higgs masses for $m_H = 125 \text{ GeV}$ (black histogram); the fit to a Crystal Ball distribution is shown in red line.

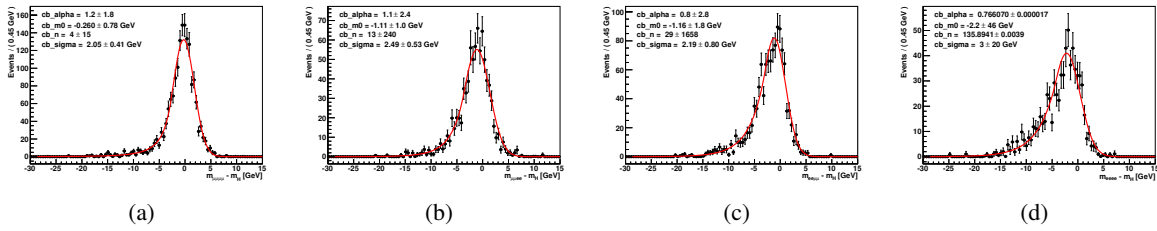


Figure 75: Difference between reconstructed and simulated Higgs masses for $m_H = 130 \text{ GeV}$ (black histogram); the fit to a Crystal Ball distribution is shown in red line.

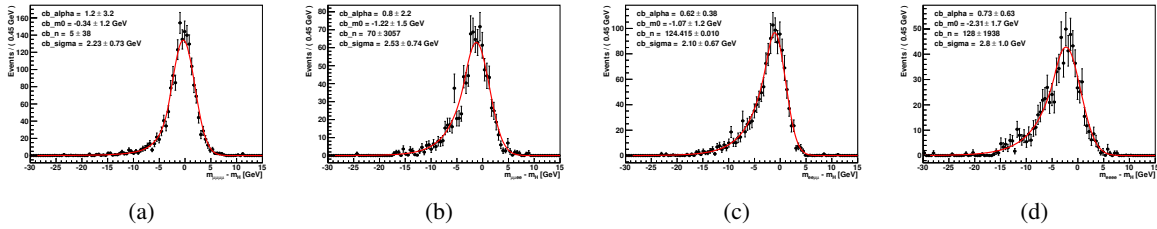


Figure 76: Difference between reconstructed and simulated Higgs masses for $m_H = 135 \text{ GeV}$ (black histogram); the fit to a Crystal Ball distribution is shown in red line.

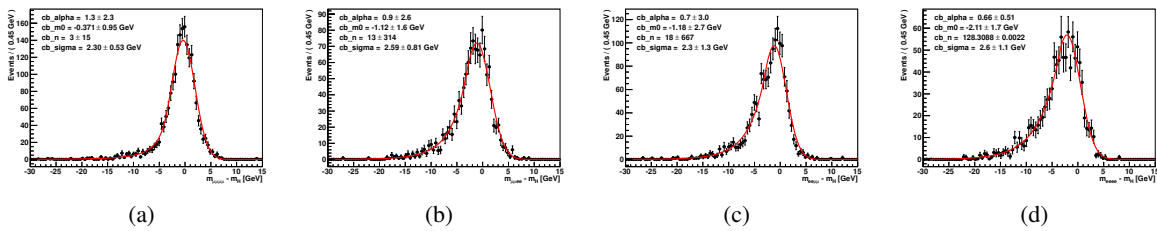


Figure 77: Difference between reconstructed and simulated Higgs masses for $m_H = 140 \text{ GeV}$ (black histogram); the fit to a Crystal Ball distribution is shown in red line.

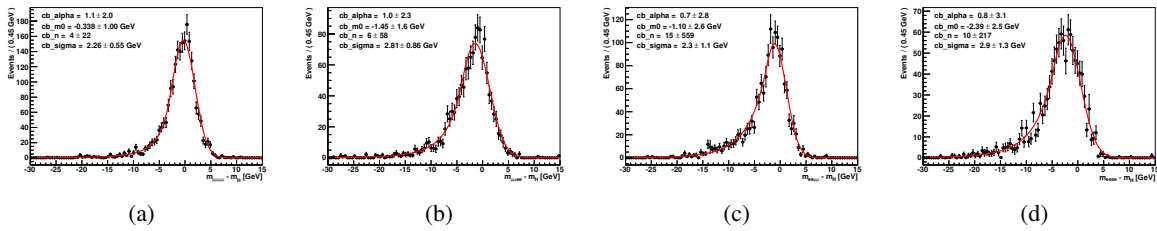


Figure 78: Difference between reconstructed and simulated Higgs masses for $m_H = 145 \text{ GeV}$ (black histogram); the fit to a Crystal Ball distribution is shown in red line.

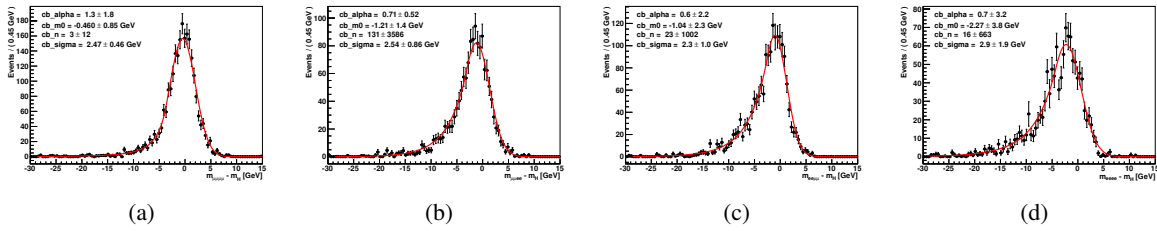


Figure 79: Difference between reconstructed and simulated Higgs masses for $m_H = 150 \text{ GeV}$ (black histogram); the fit to a Crystal Ball distribution is shown in red line.

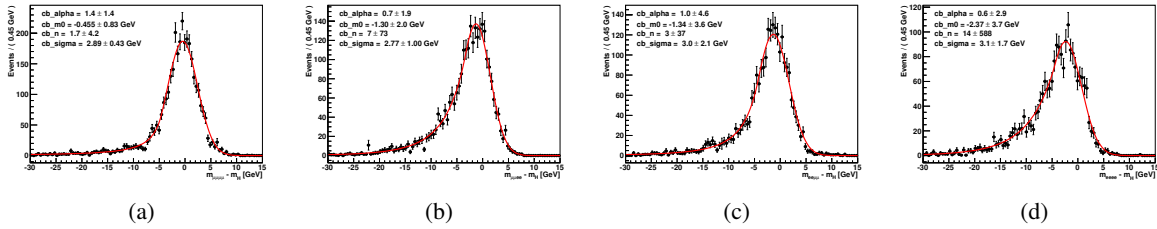


Figure 80: Difference between reconstructed and simulated Higgs masses for $m_H = 180 \text{ GeV}$ (black histogram); the fit to a Crystal Ball distribution is shown in red line.

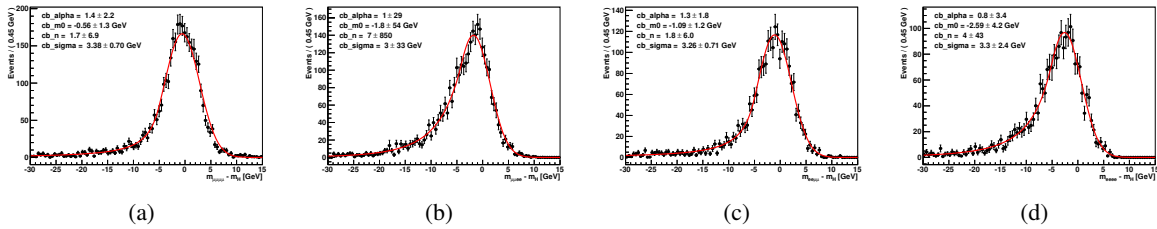


Figure 81: Difference between reconstructed and simulated Higgs masses for $m_H = 200 \text{ GeV}$ (black histogram); the fit to a Crystal Ball distribution is shown in red line.

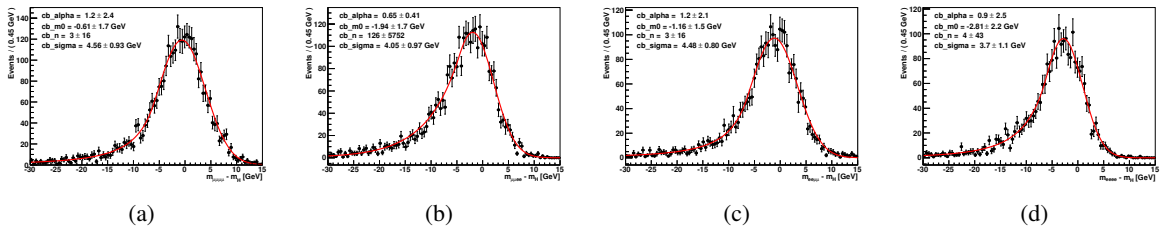


Figure 82: Difference between reconstructed and simulated Higgs masses for $m_H = 260$ GeV (black histogram); the fit to a Crystal Ball distribution is shown in red line.

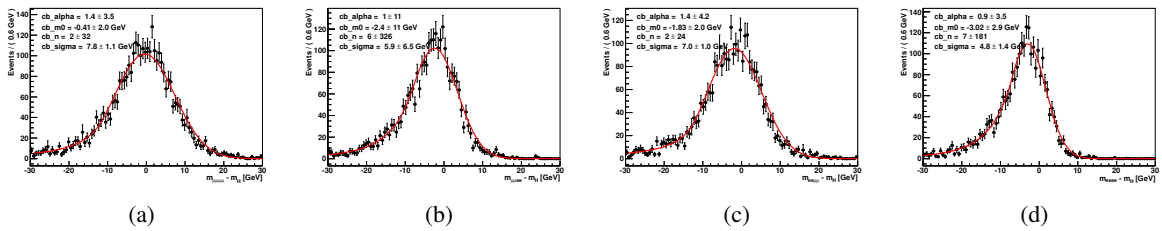


Figure 83: Difference between reconstructed and simulated Higgs masses for $m_H = 360$ GeV (black histogram); the fit to a Crystal Ball distribution is shown in red line.

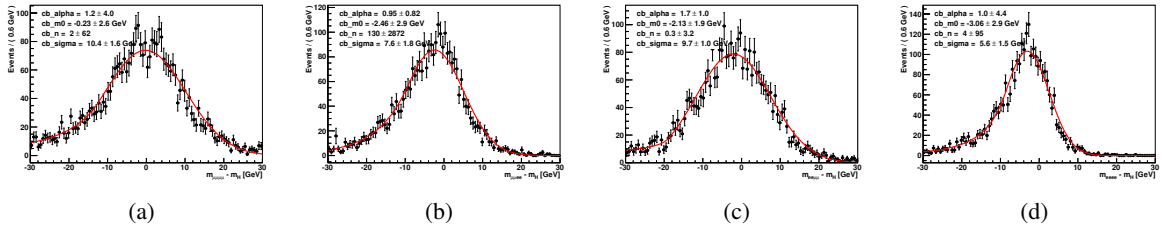


Figure 84: Difference between reconstructed and simulated Higgs masses for $m_H = 460$ GeV (black histogram); the fit to a Crystal Ball distribution is shown in red line.

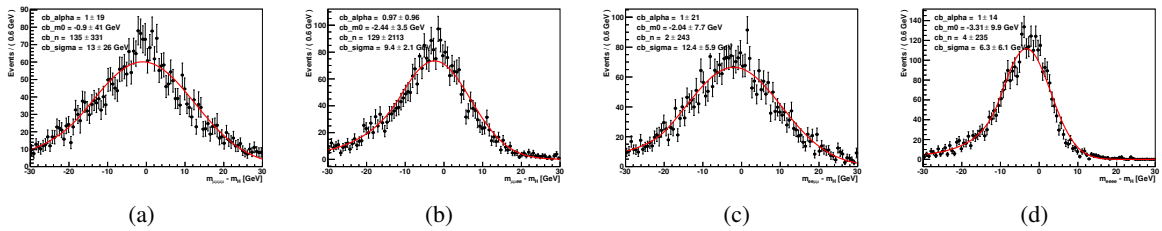


Figure 85: Difference between reconstructed and simulated Higgs masses for $m_H = 600$ GeV (black histogram); the fit to a Crystal Ball distribution is shown in red line.

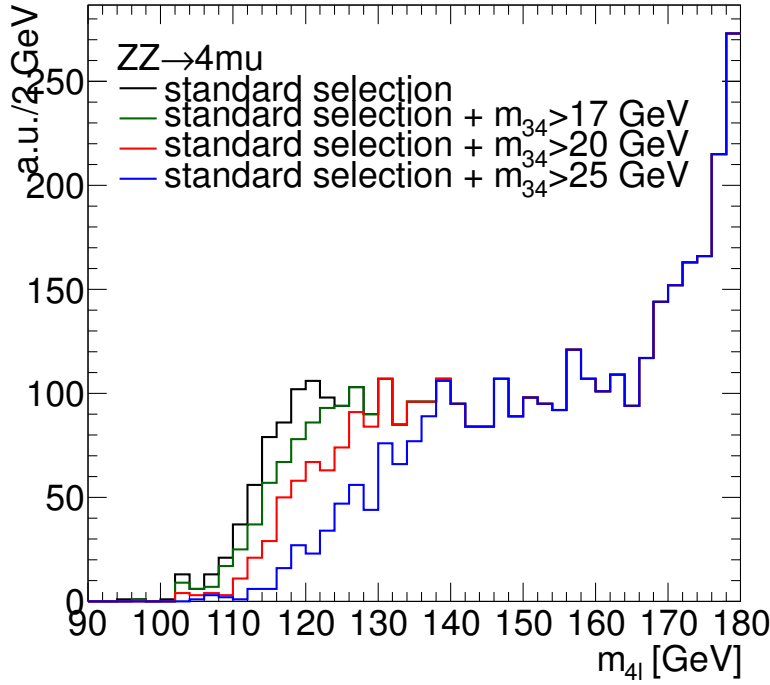


Figure 86: Effect of the m_{34} threshold to the $ZZ \rightarrow 4\mu$ mass spectrum.

H Additional selection on electrons (efficiency determination with tag-and-probe)

The efficiencies of the electron isolation and impact parameter cuts are computed using a tag-and-probe approach (described below).

Data samples For the data, a luminosity of $\sim 4.4 fb^{-1}$ is used from the Higgs D3PD datasets (2-lepton skimming). For the simulation, the Zee and di-jet QCD (JF17) samples is used. They were generated with Pythia and the statistics consists in 4999076 events for Zee and 9997057 events for JF17.

Electron selection For the data, the *egamma* good run list and object quality check are applied. The events are selected with the trigger items EF_e20_medium and EF_2e12_medium for period B-J, EF_e22_medium and 2e12T_medium for period K and EF_e22_medium1 and 2e12T_medium for period L-M, and we require the presence of one vertex with at least three tracks. For electrons, the reconstruction algorithm is asked to be *egamma* (author 1 or 3) and we reject electrons in the high pseudo-rapidity regions $|\eta| > 2.47$. Then, we only keep loose++ electrons with a transverse momentum greater than 10 GeV, since the p_T spectrum of electrons from the Z decay does not provide us with many candidates below 10 GeV. Finally, Z boson candidates are created by pairing oppositely charged electrons.

Tag-and-probe method We define tag electrons as tight electrons associated with a Z boson with an invariant mass in a window of 15 GeV around the nominal mass. Additionally, these electrons are supposed to be isolated $\sum p_T^{\Delta R=0.2}/p_T < 0.15$. We define probe electrons those electrons associated with

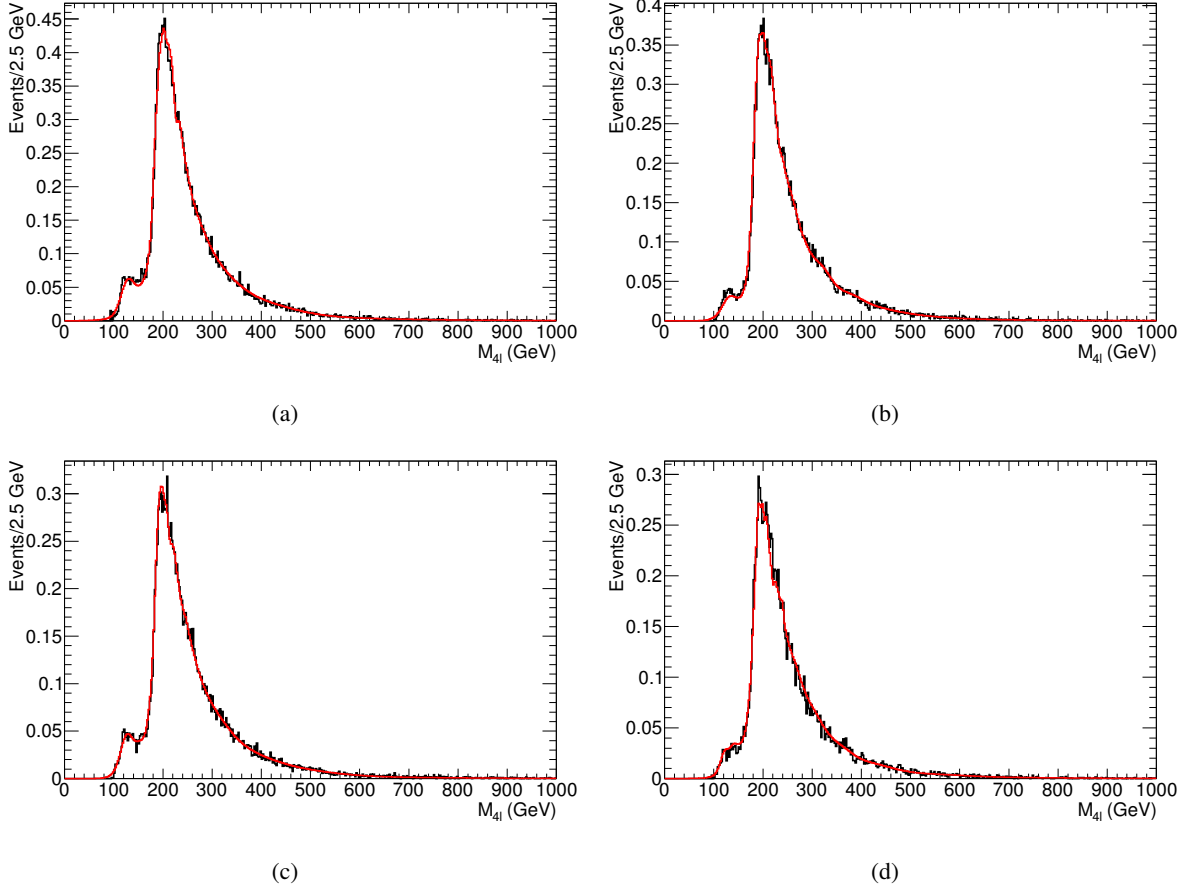


Figure 87: The $ZZ \rightarrow 4\ell$ mass spectrum as obtained by the PYTHIA simulation (black) and after the smoothing procedure (red) for the (a) 4μ , (b) $2\mu 2e$, (c) $2e 2\mu$ and (d) $4e$ final states.

a tag electron. The efficiency of the cut C is:

$$\varepsilon(C) \equiv \frac{\text{number of signal probes passing cuts}}{\text{total number of probes}}.$$

Figure 90 shows the Z invariant mass distribution for both data and simulation after selection with at least one tag electron in the electrons pairs. The contribution of JF17 is negligible and the background is extremely small.

Figures 88 and 89 show the various fits performed for the different ranges of E_T^{probe} . At lower energies the contribution from background sources is more relevant, while at high E_T^{probe} this same contribution becomes very small.

Electron isolation efficiencies In this study, the following cuts have been studied: the track isolation ($\sum p_T^{\Delta R=0.2}/p_T < 0.15$) (the contribution of overlapping leptons is removed for $\Delta R < 0.20$), the electromagnetic isolation ($\sum E_T^{\Delta R=0.2}/p_T < 0.3$) (the contribution of overlapping leptons is removed for $\Delta R < 0.18$) and the impact parameter significance ($|d_0/\sigma_{d_0}| < 6$). The results for both data and simulation are shown as a function of p_T , figure 91, η , figure 92 and N_{PV} , figure 93.

The efficiencies for the isolation cut and for the impact parameter cut are above 99%. These efficiencies decrease by few percent when moving to lower E_T electrons. In this region and in the region

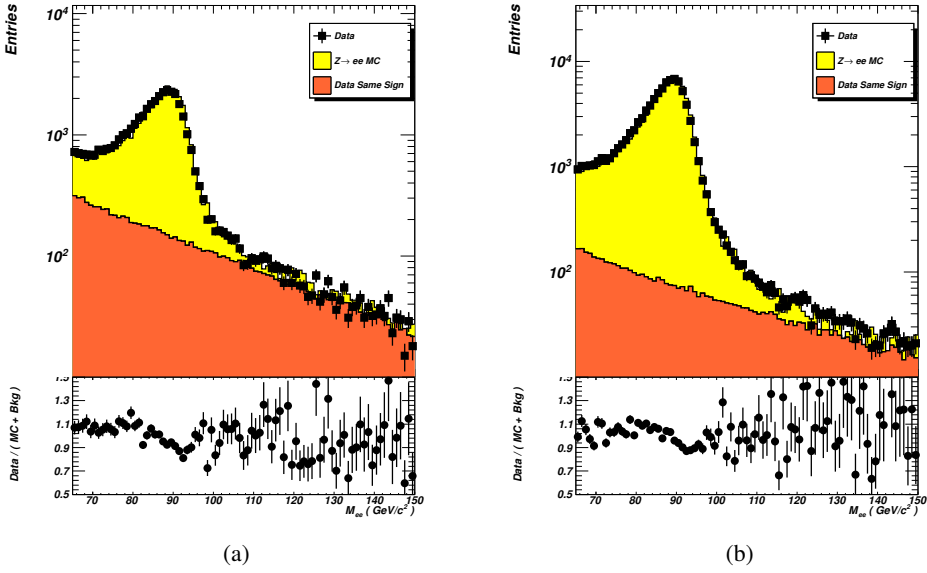


Figure 88: Invariant mass distributions for the tag and probe pairs, for Data and Monte Carlo, for $10 < E_T^{probe} < 15$ in (a) and $15 < E_T^{probe} < 20$ in (b). In orange the distribution of those events which do not pass the opposite charge requirement and are used in the fit to estimate the number of background events.

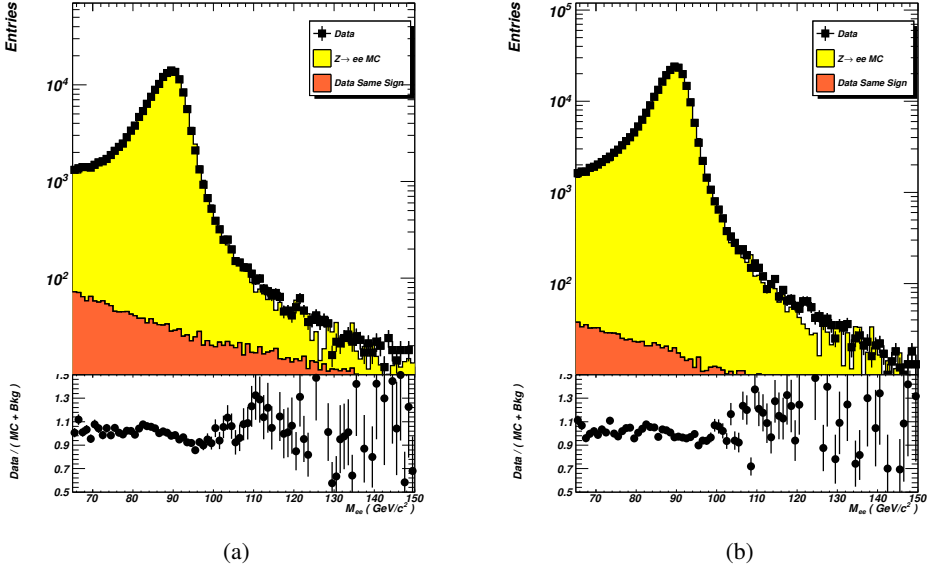


Figure 89: Invariant mass distributions for the tag and probe pairs, for Data and Monte Carlo, for $20 < E_T^{probe} < 25$ in (a) and $25 < E_T^{probe} < 30$ in (b). In orange the distribution of those events which do not pass the opposite charge requirement and are used in the fit to estimate the number of background events.

$1.52 < |\eta| < 2.01$ some disagreements are observed between data and Monte-Carlo.

At a luminosity $\mathcal{L} > 10^{33} \text{ cm}^{-2} \text{s}^{-1}$, the pileup effect has to be considered. It is known that the track isolation is not affected, the electromagnetic isolation has been chosen in order to minimize the pileup effects. Figure 93 shows the efficiencies as a function of the number of primary vertices with at least two

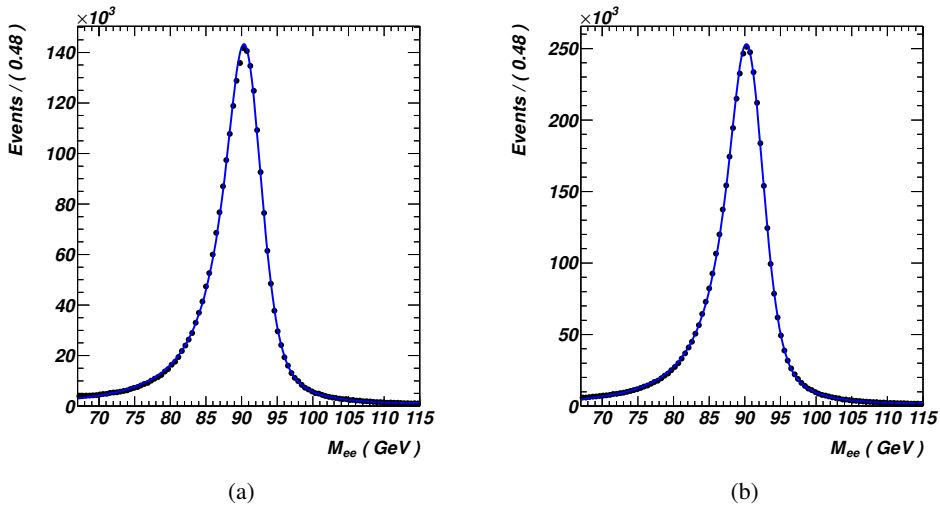


Figure 90: Z invariant mass distribution for both data (a) and simulation (b) after selection with at least one tag electron.

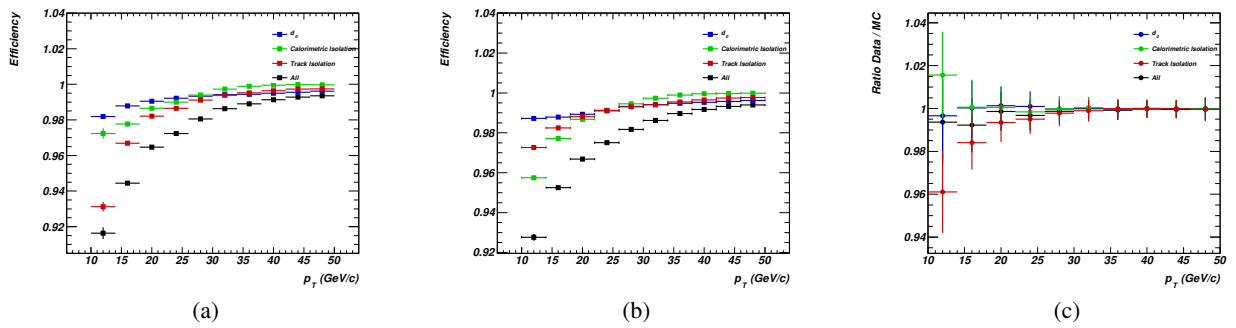


Figure 91: Efficiencies vs p_T , data (a), MC (b) and Data/MC ratio (c).

primary tracks.

Conclusion The integrated efficiencies are always greater than 99% for the isolation cuts and for the impact parameter cut. The combination of these three cuts gives us an overall efficiency which is just below 99%. The overall agreement between Data and Monte Carlo appears to be good, as shown by the ratio of efficiencies in Data and Monte Carlo, especially as a function of η and the number of primary vertices.

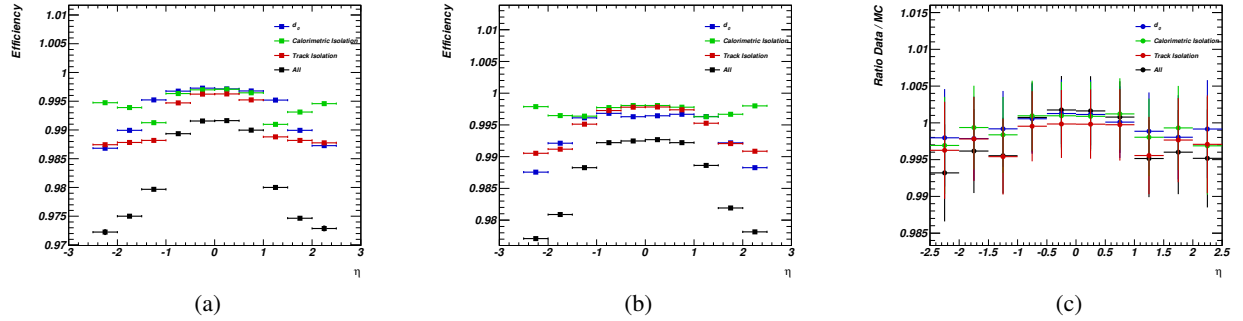


Figure 92: Efficiencies vs η , data (a), MC (b) and Data/MC ratio (c).

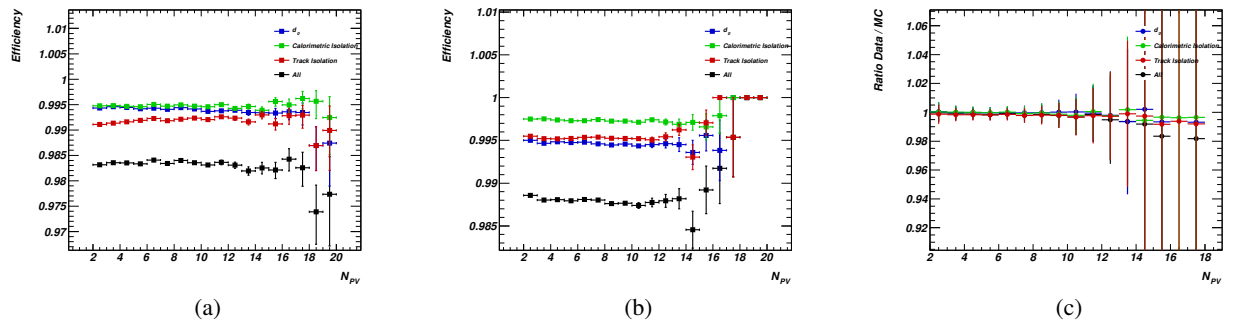


Figure 93: Efficiencies vs number of primary vertices, data (a), MC (b) and Data/MC ratio (c).

I Additional selection on muons (efficiency determination with tag and probe)

I.1 Combined or segment-tagged muons

The muon isolation and impact parameter cuts for signal-like muons have been derived using a similar Tag and Probe approach as described in the previous section. The selection criteria under study are $\Sigma p_T/p_T < 0.15$ (track isolation), $\Sigma E_T/E_T < 0.3$ (calorimeter isolation) and $d_0/\sigma_{d_0} < 3.5$ (transverse impact parameter significance). For both the track and calorimetric isolation a cone of 0.2 around the muon has been used. This study is performed on the 4.48 fb^{-1} 2011 data and several Monte Carlo samples both for the signal ($Z \rightarrow \mu^+ \mu^-$ generated by Alpgen) and the backgrounds. For the latter a $t\bar{t}$ sample generated by MC@NLO and a $Z \rightarrow \tau^+ \tau^-$ one generated by Alpgen have been used. All Monte Carlo samples correspond to 50 ns of bunch spacing configuration.

In an attempt to study the efficiency of signal-like muons with as low as possible p_T , different p_T intervals for the probe muon are used down to 7 GeV. In this low p_T region there is considerable contribution from QCD background processes. For the Tag and Probe method, the highest p_T muon selected as the Tag one is required to be a combined one satisfying the MCP requirements (Section 3), with $p_T > 20 \text{ GeV}$ and longitudinal impact parameter with respect to the primary vertex less than 10 mm in order to reduce the background contribution.

The Probe muon is the remaining highest- p_T muon, either combined or segment tagged satisfying the MCP requirements. For background rejection it is also required to have $p_T > 7 \text{ GeV}$ and longitudinal impact parameter with respect to the primary vertex less than 10 mm. Dimuon pairs are formed (Tag and Probe) with an opposite charge combination and their invariant mass distribution is used to estimate the selection criteria efficiency on the probe muon.

The resulting mass distributions for every probe p_T bin are fitted using a shape template from the $Z \rightarrow \mu^+ \mu^-$ Monte Carlo sample to describe the signal, including the smearing MCP corrections. To describe the QCD background, templates from the same charge combination invariant mass distribution are being used while templates from the $Z \rightarrow \tau^+ \tau^-$ and $t\bar{t}$ Monte Carlo samples are also taken into account. The latter background contributions are normalized to the luminosity used, before and after applying the selection criteria separately and the QCD normalization is left free in the combined fit in the mass range 66-116 GeV. In order to estimate the efficiency, only a mass range of 3 GeV around the Z mass peak is considered in order to introduce as less as possible uncertainties due to the background estimation.

The results of the fits on the opposite and same charge combination invariant mass distributions are presented for all probe p_T bins in the Figures 94 to 102 in the case of the track isolation cut (4.48 fb^{-1}). The blue dashed line corresponds to the QCD estimation using the same charge templates from the data. The red dashed line corresponds to the estimated $Z \rightarrow \tau^+ \tau^-$ and the green one to the $t\bar{t}$ contribution. The combination of all the templates is shown with the continuous blue line. The combination of the templates is in agreement with the data in all probe p_T bins.

The resulting efficiency estimation can be seen in Figure 103(a) for both data and Monte Carlo while for the calorimetric isolation and the d_0 significance, the corresponding results are shown in Figures 103(b) and 103(c) and in Figure 103(d) for the simultaneous appliance of all three cuts. In Table 40 the efficiencies of the cuts along with the efficiency ratio for data and Monte Carlo are presented and in Figure 104 the scale factors are presented. All results correspond to 4.48 fb^{-1} luminosity data.

In Figures 103 and 104 the color bands correspond to the systematic uncertainties. In order to estimate them a larger range has been considered for the calculation of the efficiency (10 GeV around the Z peak), a broader fitting range has been used (56-126 GeV) and a Pythia generated $Z \rightarrow \mu^+ \mu^-$ Monte Carlo sample has been taken into account. The systematics study has been performed in detail in earlier

Table 40: Selection criteria efficiencies and their ratio between data (4.48 fb^{-1}) and Monte Carlo.

probe p_T (GeV)	Track Isolation			Calorimeter Isolation			d_0 significance			all three		
	Data	MC	ratio	Data	MC	ratio	Data	MC	ratio	Data	MC	ratio
7 - 12	0.973	0.965	1.009	0.994	0.983	1.011	0.994	0.988	1.006	0.965	0.952	1.014
12 - 15	0.979	0.976	1.003	0.995	0.987	1.008	0.992	0.988	1.004	0.969	0.965	1.005
15 - 20	0.987	0.983	1.003	0.998	0.991	1.007	0.991	0.991	1.000	0.976	0.975	1.001
20 - 25	0.989	0.987	1.002	0.997	0.994	1.004	0.993	0.992	1.001	0.981	0.981	1.001
25 - 30	0.993	0.991	1.003	0.999	0.996	1.003	0.993	0.993	1.000	0.986	0.985	1.001
30 - 35	0.995	0.994	1.001	0.999	0.997	1.002	0.994	0.993	1.000	0.988	0.988	1.000
35 - 40	0.998	0.997	1.001	1.000	0.998	1.001	0.993	0.994	0.999	0.991	0.991	0.999
40 - 45	0.999	0.998	1.001	1.000	0.999	1.001	0.993	0.994	0.999	0.992	0.993	0.999
45 - 50	0.999	0.996	1.003	1.000	0.997	1.003	0.994	0.993	1.001	0.993	0.992	1.002

documents (support note from eps cite).

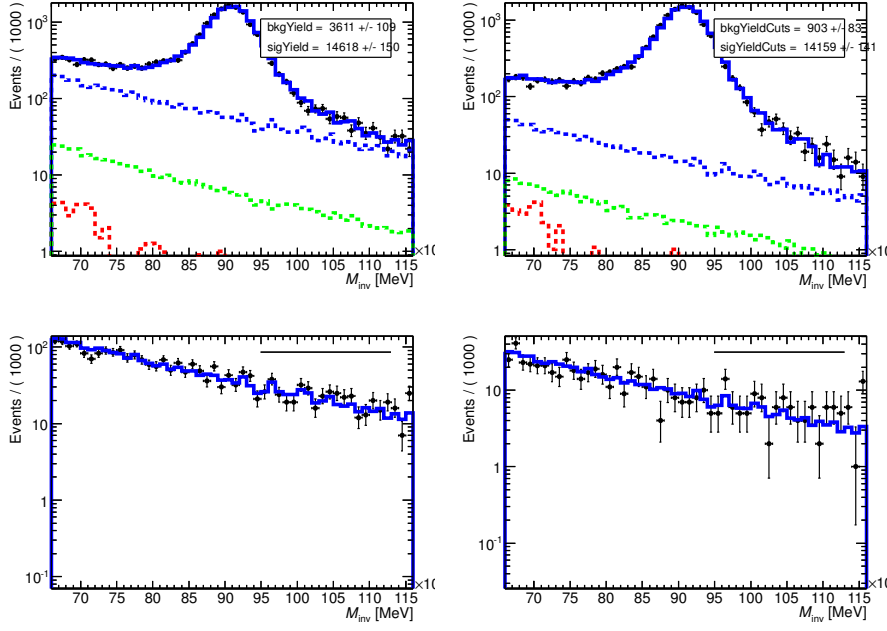


Figure 94: Invariant mass distributions for the opposite sign muon pairs (top plots) and same sign ones (bottom plots) before (left plots) and after (right plots) applying the track isolation cut, using the Tag and Probe method for the probe pt bin 7 to 12 GeV (4.48 fb^{-1}).

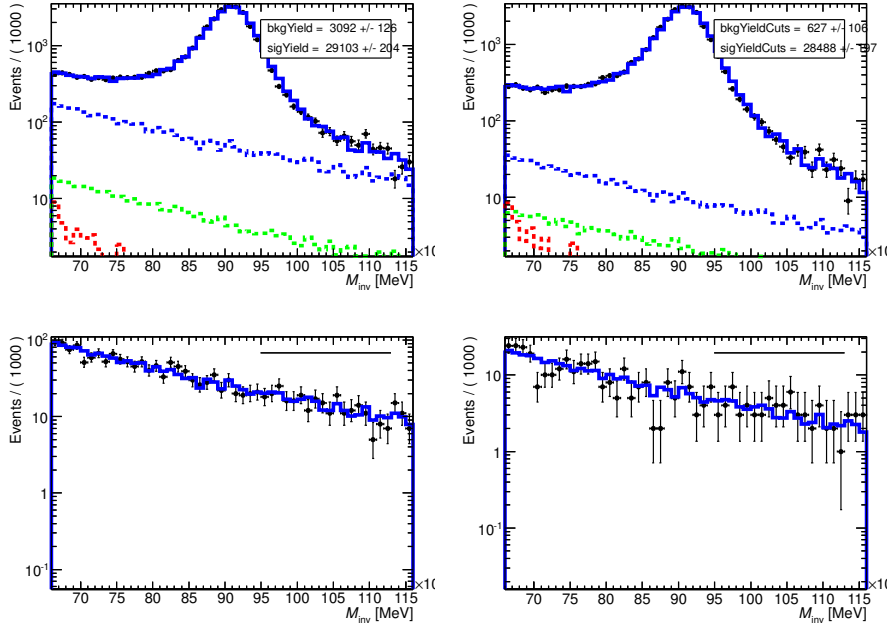


Figure 95: Invariant mass distributions for the opposite sign muon pairs (top plots) and same sign ones (bottom plots) before (left plots) and after (right plots) applying the track isolation cut, using the Tag and Probe method for the probe pt bin 12 to 15 GeV (4.48 fb^{-1}).

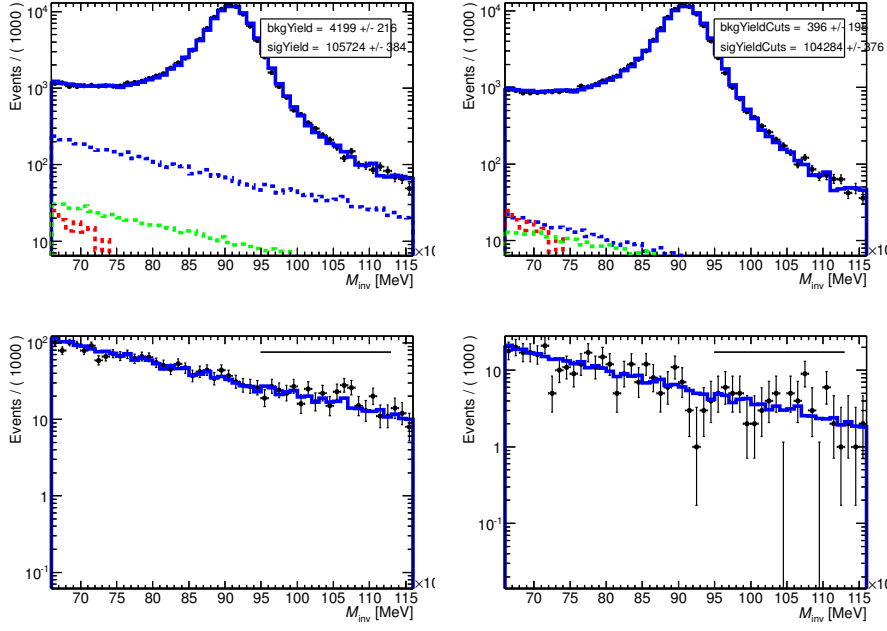


Figure 96: Invariant mass distributions for the opposite sign muon pairs (top plots) and same sign ones (bottom plots) before (left plots) and after (right plots) applying the track isolation cut, using the Tag and Probe method for the probe p_t bin 15 to 20 GeV (4.48 fb^{-1}).

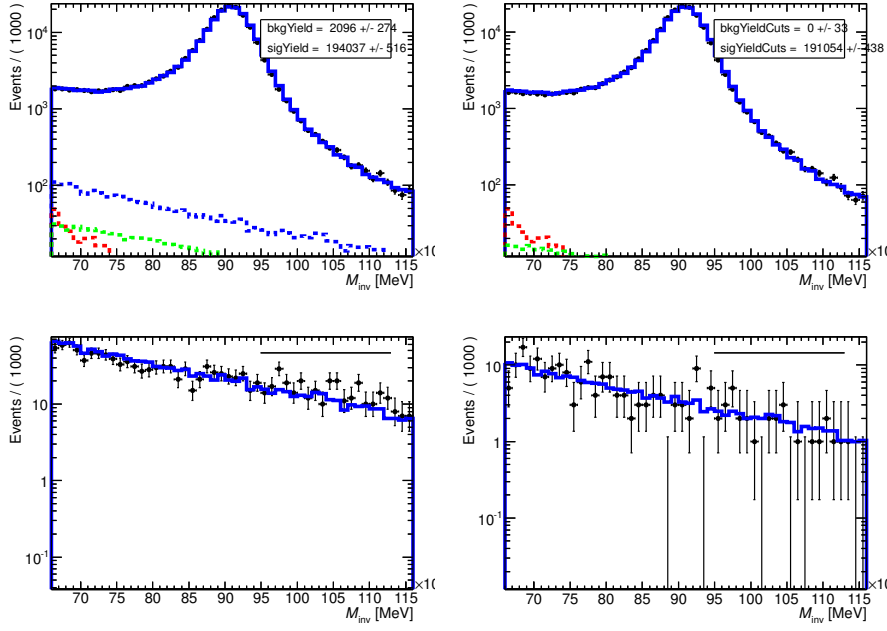


Figure 97: Invariant mass distributions for the opposite sign muon pairs (top plots) and same sign ones (bottom plots) before (left plots) and after (right plots) applying the track isolation cut, using the Tag and Probe method for the probe p_t bin 20 to 25 GeV (4.48 fb^{-1}).

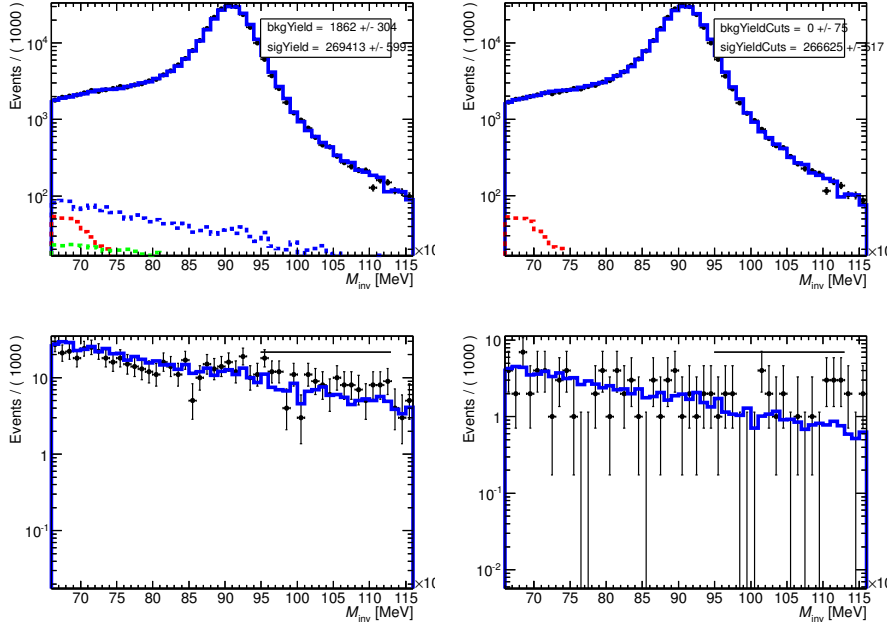


Figure 98: Invariant mass distributions for the opposite sign muon pairs (top plots) and same sign ones (bottom plots) before (left plots) and after (right plots) applying the track isolation cut, using the Tag and Probe method for the probe pt bin 25 to 30 GeV (4.48 fb^{-1}).

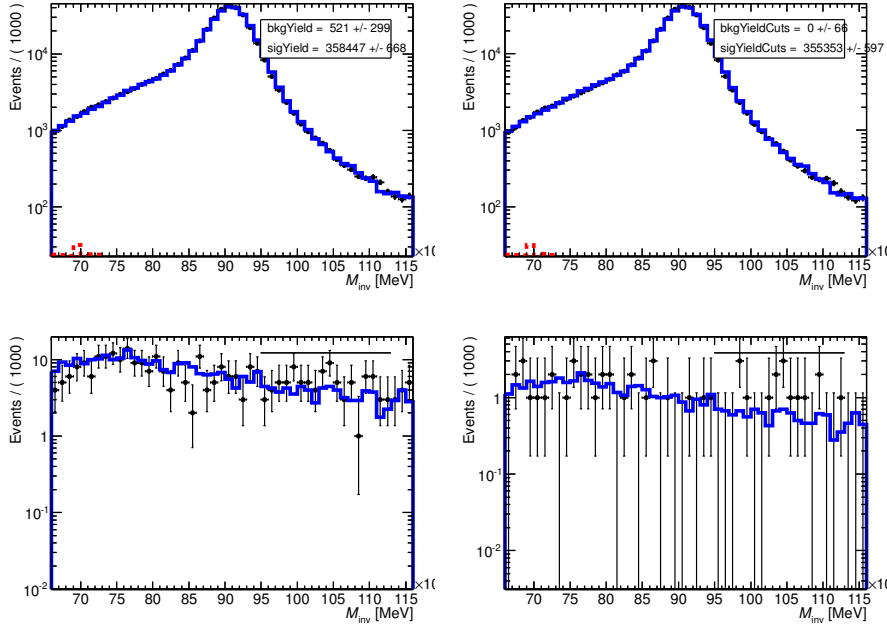


Figure 99: Invariant mass distributions for the opposite sign muon pairs (top plots) and same sign ones (bottom plots) before (left plots) and after (right plots) applying the track isolation cut, using the Tag and Probe method for the probe pt bin 30 to 35 GeV (4.48 fb^{-1}).

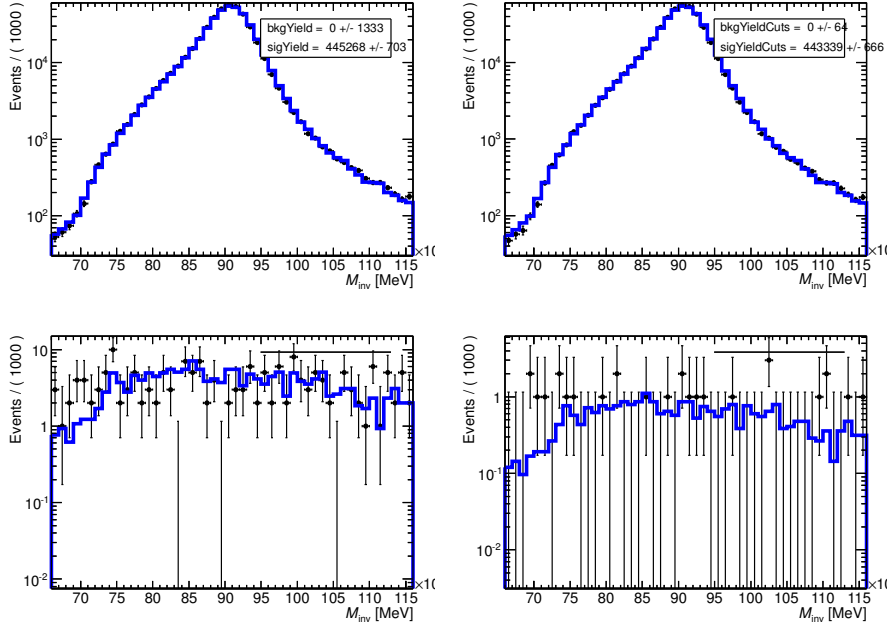


Figure 100: Invariant mass distributions for the opposite sign muon pairs (top plots) and same sign ones (bottom plots) before (left plots) and after (right plots) applying the track isolation cut, using the Tag and Probe method for the probe pt bin 35 to 40 GeV (4.48 fb^{-1}).

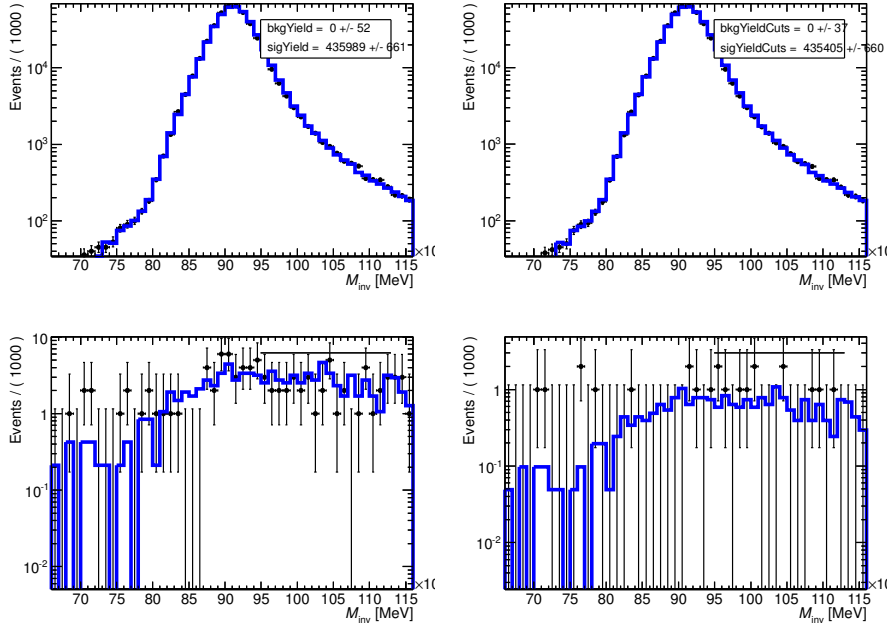


Figure 101: Invariant mass distributions for the opposite sign muon pairs (top plots) and same sign ones (bottom plots) before (left plots) and after (right plots) applying the track isolation cut, using the Tag and Probe method for the probe pt bin 40 to 45 GeV (4.48 fb^{-1}).

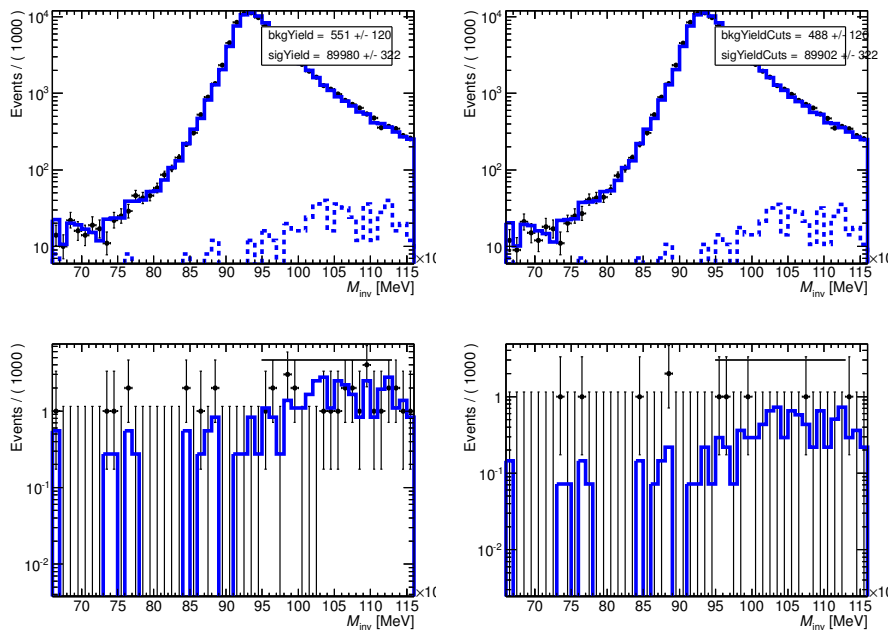


Figure 102: Invariant mass distributions for the opposite sign muon pairs (top plots) and same sign ones (bottom plots) before (left plots) and after (right plots) applying the track isolation cut, using the Tag and Probe method for the probe pt bin 45 to 50 GeV (4.48 fb^{-1}).

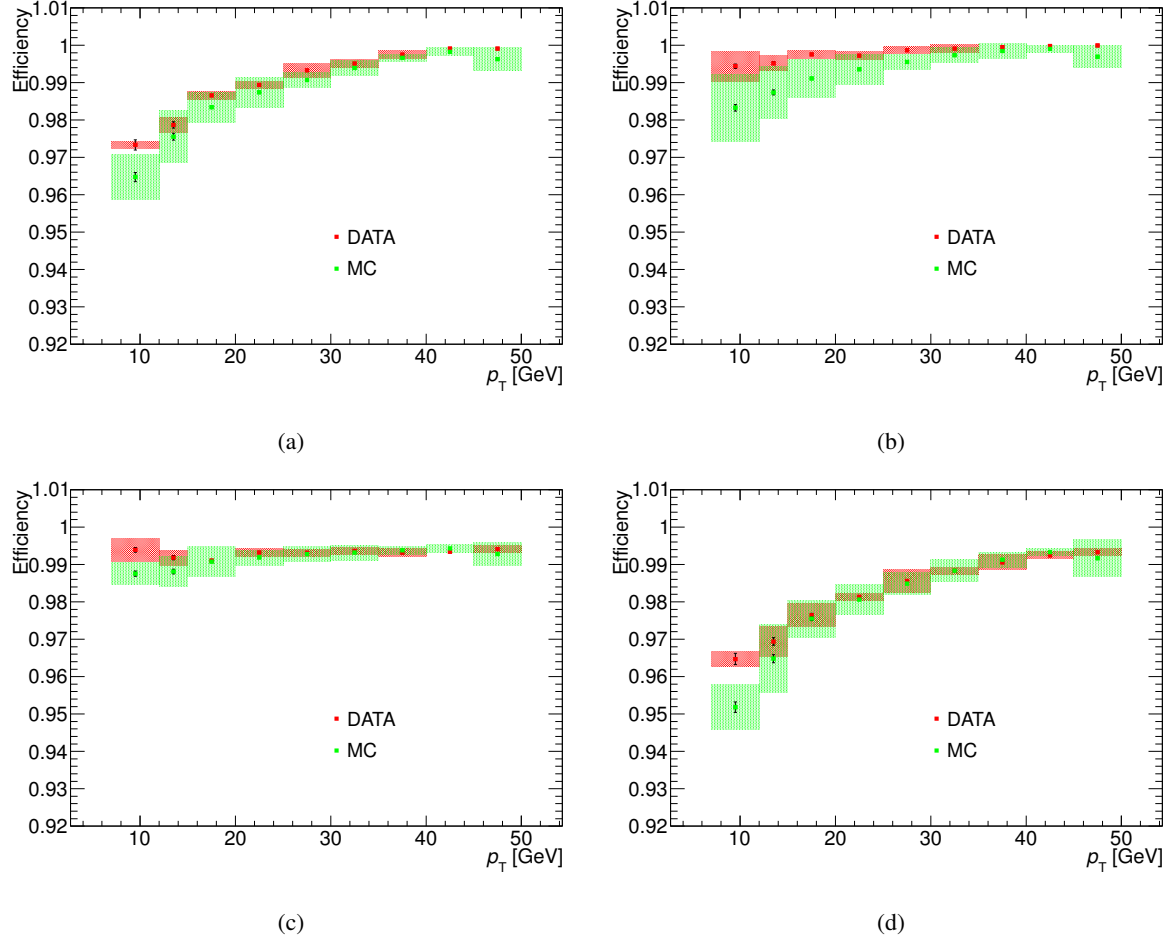


Figure 103: Probe muon efficiencies as function of the transverse momentum of the probe muon for both data and Monte Carlo for (a) the track isolation cut of 0.15 using a cone of 0.2, (b) the calorimeter isolation cut of 0.3 using a cone of 0.2, (c) the d_0 impact parameter cut of 3.5 and (d) all three cuts combined (4.48 fb^{-1}).

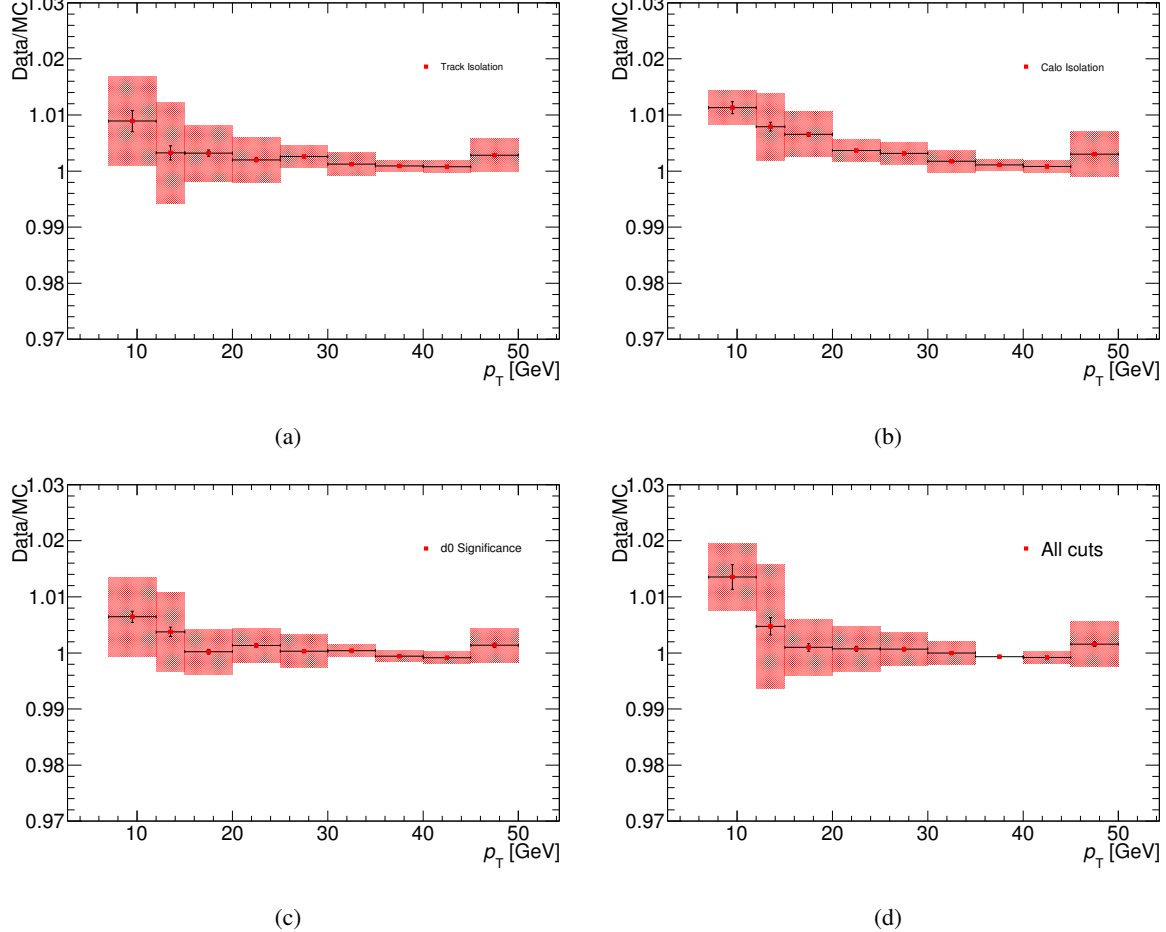


Figure 104: Scale factors for the efficiencies as function of the transverse momentum of the probe muon for both data and Monte Carlo for (a) the track isolation cut of 0.15 using a cone of 0.2, (b) the calorimeter isolation cut of 0.3 using a cone of 0.2, (c) the d_0 impact parameter cut of 3.5 and (d) all three cuts combined (4.48 fb^{-1}).

J Trigger

The turn-on curves for the single-lepton triggers used in the analysis in the different data taking periods are shown in Figure 105 and 106 for the electron and muon triggers respectively. The efficiencies are computed with respect to true electrons and muons in a MC signal sample, for an Higgs mass of 130 GeV.

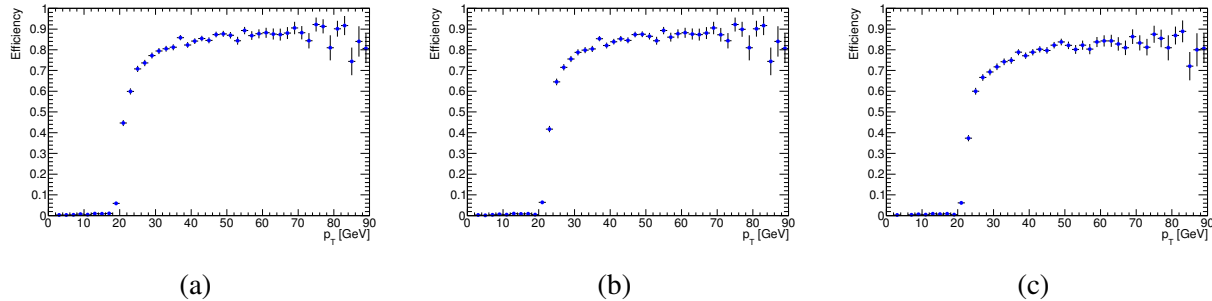


Figure 105: Efficiencies vs E_T of the trigger: EF_e20_medium (a), EF_e22_medium (b), EF_e22_medium1 (c)

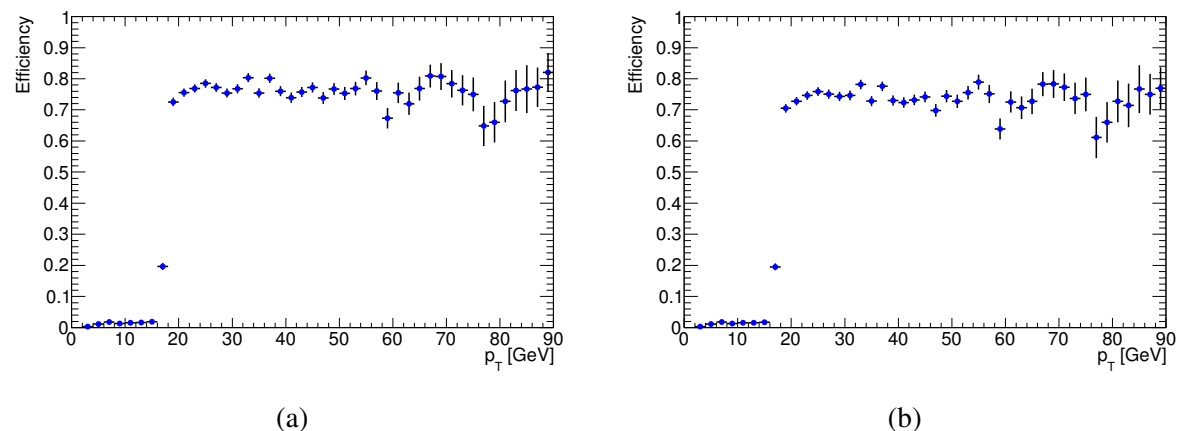


Figure 106: Efficiencies vs p_T of the trigger: EF_mu18_MG (a) and EF_mu18_MG_medium.

MC events are reweighted to account for differences in the efficiencies with respect to those measured on real data. Efficiencies in real data are measured with tag-and-probe methods, using $Z \rightarrow \mu\mu$ and $Z \rightarrow ee$ events. The event weight is calculated on the basis of the single-lepton efficiencies, combining them according to the formula:

$$w = \frac{[1 - \Pi(1 - \epsilon_i)]_{\text{Data}}}{[1 - \Pi(1 - \epsilon_i)]_{\text{MC}}} \quad (3)$$

where the product runs over all leptons selected for the analysis. The distributions of the event weights for the four channels are shown in Figure 107

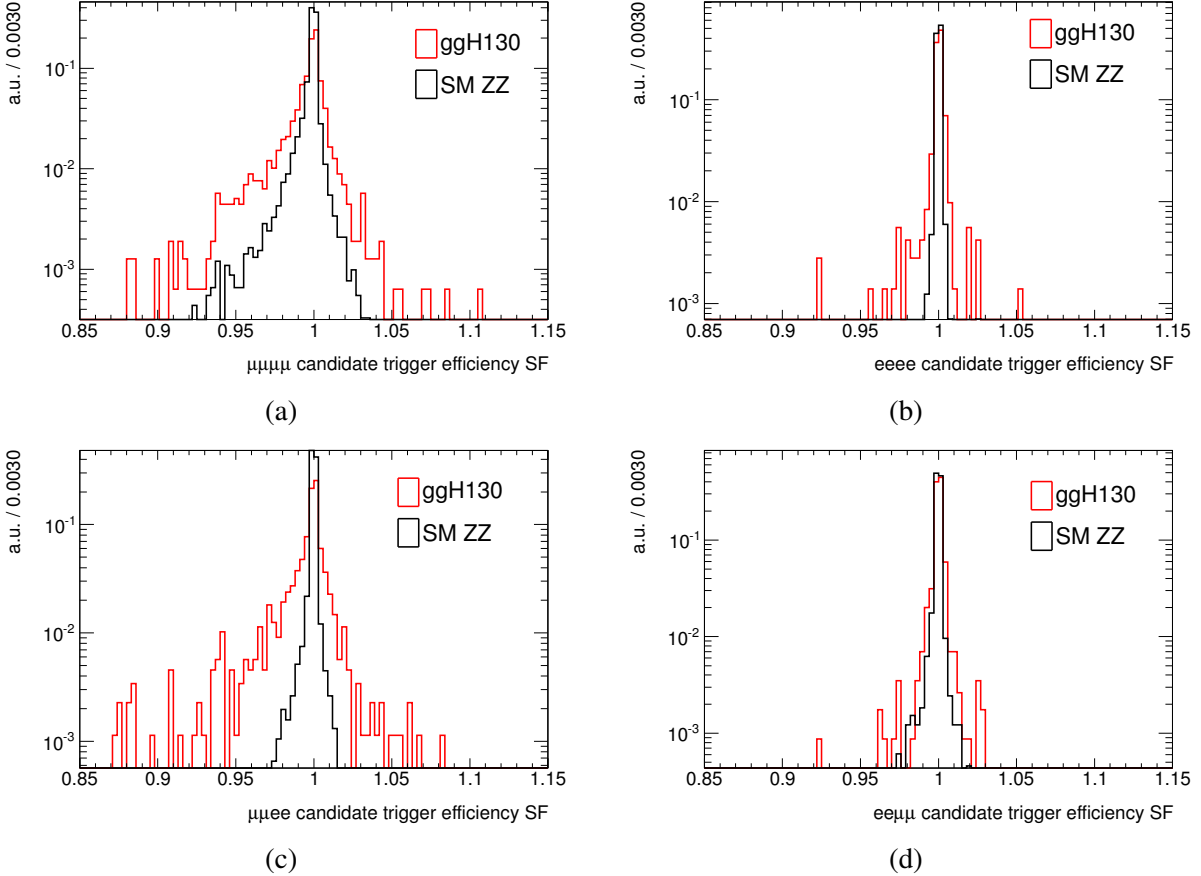


Figure 107: Distributions of the trigger weights for the signal (130 GeV Higgs) and the $ZZ^{(*)}$ background. The weights shown are for: (a) the 4μ channel, (b) the $4e$ channel, (c) the $2\mu 2e$ channel and (d) the $2e 2\mu$ channel.

K List of candidates

The number of events observed in each final state, separately for $m_{4\ell} < 180$ GeV and $m_{4\ell} \geq 180$ GeV, compared with the expectations for background and signal for various m_H hypotheses are shown in Table 24. In total 71 candidate events are selected by the analysis: 24 4μ , 30 $2e2\mu$, and 17 $4e$ events, while in the same mass range 62 ± 9 events are expected from the background processes. In Table 41, Table 42 and Table 43 the list of the candidates for the three final states (4μ , $2e2\mu$ and $4e$), respectively, can be found.

In Table 44 and Table 45 information on the three low mass candidates with $m_{4\ell} < 130$ GeV are presented.

The low mass electron-positron pair for the $2\mu2e$ event in run 186877 has been examined in detail. More information for this pair is provided in Table Table 46. Both the electron and positron only pass the loose++ identification, and the positron falls in the crack between the barrel and the endcap calorimeters. The electron passes all tight cuts except the strips width cut (wstot): its value of 2.90 is close to the tight++ cut value 2.80 (cut values are 3.20/2.85 for loose++/medium++). The positron in the crack is a good electron in terms of the tracker: it has a TRT high threshold value 0.256 well above the tight cut 0.115, and as well, the track fit with the Gaussian Sum Filter (GSF) gives a difference of the momentum at the end of the track relative to the momentum at the perigee ($\delta p/p$) of 0.56 where the distribution for pions at this momentum peaks at 0.15 and falls to 0 at 0.4. This is a good indication of Bremsstrahlung along the trajectory of the reconstructed track. For the rest of the identification criteria, the positron fails the tight $\delta\eta$ and $\delta\phi$ cuts. These are the difference in η and ϕ of the electron after extrapolation to the first (for η) and second (for ϕ) samplings. For $\delta\eta$, the value is 0.012 (tight++ cut is at 0.005) and is in the tail of the distribution for corresponding Monte Carlo electrons in the crack. For the $\delta\phi$, the value is -0.08 which is as well in the tail of the corresponding Monte Carlo distribution. The $\delta\phi$ offset is primarily due to the poor E/p which is 2.7 (tight++ cut is at 2.5). One can check that this is due to an undetected early Brem, most likely in the pixels, by extrapolating the track after rescaling the momentum to the measure cluster energy. This gives a $\delta\phi$ of 0.20 which is close to the tight++ cut of 0.015. Finally, the percentage energy distribution of the electron in the crack is: 42/15/10/34 for the presampler/sampling1/sampling2/scintillator. The large energy fraction in the presampler and the scintillor are due to the important amount of material before the calorimeter and in the crack. For example, the presampler has typically 10% of the energy in the barrel. This distribution agrees well with that seen in the Monte Carlo for electrons in the crack. So in conclusion, this looks like an electron-positron pair even if the positron falls into the more difficult to measure region between barrel and endcap.

N	RunNumber	Event Number	LB	Mass 4ℓ	Mass Z1	Mass Z2
1	182284	91584073	745	277.75	90.86	98.34
2	182486	33852510	282	208.55	83.81	76.93
3	182766	5404925	213	242.96	91.12	85.35
4	183003	44433120	385	222.18	93.75	100.62
5	183003	121099951	723	603.48	85.9	99.69
6	183391	19834577	303	204.93	97.5	82.48
7	183426	47756740	317	455.32	89.57	94.32
8	183602	282919	20	239.69	89.18	88.03
9	184130	194694606	1304	182.9	93.31	76.79
10	186156	65491657	381	234.42	89.91	86.33
11	187219	88203394	476	372.2	89.14	93.96
12	189207	79774710	330	250.69	89.65	87.96
13	189207	81313827	338	171.92	83.92	62.12
14	189280	82801561	439	208.74	87.9	85.3
15	189280	128083498	640	220.63	91.06	92.55
16	189280	143576946	713	124.56	89.7	24.57
17	189561	20659041	117	207.3	91.92	73.42
18	189693	10714212	266	209.64	92.2	87.37
19	189822	75634934	460	216.97	102.37	71.6
20	190116	60445481	341	199.76	91.93	88.76
21	190300	60554334	325	145.75	94.3	29.68
22	190872	52781235	212	264.18	91.04	91.54
23	191426	60906769	447	226.47	91.61	93.19
24	191676	1888359	380	485.53	91.27	96.94

Table 41: List of the 4μ candidates passing the full selection, for an average luminosity of 4.8 fb^{-1} .

N	RunNumber	Event Number	LB	Mass 4ℓ	Mass Z1	Mass Z2
1	183426	50303812	330	251.85	84.37	104.75
2	186399	14250520	331	325.12	91.27	93.06
3	186877	84622334	602	123.64	89.31	30.02
4	187014	105211056	963	291.89	91.36	89.76
5	189242	7233912	57	158.2	102.43	46.89
6	189561	105481981	570	214.15	88.6	87.11
7	189781	8619753	57	568.1	91.67	90.07
8	190878	57044890	309	200.22	91.53	92.8
9	190975	62905396	449	268.19	90.2	101.85
10	191218	1072214	9	250.57	93.23	87.09
11	191428	25718643	213	236.44	92.07	97.76
11	179710	25946709	422	234.52	90.48	92.76
12	180636	71391739	407	242.86	90.87	86.11
13	180710	37143864	561	247.28	92.59	94.22
14	182747	63217197	281	209.19	85.59	85.46
15	182796	74566644	413	124.35	76.84	45.67
16	183407	136901836	930	188.95	90.02	93.35
17	183462	75344317	798	486.79	92.37	86.9
18	186877	12509901	232	190.99	90.14	93.98
19	186923	96974859	507	238.71	85.95	82.8
20	189483	1021987	10	460.22	92.5	105.13
21	189719	37988693	382	314.72	89.11	88.58
22	190046	8638208	105	267.07	87.87	87.23
23	190300	17344710	114	321.7	91.54	91.95
24	190878	50034828	274	210.88	90.24	92.18
25	190975	20471852	272	281.41	90.64	89.06
26	191138	15762515	64	199.43	88.09	80.24
27	191150	5742674	170	244.96	92.21	92.62
28	191150	45707611	308	221.54	90.63	96.55
29	191190	76273161	513	209.87	87.92	82.26

Table 42: List of the $2e2\mu$ candidates passing the full selection, for an average luminosity of 4.8 fb^{-1} .

N	RunNumber	Event Number	LB	Mass 4ℓ	Mass Z1	Mass Z2
1	182787	35518831	265	196.03	93.17	85.77
2	183216	75692579	371	270.31	84.99	111.47
3	184022	20046902	320	245.42	92.16	99.77
4	184022	78541915	625	493.98	92.46	84.83
5	186216	36894463	176	157.55	81.29	36.02
6	186216	10253640	49	264.38	91.13	90.06
7	186729	203362752	1004	199.68	89.46	83.95
8	186934	65787798	649	230.68	89.96	87.8
9	187453	34960141	622	225.99	90.21	93.77
10	187552	3744932	16	331.2	91.06	86.72
11	187763	83732606	528	172.0	89.84	76.9
12	189483	33468656	145	238.38	86.74	68.4
13	189751	51800361	355	184.89	90.52	88.63
14	190933	99272087	804	426.16	91.59	94.19
15	191138	17388332	70	194.61	90.53	100.16
16	191139	5871977	305	202.26	84.34	99.15
17	191635	2200900	568	315.01	89.49	101.99

Table 43: List of the 4e candidates passing the full selection, for an average luminosity of 4.8 fb^{-1} .

type	RunNumber	LB	EventNumber	LAr error	Pileup	$m_{4\ell}$	m_{12}	m_{34}	missing E_T
4μ	189280	713	143576946	0	7	124.6	89.7	24.6	34.5
$2\mu 2e$	186877	602	84622334	0	2	123.6	89.3	30.0	9.1
$2e 2\mu$	182796	413	74566644	0	8	124.3	76.8	45.7	19.9

Table 44: List of the four lepton candidates passing the full selection, for an average luminosity of 4.8 fb^{-1} in the low mass region.

[Not reviewed, for internal circulation only]

Type	Run	Event	ℓ	Charge	p_T	η	ϕ	Track Isolation	Calorimeter Isolation	d_0/σ_{d_0}	Quality
4μ	189280	143576946	μ	-1	61.2	-0.66	0.93	0.0	0.002	1.00	combined
			μ	+1	33.1	-0.69	-2.38	0.0	0.031	0.27	combined
			μ	+1	17.8	-0.53	-1.49	0.0	0.037	0.35	combined
$2\mu 2e$	186877	8462334	μ	-1	11.6	-1.47	0.08	0.0	-0.017	0.53	combined
			μ	-1	43.9	-0.13	0.78	0.0	0.003	1.19	combined
			e	+1	43.5	0.28	-2.34	0.0	0.011	2.61	combined
$2e 2\mu$	182796	7456644	e	+1	9.9	-1.46	1.60	0.0	0.160	3.39	loose++
			e	-1	11.2	0.32	-1.29	0.0	0.019	0.19	loose++
			e	+1	41.5	0.56	-2.77	0.037	0.033	0.52	tight++

Table 45: List of the four lepton candidates passing the full selection, for an average luminosity of 4.8 fb^{-1} in the low mass region.

Type	Run	Event	ℓ	Charge	p_T	η	ϕ	cluster η	Track p_T	nBL	nPix	nSCT	nTRT	TRT HighThresh	dP/p
$2\mu 2e$	186877	84622334	e	+1	9.9	-1.46	1.60	-1.48	3.7	1	3	8	39	0.256	0.56
			e	-1	11.2	0.32	-1.29	0.25	9.1	2	4	9	37	0.189	0.07

Table 46: Further characteristics of the electrons for the low mass $2\mu 2e$ candidate.

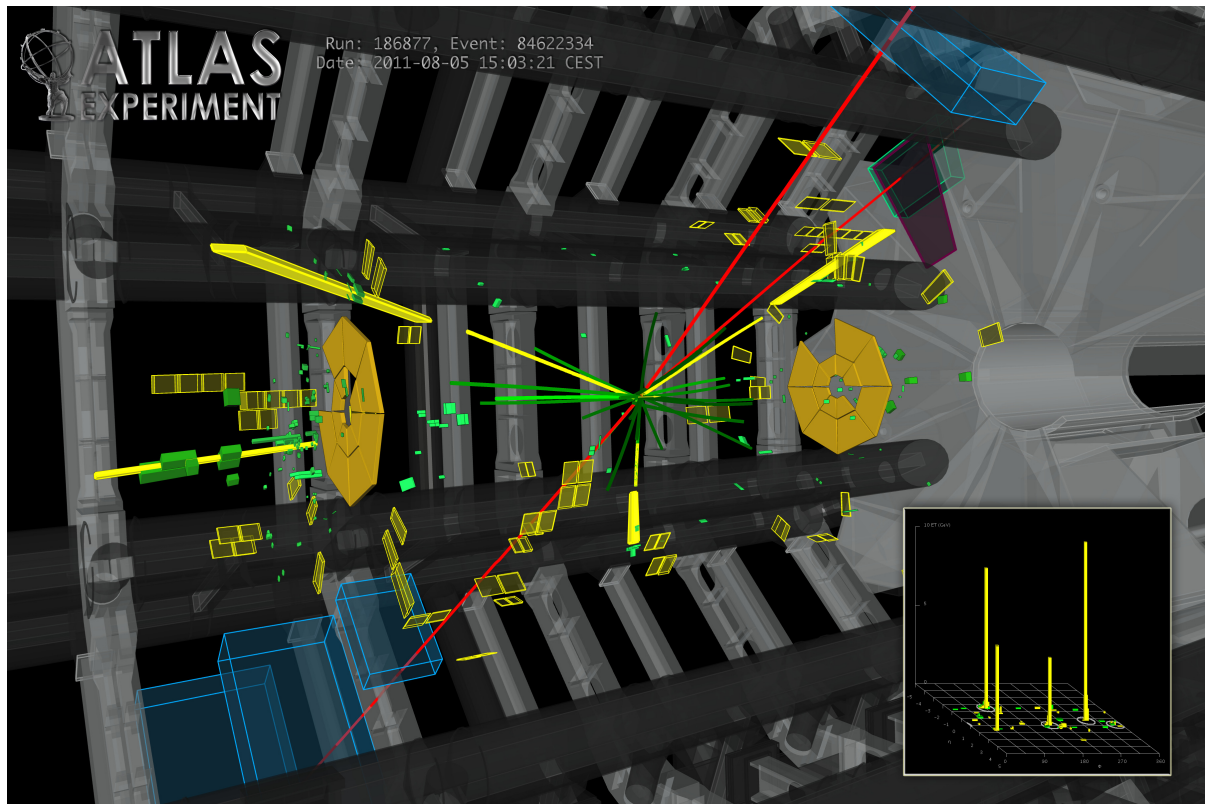


Figure 108: Event display of a $2\mu 2e$ candidate event with $m_{4l} = 123.6$ GeV. The masses of the lepton pairs are 89.3 and 30.0 GeV respectively.

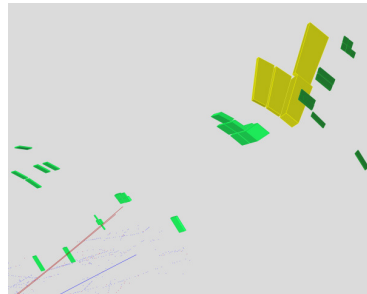


Figure 109: Event display of a $2\mu 2e$ candidate event with $m_{4l} = 123.6$ GeV in a x-y view. The masses of the lepton pairs are 89.3 and 30.0 GeV respectively.

L Event displays of a few candidates

In total 71 candidate events are selected by the analysis: 24 4μ , 30 $2e 2\mu$, and 17 $4e$ events. In the following event displays of a few selected events are provided.

L.1 Low mass

Event displays for candidates in the low mass region ($m_{4l} < 150$ GeV) are shown in Figure ??, Figure 111, Figure 116, Figure 113 and Figure 115.

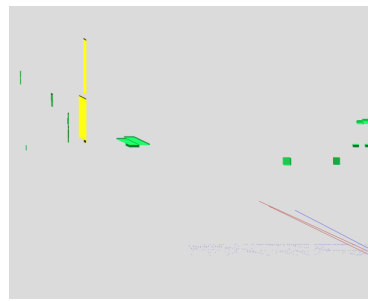
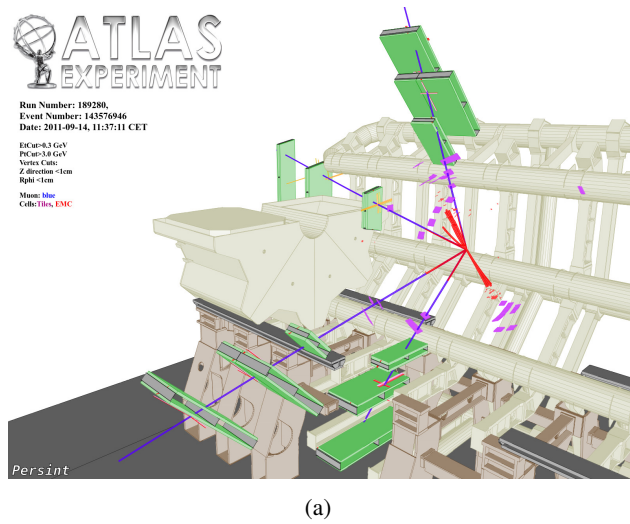
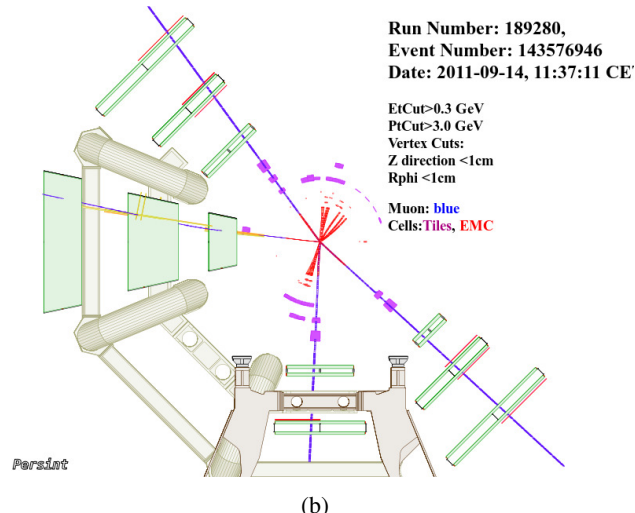


Figure 110: Event display of a $2\mu 2e$ candidate event with $m_{4\ell} = 123.6$ GeV in a x-y view. The masses of the lepton pairs are 89.3 and 30.0 GeV respectively.



(a)



(b)

Figure 111: Event display of a 4μ candidate event with $m_{4\ell} = 124.6$ GeV in a (a) lateral and (b) transverse view. The masses of the lepton pairs are 89.7 and 24.6 GeV respectively.

L.2 Intermediate mass

Event display for a candidate in the intermediate mass region ($150 \text{ GeV} < m_{4\ell} < 250 \text{ GeV}$) is shown in 117.

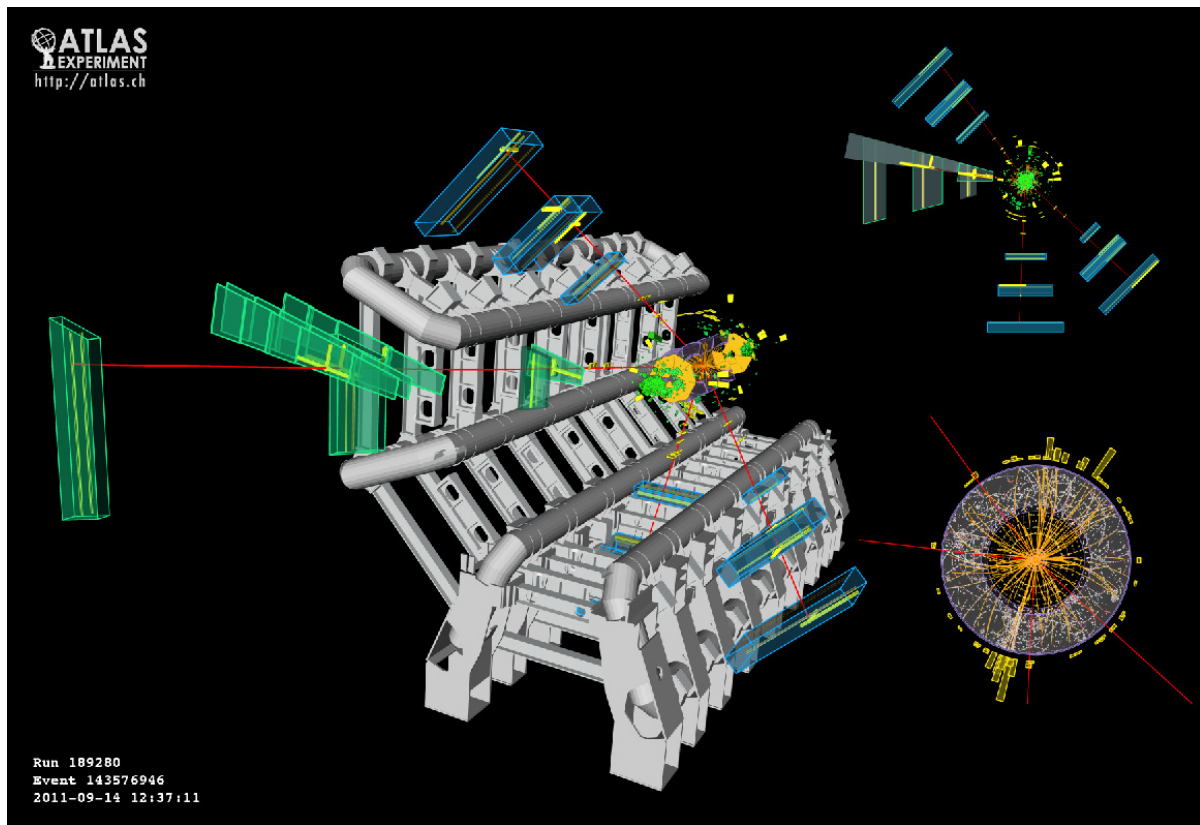
Not reviewed, for internal circulation only

RunNumber	EventNumber	Lbn	Period	type	M(4l) (GeV)	MET (GeV)	Comments
179710	25946709	422	D	2e2 μ	234.5	42.0	2 tight electrons MET close to one muon(in phi)
180636	71391739	407	E	2e2 μ	242.9	123	2 tight electrons
180710	37143864	561	E	2e2 μ	247.3	74.5	1 medium and 1 tight Several other clusters
182766	5404925	213	G	4 μ	243.0	5.1	No comment
183602	282919	20	H	4 μ	239.7	26.1	1muon at eta=2.557
184022	20046902	320	H	4e	245.4	17.4	3 tight and 1 medium
186156	65491657	381	I	4 μ	234.4	90.0	No comment
186923	96974859	507	L	2e2 μ	238.7	92	1 tigh electron and one loose++ only
186934	65787798	649	L	4e	230.7	6.2	3 tight and 1 medium
189483	33468656	145	L	4e	238.4	35.1	3 medium++ electrons
191150	5742674	170	M	2e2 μ	244.1	25.1	2 tight electrons
191218	1072214	9	M	2 μ 2e	249.7	16.0	2 tight electrons
191428	2518643	213	M	2 μ 2e	235.4	67.9	1 tight electron in crack and 1 loose++ only

Table 47: List of the four lepton candidates with invariant mass between 230 and 250GeV

L.3 High mass

Event display for a candidate in the high mass region ($m_{4\ell} > 250$ GeV) is shown in 118.



(a)

Figure 112: Event display of a 4μ candidate event with $m_{4l} = 124.6$ GeV in a (a) lateral and (b) transverse view. The masses of the lepton pairs are 89.7 and 24.6 GeV respectively.

M MC truth efficiencies as a function of number of primary vertices

The following figures show the fraction of MC truth $H \rightarrow 4l$ events passing all selection cuts for $M_{4l} = 110, 120$ and 130 GeV.

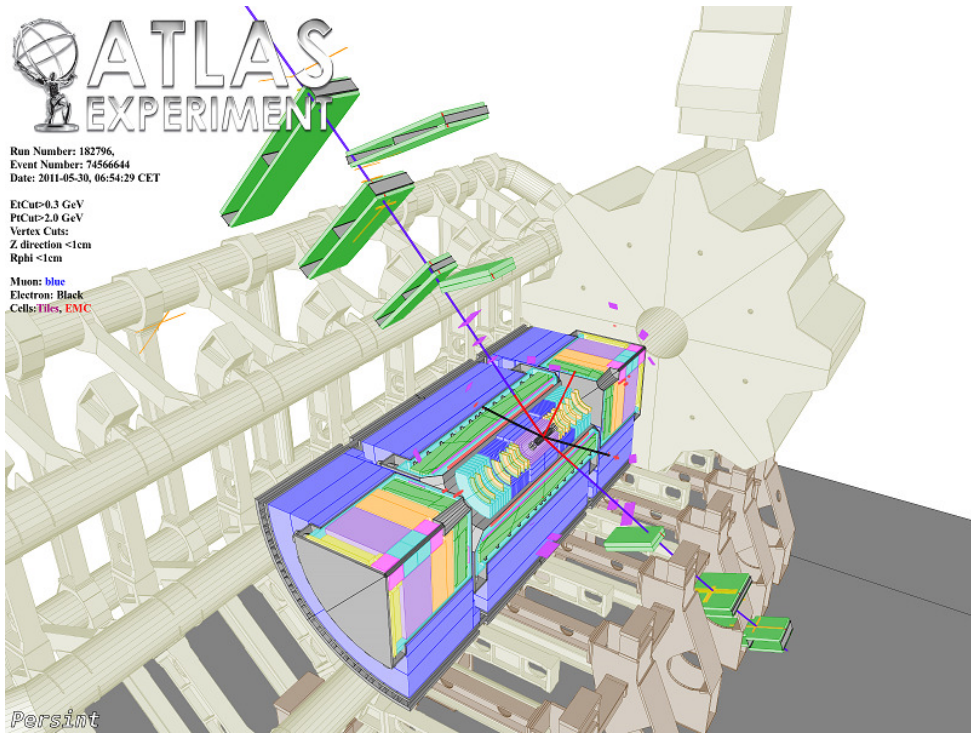


Figure 113: Event display of a $2e2\mu$ candidate event with $m_{4l} = 124.3$ GeV. The masses of the lepton pairs are 76.8 and 45.7 GeV respectively.

N Maximum likelihood fits of background only and signal+background models

This study was prepared using the full 4.8 fb^{-1} dataset. The fit parameters for the background-only model are as follows:

$$\begin{aligned}
 Lumi &= 1.00834 \pm 0.0379102(\text{limited}) \\
 \alpha_{EFF_Sig}^{ATLAS} &= -1.84972e-11 \pm 0.993348(\text{limited}) \\
 \alpha_{E_CUTS_EFF}^{ATLAS} &= 0.0407845 \pm 0.979161(\text{limited}) \\
 \alpha_{E_EFF}^{ATLAS} &= 0.0176524 \pm 0.982646(\text{limited}) \\
 \alpha_{M_EFF}^{ATLAS} &= 0.00676422 \pm 0.992995(\text{limited}) \\
 \alpha_{Norm_Z}^{ATLAS} &= -0.35881 \pm 0.837747(\text{limited}) \\
 \alpha_{Norm_Zbb}^{ATLAS} &= -0.0109854 \pm 0.992517(\text{limited}) \\
 \alpha_{ATLAS}^{ATLAS} &= 0.565292 \pm 0.832562(\text{limited}) \\
 \alpha_{QCDshape_VV}^{ATLAS} &= 0.565292 \pm 0.832562(\text{limited}) \\
 \alpha_{Shape_Z}^{ATLAS} &= -0.00148596 \pm 0.895142(\text{limited}) \\
 \alpha_{Shape_Zbb}^{ATLAS} &= 0.00436671 \pm 0.955807(\text{limited}) \\
 \alpha_{VH}^{QCDscale} &= -1.84972e-11 \pm 0.993348(\text{limited}) \\
 \alpha_{VV}^{QCDscale} &= 0.24977 \pm 0.955362(\text{limited}) \\
 \alpha_{ggH}^{QCDscale} &= -1.84972e-11 \pm 0.993348(\text{limited}) \\
 \alpha_{qqH}^{QCDscale} &= -1.84972e-11 \pm 0.993348(\text{limited}) \\
 \alpha_{gg}^{pdf} &= -0.000386558 \pm 0.993894(\text{limited}) \\
 \alpha_{qbar}^{pdf} &= 0.237693 \pm 0.969148(\text{limited})
 \end{aligned}$$

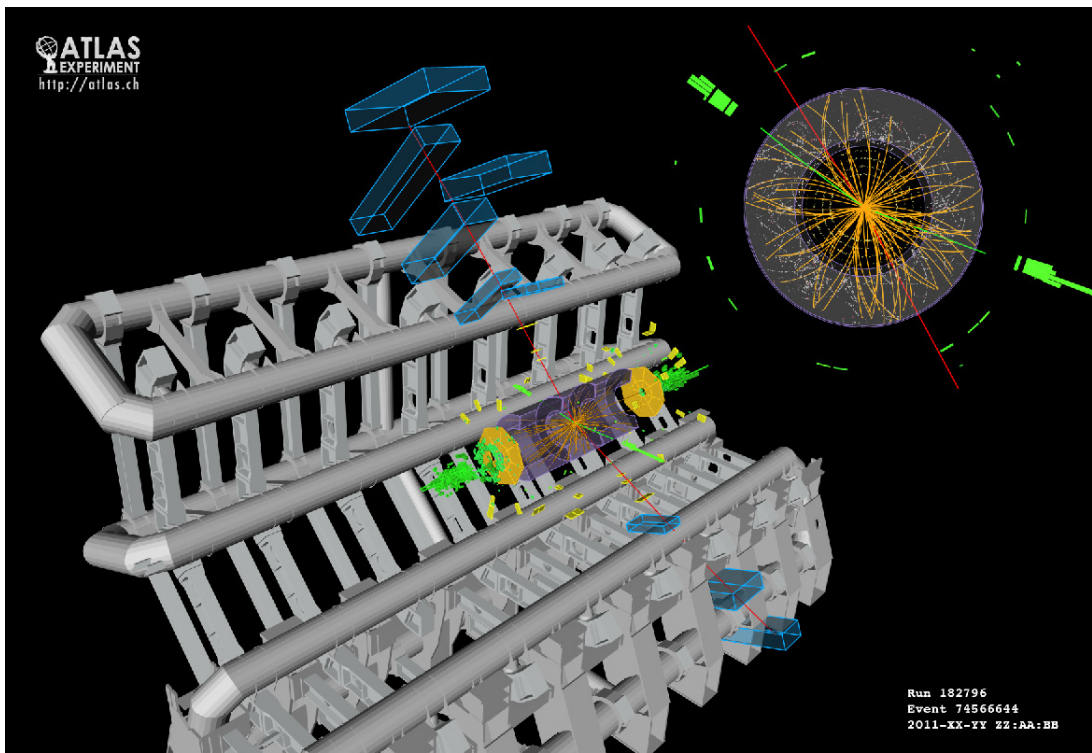


Figure 114: Event display of a $2e2\mu$ candidate event with $m_{4l} = 124.3$ GeV. The masses of the lepton pairs are 76.8 and 45.7 GeV respectively.

The fit parameters for $\mu = 1$:

$$\begin{aligned}
 Lumi &= 1.00728 \pm 0.0378888 \text{ (limited)} \\
 \alpha_{EFF_Sig}^{ATLAS} &= 0.00904127 \pm 0.990969 \text{ (limited)} \\
 \alpha_{ATLAS}^{ATLAS} &= 0.0495391 \pm 0.980986 \text{ (limited)} \\
 \alpha_{E_CUTS_EFF}^{ATLAS} &= 0.00799241 \pm 1.01133 \text{ (limited)} \\
 \alpha_{M_EFF}^{ATLAS} &= 0.00558476 \pm 0.992982 \text{ (limited)} \\
 \alpha_{Norm_Z}^{ATLAS} &= -0.473906 \pm 0.847183 \text{ (limited)} \\
 \alpha_{Norm_Zbb}^{ATLAS} &= -0.117744 \pm 0.964933 \text{ (limited)} \\
 \alpha_{QCDshape_VV}^{ATLAS} &= 0.540205 \pm 0.833848 \text{ (limited)} \\
 \alpha_{Shape_Z}^{ATLAS} &= 0.00121623 \pm 1.00332 \text{ (limited)} \\
 \alpha_{Shape_Zbb}^{ATLAS} &= 0.00642317 \pm 1.00985 \text{ (limited)} \\
 \alpha_{VH}^{QCDscale} &= 0.000294216 \pm 0.988109 \text{ (limited)} \\
 \alpha_{VV}^{QCDscale} &= 0.208361 \pm 0.95551 \text{ (limited)} \\
 \alpha_{ggH}^{QCDscale} &= 0.0411812 \pm 0.989082 \text{ (limited)} \\
 \alpha_{qgH}^{QCDscale} &= 8.23771e-05 \pm 0.993339 \text{ (limited)} \\
 \alpha_{gg}^{pdf} &= 0.0289261 \pm 0.991361 \text{ (limited)} \\
 \alpha_{qgbar}^{pdf} &= 0.194275 \pm 0.969164 \text{ (limited)}
 \end{aligned}$$

Figure 121 shows the background-only and signal+background maximum likelihood fit results for each sub-channel for a Higgs boson mass hypothesis of 125 GeV.

For $m_H = 126$ GeV, the distribution of fitted nuisance parameter in pseudo-experiments (roughly grouped depending on their function) are shown from figures 122 to 126. overlaid, in red, each figure

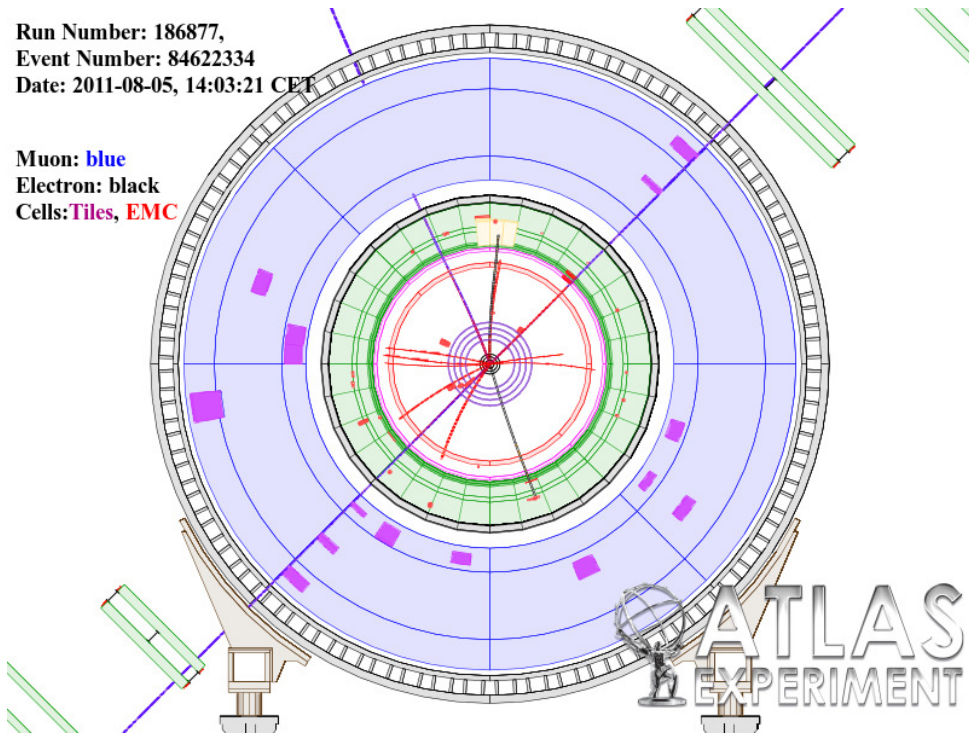


Figure 115: Event display of a $2\mu 2e$ candidate event with $m_{4l} = 123.6$ GeV. The masses of the lepton pairs are 89.3 and 30.0 GeV respectively.

also shows the Gaussian curve with mean value 0 and RMS close to 1, illustrating that these nuisance parameters are well described by a Normal distribution, which means that they are not over-constrained in the likelihood model.

Figure 127 represents the correlation matrix for the fit to the data at $m_H = 126$ GeV.

N.1 Constraining the ZZ production only from the data

As described earlier, for the nominal results presented in section 11, the yield of the Standard Model ZZ production was assigned a theoretical uncertainty of 15%. Since this process constitutes the main background for the search, this section explores the effect of using a much larger uncertainty for its rate.

To this effect, the uncertainty on the ZZ cross section is increased much above the nominal value. Instead of 15%, the ZZ rate uncertainty is set to a factor 3 above or below the nominal value. As a result, the ZZ rate is effectively constrained only by the available data; more specifically, by the region above $m_{4l} = 200$ GeV, where a sizeable number of events are expected from ZZ production.

Figure 128 compares the p_0 -values obtained in the two scenarios: the black lines show the observed and expected p_0 when the nominal value (of 15%) is used for the ZZ uncertainty; the green lines correspond to the use of an increased uncertainty. Although the two scenarios differ for $m_{4l} > 200$ GeV, they maintain a similar behavior as a function of m_{4l} and are almost identical in the low mass region; i.e., even with uncertainties much above the nominal values, the ZZ background is kept under control by the data, and there is almost no impact on the low mass region. This can be explained qualitatively as follows: the region $m_{4l} > 200$ GeV contains most of the 4-lepton candidates and, at the same time, it is expected to contain mainly ZZ events; when no information is provided about the total ZZ rate (i.e., when a large uncertainty is assigned to it), the fit will find it relatively easy to assign most events in that region to ZZ, reducing the significance of a potential excess (and hence increasing the p_0). On the other hand, a signal

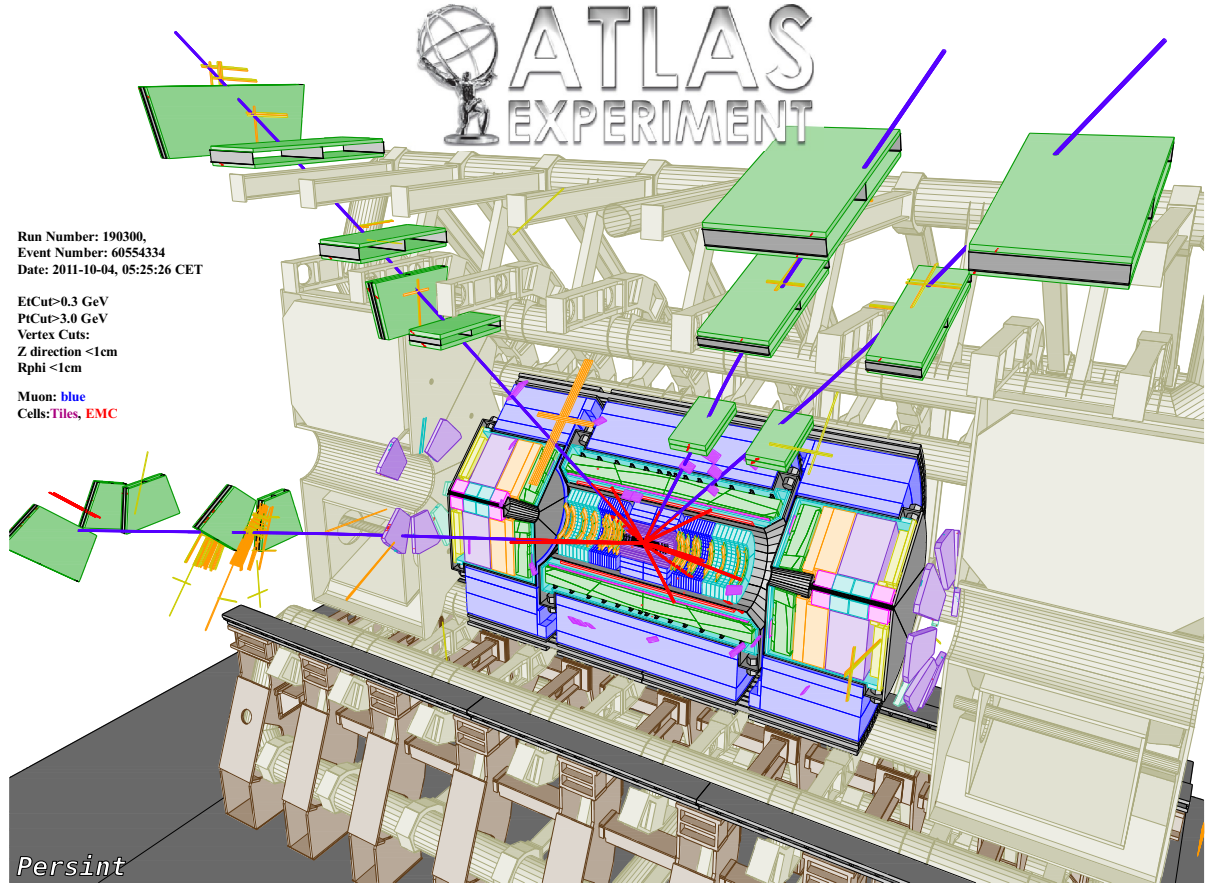


Figure 116: Event display of a 4μ candidate event with $m_{4l} = 145.8$ GeV. The masses of the lepton pairs are 94.3 and 29.7 GeV respectively.

event in the low mass region cannot be explained away by a corresponding increase in the total ZZ rate because this total rate is constrained by the number of candidates in the high mass region, which leaves the low-mass p_0 almost unaffected. We believe that this is a nice demonstration that the analysis is robust in this respect.

Tables 48 and 49 show the fit parameters for the background-only fit in the two cases. Note that in the large-uncertainty case the *uncertain* parameter $\alpha_{q\bar{q}bar}^{pdf}$ [0.14961 ± 0.152016 (limited)] is practically a measurement of the ZZ cross-section (however, its interpretation needs to be considered carefully in view of the very large uncertainty used).

N.2 Profiling nuisance parameters for expected p0

We profiled nuisance parameters at $\mu = 0, 1, \hat{\mu}$. Fig 129 shows the effect of each of these choices. Profiling at $\mu = 1$ gives different results to that profiling at $\hat{\mu}$, implying that signal-related uncertainties have non-negligible effects. Forcing $\mu = 1$ can potentially pull the nuisance parameters far from their expected values, which is undesirable. For the main results, we profile at $\mu = 0$, which is also consistent with the choice made for the $H \rightarrow \gamma\gamma$ analysis.

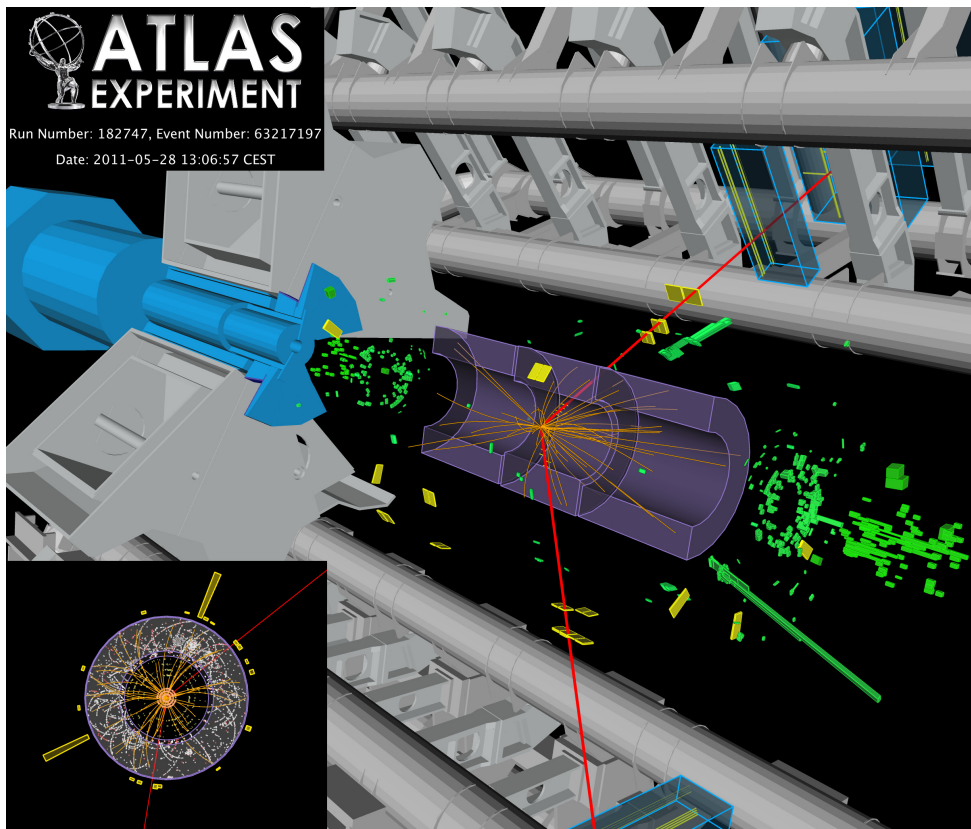


Figure 117: Event display of a $2e2\mu$ candidate event with $m_{4l} = 209.2$ GeV. The masses of the lepton pairs are 85.6 and 85.5 GeV respectively.

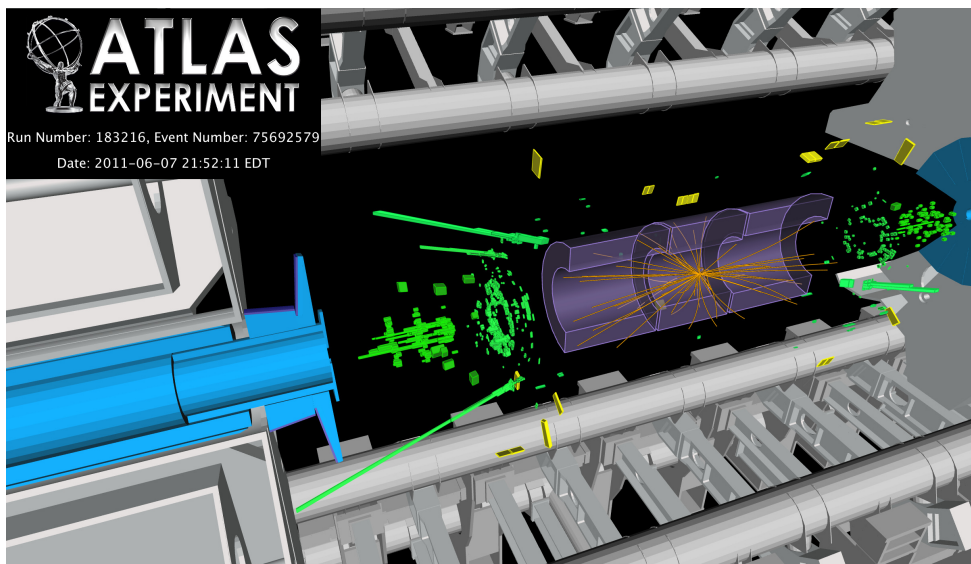


Figure 118: Event display of a $4e$ candidate event with $m_{4l} = 270.3$ GeV. The masses of the lepton pairs are 85.0 and 111.5 GeV respectively.

O CaloMuons

In the central pseudorapidity region, $|\eta| < 0.1$, the muon spectrometer coverage is incomplete.

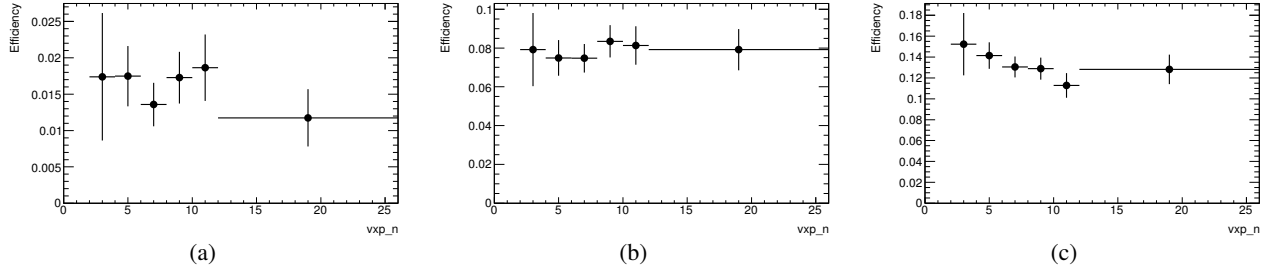


Figure 119: Fraction of MC truth $H \rightarrow 4e$ events passing all selection cuts (without scaling or smearing) as a function of the number of primary vertices for M_{4e} = (a.) 110 GeV, (b.) 120 GeV and (c.) 130 GeV.

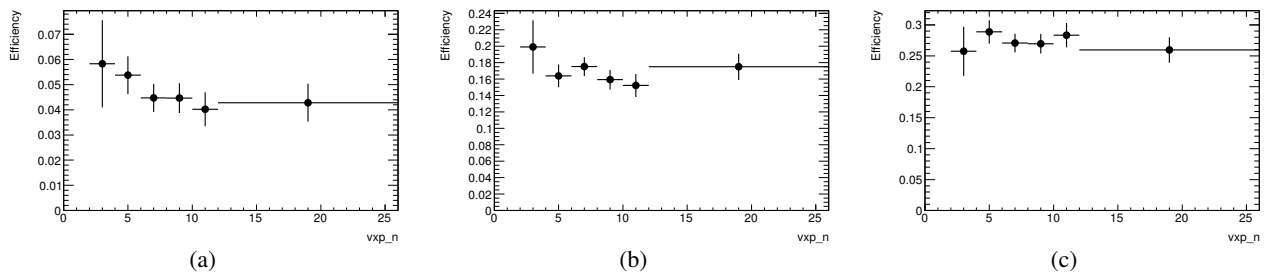


Figure 120: Fraction of MC truth $H \rightarrow 4\mu$ events passing all selection cuts (without scaling or smearing) as a function of the number of primary vertices for $M_{4\mu}$ = (a.) 110 GeV, (b.) 120 GeV and (c.) 130 GeV.

It is possible to recover acceptance in this area by using the calorimeters to identify tracks in the inner detectors as muons. This is done by requiring the presence of a minimal energy deposit in all calorimeter layers along the tracks's projected trajectory, and rejecting cases where the deposit is too large for the muon hypothesis to avoid backgrounds.

Muons from secondary decays of pions and kaons are expected to be a non-negligible background to this supplementary form of muon reconstruction.

To estimate this background as a prerequisite to a possible extension of the analysis muon selection, inner detector tracks that pass all requirements imposed on the tracks of calorimeter muons are selected. These requirements include a sufficient number of hits in the Pixel and SCT subsystems, a pseudorapidity $|\eta| < 0.1$ and a high $p_T > 15$ GeV. Tracks belonging to reconstructed STACO loose muons or electrons are removed from the selection. For the surviving tracks, which are in principle available for calorimeter tagging, the probability of being misidentified as a calorimeter muon is obtained from Monte Carlo using the truth record.

Using this probability, events with a well-reconstructed Z passing the Z1 requirement of the main analysis, a further isolated muon and an ID track forming a second opposite-charge pair with the extra muon are scaled to extrapolate the expected background counts consisting of $Z + \mu + a$ misidentified calorimeter muon. To validate this approach, a check is performed in the $Z + 1$ calo muon control region, where it is possible to count the actual event numbers of this type with reasonable statistics. This is realized through a comparison of the results on MC and data.

Within the uncertainties of the method, the prediction is well matched by the data in the high-statistics region.

Not reviewed, for internal circulation only

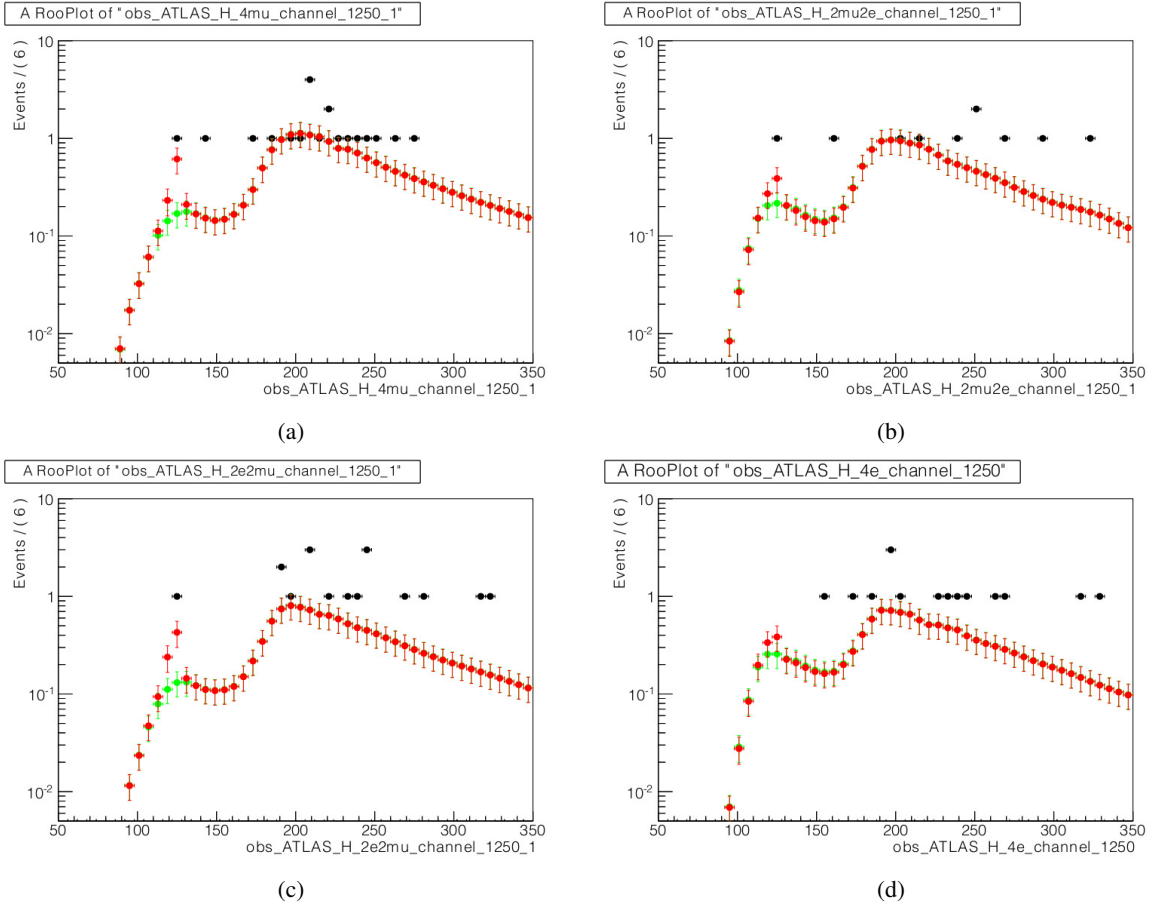


Figure 121: Background-only (green) and signal+background (red) maximum likelihood fits for the dataset of 4.8 fb^{-1} . The simultaneous fits in the (a) 4μ , (b) $2\mu 2e$, (c) $2e 2\mu$ and (d) $4e$ sub-channels is presented for the Higgs boson mass hypothesis of 125 GeV.

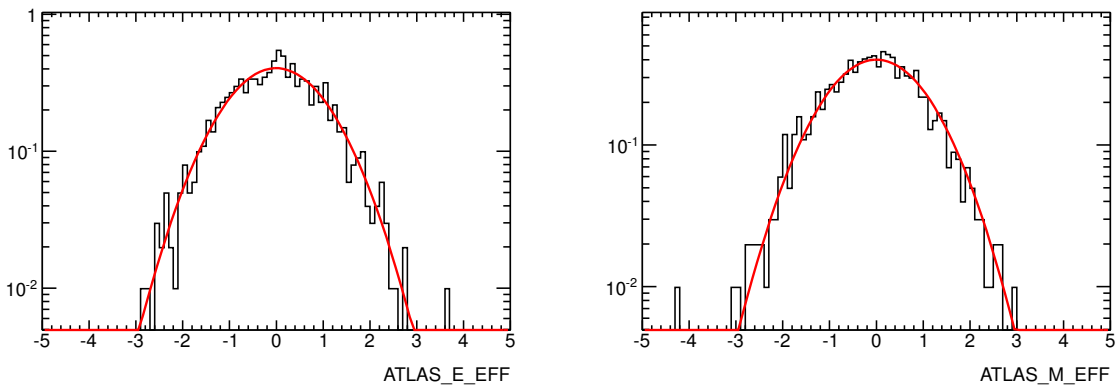


Figure 122: Sampling distributions of the fitted nuisance parameters corresponding to single electron (right) and single muon (left) efficiencies.

Region	Data estimated misID	MC estimated misID
Z+1 Calo, any isolation	250 ± 35	273 ± 35
Z+1 Calo, isolated	67.7 ± 11.3	75.9 ± 11.8
Z+ μ + Calo, any isolation	1.7 ± 0.3	1.5 ± 0.2
Z+ μ + isolated Calo	0.5 ± 0.1	0.41 ± 0.06
Z+ isolated μ + isolated Calo	0.12 ± 0.04	0.06 ± 0.01
	120	

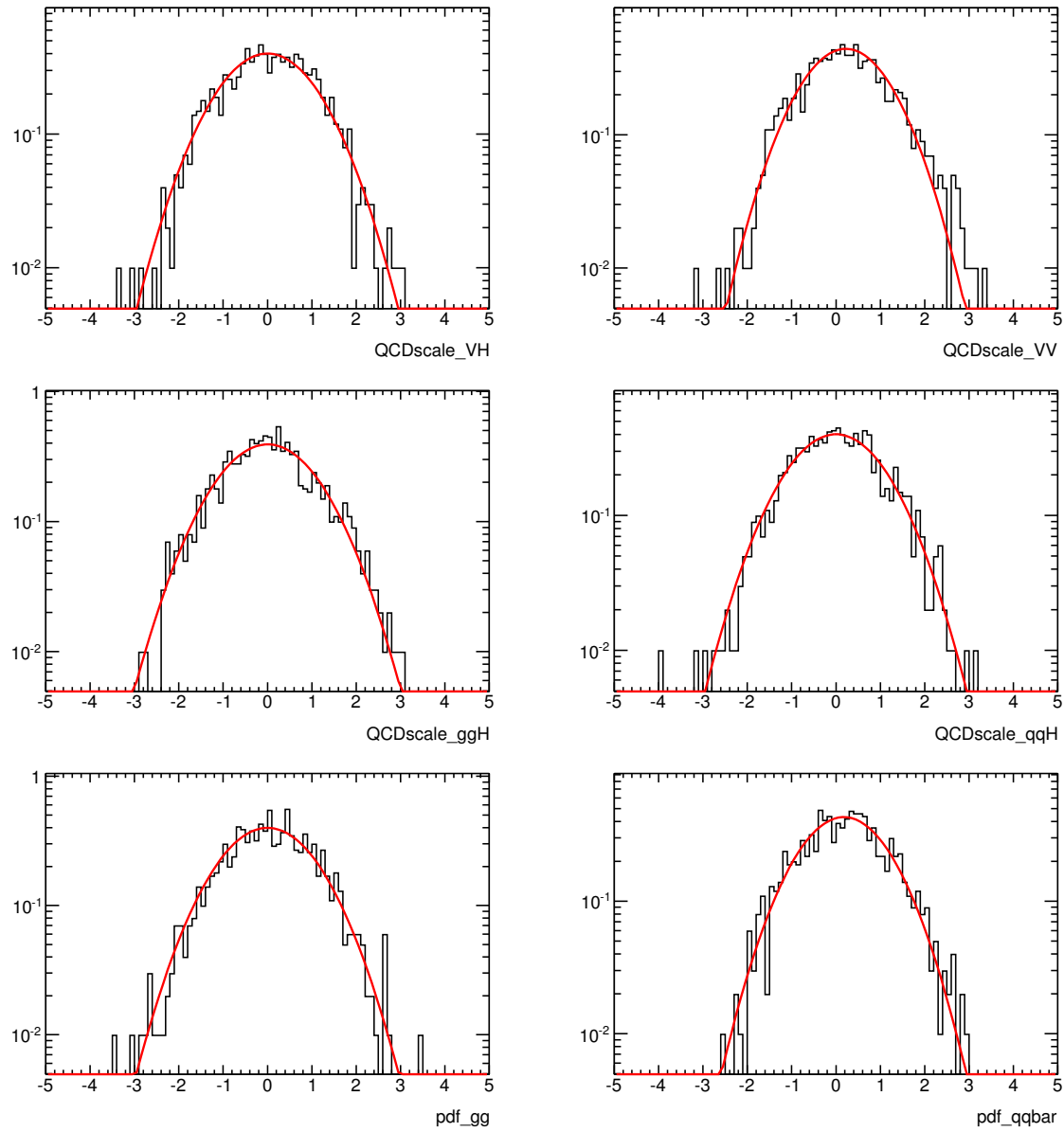


Figure 123: Sampling distributions of the fitted nuisance parameters related to theoretical uncertainties.

The expectation on data is thus (0.12 ± 0.04) extra background counts from misidentification if calorimeter muons are added to the analysis selection.

P SAMuons

While the Inner Detector acceptance of ATLAS goes up to $|\eta| = 2.5$, the Muon Spectrometer extends up to $|\eta| = 2.7$. In the region between $2.5 < |\eta| < 2.7$, called hereafter “high eta” region, the Muon Spectrometer is equipped with precision chambers of the CSC technology at the innermost layer and Endcap MDT at the middle (EM) and outer (EO) layers as well as trigger chambers of TGC technology. A schematic view in the RZ plane of the ATLAS detector elements is shown in Figure 133. It is interesting to note that despite the fact that the “high eta” region is outside the coverage of the ID, it is still possible

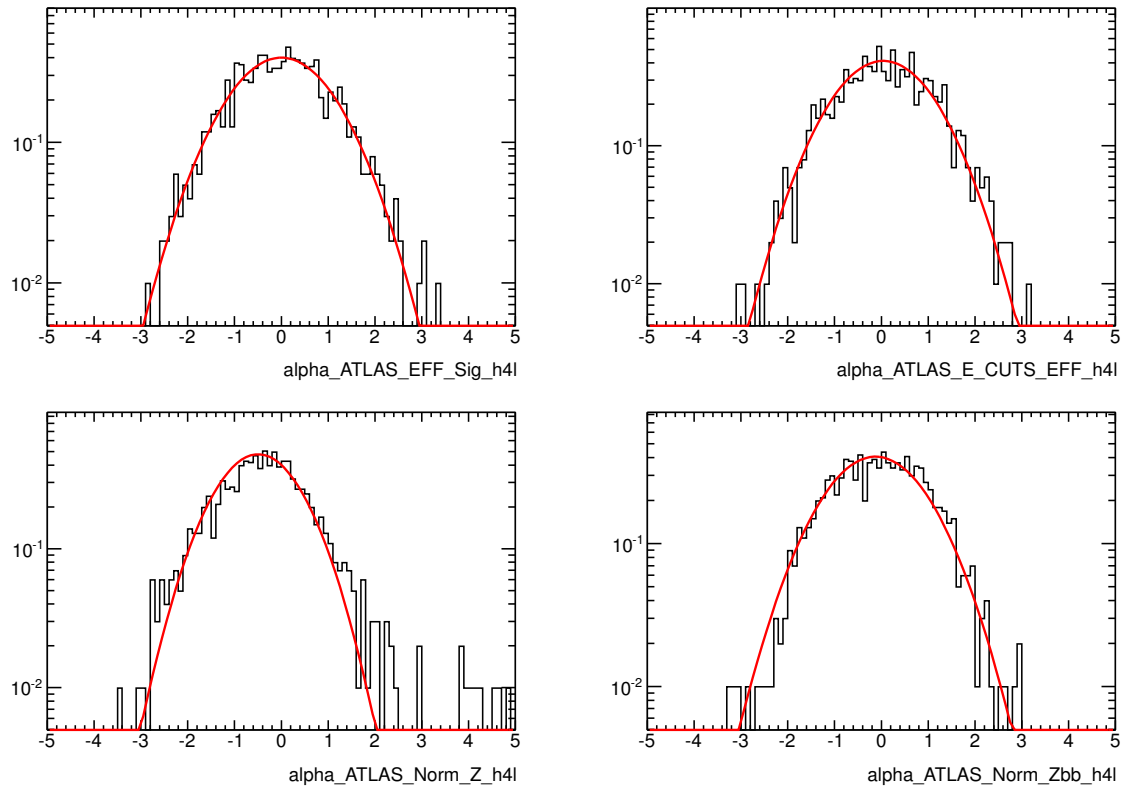


Figure 124: Sampling distributions of fitted nuisance parameters related to selection efficiencies and background normalization.

for a muon traversing layers of the SCT and pixel to bend from the toroid magnetic field in such a way that will enter the “high eta” regions of the MS, favoring positive charge muons in one side and negative charge on the other side of the detector. An example is given in Fig 134. The performance of the Muon Spectrometer with muons reconstructed in the range $2.5 < |\eta| < 2.7$ (“high eta”) is investigated by studying the Z candidates decaying into a pair of muons with one muon falling inside the ID acceptance ($|\eta| < 2.5$) and one muon in the region $2.5 < |\eta| < 2.7$. Results on the muon momentum resolution in the “high eta” region are compatible with the ones obtained in the end-cap regions, indicating that a unique p_T smearing function can be used in the whole end-cap region. The muon reconstruction efficiency scale factors for the “high eta” region are derived, together with their statistical and systematic uncertainties. It has been found that $\approx 20\%$ of these “high eta” muons are “combined” and extend up to the region of $|\eta| \leq 2.6$ whereas for the region between $2.6 < |\eta| < 2.7$ muons are reconstructed only in the Muon Spectrometer leading to “standalone muons”. The Inner Detector quality criteria as defined by the MCP group for the “combined” muons have an efficiency of $\approx 80\%$ in the “high eta” region mainly due to geometrical acceptance of the ID. In this study the quality of the “standalone muons” is also investigated, and recommendations for the selection criteria of these muon tracks are derived as a result of this search, point to the use of tracks reconstructed in all the three chambers (CSCs and MDTs at the middle and outer layers).

The current analysis, profits from the existence of “high eta” muons that are reconstructed as “combined” only, by relaxing the cut at $|\eta|$ for the muon candidates up to 2.7, while keeping all the Inner Detector hit quality criteria for these tracks as defined by the MCP group.

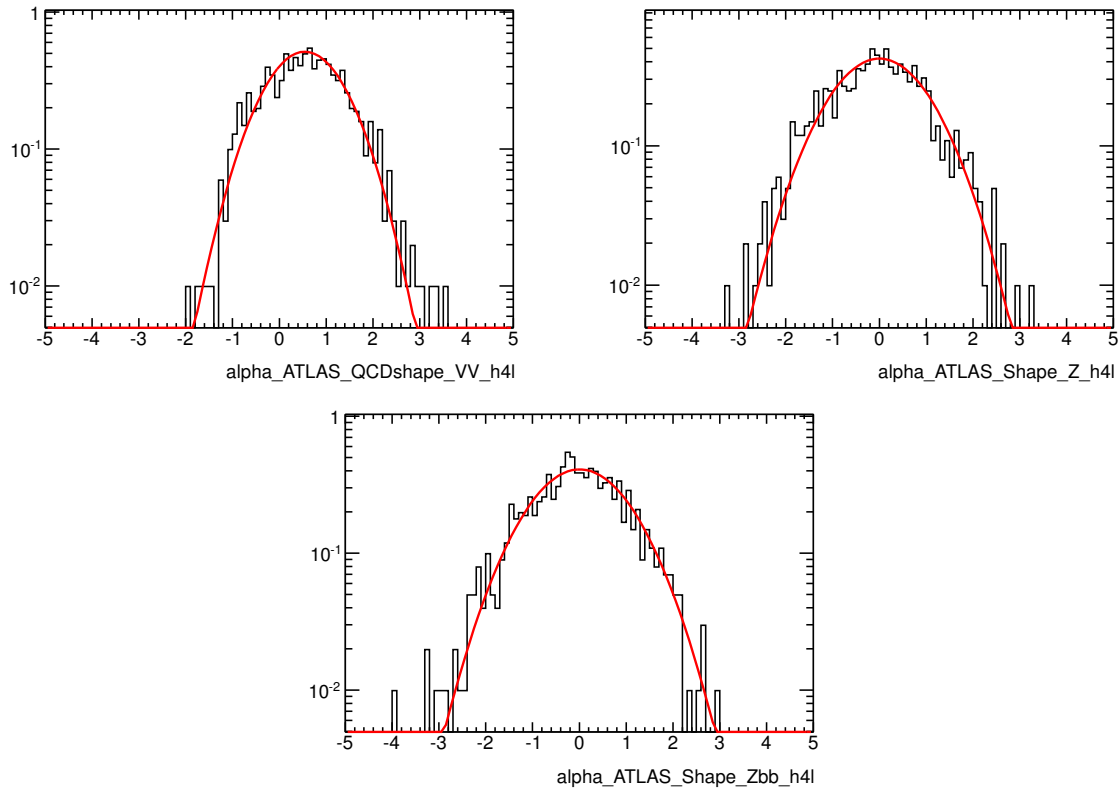


Figure 125: Sampling distributions of fitted nuisance parameters related to the shape of the 4-lepton invariant mass distribution of the background processes.

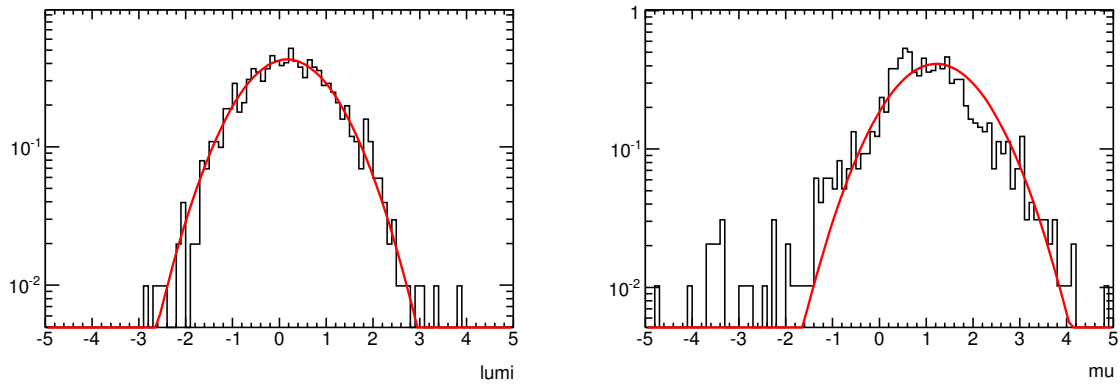


Figure 126: Sampling distributions of the fitted nuisance parameters related to luminosity and signal strength.

Q Additional plots for the Z plus heavy quark and Z plus light jets backgrounds

In this section, additional plots are presented concerning the Z plus heavy quark and Z plus light jets backgrounds. In Figure 135, apart from the selection in Figure 25 of 7.3.3, inverted selection criteria for the impact parameter significance of at least one of the leptons in the subleading dilepton have been applied in order to form the $Zb\bar{b}$ CR.

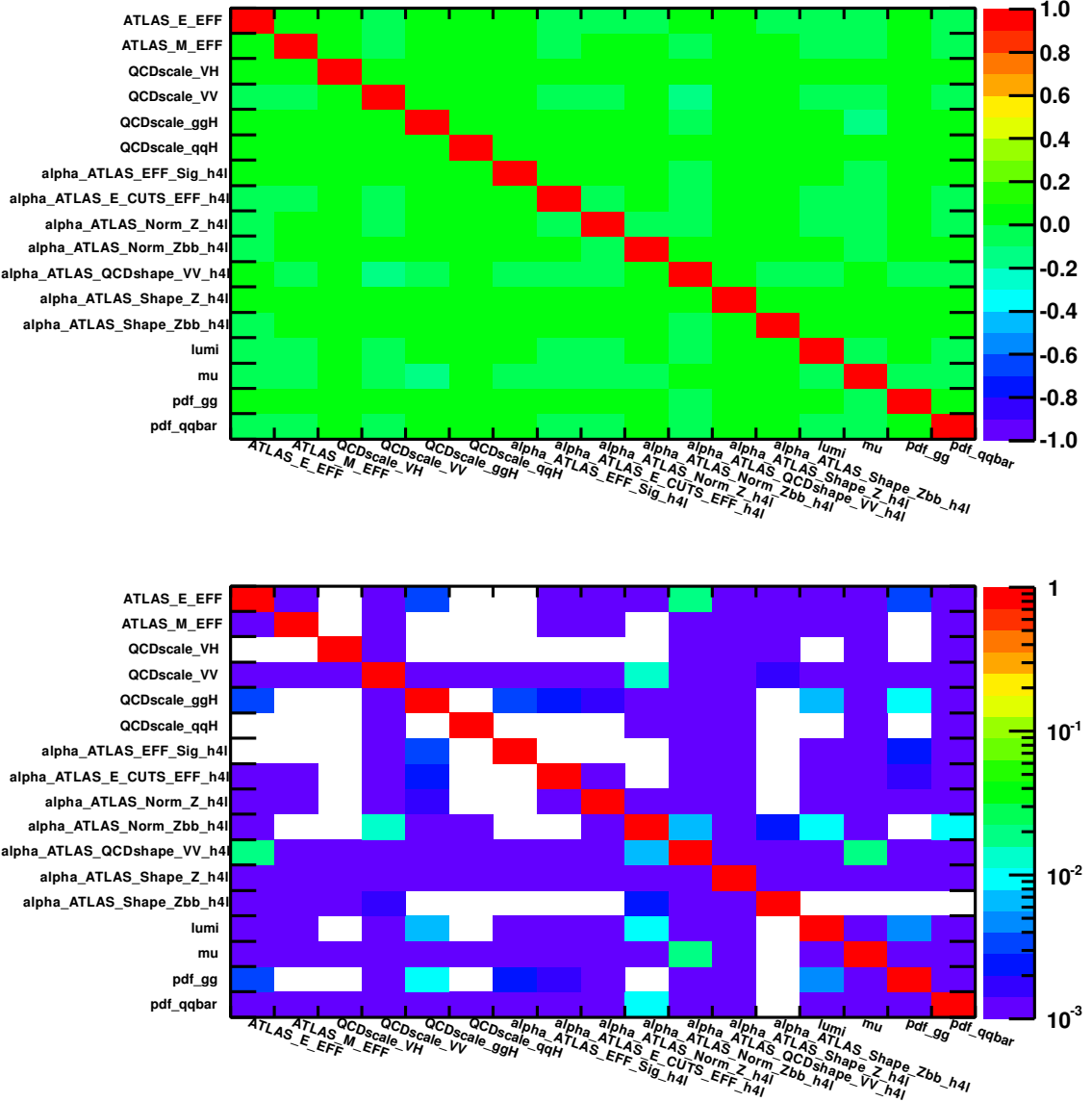


Figure 127: Correlation matrix between the fit parameters for $m_H = 126$ GeV (top and bottom plots: linear and log color scale, respectively) .

In Figure 136, apart from the selection in Figure 25 of 7.3.3, standard selection criteria for the impact parameter significance of the subleading dilepton have been applied whereas the track isolation criteria for this dilepton have been inverted for at least one of the leptons in order to form the $Z+jets$ CR.

In Figure 137, apart from the selection in Figure 25 of 7.3.3, inverted impact parameter significance requirement has been applied to the muon of the subleading dilepton.

R Signal selection optimization studies

subsection Optimization of the analysis for low mass Higgs search.

For Higgs masses below 150 GeV, the acceptance becomes strongly limited by the cuts on the p_T of

Table 48: Fit parameters for the background-only fit to the data using a large uncertainty in the ZZ yield, for $m_H = 126$ GeV.

α_{EFFsig}^{ATLAS}	1.06866e-11	0.993348
$\alpha_{ECUTS_{EFF}}^{ATLAS}$	-0.0572963	0.986516
$\alpha_{E_{EFF}}^{ATLAS}$	-0.0243447	0.985156
$\alpha_{M_{EFF}}^{ATLAS}$	0.000772382	0.993094
α_{ATLAS}^{ATLAS}	-0.394482	0.838402
α_{Normz}^{ATLAS}	-0.0343304	0.981842
$\alpha_{Normzb_b}^{ATLAS}$	0.0552717	0.983204
$\alpha_{QCDshape_{V}}^{ATLAS}$	-0.000650017	0.681437
$\alpha_{Shape_z}^{ATLAS}$	0.00385756	0.958873
$\alpha_{Shapezb_b}^{ATLAS}$	1.06866e-11	0.993348
$\alpha_{VH}^{QCDscale}$	0.00620708	0.992602
$\alpha_{VV}^{QCDscale}$	1.06866e-11	0.993348
$\alpha_{ggH}^{QCDscale}$	1.09379e-11	0.993348
$\alpha_{qqH}^{QCDscale}$	-0.00056521	0.998166
α_{gg}^{pdf}	0.14961	0.152016

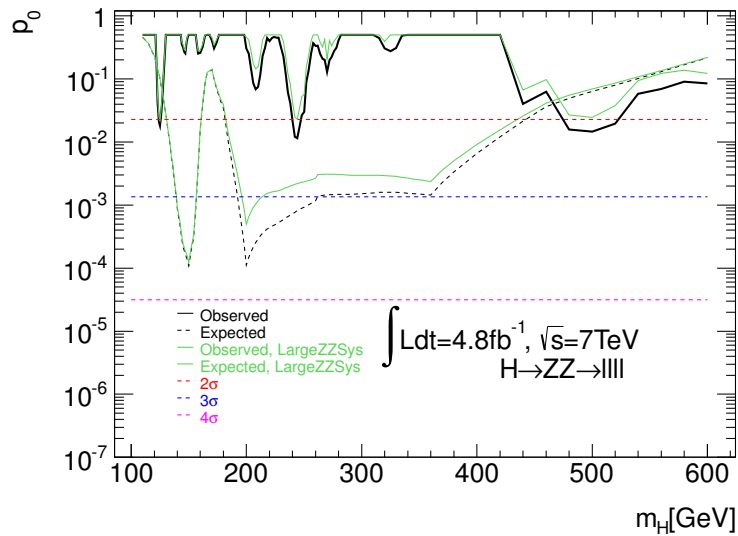


Figure 128: Comparison of the p_0 -values obtained using the nominal uncertainty on the Standard Model ZZ yield (in black) and a much larger uncertainty for it (in green).

the two highest p_T leptons, and the cut on their invariant mass. Indeed for Higgs masses decreasing well below the $2m_Z$ threshold, the mass of the highest mass dilepton tends to depart from the Z mass, and some acceptance can be gained by opening the cut on the highest dilepton mass from $m_Z - 15 < m_Z + 15$ to $m_Z - 30 < m_Z + 15$ GeV. Similarly, acceptance can be gained by lowering the p_T cut on these leptons from 20 to 15 GeV. Such new cuts have been studied with the same Monte Carlo simulations as the baseline analysis. The factor of merit (significance) is taken as:

$$\sigma = \sqrt{2((s+b)\log(1+s/b) - s)}$$

where s and b are the number of signal and background events.

Table 49: Fit parameters for the background-only fit to the data using a large uncertainty in the ZZ yield, for $m_H = 126$ GeV.

α_{EFFsig}^{ATLAS}	4.3566e-11	0.993348
$\alpha_{ECUTS_{EFF}}^{ATLAS}$	0.0370445	0.981296
$\alpha_{E_{EFF}}^{ATLAS}$	0.0195701	0.98358
$\alpha_{M_{EFF}}^{ATLAS}$	0.00680054	0.992996
α_{ATLAS}^{ATLAS}	-0.358734	0.837417
α_{Normz}^{ATLAS}	-0.0111206	0.992112
$\alpha_{QCDshapevV}^{ATLAS}$	0.565462	0.832172
α_{Shapez}^{ATLAS}	-0.00149896	0.895246
$\alpha_{Shapezb_{bb}}^{ATLAS}$	0.00441989	0.956024
$\alpha_{QCDscale}^{VH}$	4.3566e-11	0.993348
$\alpha_{VV}^{QCDscale}$	0.248612	0.955265
$\alpha_{ggH}^{QCDscale}$	4.3566e-11	0.993348
$\alpha_{qqH}^{QCDscale}$	4.3566e-11	0.993348
α_{gg}^{pdf}	-0.000387459	0.993894
α_{qqbar}^{pdf}	0.23851	0.969093

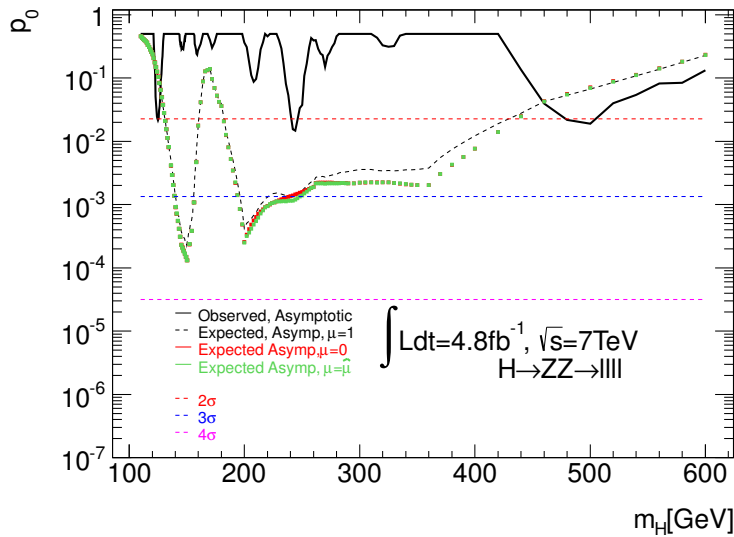


Figure 129: Comparison of the p_0 -values obtained profiling μ at 0, 1, $\hat{\mu}$.

Table 52 shows the number of background events with $m_{4l} < 180$ GeV expected from the Monte-Carlo simulation. Table 53 shows the number of signal events and the significance as defined above. Both tables display event numbers from the Monte Carlo simulation for 4.5 fb^{-1} . This indicates that these wider cuts offer a clear potential gain of significance. However of course this needs a detailed understanding of the efficiencies and backgrounds in the data.

subsection Optimization of the analysis for low mass Higgs search.

For Higgs masses below 150 GeV, the acceptance becomes strongly limited by the cuts on the p_T of the two highest p_T leptons, and the cut on their invariant mass. Indeed for Higgs masses decreasing well below the $2m_Z$ threshold, the mass of the highest mass dilepton tends to depart from the Z mass, and

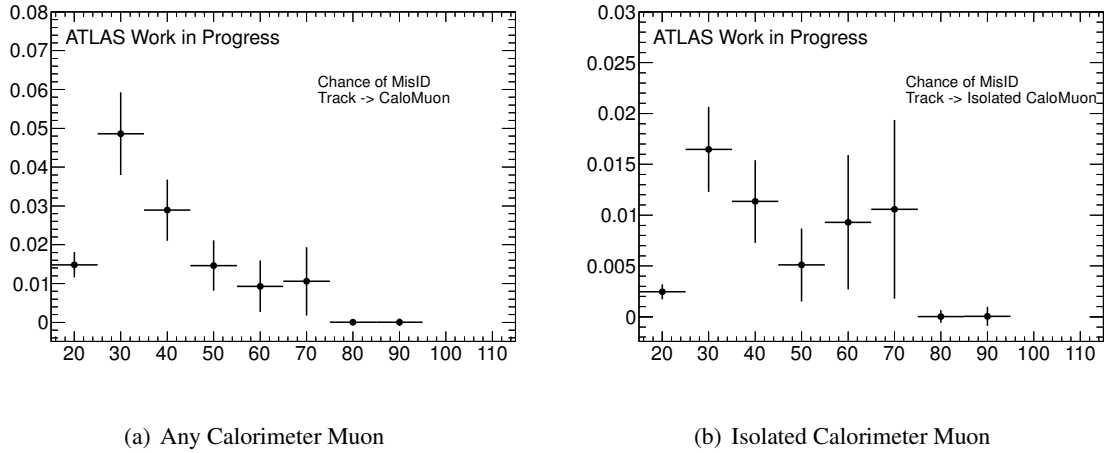


Figure 130: Probability for an inner detector track to be misidentified as a muon

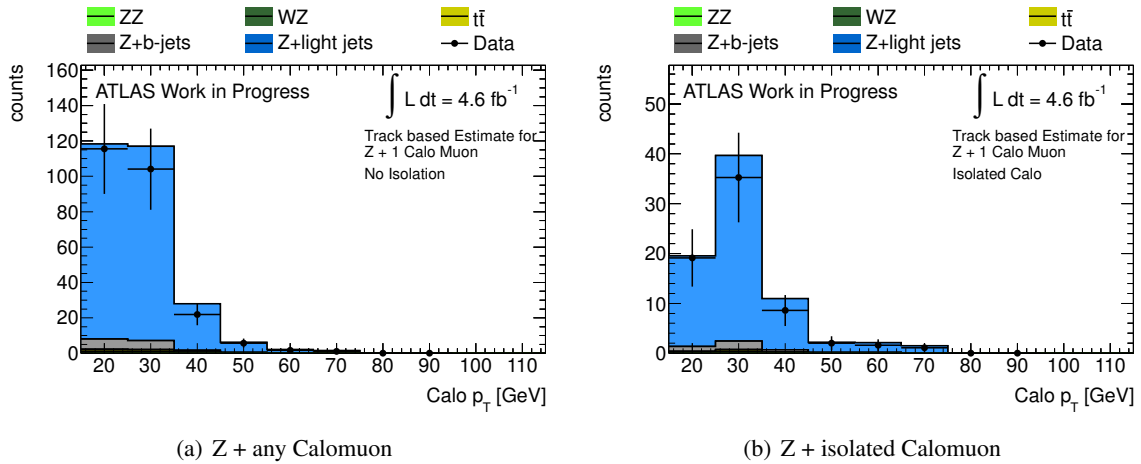


Figure 131: Validation of the track-based CaloMuons misidentification background estimate

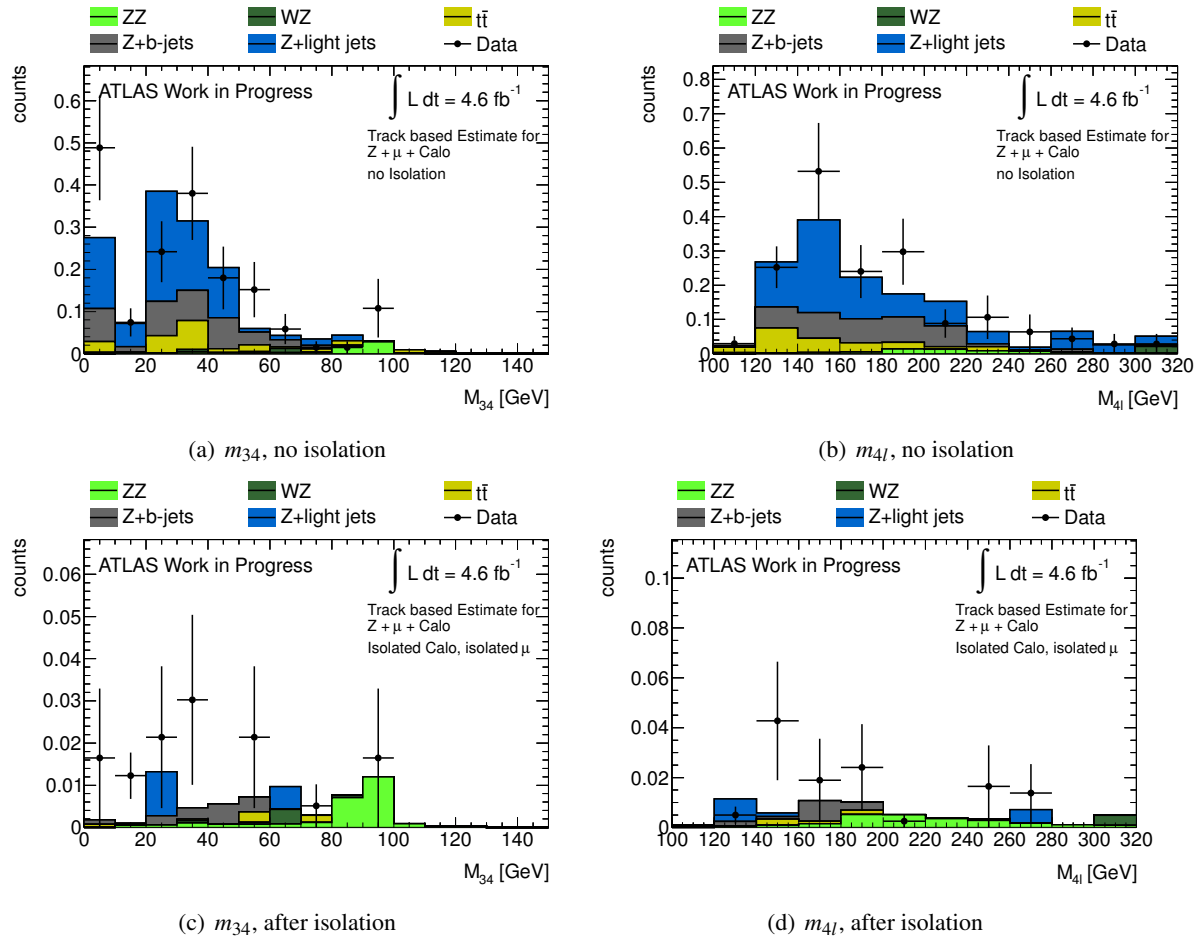


Figure 132: Result of the track-based CaloMuon misidentification background estimate

Not reviewed, for internal circulation only

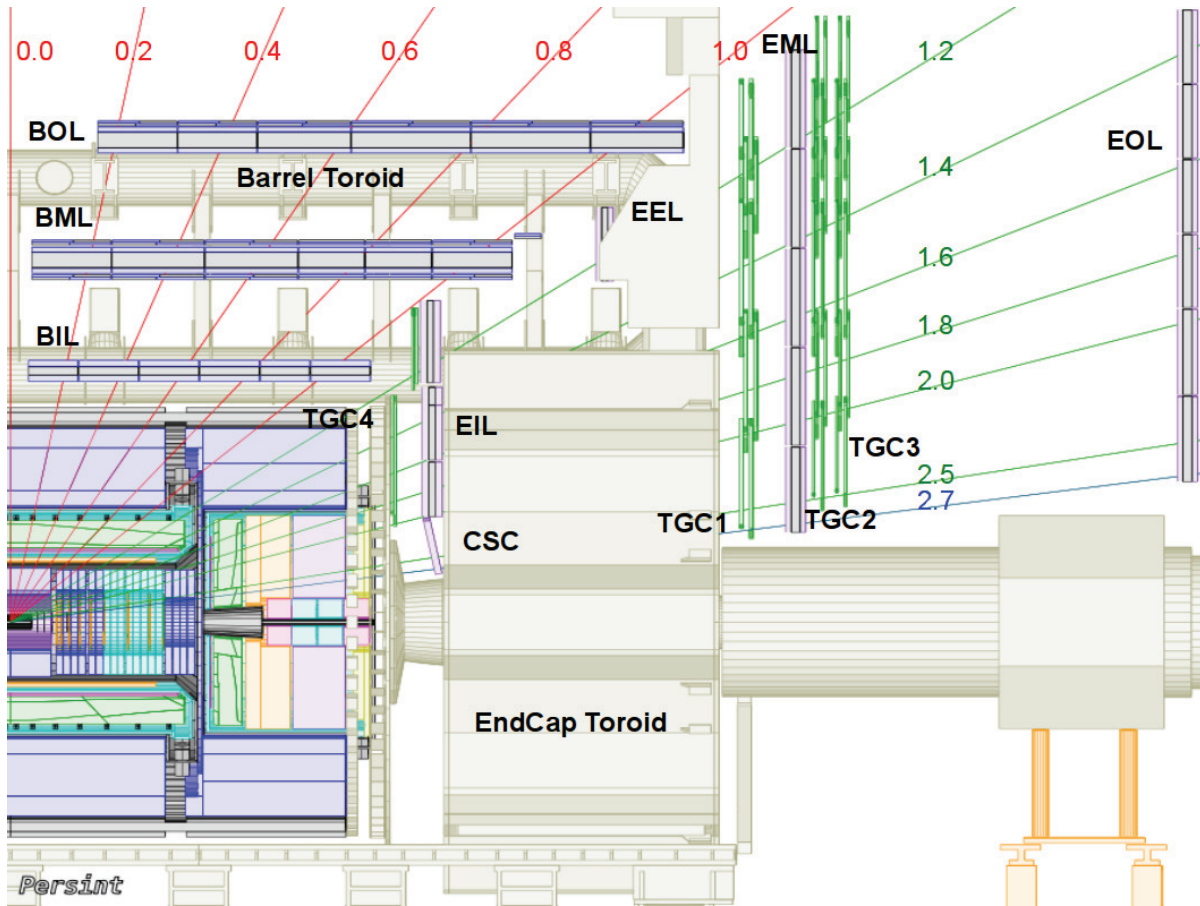


Figure 133: Schematic view in the RZ plane of the ATLAS detector elements.

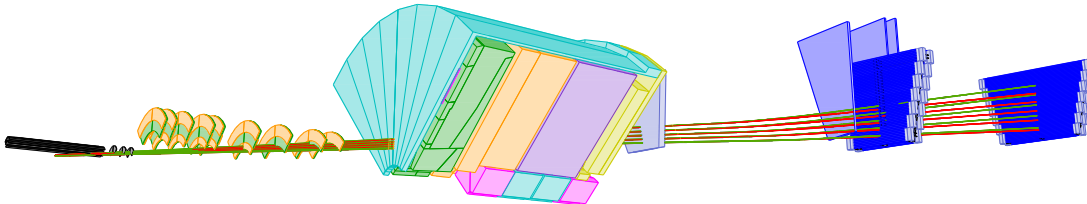


Figure 134: Schematic view of the ATLAS detector elements that a muon with p_T of 10 GeV (green) and 15 GeV (red) traverses when bended in the toroid magnetic field. The pseudo-rapidity of the tracks is in the region of 2.5 to 2.7 and a step of 0.5 is used.

some acceptance can be gained by opening the cut on the highest dilepton mass from $m_Z - 15 < m_Z + 15$ to $m_Z - 30 < m_Z + 15$ GeV. Similarly, acceptance can be gained by lowering the p_T cut on these leptons from 20 to 15 GeV. Such new cuts have been studied with the same Monte Carlo simulations as the baseline analysis. The factor of merit (significance) is taken as:

$$\sigma = \sqrt{2((s+b)\log(1+s/b) - s)}$$

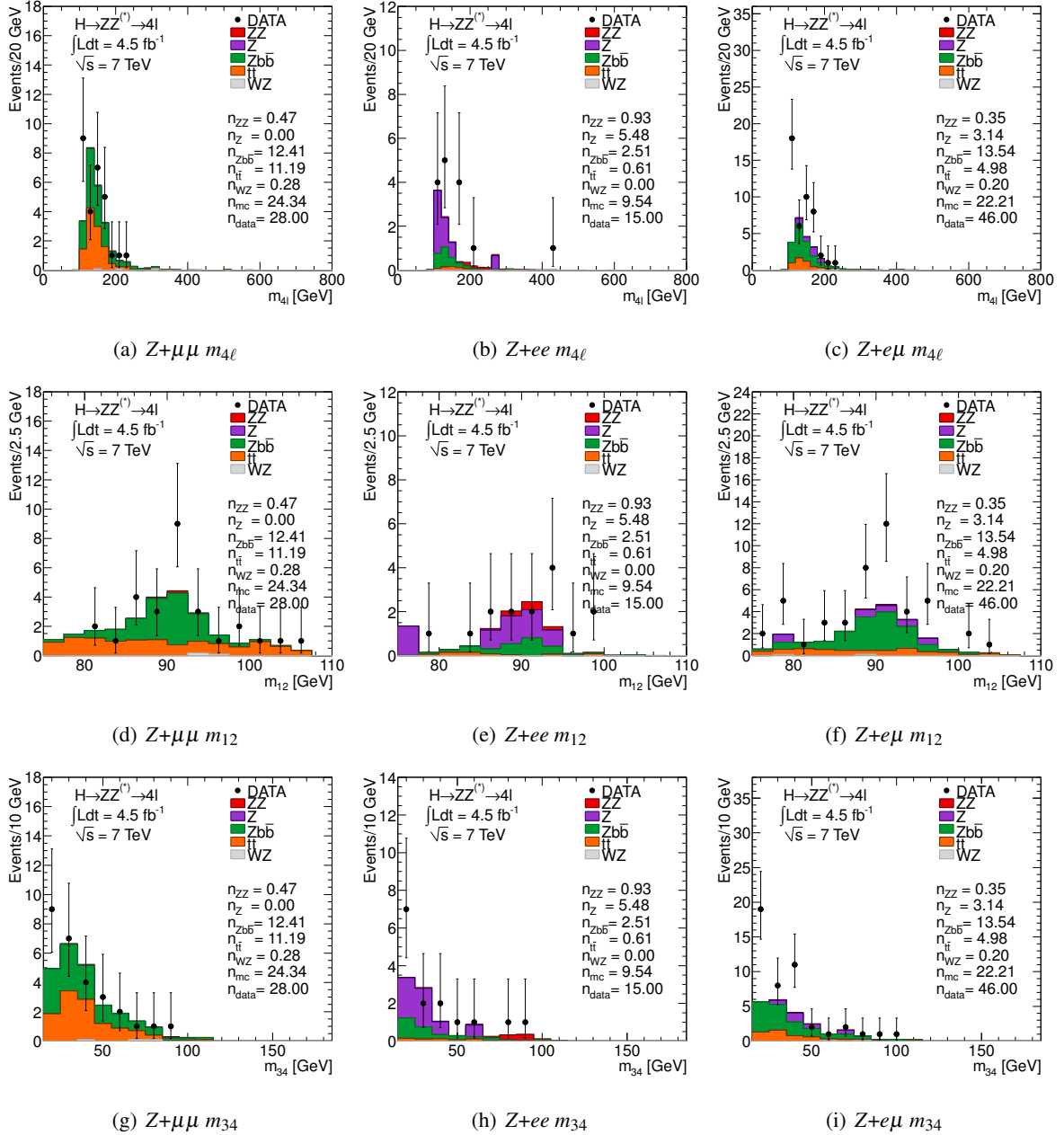


Figure 135: The invariant mass distributions for the three final states after the kinematic cuts, invariant mass requirements, track and calorimetric isolation of the leading dilepton pair and inverted impact parameter significance cuts for at least one lepton in the subleading dilepton so that the $Zb\bar{b}$ CR is formed.

where s and b are the number of signal and background events.

Table 52 shows the number of background events with $m_{4l} < 180\text{GeV}$ expected from the Monte-Carlo simulation. Table 53 shows the number of signal events and the significance as defined above. Both tables display event numbers from the Monte Carlo simulation for 4.5fb^{-1} . This indicates that these wider cuts offer a clear potential gain of significance. However of course this needs a detailed understanding of the efficiencies and backgrounds in the data.

The optimization of the values for the cuts on the on-shell Z mass $Z1$ and on the leading leptons p_T

Not reviewed, for internal circulation only

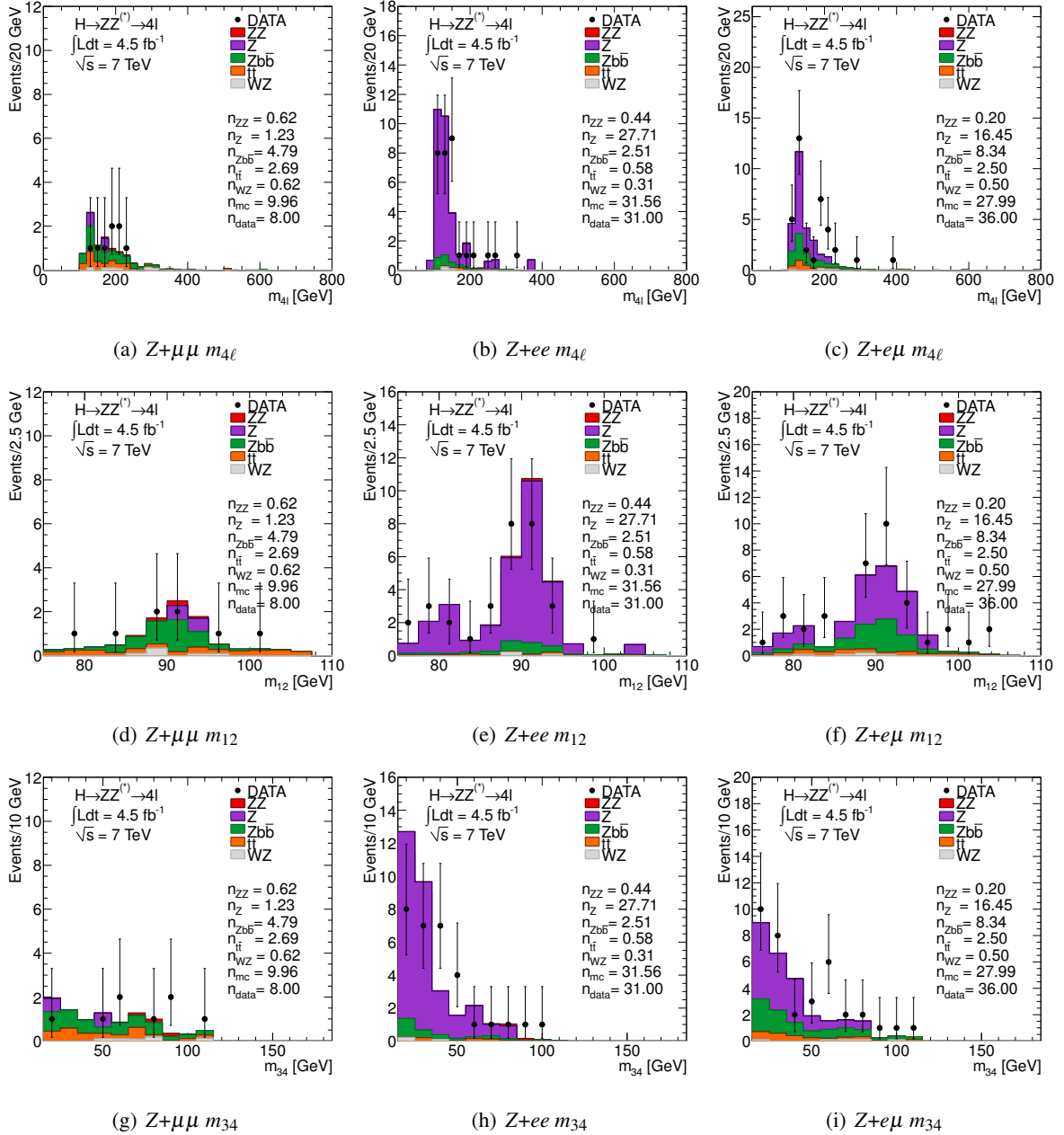


Figure 136: The invariant mass distributions for the three final states after the kinematic cuts, invariant mass requirements, track and calorimetric isolation of the leading dilepton pair, impact parameter significance cuts and inverted track isolation for at least one lepton in the subleading dilepton for the $Z + \text{jets}$ CR.

has been studied using as figure of merit the significance computed as previously indicated with the score function:

$$\sigma = \sqrt{2((s+b)\log(1+s/b) - s)}$$

where s and b are the number of signal and background events, respectively. The lower cut on the Z_1 mass has been varied between $m_Z - 50$ GeV and $m_Z - 15$ GeV (the latter value being the one used in this analysis), while the cut on the leading leptons p_T has been varied between 10 and 20 GeV. The significance as a function of the two cut values, for integrated luminosities of 5 fb^{-1} and 13 fb^{-1} , is

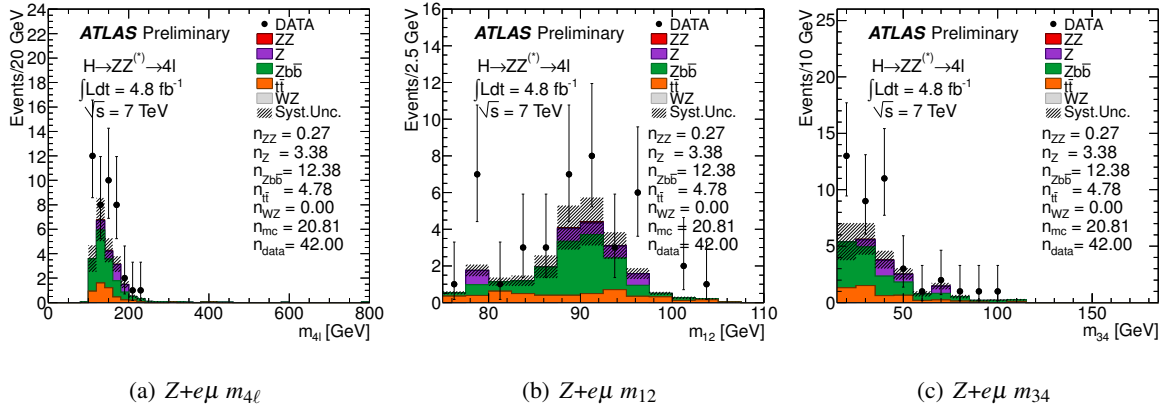


Figure 137: The invariant mass distributions for the $Z + e\mu$ final states after the kinematic cuts, invariant mass requirements, track and calorimetric isolation of the leading dilepton pair. The muon of the second lepton pair is required to have an impact parameter significance $\zeta > 3.5$

Selection	$Z+\text{jets}$	$Z\text{bb}+\text{jets}$	$t\bar{t}$	ZZ
Standard events	3.9	0.49	0.00	5.6
ratio	1	1	1	1
$p_T > 15 \text{ GeV}$	3.9	0.57	0.00	5.7
ratio	1	1.16	1	1.03
$m_Z - 30 \text{ GeV}$	4.9	0.63	0.35	6.4
ratio	1.26	1.28	-	1.14
Both	4.9	0.75	0.35	6.8
ratio	1.26	1.51	-	1.22

Table 50: Expected number of background events (Monte Carlo) for relaxed cuts (see text) compared to the baseline analysis

Higgs mass	110 GeV		120 GeV		130 GeV	
	Selection	Events	Significance			
Standard	0.06	0.018	0.71	0.22	2.43	0.74
ratio	1	1	1	1	1	1
$p_T > 15 \text{ GeV}$	0.06	0.020	0.76	0.24	2.54	0.77
ratio	1.09	1.07	1.07	1.06	1.04	1.03
$m_Z - 30 \text{ GeV}$	0.15	0.044	0.95	0.27	2.92	0.80
ratio	2.68	2.41	1.34	1.21	1.20	1.08
Both	0.17	0.047	1.02	0.28	3.06	0.82
ratio	2.95	2.60	1.44	1.27	1.26	1.11

Table 51: Expected number of signal events (Monte Carlo) and significance for relaxed cuts (see text) compared to the baseline analysis

shown in Figure 138, for an Higgs mass of 140 GeV.

The significance obtained varying each of the cuts, while keeping the other fixed at the value used in

Selection	Z+jets	Zbb+jets	$t\bar{t}$	ZZ
Standard events	3.9	0.49	0.00	5.6
ratio	1	1	1	1
$p_T > 15 \text{ GeV}$	3.9	0.57	0.00	5.7
ratio	1	1.16	1	1.03
$m_Z - 30 \text{ GeV}$	4.9	0.63	0.35	6.4
ratio	1.26	1.28	-	1.14
Both	4.9	0.75	0.35	6.8
ratio	1.26	1.51	-	1.22

Table 52: Expected number of background events (Monte Carlo) for relaxed cuts (see text) compared to the baseline analysis

Higgs mass	110 GeV		120 GeV		130 GeV	
Selection	Events	Significance				
Standard	0.06	0.018	0.71	0.22	2.43	0.74
ratio	1	1	1	1	1	1
$p_T > 15 \text{ GeV}$	0.06	0.020	0.76	0.24	2.54	0.77
ratio	1.09	1.07	1.07	1.06	1.04	1.03
$m_Z - 30 \text{ GeV}$	0.15	0.044	0.95	0.27	2.92	0.80
ratio	2.68	2.41	1.34	1.21	1.20	1.08
Both	0.17	0.047	1.02	0.28	3.06	0.82
ratio	2.95	2.60	1.44	1.27	1.26	1.11

Table 53: Expected number of signal events (Monte Carlo) and significance for relaxed cuts (see text) compared to the baseline analysis

this analysis, is shown in Figure 139.

Choosing the optimal cut values improves the significance by about 7% also for an Higgs mass of 140 GeV.

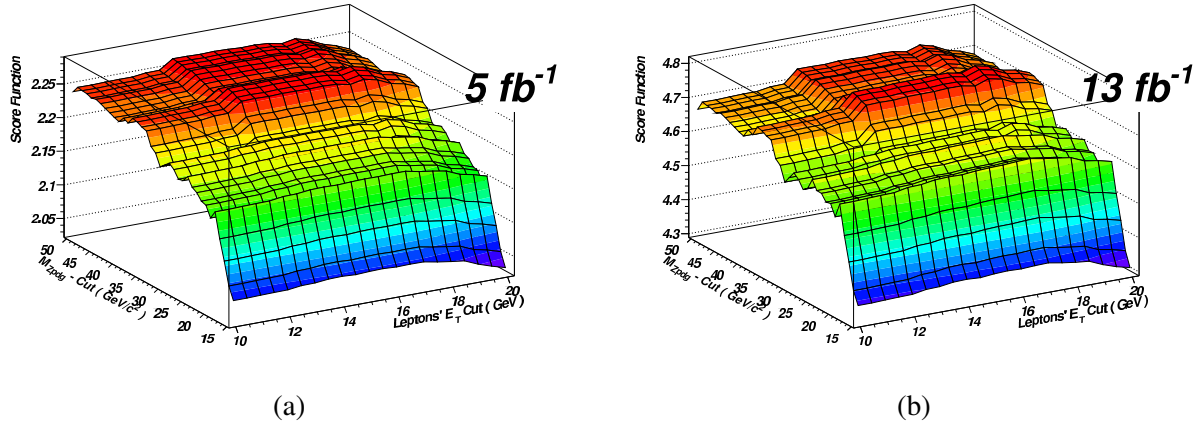


Figure 138: The significance as a function of the lower cut on the Z1 invariant and of the cut on the leading leptons p_T , for an integrated luminosity of 5 fb^{-1} (a) and 13 fb^{-1} (b) and for an Higgs mass of 140 GeV .

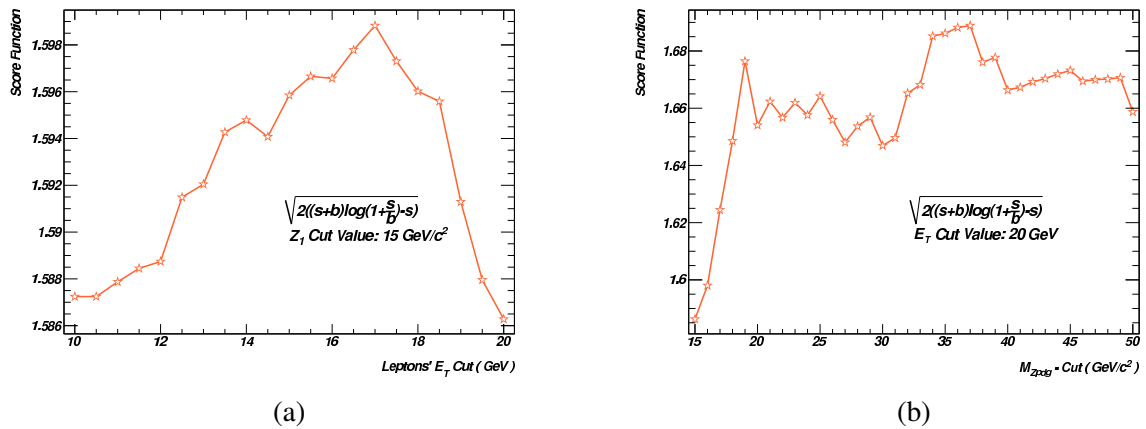


Figure 139: The significance obtained varying the cut on the leading leptons p_T cut, keeping the Z1 mass cut at $m_Z - 15 \text{ GeV}$ (a), and the significance obtained varying the Z1 mass cut while keeping the leading leptons p_T cut fixed at 15 GeV (b). The Higgs mass is 140 GeV .

R.1 Angular analysis

Angular analyses can be used to improve the discrimination between the Higgs to 4 leptons signal and the main irreducible background, namely the ZZ production and decay in 4 leptons. This can be done along two different lines: first, due to the different spin properties of the Higgs, that is a scalar, with respect to ZZ, that is a mixture of different spin states, the decay angles of the two Z and of the leptons are expected to have also different distributions; second, due to the different production mechanism of the Higgs boson with respect to the ZZ, the transverse momentum p_T of the 4 leptons system is expected to be different in the two cases.

Several theoretical papers have addressed the problem [66]. In particular the recent [67] presents an analysis scheme and evaluates the discrimination power of some relevant angular variables.

We have considered the possibility to use a similar set of variables to study the discrimination capability of ATLAS using angular variables in the 4 leptons analysis. In the following we present angular distributions based on MC samples of signal and backgrounds. We have considered 2 Higgs masses (130 GeV, 360 GeV), and limited our analysis to the ZZ background, neglecting the lower contribution of Zbb and $t\bar{t}$ surviving events. For the ZZ background we have considered a low mass region (<180 GeV) as background for the 130 GeV Higgs signal, and a high mass region ($300 \div 420$ GeV) as background for the 360 GeV Higgs signal.

In the following, after a description of the MC samples used, we discuss first the discrimination power using decay angles, then the one using production angles.

R.1.1 Montecarlo samples

For the signal we have used the Pythia generator (PythiaH130zz4l). For comparison between gluon-gluon fusion (ggf in the following) and vector boson fusion (vbf in the following) processes, we have used Powheg interfaced to Pythia PowHegPythia_ggH130_ZZ4lep and PowHegPythia_VBFH130_ZZ4lep). For the ZZ background we have used also Pythia (Pythiazz4l_3MultiLeptonFilterElecMu) and a Jimmy sample for the sub-dominant ggf production mode (gg2ZZ_JIMMY_ZZ4lep).

The plots shown below are based on reconstructed variables at the end of the standard analysis selection.

R.1.2 Decay angles

The angles used in the following are defined in fig.140

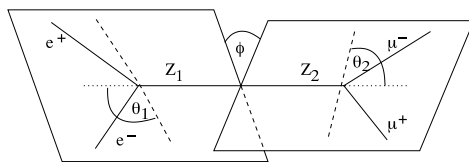


Figure 140: Angular variables, $\cos \theta_{1,2}, \phi$.

Focusing on the decay of the two Zs, namely Z_1 and Z_2 with Z_1 the one with an invariant mass closer to the Z mass, we can define $\theta_{1,2}$ as the angle between the decaying leptons and the Z direction in the 2 Zs center of mass (as shown in fig.140):

$$\cos \theta_{1,2} = \frac{\vec{P}_{lep}^* \cdot \vec{P}_Z^*}{|\vec{P}_{lep}^* \vec{P}_Z^*|} \quad (4)$$

where \vec{P}_{lep}^* is the lepton 3-momentum in the Z reference frame whereas \vec{P}_Z^* is the Z 3-momentum in the 2Zs center of mass. Figs.141 and 142 compare, for the two angles defined above, the distributions for the 130 and 360 GeV Higgs signal and the corresponding ZZ backgrounds.

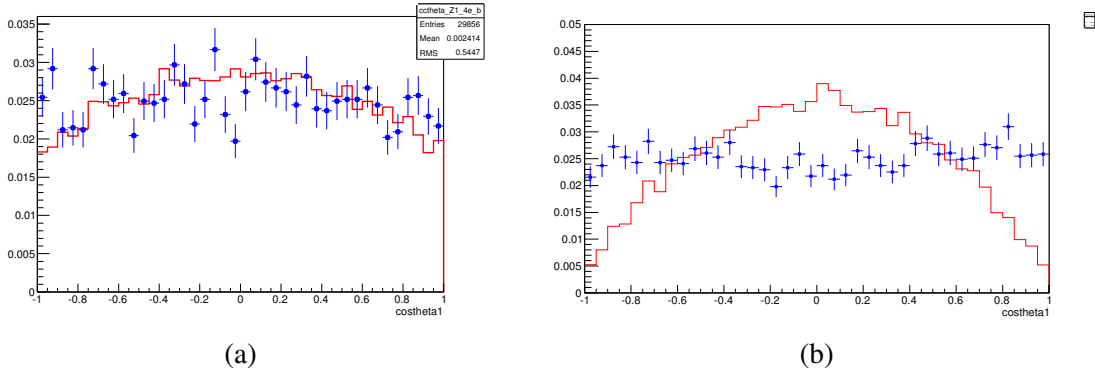


Figure 141: Distribution of the $\cos \theta_1$ angle, $m_H=130$ GeV (a) and $m_H=360$ GeV (b). The red histogram shows the distribution for the Higgs signal, the blue points for the $ZZ^{(*)}$ irreducible background.

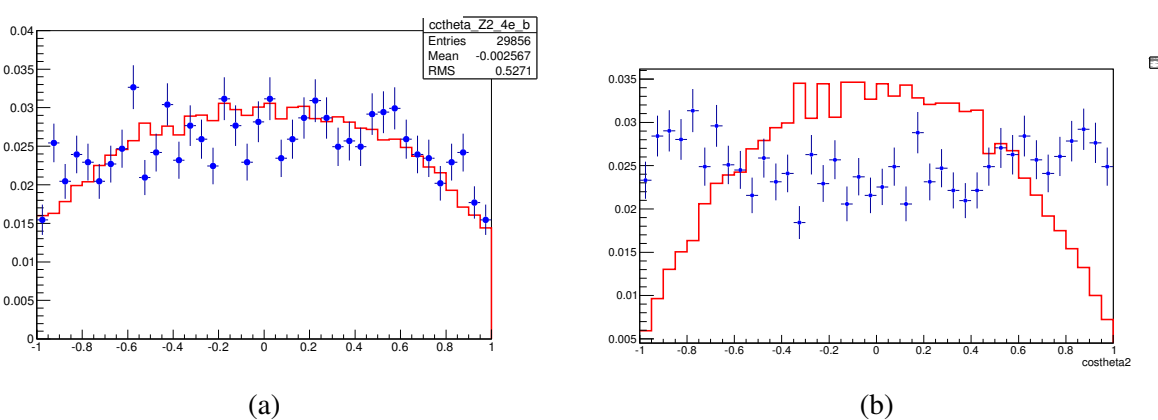


Figure 142: Distribution of the $\cos \theta_2$ angle, $m_H=130$ GeV (a) and $m_H=360$ GeV (b). The red histogram shows the distribution for the Higgs signal, the blue points for the $ZZ^{(*)}$ irreducible background.

Moving on to the Higgs reference frame the 2 Zs are produced back to back. Since the Higgs is a spin-0 scalar boson, the 2 Zs emission is consequently isotropic in space, thus the signal shape has to be flat within the angular ranges. We can define Θ as the angle between the the 2 decaying Zs direction in the Higgs reference frame and the z axis.

$$\Theta = \arctan\left(\frac{p_T^*}{p_Z^*}\right) \quad (5)$$

Figure 143 shows the comparison between the 130 and 360 GeV Higgs signals and the corresponding low mass and high mass backgrounds.

The results shown in this section indicate that decay angles allow to have some discriminating power at high mass, but a negligible one at low mass.

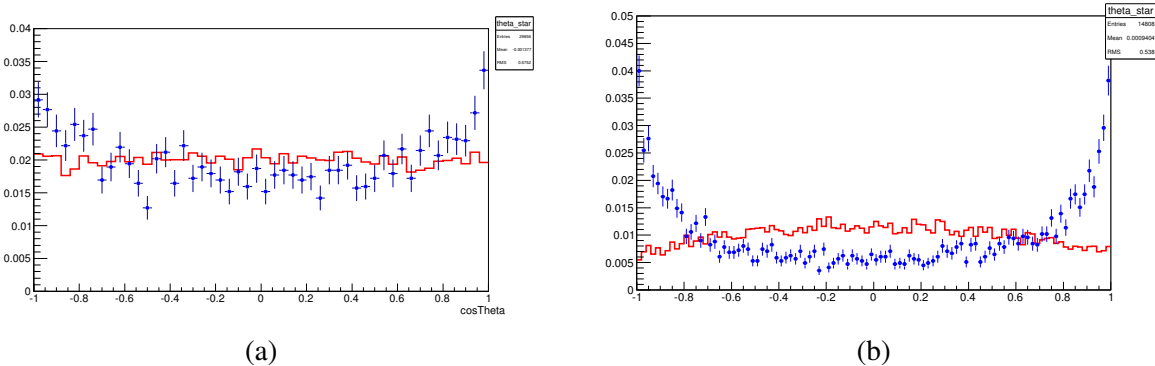


Figure 143: Distribution of the $\cos \Theta$ angle, $m_H=130$ GeV (a) and $m_H=360$ GeV (b). The red histogram shows the distribution for the Higgs signal, the blue points for the $ZZ^{(*)}$ irreducible background.

R.1.3 Production angles

Several theoretical analyses show that the p_T distribution of the Higgs boson is significantly harder than the one of the ZZ pair in the background process. This is true in the case of the dominant Higgs production mechanism, namely the ggf, and even more evident in the sub-dominant vbf production mechanism, where the Higgs is naturally boosted.

In order to exploit this feature, we have considered the $\Delta\phi_{ZZ}$ angle, calculated now in the laboratory reference frame as the difference between the two following angles:

$$\phi_{Z1}^A = \arctan\left(\frac{p_{y1}}{p_{x1}}\right) \quad (6)$$

$$\phi_{Z2}^A = \arctan\left(\frac{p_{y2}}{p_{x2}}\right) \quad (7)$$

$\Delta\phi_{ZZ}$ defined is the azimuthal angle between the 2 Zs in the transverse plane in the lab reference frame:

$$\Delta\phi_{ZZ} = |\phi_{Z1}^A - \phi_{Z2}^A| \quad (8)$$

This angle is clearly correlated to the Higgs p_T . Infact, the higher is the Higgs p_T the smaller is the aperture of the two Z in the transverse plane. Figure 144 shows the distribution of the $\Delta\phi_{ZZ}$ angle for the signal and the irreducible $ZZ^{(*)}$ background, for Higgs masses of 130 GeV and 360 GeV.

In order to evaluate the systematics on this variable due to the MC generation scheme, we have compared, for the 130 GeV Higgs signal, the reconstructed distributions starting from three different generators: Powheg NLO, Mc@NLO, and Hqt2 NNLO. The comparison among the outcome with the three generators is shown in fig.145. It can be seen that the main feature of the distribution, namely the prominence of values of the angle close to 0, doesn't depend too much on the generation scheme.

Given the promising separation between signal and background, at low masses, we have considered different Higgs and ZZ irreducible background production mechanisms (ggf vs vbf for the signal production, $qq \rightarrow ZZ$ vs $gg \rightarrow ZZ$ for the background). Figure 146 compares the $\Delta\phi_{ZZ}$ distributions of the signal between ggf and vbf production mechanisms.

The study presented in this appendix shows that adding angular information in the signal search can give additional discriminating power between signal and ZZ background. The discriminating power is such, that the variables will have to be combined in a multivariate analysis. In particular we have seen that decay angular distributions can be useful at high Higgs masses while, on the other hand production angular distributions can be useful mainly at low masses. These variables are not used in the present

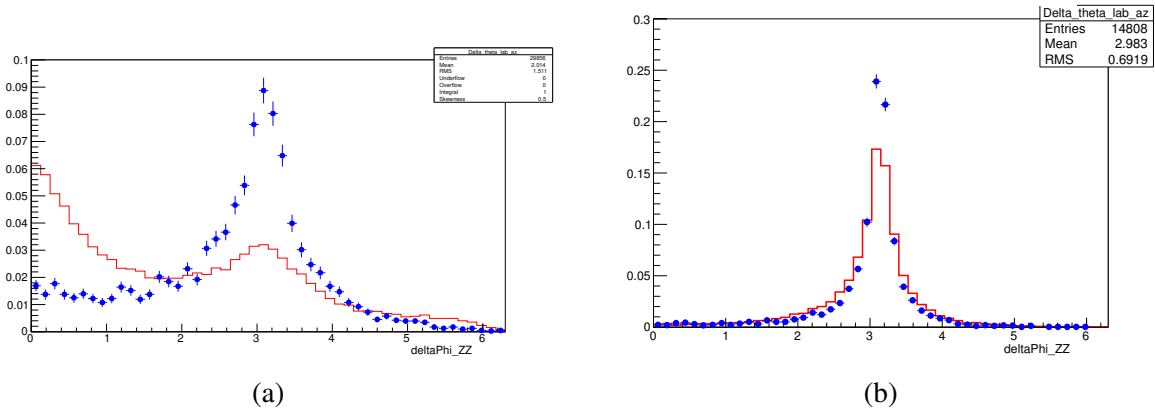


Figure 144: Distribution of the $\Delta\phi_{ZZ}$ angle, $m_H=130$ GeV (a) and $m_H=360$ GeV (b). The red histogram shows the distribution for the Higgs signal, the blue points for the $ZZ^{(*)}$ irreducible background.

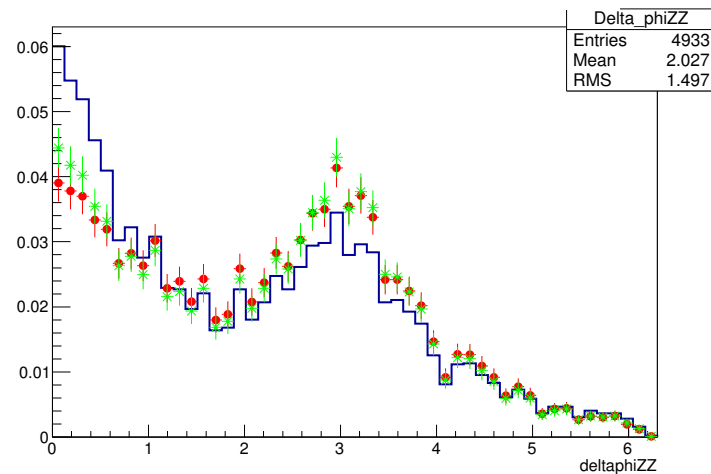


Figure 145: $\Delta\phi_{ZZ}$ for $m_H=130$ GeV: comparison of a simulation based on Powheg NLO (blue histogram), Mc@NLO (red points) and Hqt2 NNLO (green points).

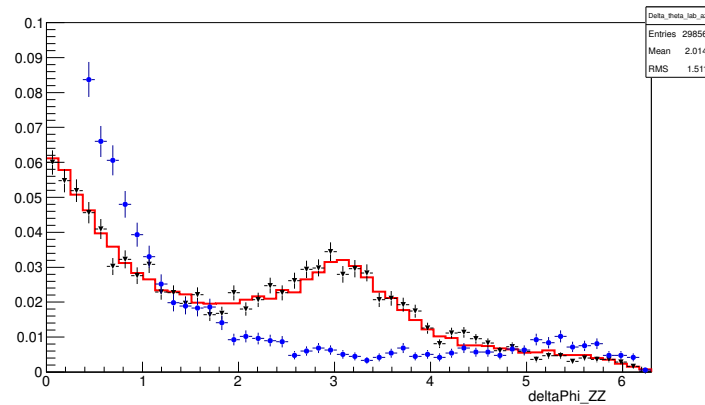


Figure 146: $\Delta\phi_{ZZ}$, $m_H = 130$ GeV; Pythia distribution in red; ggf signal in black, vbf in blue.

analysis. A quantitative assessment of the improvement in sensitivity is in progress, in view of the use of them in the 2012 analysis.